PELDOR and Hyperfine Spectroscopy as Complementary Tools to Investigate a Tetracycline-binding RNA Aptamer

Dissertation
for obtaining the PhD degree
of natural sciences

Submitted to Department 14
of the Goethe University Frankfurt
in Frankfurt am Main

by
Thilo Fritz Bodo Hetzke
from Frankfurt am Main, Germany

Frankfurt am Main, 2019
(D30)

Accepted by Department 14: Biochemistry, Chemistry and Pharmacy
of the Goethe University Frankfurt as a dissertation

Dean:	Professor Clemens Glaubitz
First expert assessor:	Professor Thomas Prisner
Second expert assessor:	Professor Josef Wachtveitl
Date of the disputation:	.....

Keeping it cool with cryo

—Foals, On the Luna

Abstract

Since the early 2000s, nucleic acid aptamers have gained considerable attention of life science communities. This is in particular due to the fact that aptamers are known to function as artificial riboswitches, which presents an efficient way to regulate gene expression. A promising candidate is the tetracycline-binding RNA aptamer (TC-aptamer) since the TC-aptamer is known to function in vivo and exhibits a very high affinity towards its ligand tetracycline (TC) ($K_d = 800\,\mathrm{pM}$ at $10\,\mathrm{mM}$ Mg^{2+}). Although a highly resolved crystal structure exists in the ligand bound state, questions related to dynamics cannot be answered with X-ray crystallography. In this work, pulsed electron paramagnetic resonance (EPR) spectroscopy was used to study different biochemical and structural aspects of the TC-aptamer.

On the one hand, pulsed hyperfine spectroscopy was used to study the binding of TC via Mn^{2+} to the TC-aptamer at lower and thus more physiological divalent metal ion concentrations. In a first step, a protocol for the relatively new pulsed hyperfine technique electron-electron double resonance detected NMR (ELDOR-detected NMR or just EDNMR) was developed for Q-band frequencies (34 GHz). After a successful verification of the EDNMR technique at Q-band frequencies on Mn^{2+} model complexes ($[Mn(H_2O)_6]^{2+}$ and Mn-DOTA), two-dimensional hyperfine techniques were used to confirm the formation of a ternary RNA-Mn^{2+}-TC complex at physiological divalent metal ion concentrations. Correlation signals between ^{13}C (^{13}C-labeled TC) and ^{31}P (from the RNA backbone) to the same Mn^{2+} electron spin were detected with 2D-EDNMR and triple hyperfine correlation spectroscopy (THYCOS).

On the other hand, pulsed electron-electron double resonance (PELDOR) spectroscopy on a doubly nitroxide-labeled TC-aptamer was used to investigate

the conformational rearrangement upon ligand binding and how the conformational flexibility is affected by different Mg^{2+} concentrations. The Çm spin label was used as a nitroxide spin probe. Due to its rigidity and low degree of internal flexibility, the Çm spin label yields very narrow distance distributions and pronounced orientation selection (OS). As a consequence, the width of the distance distributions can be used to draw conclusions about the conformational flexibility of the spin-labeled helices. Analysis of the distance distributions showed that at high Mg^{2+} concentrations, the TC-aptamer is in its folded state, irrespective of the fact if TC is present or absent. Orientation selective PELDOR revealed that the orientation of the spin-labeled helices in frozen solution is the same as in the crystal structure.

First Mn^{2+}-nitroxide pulsed electron-electron double resonance (PELDOR) measurements on a singly nitroxide-labeled and Mg^{2+}/Mn^{2+}-substituted TC-aptamer at different Mn^{2+} concentrations in the presence and absence of TC gave insight into the affinities of the additional divalent metal ion binding sites of the TC-aptamer.

Acknowledgments

At first I would like to thank Professor Thomas Prisner for his constant support during my PhD thesis. The regular discussions were always very helpful for enlighten dark spots of my magnetic resonance knowledge, for planning further research and for writing publications. I was wowed by his way of supervising PhD students and thinking about science. I am also strongly indebted to Dr Alice Bowen for introducing me into operating EPR spectrometers, scientific thinking and planning of experiments and for bringing wine gums from the UK to Frankfurt.

I owe deep gratitude to the collaborators of my PhD projects - without these people none of the projects could have been realized. Professor Beatrix Suess, Dr Marc Vogel and Dr Julia Weigand are thanked for their constant supply of RNA and fruitful discussions of RNA-related problems. Professor Snorri Sigurdsson, Dr Dnyaneshwar Gophane, Dr Subham Saha and Anna-Lena Segler are thanked for their supply of high-quality spin labels.

I would like to thank Katja for being a fantastic office colleague. We had lots of fun-filled hours. I would also like to thank my other office colleagues - especially Sigrid Kämmerer and Dr Juan Carlos Lagomacini. The whole AK Prisner group provided a great working atmosphere. I wish to acknowledge Dr Burkhard Endeward for having an answer to essentially everything. I thank Philipp van Os for his gift of predicting football games and his ability to make a joke out of every sentence possible. I am grateful to Dimi for explaining a lot on Mn^{2+}-based EPR theory. Nicole helped in solving MATLAB related problems of OS PELDOR programs. I want to thank several people for proof-reading parts of the thesis, namely: Carsten, Burkhard, Helen, Katja, Manik, Max, Philip and Sonja.

I am thankful to kicker.de and NFL.com for not having downtimes in the past five years that lasted more than 10 minutes. I DO NOT thank the unknown person who put licorice on my table. (If the unknown licorice person is among the people who were already acknowledged, the “thank you” outweighs the “do not thank you”).

Last but not least, I thank my family and especially my wife for their constant support during my PhD program.

Table of Contents

List of Figures and Tables

List of Abbreviations

2D EDNMR	two-dimensional electron-electron double resonance detected NMR
AWG	arbitrary waveform generator
cryo-EM	cryogenic electron microscopy
CW	continuous wave
DEER	double electron-electron resonance
DFT	density functional theory
DOTA	1,4,7,10-Tetraazacyclododecane-1,4,7,10-tetraacetic acid
DQ	double quantum
dsRNA	double stranded RNA
EDNMR	electron–electron double resonance detected NMR
EFG	electric field gradient
ELDOR	electron-electron double resonance
ENDOR	electron-nuclear double resonance
EPR	electron paramagnetic resonance
ESEEM	electron spin echo envelope modulation
FRET	Förster resonance energy transfer
FWHM	full width at half maximum
HYSCORE	hyperfine sublevel correlation spectroscopy
ITC	isothermal titration calorimetry
MAS-DNP	magic angle spinning dynamic nuclear polarization
MD	molecular dynamics

MQ	multi quantum
mRNA	messenger RNA
MTSL	S-(1-oxyl-2,2,5,5-tetramethyl-2,5-dihydro-1H-pyrrol-3-yl)methyl methanesulfonothioate
MW	microwave
NMR	nuclear magnetic resonance
OS	orientation selection
PDA	point dipole approximation
PDS	pulsed dipolar spectroscopy
PELDOR	pulsed electron-electron double resonance
RF	radio frequency
RIDME	relaxation induced dipolar modulation enhancement
RMSD	root-mean-square deviation
RNA	ribonucleic acid
SANS	small angle neutron scattering
SAXS	small angle X-ray scattering
SELEX	systematic evolution of ligands by exponential enrichment
SNR	signal-to-noise ratio
SOC	spin-orbit coupling
SQ	single quantum
SSC	spin-spin coupling
ssRNA	single stranded RNA
TC	tetracycline
TC-aptamer	tetracycline-binding RNA aptamer
THYCOS	triple hyperfine correlation spectroscopy
TQ	triple quantum
TRIPLE	ENDOR triple resonance
UV/VIS	ultraviolet-visible
VMT Mims ENDOR	variable mixing time Mims ENDOR

List of Symbols

A_{eff}	effective hyperfine coupling
A	secular part of the hyperfine interaction
$\boldsymbol{A}$	hyperfine tensor, (A_x, A_y, A_z)
a_{iso}	isotropic hyperfine interaction
a_{ij}	transition amplitude of a transition connecting energy levels i and j
a	cubic zero-field parameter
B_0	external magnetic field
$\boldsymbol{B_0}$	external magnetic field vector
B_1	microwave field
B	pseudo-secular part of the hyperfine interaction
Çm	rigid nitroxide-containing cytidine derivative
D	axial zero-field parameter
$\boldsymbol{D}$	zero-field tensor
$\boldsymbol{d}$	electron dipole-dipole tensor
E	rhombic zero-field parameter
E-TU	semi-rigid tetraethylisoindolin spin label
e	elementary charge, $1.6022 \times 10^{-19}\,\mathrm{C}$
g_{eff}	effective g value
g_e	g value of the free electron, 2.0023
g_n	nuclear g value
$\boldsymbol{g}$	g tensor, (g_x, g_y, g_z)
$\mathcal{H}_0$	static spin Hamiltonian
$\mathcal{H}_1$	oscillatory spin Hamiltonian

$\hbar$	reduced planck constant, $1.0546 \times 10^{-34}\,\mathrm{J\,s}$, $h = \hbar 2\pi$
I	nuclear spin quantum number
$\boldsymbol{I}$	nuclear spin vector operator
I_a	transition probability of an allowed transition
I_f	transition probability of a forbidden transition
K_d	dissociation constant
m_I	nuclear spin magnetic quantum number
m_S	electron spin magnetic quantum number
Q	nuclear quadrupole moment
eq	electric field gradient parameter
$e\boldsymbol{q}$	electric field gradient tensor, (V_x, V_y, V_z)
S	electron spin quantum number
$\boldsymbol{S}$	electron spin vector operator, (S_x, S_y, S_z)
$\boldsymbol{T}$	dipolar hyperfine tensor
t_p	length of a pulse, (t_{ELD} for an ELDOR pulse)
β	flip angle, (β_{ELD} for an ELDOR pulse)
β_e	Bohr magneton, $9.2740 \times 10^{-24}\,\mathrm{J\,T^{-1}}$
β_n	nuclear magneton, $5.0508 \times 10^{-27}\,\mathrm{J\,T^{-1}}$
η	asymmetry parameter of nuclear quadrupole interaction
η_α	branching angle describing the nuclear quantization axis in the electron α manifold
η_β	branching angle describing the nuclear quantization axis in the electron β manifold
η	half the angle of the two branching angles η_α and η_β
η_S	Davies ENDOR selectivity parameter
θ	polar angle between z-axis and vector
Δ	modulation depth
λ	spin flip probability
μ_0	magnetic constant, $1.2566 \times 10^{-6}\,\mathrm{T^2\,m^3\,J^{-1}}$
σ	density operator

φ	bend angle between two RNA helices
ϕ	polar angle in the xy-plane
ω_I	nuclear Larmor frequency, $\nu_I = \omega_I/2\pi$
ω_α	nuclear frequency in the electron α manifold, $\nu_\alpha = \omega_\alpha/2\pi$
ω_β	nuclear frequency in the electron β manifold, $\nu_\beta = \omega_\beta/2\pi$
ω_{dd}	electron dipole-dipole coupling constant, $\nu_{dd} = \omega_{dd}/2\pi$
ω_1	microwave field strength of a microwave pulse in $\mathrm{rad\,s^{-1}}$ (ω_{ELD} for an ELDOR pulse)

Chapter 1

Introduction

1.1 Role of EPR Spectroscopy in Structural Biology

Structural biology is a branch of molecular biology, that is dedicated to determine and understand the molecular structure of biological macromolecules like proteins and nucleic acids and how the structure of a biological macromolecule is related to its function. Especially the last aspect cannot be overstated, as this relation draws a direct connection between structural biology and all biochemical transformations in cells.

It is therefore not surprising that scientists have a wide range of methods at their disposal to elucidate the structure of biological macromolecules. Among the most frequently used techniques are nuclear magnetic resonance (NMR) spectroscopy and X-ray crystallography. These techniques can yield a highly resolved three-dimensional atomistic structure. Despite a constant development of new pulse sequences, liquid NMR-based structure elucidation is still limited by the size of the macromolecule under investigation, which is 100 nucleotides for nucleic acids ($\approx 30\,\mathrm{kDa}$) [1] and $\approx 100\,\mathrm{kDa}$ for proteins [2]. X-ray crystallography comes with the drawback that seeding of single crystals can be a tedious endeavor. Due to its static nature, X-ray crystallography does not offer any insights into questions related to structural dynamics.

A rapidly emerging field in the past years is cryogenic electron microscopy (cryo-EM), in which an electron beam is transmitted through a specimen at

cryogenic temperatures which is embedded in a glassy water matrix [3]. If sufficient computational power is available, cryo-EM allows a near-atomistic structure determination. In contrast to NMR, however, cryo-EM is not able to capture atomistic structures of macromolecules with a size smaller than $\approx 75\,\mathrm{kDa}$ [4, 5]. This is due to increasing problems in image processing for smaller macromolecules.

Other structural biology methods include mass spectrometry [6], small angle X-ray scattering (SAXS) and small angle neutron scattering (SANS) [7], solid-state NMR under magic angle spinning dynamic nuclear polarization (MAS-DNP) conditions [8] as well as fluorescence-based methods such as Förster resonance energy transfer (FRET) spectroscopy [9].

Another important tool in structural biology is electron paramagnetic resonance (EPR) spectroscopy, in which physical properties of unpaired electron spins are used to obtain structural information of biological macromolecules [10]. Pulsed EPR spectroscopy can be subdivided into pulsed dipolar spectroscopy (PDS) and pulsed hyperfine spectroscopy. Whereas PDS techniques can be used to measure long distance distribution constraints in the nanometer regime (2 to 16 nm [11]), pulsed hyperfine spectroscopy can be used to probe the interaction of coupled nuclear and electron spins up to a distance of 1 nm [12]. Although EPR spectroscopy is not able to resolve a three-dimensional structure on its own, is has some unique advantages over NMR, cryo-EM and X-ray crystallography. Firstly, EPR spectroscopy is not constrained by the size of the macromolecule. Secondly, very specific moieties or regions of the macromolecule can be observed with EPR spectroscopy. This is because the macromolecule itself is EPR-silent in most cases, hence the site-specific introduced EPR spin label is the sole source of an EPR signal. This stands in contrast to the aforementioned high-resolution techniques, where signal assignment is often a non-trivial task as signals occur in high abundance. Thirdly, extraction of EPR data is a parameter free approach, thus simplifying data interpretation. FRET measurements, for example, rely critically on the orientation factor κ.

The only requirement for EPR measurements is typically the introduction of spin labels. Nowadays, nitroxides are the most commonly used form of EPR spin probes. In some cases, paramagnetic co-factors (transition metals) can

be used for EPR measurements, which makes the introduction of nitroxide radicals obsolete. Sometimes, diamagnetic metal ions can be substituted by paramagnetic metal ions, e.g., substitution of Mg^{2+} with Mn^{2+} [13]. The only caveat of pulsed EPR is that measurements are typically performed at cryogenic temperatures of 50 K or lower. This is necessary, since electron spins possess a rather short spin decoherence time, which makes an observation at ambient temperatures challenging if not impossible. If possible, it is advisory to compare pulsed EPR measurements of a frozen solution to data from other structural biology techniques obtained at ambient temperature and physiological conditions (integrative structural biology).

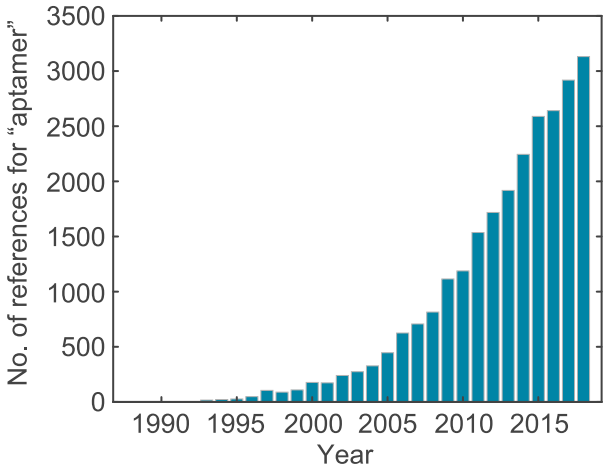

Figure 1.1: Bar graph of SciFinder references containing the word "aptamer" as a function of the year of publication.

Until the late 1990s, structural biology was mainly focused on understanding the structure and function of proteins. With the "awakening" of nucleic acid aptamers (Figure 1.1), however, nucleic acid molecules gained attention among structural biologists. Unfortunately, nucleic acid (aptamer) structural biology is more challenging than protein structural biology. For instance, cryo-EM struggles with resolving the structure of macromolecules with a mass smaller than 50 kDa, which is the typical molecular weight of aptamers. Nucleic acid X-ray crystallography suffers from the disadvantage that nucleic acids exhibit a higher intrinsic degree of freedom than folded protein structures, which makes

nucleic acids more difficult to crystallize. In addition, nucleic acids bear one negative charge at the phosphate group per residue, whereas the net charge of proteins is rather small. As a consequence, repulsion forces between two nucleic acid molecules are stronger than between two protein molecules, which hampers nucleic acid crystallization even further.

Nucleic acid NMR spectroscopy suffers from the drawback that the chemical-shift dispersion is much smaller than for protein NMR spectroscopy. This is because nucleic acids are composed of only 4 different nucleobases, whereas for proteins 21 different proteinogenic amino acids exist for eukaryotes. In addition, proteins exhibit various secondary structure elements, each with a specific NMR-fingerprint. In contrast, ribonucleic acid (RNA) molecules are mainly composed of the A-form helix as the sole secondary structure element. Furthermore, nucleic acid NMR spectroscopy cannot rely on D_2O as a signal-enhancing solvent, since the high percentage of nucleic acid exchangeable protons would render the detection of hydrogen nuclei impossible.

On the other hand, nucleic acid EPR spectroscopy is not handicapped by any of the aforementioned problems. Quite the contrary, nucleic acid EPR spectroscopy offers a wide choice of labeling schemes and spin labels [14]. For example, nucleic acid molecules can be labeled with rigid nitroxide spin labels [15, 16], which is so far not possible for proteins. Rigid spin labels allow to extract angular information besides distance distribution restraints. The previous paragraphs show that EPR spectroscopy may be even more important in nucleic acid structural biology than in protein structural biology.

1.2 The Tetracycline-binding RNA Aptamer

Aptamers describe a class of macromolecules that bind a small molecule with high affinity. Although the term also applies to proteins [17], the word aptamer normally refers to nucleic acid aptamers. Nucleic acid aptamers rarely exceed 100 nucleotides, which translates into $\approx 33\,\mathrm{kDa}$. Oligonucleotide sequences that show a high affinity toward a specific ligand are normally discovered by an in vitro selection procedure also called systematic evolution of ligands by expo-

nential enrichment (SELEX) [18, 19]. The tetracycline-binding RNA aptamer (TC-aptamer) was discovered by SELEX in the Schroeder lab [20]. Chemical probing experiments suggested a secondary structure which involves three helical stems and a bulge region where ligand binding occurs [21]. An exceptionally low dissociation constant of $K_d = 800\,\text{pM}$ was later found with fluorescence spectroscopy and isothermal titration calorimetry (ITC) for an optimized TC-aptamer secondary structure ("minimer") [22]. This is one of the lowest K_d values reported so far among small molecule RNA aptamers.

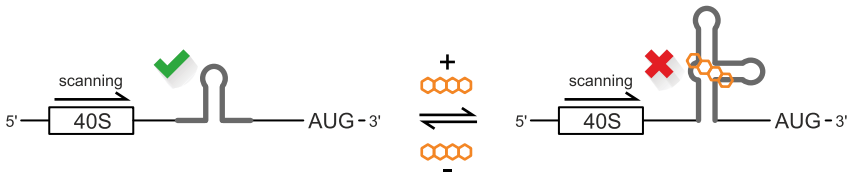

Figure 1.2: Possible mechanism for the TC-aptamer as an artificial riboswitch. If incorporated into mRNA, the scanning process of the ribosomal 40S subunit proceeds as usual if no TC is present. Upon addition of TC, however, a conformational change is induced which stops the scanning process and therefore inhibits translation [23].

In addition, the TC-aptamer is one of only a few aptamers that are capable to control translation and splicing even in living cells [24–26]. This opens the exciting possibility of using the TC-aptamer as an artificial riboswitch. This way, gene regulation is no longer controlled by large macromolecules but rather by small molecules, i.e., tetracycline (TC), provided that the aptamer was previously successfully incorporated into messenger RNA (mRNA) (Figure 1.2). The aforementioned properties, paired with the low-toxicity and good cell permeability of TC [27], make the TC-aptamer an interesting system for structural biologists.

The crystal structure of the TC-aptamer in the ligand-bound state confirmed the hypothesis of three helices and a bulge region that is part of the ligand binding pocket (Figure 1.3A) [28]. In addition, it was found that TC binds via a Mg^{2+} chelate complex to the RNA. More Mg^{2+} ions were found to bind the aptamer via phosphate backbone interactions, which confirmed the important role of Mg^{2+} ions in the folding process of the aptamer as already suggested by chemical probing experiments [24]. Fluorescence, ultraviolet-visible (UV/VIS)

spectroscopy and thermodynamical studies subsequently tackled the question of conformational dynamics and how the Mg^{2+} concentration affects ligand binding and RNA folding. It was concluded that nucleotide $A9$ is essential for TC binding and folding, which was best described by a 2-step binding model [29]. In a follow-up study, Reuss et al. investigated the influence of Mg^{2+} concentration on the folding process [30]. The authors found that TC is a crucial factor at intermediate Mg^{2+} concentrations for forming the tertiary structure. At high Mg^{2+} concentrations, Mg^{2+} alone is sufficient to induce folding of the RNA.

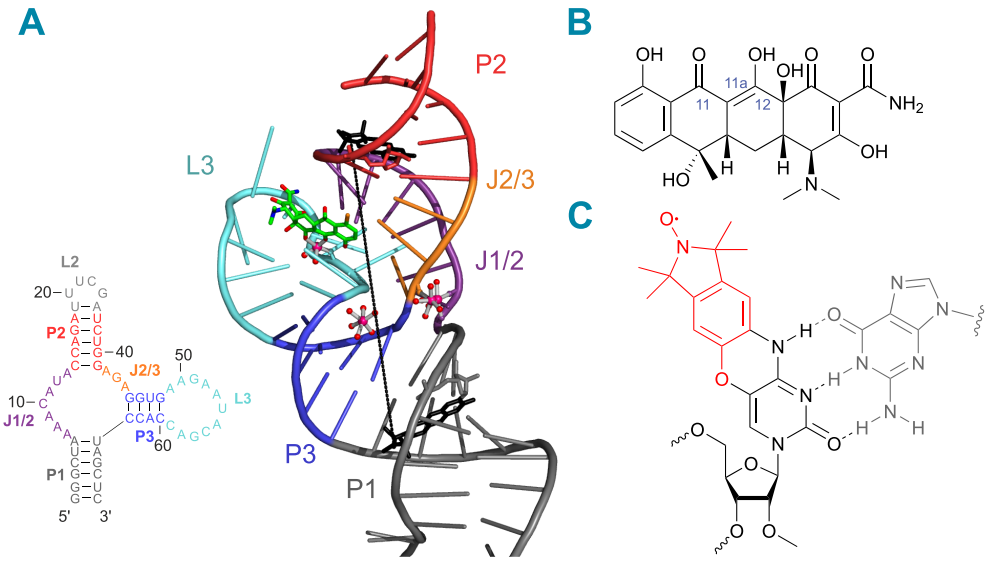

Figure 1.3: A) Secondary structure of the TC-aptamer as used in the study by Reuss et al. [30] and tertiary structure of the TC-aptamer based on the crystal structure by Xiao et al. [28]. The ligand TC is shown in green, Mg^{2+} ions are shown in magenta. Two Çm spin labels were attached to the molecular model at positions $C3$ and $C15$ (black). B) Chemical structure of TC. C) Chemical structure of the rigid Çm spin label [16].

In a pulsed EPR study using flexible nitroxide spin labels at X-band frequencies (9.4 GHz), Wunnicke et al. focused on obtaining a deeper insight into structural rearrangements of the aptamer upon addition of the ligand [31]. They concluded that mainly junction $J1/2$ is displaced if TC is added.

Figure 1.3A shows the tertiary structure of the TC-aptamer based on the crystal structure [28]. The secondary structure shown in Figure 1.3A resembles

the one that was used in previous EPR and thermodynamic studies [29–31]. The secondary structure of the crystal structure does not contain loop $L2$. Instead, the secondary structure contains a capping region at helix $P1$, which also accommodates a protein $U1A$ binding site to facilitate crystallization of the TC-aptamer (not shown in figure 1.3A). Two Çm spin labels, used for pulsed EPR measurements and introduced via solid-phase synthesis at positions $C3$ and $C15$, are shown in black. The labeling positions were chosen to be as close as possible to the binding pocket without disturbing ligand binding and folding of the RNA. In silico simulations of the crystal structure with two Çm spin labels did not show any sterical clashes. Figure 1.3B shows the chemical structure of TC. Metal ligation typically occurs via the oxygen atoms $O11$ and $O12$ [32, 33]. Figure 1.3C shows the chemical structure of the rigid Çm spin labels. In contrast to commonly used nitroxide spin labels like MTSL, Çm does not contain a flexible linker region. As a result, the internal rigidity of Çm allows to directly investigate the conformational flexibility of the spin-labeled RNA helices.

1.3 Motivation and Aim

The overal goal of this PhD project was to characterize and investigate a TC-aptamer with state-of-the-art pulsed EPR spectroscopy. To achieve this, new spin labels, novel EPR pulse sequences and different EPR techniques were used. Since different biochemical and structural aspects of the TC-aptamer were investigated, the global objective of this thesis was further subdivided into different subgoals and subprojects.

The first aim of the thesis was to study the conformational rearrangements upon TC binding and how the conformational flexibility of the tertiary structure of the TC-aptamer is affected by binding and the divalent metal ion concentration. Although recent thermodynamic and fluorescence studies already investigated the folding of the TC-aptamer on a macroscopic scale [29, 30], no studies exist that study the structural rearrangements upon ligand binding and the stability of the tertiary structure on an atomistic level. To achieve this aim, pulsed electron-electron double resonance (PELDOR) spectroscopy in combination with the rigid

Çm spin label at X-band (9.4 GHz) and Q-band frequencies (34 GHz) was used. Special emphasis was put on the evaluation of the properties of the Çm spin label, which not only allows to extract distance restraints and conformational flexibilities but also allows to obtain angular information and the bend angle φ between two spin-labeled RNA helices. To the authors knowledge, application of Çm to the TC-aptamer is the first time that the Çm spin label was used to answer questions on a biological relevant RNA.

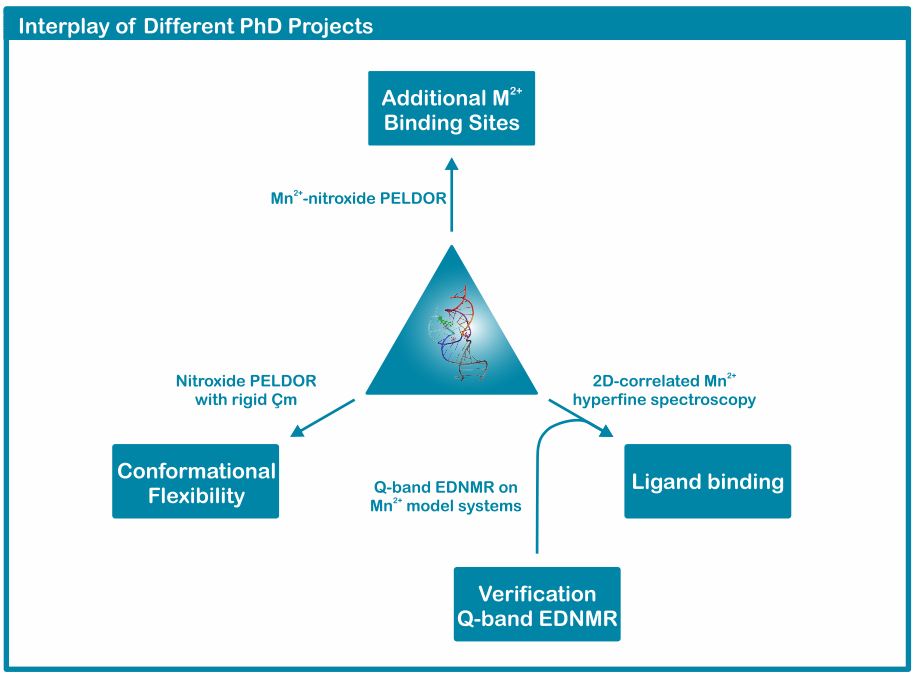

The second aim of the thesis was to study ligand binding and the local geometry of the ligand binding center. Even though it is known that ligand binding is strong at high Mg^{2+} concentrations, less information is available for ligand binding at lower and more physiological concentrations. Apart from the crystal structure, the local geometry of the ligand binding pocket has thus far not been investigated on an atomistic level. To gain more insights into these questions, pulsed EPR hyperfine spectroscopy and substitution of diamagnetic Mg^{2+} with paramagnetic Mn^{2+} was used. More specifically, the local geometry of the divalent metal ion binding sites was investigated with pulsed ^{13}C and ^{31}P electron-nuclear double resonance (ENDOR) techniques. The binding of TC via a Mn^{2+} ion to the TC-aptamer was probed by correlating ^{13}C nuclei from

^{13}C-labeled TC to ^{31}P nuclei from the RNA backbone to the same Mn^{2+} electron spin. This required the use of novel two-dimensional hyperfine techniques such as two-dimensional electron-electron double resonance detected NMR (2D EDNMR) and triple hyperfine correlation spectroscopy (THYCOS) [34, 35]. The advantages and disadvantages of both methods to investigate ternary paramagnetic Mn^{2+} complexes on an atomistic level were evaluated.

2D EDNMR and THYCOS are based on the electron–electron double resonance detected NMR (EDNMR) experiment. As the EDNMR technique is a rather new pulsed hyperfine technique [36] and has so far only been applied at higher magnetic fields, i.e., W-band (94 GHz), the applicability of EDNMR at Q-band frequency was first verified in a proof of concept study. To this end, Q-band EDNMR was performed and optimized on Mn^{2+} model systems, e.g., $[Mn(H_2O)_6]^{2+}$ and Mn^{2+} ligated with ^{13}C-enriched DOTA (Mn-^{13}C-DOTA).

The third aim of the thesis was to study the affinity of the additional divalent metal ion binding sites and their importance for RNA folding. Although numerous additional binding sites are resolved in the crystal structure, little is known about their function and affinity. In the past, biochemical and thermodynamic studies highlighted the importance of several nucleotides and secondary structure elements [21, 22, 29–31]. However, none of theses studies draw a conclusion about the affinity and function of the additional divalent metal ion binding sites. In order to tackle these challenges, Mn^{2+}-nitroxide PELDOR on a Mg^{2+}/Mn^{2+} substituted and singly nitroxide-labeled TC-aptamer at different Mn^{2+} concentrations in the absence and presence of the ligand TC was performed. Binding affinities of the additional Mn^{2+} binding sites could be interpreted by comparing the distance distribution probabilities of different binding sites at different divalent metal ion concentrations in the presence and absence of the ligand TC to distances extracted from the crystal structure.

Chapter 2

Principles and Theory

2.1 Spin Hamiltonian

2.1.1 Zeeman Interactions

EPR spectroscopy describes the magnetic interaction of an unpaired electron spin S with the external magnetic field $\boldsymbol{B_0}$ vector, other electrons spins S or nuclear spins I. Such interactions are described by a static spin Hamiltonian $\mathcal{H}_0$, first derived by Abragam and Pryce using perturbation theory [37]. The word "static" refers to the fact that $\mathcal{H}_0$ only contains electron and nuclear spin coordinates and furthermore does not include time-dependent external microwave (MW) fields. Often, the electron Zeeman interaction $\mathcal{H}_{EZ}$ is the dominant interaction of $\mathcal{H}_0$. It is given by

$$\begin{aligned} \mathcal{H}_{EZ} &= \beta_e \boldsymbol{B_0} \boldsymbol{g} \boldsymbol{S} / \hbar, \\ &= \beta_e \boldsymbol{B_0} \left(g_x sin\theta cos\phi S_x + g_y sin\theta sin\phi S_y + g_z cos\theta S_z \right) / \hbar, \end{aligned} \tag{2.1}$$

where β_e describes the Bohr magneton, $\boldsymbol{g}$ the g tensor and $\boldsymbol{S}$ the electron spin vector operator. S_x, S_y and S_z describe the respective Pauli matrices and θ and ϕ are the polar angles which describe the orientation of B_0 with respect to the g tensor molecular frame. The g factor is a proportionality coefficient between the experimentally measured and theoretically predicted magnetic moment from the angular momentum of a spin. It can be an anisotropic or isotropic quantity and is described by a 3×3 tensor. In its principal axis system, $\boldsymbol{g}$ is a diagonal

matrix with the principal values g_x, g_y and g_z. Equation 2.1 can be diagonalized by a unitary transformation and rewritten as

$$\mathcal{H}_{EZ} = \beta_e B_0 g_{eff} S_z / \hbar. \tag{2.2}$$

In Equation 2.2, the orientation of the g tensor to B_0 is now included in g_{eff}:

$$g_{eff} = (g_x^2 sin^2\theta cos^2\phi + g_y^2 sin^2\theta sin^2\phi + g_z^2 cos^2\theta)^{1/2}. \tag{2.3}$$

For Equation 2.2, the diagonal elements are equal to the eigenvalues and therefore represent the energy levels of a $S = 1/2$ spin system:´

$$\epsilon_{\alpha,\beta} = \pm\frac{1}{2}\beta_e B_0 g_{eff}. \tag{2.4}$$

Similar to $\mathcal{H}_{EZ}$, $\mathcal{H}_{NZ}$ describes the interaction of a nuclear spin I with the external magnetic field vector $\boldsymbol{B_0}$:

$$\mathcal{H}_{NZ} = g_n \beta_n \boldsymbol{B_0 I} / \hbar, \tag{2.5}$$

where $\boldsymbol{I}$ describes the nuclear spin vector operator. For most EPR experiments, the nuclear g value g_n can be assumed to be isotropic, although this is strictly speaking not true [38, p. 142]. Nuclear g values are intrinsic properties of the nuclear species and can adopt positive and negative values. Due to its smaller magnitude, $\mathcal{H}_{NZ}$ typically does not affect the EPR spectrum ($g_{1H} = 1/658 \times g_e$), however, $\mathcal{H}_{NZ}$ plays an essential role in hyperfine spectroscopy.

2.1.2 Hyperfine Interaction

The interaction of magnetic moments of electron and nuclear spins is described by the hyperfine tensor $\boldsymbol{A}$:

$$\mathcal{H}_{HF} = \boldsymbol{SAI} = \boldsymbol{S} a_{iso} \boldsymbol{I} + \boldsymbol{STI}. \tag{2.6}$$

$\boldsymbol{A}$ can be further separated into an isotropic "through-bond" component a_{iso} (also called Fermi contact interaction) and a dipolar "through-space" interaction

$\boldsymbol{T}$. In its principal axis system, $\boldsymbol{A}$ is described by three principal values. Within the point dipole approximation (PDA), $\boldsymbol{T}$ is an axial and traceless tensor and $\boldsymbol{A}$ can thus be described by only two independent variables a_{iso} and T:

$$\boldsymbol{A} = \begin{pmatrix} A_x & & \\ & A_y & \\ & & A_z \end{pmatrix} \xrightarrow{\text{PDA}} \begin{pmatrix} A_\perp & & \\ & A_\perp & \\ & & A_\parallel \end{pmatrix} = a_{iso} + \begin{pmatrix} -T & & \\ & -T & \\ & & 2T \end{pmatrix}. \quad (2.7)$$

In principle, three more variables α, β and γ are needed to describe the hyperfine tensor $\boldsymbol{A}$. α, β and γ are Euler angles that transform the principal hyperfine tensor frame into the molecular frame, which is often defined as the principal frame of the g tensor. In cases where the principal frame of the g tensor and hyperfine tensor are (almost) collinear, e.g., nitroxides [39], or the g tensor is isotropic, e.g., Mn^{2+} [40], α, β and γ are all zero.

The isotropic hyperfine interaction a_{iso} is a measure for the probability of the electron spin to be located at the nucleus:

$$a_{iso} = \frac{2}{3}\frac{\mu_0}{\hbar} g_e \beta_e g_n \beta_n |\Psi_0(0)|^2, \quad (2.8)$$

where $|\Psi_0(0)|^2$ is the electron spin density at the nucleus. Equation 2.8 suggests that only electron spins located in a s orbital exhibit an isotropic hyperfine interaction. However, many $3d^5$ transition metal ions, e.g., Cr^+, Fe^{3+}, Mn^{2+} and Co^{4+}, show a rather pronounced isotropic hyperfine value. Configuration interaction of $3s^2 3d^5$ with $3s 3d^5 4s$ as well as strong spin polarization of the inner-filled $2s$ and $3s$ orbitals are reasons for strong isotropic hyperfine interactions of the aforementioned transition metals with half-filled $3d$ orbitals [41, 42].

As a "through-space" interaction, the dipolar hyperfine coupling $\boldsymbol{T}$ depends on the distance r between a nucleus and the electron spin-containing atomic orbital. In cases where $r \geq 0.25\,\text{nm}$, the PDA can be used to describe the dipolar hyperfine tensor:

$$\boldsymbol{T} = \frac{\mu_0}{4\hbar}\frac{g_e \beta_e g_n \beta_n \rho_M}{r^3} \begin{pmatrix} -1 & & \\ & -1 & \\ & & 2 \end{pmatrix} = \begin{pmatrix} -T & & \\ & -T & \\ & & 2T \end{pmatrix}. \quad (2.9)$$

ρ_M stands for the electron spin density at the central ion. For positively charged transition metal ions it is often justified to assume $\rho_M = 1$. If a_{iso} and $\boldsymbol{T}$ are known, the spin population in ligand orbitals can be calculated using the table by Morton and Preston [43]. Assuming an isotropic hyperfine coupling of $a_{iso} = 4\,\mathrm{MHz}$ for a first-coordination-sphere-coupled ^{31}P-Mn^{2+} nucleus, this translates into 0.03 % spin population in the ^{31}P $3s$ orbital (the isotropic hyperfine interaction for a unit spin density in the $3s$ orbital is 13 306 MHz [43]). The spin population in a ^{31}P $3p$ orbital can be obtained by multiplying the angular factors for p orbitals $(-2/5, -2/5, 4/5)$ with the corresponding anisotropic hyperfine parameter P, which were reported by Morton and Preston (917 MHz for ^{31}P $3p$ orbitals) [43]. For an experimentally measured value of $T = 0.9\,\mathrm{MHz}$, this yields a spin population of 0.25 % in the $3p$ orbital and thus a total spin population of 0.28 % on the ^{31}P nucleus. In this case it is therefore justified to assume $\rho_M = 1$.

In some cases, it is convenient to express the hyperfine interaction in the laboratory frame. $\mathcal{H}_{HF}$ then becomes

$$\mathcal{H}_{HF} = \boldsymbol{SAI} = AS_zI_z + BS_zI_x. \tag{2.10}$$

Non-secular terms containing S_x and S_y are discarded due to assumption of the high-field approximation. The quantities $A = A_{zz}$ and $B = \sqrt{A_{zx}^2 + A_{zx}^2}$ describe the secular and pseudo-secular term of the hyperfine interaction. They are related to the principal values of $\boldsymbol{A}$ by the following equations:

$$A = A_{\parallel}cos^2\theta + A_{\perp}sin^2\theta = a_{iso} + T(3cos^2\theta - 1) \tag{2.11A}$$

$$, B = (A_{\parallel} - A_{\perp})sin\theta cos\theta = 3Tsin\theta cos\theta. \tag{2.11B}$$

Later on, A and B become important for predicting and understanding the nuclear frequencies ω_α and ω_β and transition probabilities of allowed and forbidden transitions (Section 2.4).

2.1.3 High-Spin Interactions

For electron and nuclear high-spin systems ($S > 1/2$ and $I > 1/2$), additional interactions have to be considered. In case of electron spins, this interaction is

referred to as the zero-field interaction. As the name suggests, the zero-field interaction lifts the degeneracy of the electron spin manifolds, even at zero field. One possible physical origin of the zero-field interaction is the spin-spin coupling (SSC), in which two or more electron spins in the same paramagnetic spin center are dipolar coupled. Another possibility is the spin-orbit coupling (SOC). Here, different projections of the electron spin vector can couple in different magnitudes to the orbital angular momentum of the ground and/or excited state, thus lifting degeneracy already at zero field.

Organic triplet states ($S = 1$) and paramagnetic transition metal ions are typically affected by a rather strong zero-field interaction. In a qualitative perspective, the zero-field interaction describes the deviation from spherical symmetry of the electron spin distribution. Therefore, all electron high-spin systems will exhibit a zero-field interaction if the symmetry is lower than spherical. For an axial symmetry or lower, the tensor notation of the zero-field interaction takes the form

$$\mathcal{H}_{ZF} = \boldsymbol{SDS} = D_x S_x^2 + D_y S_y^2 + D_z S_z^2, \tag{2.12}$$

where $\boldsymbol{D}$ is the zero-field tensor and D_x, D_y and D_z are its principal values. In its principal axis system $\boldsymbol{D}$ is a diagonal and traceless tensor. As a consequence, the zero-field interaction is averaged out at room temperature and fast tumbling rates of the molecule. Equation 2.12 is sometimes referred to as a second-order zero-field interaction because it contains the square of S_x, S_y and S_z. Equation 2.12 can be transformed into its commonly used mathematical formula

$$\mathcal{H}_{ZF} = D\left\{S_z^2 - \frac{1}{3}S\left(S+1\right)\right\} + E\left(S_x^2 - S_y^2\right). \tag{2.13}$$

D is the axial zero-field parameter defined as $D = 3/2D_z$ and E is the rhombic zero-field parameter defined as $E = (D_x - D_y)/2$. At axial symmetry $D \neq 0$, $E = 0$ and at rhombic symmetry $D, E \neq 0$. For electron high-spin systems with $S > 2$, additional higher-order zero-field terms, i.e., fourth-order, have to be considered [44, p. 437]:

$$\mathcal{H}_{ZF,*} = \frac{F}{180} \times \left[35S_z^4 - 30S\left(S+1\right)S_z^2 + 2SS_z^2 - 6S\left(S+1\right) + 3S^2\left(S+1\right)^2\right]. \tag{2.14}$$

The expression in Equation 2.14 is typically small in comparison to the second-order zero-field expression, but they gain significant character for truly octahedral or tetrahedral symmetries, as here $D, E = 0$. Equation 2.14 and the parameter F is not to be confused with the zero-field interaction for a purely cubic symmetry, which also shows a fourth-order dependence and takes the form [44, p. 142]

$$\mathcal{H}_{ZF,cubic} = \frac{a}{6}\left[S_x^4 + S_y^4 + S_z^4 - \frac{1}{5}S\left(S+1\right)\left(3S^2 + 3S - 1\right)\right]. \tag{2.15}$$

a is referred to as the fourth-order or cubic zero-field parameter, as its part comes into play only at truly cubic environments. For Mn^{2+}-doped KN_3 salt, a was found to be as large as 28 MHz [45]. In comparison to a (theoretical) high-spin complex with no zero-field interaction, the presence of zero-field interaction leads to a line broadening [46] and additional splitting of signals, since the different allowed EPR transitions are no longer degenerate.

The nuclear quadrupole interaction is the nuclear spin analogue of the zero-field interaction. It arises because every high-spin nucleus ($I > 1/2$) has a non-spherical distribution of its nuclear spins. The deviation from spherical symmetry is an intrinsic property of the nuclear species and is defined by the nuclear quadrupole moment Q. Q couples with the electric field gradient (EFG) tensor $e\boldsymbol{q}$ generated by the negative charge distribution of the surrounding electrons. As a consequence, the orientation of the non-spherical nuclear charge distribution with respect to the external electric field is energy-dependent. The smallest energy is obtained for an orientation, in which the edges of a prolate ellipsoid of the nuclear charge distribution ($Q > 0$) are very close to the electron-rich part of the external electric field [47, p. 96]. Consequently, a high energy is obtained if the edges of the prolate ellipsoid are far away from the electron-rich part of the external electric field. The orientation-dependent electrostatic energy of a high-spin nucleus is then described by

$$\mathcal{H}_{NQI} = \frac{1}{6} \sum_{i,j=x,y,z} V_{ij} Q_{ij}, \tag{2.16}$$

where V_{ij} and Q_{ij} are the components of the EFG tensor $e\boldsymbol{q}$ and the nuclear quadrupole moment. In the principal axis system of $e\boldsymbol{q}$ and by transforming Q_{ij} into a formula where it only depends on Q, $\boldsymbol{I}$ and I, $\mathcal{H}_{NQI}$ can be rewritten as

$$\mathcal{H}_{NQI} = \frac{e^2 q Q}{4I\,(2I-1)} \left[\left(3I_z^2 - I\,(I+1)^2 \right) + \eta \left(I_x^2 - I_y^2 \right) \right], \tag{2.17}$$

where e is the elementary charge, eq is the electric field gradient parameter and η is the asymmetry parameter of the nuclear quadrupole interaction [47, p. 97]. Similar to the zero-field interaction, eq and η are connected to the EFG tensor $e\boldsymbol{q}$ by $eq = V_z$ and $\eta = (V_x - V_y)/V_z$. In literature, the quantities e^2Qq/h and η are often given to describe the nuclear quadrupole interaction. Relevant quadrupole nuclei for Mn^{2+}-based EPR are, inter alia, ^{14}N, ^{17}O and ^{55}Mn. For these nuclei, electric field gradient parameters of $e^2Qq/h = 4.3\,\mathrm{MHz}$ for ^{14}N [48], $6.0\,\mathrm{MHz}$ for ^{17}O [49] and $10.7\,\mathrm{MHz}$ or $-2.7\,\mathrm{MHz}$ for ^{55}Mn [50] were measured. In EPR spectra, the nuclear quadrupole interaction manifests itself as a slight shift in resonance frequency for the allowed EPR transitions, which is difficult to observe experimentally. The nuclear quadrupole interaction, however, can be detected by pulsed hyperfine techniques. Here, $\mathcal{H}_{NQI}$ leads to an additional splitting of signals, since the different nuclear transitions of high-spin nuclei in one electron spin manifold are no longer degenerate.

2.1.4 Weakly Coupled Electron-Dipole Interaction

In this work, coupled electron spins between two paramagnetic spin centers are referred to as weakly coupled electron spins (for strongly coupled electron spins see Section 2.1.3). Just as the hyperfine interaction, the weakly coupled electron-dipole interaction can be divided into an isotropic “through-bond” interaction (exchange coupling) and an anisotropic “through-space” interaction (electron dipole-dipole coupling). This section only deals with the electron dipole-dipole

interaction, as the exchange coupling is normally zero in biological systems. In the tensor notation, the dipole-dipole interaction can be expressed as

$$\mathcal{H}_{dd} = \boldsymbol{S}_1 \boldsymbol{d} \boldsymbol{S}_2, \tag{2.18}$$

where $\boldsymbol{d}$ is the electron dipole-dipole coupling tensor.

Equation 2.18 shows that its written out form contains terms with the products of the different vector elements of $\boldsymbol{S}_1$ and $\boldsymbol{S}_2$ ("dipolar alphabet"). If the electron Zeeman interaction is the dominant interaction (high-field approximation), $\mathcal{H}_{dd}$ simplifies to

$$\begin{aligned} \mathcal{H}_{dd} = & \frac{\mu_0}{4\hbar} \frac{g_1 g_2 \beta_e^2}{r_{12}^3} \\ & \times \left[S_{1z} S_{2z} \left(3cos^2\theta - 1 \right) \left(S_{1+} S_{2-} + S_{1-} S_{2+} \right) \frac{(1 - 3cos^2\theta)}{4} \right], \end{aligned} \tag{2.19}$$

where r_{12} is the magnitude of the vector connecting electron spins $\boldsymbol{S}_1$ and $\boldsymbol{S}_2$ and S_{i+} and S_{i-} describe raising and lowering operators, respectively. $\frac{\mu_0}{4\hbar} \frac{g_1 g_2 \beta_e^2}{r_{12}^3}$ is called the dipole-dipole coupling constant ω_{dd}. If the weak coupling limit applies ($\omega_1 - \omega_2 >> \omega_{dd}$, where ω_1 and ω_2 describe the respective Larmor frequencies), off-diagonal (pseudo-secular) elements can be neglected, further simplifying Equation 2.19 to

$$\mathcal{H}_{dd} = \frac{\mu_0}{4\hbar} \frac{g_1 g_2 \beta_e^2}{r_{12}^3} S_{1z} S_{2z} \left(3cos^2\theta - 1 \right). \tag{2.20}$$

The cosine term describes the orientation of r_{12} on a sphere with respect to B_0 (second Legendre polynomial). Under assumption of the PDA and in its principal axis system, $\boldsymbol{d}$ in Equation 2.18 can now be written as

$$\boldsymbol{d} = \frac{\mu_0}{4\hbar} \frac{g_1 g_2 \beta_e^2}{r_{12}^3} \begin{pmatrix} -1 & & \\ & -1 & \\ & & 2 \end{pmatrix} = \begin{pmatrix} -\omega_{dd} & & \\ & -\omega_{dd} & \\ & & 2\omega_{dd} \end{pmatrix}. \tag{2.21}$$

ω_{dd} is a traceless and axial tensor. Since ω_{dd} is inversely proportional to r_{12}^3 it can be used to obtain distance restraints in structural biology. If ω_{dd} is large

($r_{12} < 2\,\mathrm{nm}$), it can be directly extracted out of continuous wave (CW)-EPR spectra of solids or frozen solutions [51]. For larger distances, however, more sophisticated PDS techniques are required. If high-spin systems ($S > 1/2$) are involved, pseudo-secular terms of $\mathcal{H}_{dd}$ can be sufficiently large so that they can no longer be neglected [52, 53]. In addition, the zero-field interaction may lead to a violation of the high-field approximation [54, 55].

2.2 The Nitroxide Spectrum (S=1/2, I=1)

EPR spectra of nitroxides ($S = 1/2$) in the solid-like state (powders or frozen solutions) are characterized by the anisotropy of the g tensor and the anisotropy of the hyperfine coupling to the ^{14}N nucleus ($I = 1$). The physical origin of the nitroxide g tensor lies in spin-orbit coupling of the doublet ground state with excited states, of which the lowest excited state corresponds to excitation of an electron from an oxygen lone-pair orbital into the half-filled π^* orbital [56]. Typical principal values are $g_x = 2.0090$, $g_y = 2.0040$ and $g_z = 2.0021$. As a consequence of the aforementioned mechanism, the g_z value is close to the value of the free electron ($g_e = 2.0023$), whereas g_x and g_y are increased [47, p. 26].

The ^{14}N hyperfine tensor of nitroxides is anisotropic and to a good approximation an axial tensor. Common principal values of the ^{14}N hyperfine tensor are $A_x = 20\,\mathrm{MHz}$, $A_y = 20\,\mathrm{MHz}$ and $A_z = 90\,\mathrm{MHz}$.

Figure 2.1 shows simulated EPR spectra with the abovementioned g and ^{14}N hyperfine tensors using the MATLAB toolbox EasySpin [57]. The spectral width at X-band and Q-band frequencies is mainly determined by the ^{14}N hyperfine splitting. The "central" electron transition ($m_I = 0$) is only affected by the anisotropy of the g tensor and therefore has the smallest spectral width at X-band frequencies. For the high-field transition ($m_I = -1$), the anisotropy of the g and ^{14}N hyperfine tensor act in the same direction, as a consequence the allowed EPR transition with $m_I = -1$ has the largest spectral width. The opposite holds true for the low-field transition ($m_I = +1$).

At X-band frequencies, the spectral width of the g tensor decreases in comparison to the ^{14}N hyperfine tensor at Q-band frequencies. This is indicated by

the colored strips (principal values of $\boldsymbol{A}$) and the black lines in each of the central strips (principal values of $\boldsymbol{g}$) in Figure 2.1A and 2.1B. Subsequently, X-band nitroxide spectra offer the advantage that only a specific orientation of spins can be excited.

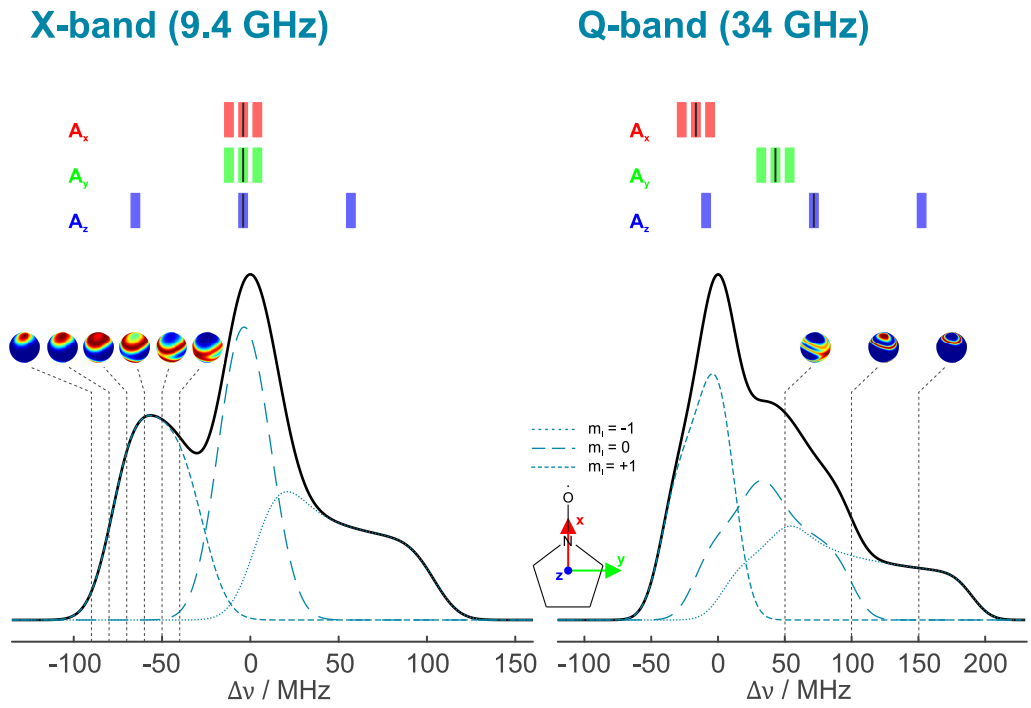

Figure 2.1: Simulated nitroxide field-sweep spectra using the MATLAB toolbox EasySpin [57] at X-band (9.4 GHz) and Q-band frequencies (34 GHz). The different allowed EPR transitions ($|m_S = \pm\frac{1}{2}, m_I\rangle \leftrightarrow |\mp\frac{1}{2}, m_I\rangle$) are shown as dashed lines. A schematic splitting of A_x, A_y and A_z is indicated by red, green or blue strips. The black lines in the middle of the central strips represent either g_x, g_y or g_z. Orientation spheres were simulated with an excitation bandwidth of 28 MHz, which corresponds to a 32 ns long rectangular pulse. Excited orientations were calculated for offsets of −40, −50, −60, −70, −80 and −90 MHz (X-band) and 50, 100 and 150 MHz (Q-band).

The orientation spheres in Figure 2.1A with offsets of −40, −50, −60, −70, −80 and −90 MHz only show a contribution of the A_z component of the hyperfine tensor (at least for larger offsets). On the contrary, Q-band orientation spheres with offsets of 50 and 100 MHz are characterized by an admixture of the A_y component to the A_z component. For an offset of 150 MHz, the admixture of A_y becomes negligibly small, however, experimentally these regions are rather

difficult to sample, as less spins are affected by the MW pulses. Excitation of specific orientations of the nitroxide spectrum is an important prerequisite for performing orientation-selective PELDOR measurements (Chapter 2.6).

Typically, little or no information can be obtained from pulsed nitroxide field-sweep spectra alone (Figure 2.1) that is relevant for structural biology. CW-EPR nitroxide field-sweep spectra, can be used to obtain distance restraints if the investigated distance is rather small [51]. In addition, the principal values of the g and ^{14}N hyperfine tensor are very sensitive to the polarity of the solvent and hydrogen bonding [58]. Changes of the principal values of the g and ^{14}N hyperfine tensor due to polarity and hydrogen bonding can be investigated using (high-field) CW-EPR [59]. CW-EPR is also suited to study rotational correlation times of nitroxides [47, p. 289].

2.3 The Mn^{2+} Spectrum (S=5/2, I=5/2)

EPR spectra of Mn^{2+} ions ($d5$ ion, $[Ar]3d5$) are characterized by the large hyperfine interaction of the Mn^{2+} electron spin ($S = 5/2$) to the ^{55}Mn nucleus ($I = 5/2$, 100 % natural abundance). Due to a strong spin polarization and almost spherical distribution of electron spins, the hyperfine interaction is mainly isotropic with a negligibly small dipolar character. For octahedral Mn^{2+} complexes, the hyperfine coupling is as large as ≈ 260 MHz. The sign of the hyperfine coupling, which cannot be determined with conventional pulsed hyperfine methods, is always negative [42].

In the gaseous phase, Mn^{2+} has a perfect spherical distribution of electron spins (no zero-field interaction) and an orbital singlet state ground configuration (^6S) with no orbital angular momentum. In the condensed phase, the orbital singlet state character is largely conserved, hence the ground state becomes ^6A_g in a crystal field with octahedral symmetry. Due to zero orbital angular momentum of the ground state and a rather high energy barrier to excited states, which effectively attenuates spin-orbit coupling with these states, the g tensor is nearly isotropic and close to the value of the free electron. In addition, the absence of any spin-orbit coupling in the ground state and the negligibly small

admixture of excited states with non-zero orbital angular momentum eliminates the relaxation mechanism via spin-orbit coupling (Kronig mechanism) [60]. As a consequence, Mn^{2+} ions are characterized by a rather narrow line width, which even allows to detect Mn^{2+} signals at room temperature using CW-EPR [61].

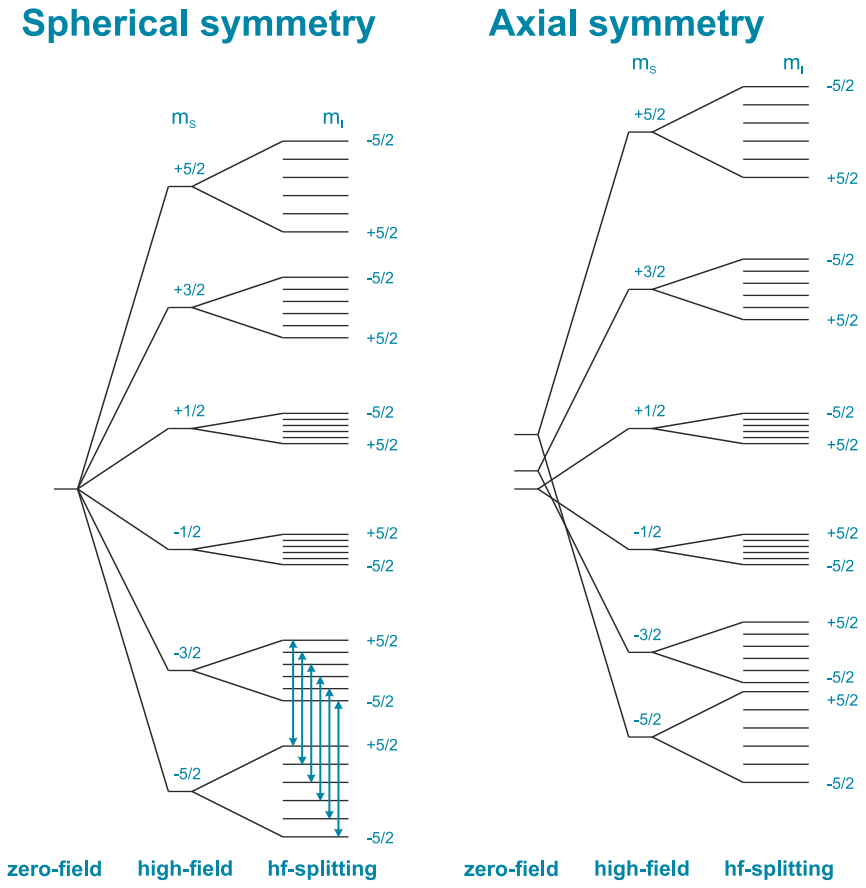

Figure 2.2: Spin ladder diagram for a Mn^{2+} ion with spherical symmetry (gaseous phase, no zero-field interaction) or rhombic symmetry (condensed phase, $D, E \neq 0$). A positive ^{55}Mn g_n value and a negative hyperfine coupling constant were assumed.

Due to an electron spin of $S = 5/2$, a Mn^{2+} ion possesses 6 electron spin manifolds. Coupling to the ^{55}Mn nucleus with $I = 5/2$ leads to a splitting of each electron spin level into 6 energy states, resulting in 36 energy states and 30 allowed EPR transitions. For perfect spherical symmetry, the allowed EPR transitions between different electron spin manifolds are degenerate. In such a case, one would only observe 6 EPR signals (five-fold degeneracy, Figure 2.2,

left). This scheme is not a bad description for the the manganese hexaaqua complex ($[Mn(H_2O)_6]^{2+}$). Here, 6 rather sharp CW-EPR signals in the liquid state and at room temperature are observed, which are a superposition of 5 almost degenerate allowed EPR transitions (Figure 2.3A). The near-degeneracy is due to rapid tumbling and the high symmetry of $[Mn(H_2O)_6]^{2+}$.

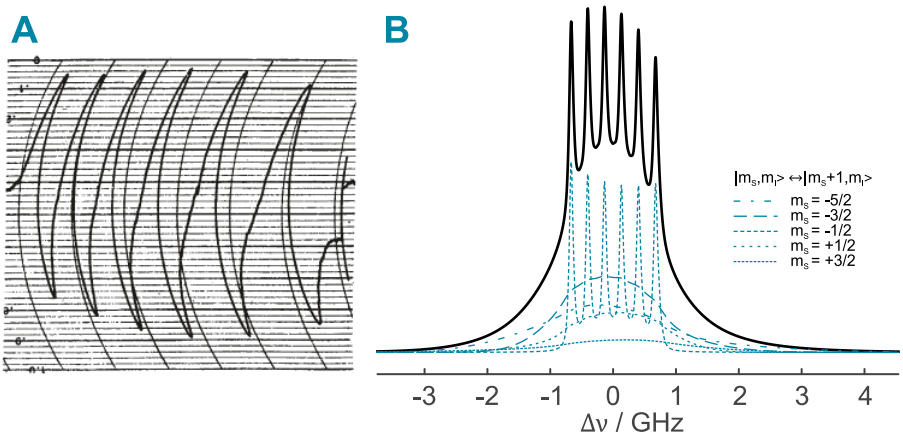

Figure 2.3: A) First ever published CW-EPR field-sweep spectrum of $[Mn(H_2O)_6]^{2+}$ recorded at 306 K and X-band frequencies by Cohn and Townsend from 1954. Reprinted with permission from Ref. [61], © Springer Nature, 1954. B) Simulated EPR field-sweep spectrum of a Mn^{2+} complex at Q-band frequencies and 5 K. An isotropic g value of $g_{iso} = 2.003\,88$, an isotropic hyperfine coupling of $a_{iso} = -269$ MHz and an axial zero-field interaction of $D = 500$ MHz with a D-strain of 1000 MHz were assumed. Different allowed EPR transitions are shown as blue lines.

For $[Mn(H_2O)_6]^{2+}$, the almost perfect octahedral symmetry ($D = E = 0$) eliminates yet another electron spin relaxation mechanism (spin relaxation via zero-field splitting). Spin relaxation via the quadratic terms of the zero field interaction (Equation 2.15) yields a theoretical smaller line width than observed for the experimental line width of $[Mn(H_2O)_6]^{2+}$. It is therefore believed that fluctuations in the zero-field interaction due to molecular collisions are the major source of electron spin relaxation for solvated $d5$ ions with octahedral symmetry [62, p. 329].

For $[Mn(H_2O)_6]^{2+}$ (and Mn^{2+} complexes in general), the EPR line width at room temperature is not only influenced by the electron spin relaxation time, but also by the large hyperfine coupling, which makes it a necessity to

take into account the non-secular terms of the hyperfine tensor. Second-order perturbation yields the resonance fields of the different allowed EPR transitions ($|m_S, m_I\rangle \leftrightarrow |m_S \pm 1, m_I\rangle$) for Mn^{2+} in the liquid state [62, p. 330]:

$$B_{res} = \frac{\hbar\omega_0}{g_e\beta_e} - a_{iso}\frac{\hbar}{\beta_e}m_I - \frac{a_{iso}^2\hbar}{2\omega_0\beta_e}\left\{I\left(I+1\right) - m_I^2 + m_I\left(2m_S+1\right)\right\}, \tag{2.22}$$

where ω_0 is the spectrometer frequency. Equation 2.22 shows that the second-order term lifts the degeneracy of the allowed EPR transitions. However, the spectral resolution of EPR is typically not sufficient to resolve these different resonance fields. Instead, the typical 6-line Mn^{2+} splitting is no longer equidistantly spaced and each EPR signal is inhomogeneously broadened to a different degree.

Pulsed EPR experiments on Mn^{2+} are routinely performed at cryogenic temperatures of $T \leq 10\,\mathrm{K}$ to enhance the signal-to-noise ratio (SNR) by increasing the transverse relaxation time. In the solid-like state (powder or frozen solution), the zero-field interaction no longer averages out and therefore has a direct influence on the spectral shape of the EPR spectrum. Fortunately, the resonance fields of the EPR transitions of the type $|m_S, m_I\rangle \leftrightarrow |m_S \pm 1, m_I\rangle$ exhibit a different dependency on the zero-field interaction for different m_S values. This was shown by perturbation theory up to third order [46, 63]. However, the different dependencies on the zero-field interaction are already apparent in the first-order terms:

$$B_{res}\left(|\pm\frac{1}{2}, m_I\rangle \leftrightarrow |\mp\frac{1}{2}, m_I\rangle\right) = \frac{\hbar\omega_0}{g_e\beta_e} - a_{iso}\frac{\hbar}{\beta_e}m_I, \tag{2.23A}$$

$$B_{res}\left(|\pm\frac{3}{2}, m_I\rangle \leftrightarrow |\pm\frac{1}{2}, m_I\rangle\right) = \frac{\hbar\omega_0}{g_e\beta_e} - a_{iso}\frac{\hbar}{\beta_e}m_I \mp \frac{\hbar}{\beta_e}\left[D\left(3cos^2\theta - 1\right) + 3Esin^2\theta cos2\phi\right], \tag{2.23B}$$

$$B_{res}\left(|\pm\frac{5}{2}, m_I\rangle \leftrightarrow |\pm\frac{3}{2}, m_I\rangle\right) = \frac{\hbar\omega_0}{g_e\beta_e} - a_{iso}\frac{\hbar}{\beta_e}m_I \mp \frac{2\hbar}{\beta_e}\left[D\left(3cos^2\theta - 1\right) + 3Esin^2\theta cos2\phi\right], \tag{2.23C}$$

As can be see from Equation 2.23A, the first-order perturbation theory expression of the central electron transition does not exhibit any zero-field interaction

dependency. The outer electron transitions, however, exhibit an anisotropic (θ- and ϕ-angle) dependency of the zero-field interaction (Equation 2.23B and Equation 2.23C). As a consequence, the outer electron transitions are typically rather broad, whereas the central electron transition is characterized by six relatively sharp signals due to the hyperfine interaction of the ^{55}Mn nucleus (Figure 2.3B). A distribution of the zero-field interaction parameters, so called D- and E-strains, lead to an additional broadening of the outer electron transitions. It should be noted that the central electron transitions exhibits a higher-order dependency on the zero-field interaction [46, 63]. These dependencies decrease with the square of the external magnetic field. Higher magnetic fields will therefore give narrower Mn^{2+} EPR lines.

Although the magnitude of the ^{55}Mn hyperfine coupling is dependent on the type of the ligand, the solvent and the pH value, these changes are typically rather small and are therefore difficult to observe in Mn^{2+} EPR field-sweep spectra (see also Section 3.1). Instead, the "signature interaction" of Mn^{2+} EPR field-sweep spectra is normally the zero-field interaction, which strongly depends on the ligands and the spatial distribution of the $d5$ electrons. The zero-field interaction parameter D is known to adopt values ranging from almost 0 MHz ($[Mn(H_2O)_6]^{2+}$) up to 7 GHz (Mn^{2+} FosA complexes) [64].

It should be noted that EPR spectra of different Mn^{2+} species, i.e., RNA-bound Mn^{2+} and "background" Mn^{2+} ($[Mn(H_2O)_6]^{2+}$), can be hard to distinguish with pulsed EPR at cryogenic temperatures, as the g value and the hyperfine coupling are in most cases very identical. The experimentally observed line width (zero-field interaction amongst other) is then a combination of the individual zero-field interactions of the two species, which is difficult to entangle.

Most pulsed Mn^{2+} experiments are performed with the magnetic field set to one of the six central hyperfine transitions. On the one hand this yields the best SNR, on the other hand it minimizes the influence of the zero-field and quadrupole interaction and the outer electron transitions, which can severely hamper data analysis.

2.4 Nuclear Frequency Spectra

Often, the hyperfine coupling of coupled electron and nuclear spins is obscured by the inhomogeneous EPR line width. In such cases, the hyperfine coupling can be studied by observing nuclear frequencies with pulsed EPR hyperfine spectroscopy. This section will therefore describe characteristics of nuclear frequency spectra, which can be obtained by pulsed hyperfine spectroscopy techniques.

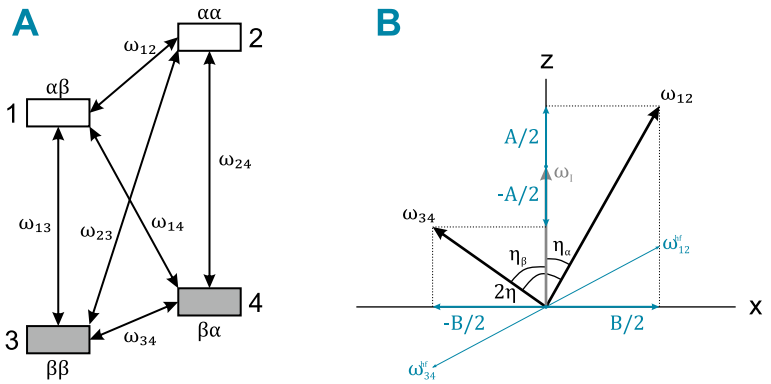

Figure 2.4: A) Energy level diagram ($|m_S, m_I\rangle$) of a weakly coupled $S = 1/2$, $I = 1/2$ model system. Allowed EPR transitions (ω_{13}, ω_{24}), allowed NMR transitions (ω_{12}, ω_{34}) and forbidden transitions (ω_{14}, ω_{23}) are indicated. B) Vector representation of the effective nuclear quantization axes in the electron α spin (ω_{12}) or electron β spin manifold (ω_{34}). ω_{12}^{hf} and ω_{34}^{hf} describe the effective hyperfine fine axes in the different electron spin manifolds. Both figures assume a positive nuclear Larmor frequency ($\omega_I > 0$ and therefore $g_n < 0$) and positive secular and pseudo-secular hyperfine coupling parameters (A, $B > 0$).

A $S = 1/2$, $I = 1/2$ model system as shown in Figure 2.4A consists of two allowed EPR transitions ($\Delta m_S = \pm 1$), two allowed NMR transitions ($\Delta m_I = \pm 1$) and two "forbidden" transitions ($\Delta m_S = \pm 1$, $\Delta m_I = \pm 1$). In this case, the spin Hamiltonian contains the electron Zeeman interaction, the nuclear Zeeman interaction and the hyperfine interaction:

$$\mathcal{H}_0 = \frac{\beta_e B_0 g S_z}{\hbar} + \frac{\beta_n B_0 g_n I_z}{\hbar} + A S_z I_z + B S_z I_x. \tag{2.24}$$

If one assumes an isotropic electron and nuclear Zeeman interaction and considers only the secular and pseudo-secular parts of the hyperfine interaction, the matrix

representation of Equation 2.24 can be diagonalized to obtain the eigenvalues. Diagonalization is achieved by rotating α electron spin matrix elements around angle η_α and β electron spin matrix elements around angle η_β (unitary transformation). η_α and η_β are the branching angles and describe the quantization axis of the nuclear spin in the electron α or β spin state.

The quantization axes ω_{12} and ω_{34} shown in Figure 2.4B are a vector sum of the nuclear Larmor frequency vector ω_I and the hyperfine vectors ω_{12}^{hf} and ω_{34}^{hf}. The hyperfine vectors ω_{12}^{hf} and ω_{34}^{hf} are, in turn, the vector sum of $\pm A/2$ and $\pm B/2$. The nuclear quantization axes therefore describe the deviation ("branching") from the z-axis of the laboratory frame due to the pseudo-secular part of hyperfine coupling (Figure 2.4B). Consequently, the branching angles can be expressed as [38, p. 60]

$$\eta_\alpha = arctan\left(\frac{-B}{A+2\omega_I}\right), \tag{2.25A}$$

$$\eta_\beta = arctan\left(\frac{-B}{A-2\omega_I}\right), \tag{2.25B}$$

where ω_I describes the angular nuclear Larmor frequency. η_α and η_β can be combined to yield the angle η:

$$\eta = \frac{\eta_\alpha - \eta_\beta}{2}. \tag{2.26}$$

Diagonalization of Equation 2.24 yields four eigenvalues and eigenfunctions, which can be used to obtain the two nuclear frequencies ω_α and ω_β:

$$\omega_\alpha = |\omega_{12}| = \left[\left(\omega_I + \frac{A}{2}\right)^2 + \frac{B^2}{4}\right]^{1/2}, \tag{2.27A}$$

$$\omega_\beta = |\omega_{12}| = \left[\left(\omega_I - \frac{A}{2}\right)^2 + \frac{B^2}{4}\right]^{1/2}. \tag{2.27B}$$

Equations 2.27 can also be expressed as a function of the principal values of $\boldsymbol{A}$ (assuming an axial tensor):

$$\omega_\alpha = \left[\left(\omega_I + \frac{A_\perp}{2}\right)^2 sin^2\theta + \left(\omega_I + \frac{A_\parallel}{2}\right)^2 cos^2\theta\right]^{1/2}, \tag{2.28A}$$

$$\omega_\beta = \left[\left(\omega_I - \frac{A_\perp}{2}\right)^2 sin^2\theta + \left(\omega_I - \frac{A_\parallel}{2}\right)^2 cos^2\theta\right]^{1/2}. \tag{2.28B}$$

Electron spin transitions can be excited, if a linearly polarized electromagnetic wave with the correct frequency ω_{MW} is applied along the transverse plane of the laboratory frame. In the Hamiltonian picture, transverse application of MW pulses are described by a time-dependent "oscillatory" Hamiltonian of the form $\mathcal{H}_1(t) = 2\omega_1 S_x cos(\omega_{MW} t + \phi)$. By converting $\mathcal{H}_1$ into the eigenbasis of the static Hamiltonian given in Equation 2.24, the oscillatory Hamiltonian becomes a function of η [38, p. 63]. The transition amplitude a_{ij} of a transition between the energy level i and j is given by $a_{ij} = \langle \phi_i \,|\, \mathcal{H}_1 \,|\, \phi_j \rangle$, where ϕ_i and ϕ_j describe the respective eigenfunctions. Since the eigenfunctions and $\mathcal{H}_1$ can be expressed as a function of η, a_{ij} needs to be proportional to η as well:

$$a_{13} \propto \omega_1 cos\eta,\ a_{24} \propto \omega_1 cos\eta, \tag{2.29A}$$

$$a_{14} \propto -\omega_1 sin\eta,\ a_{24} \propto \omega_1 sin\eta, \tag{2.29B}$$

where ω_1 describes the amplitude of the applied MW pulse. Consequently, the transition probabilities of the allowed and forbidden transitions (I_a and I_f) are defined as

$$I_a = cos^2\eta = \frac{\left|\omega_I^2 - \frac{1}{4}(\omega_\alpha - \omega_\beta)^2\right|}{\omega_\alpha \omega_\beta}, \tag{2.30A}$$

$$I_f = sin^2\eta = \frac{\left|\omega_I^2 - \frac{1}{4}(\omega_\alpha + \omega_\beta)^2\right|}{\omega_\alpha \omega_\beta}, \tag{2.30B}$$

with $I_a^2 + I_f^2 = 1$. Some important conclusions can be drawn from the aforementioned equations. Firstly, Equation 2.25 and Equation 2.26 show that η is zero at the canonical orientations ($A_\perp$, $A_\parallel$) and if the hyperfine coupling is purely isotropic. In such a case, the transitions probabilities of the forbidden transitions

become zero as well. Secondly, Equations 2.27 and Equations 2.30 show that the nominator in Equation 2.30A increases with increasing magnetic fields, whereas the nominator of Equation 2.30B stays essentially constant. Therefore, the transition probabilities of forbidden transitions decrease with higher magnetic fields. Thirdly, it can be deduced that nuclei with a smaller nuclear Larmor frequency exhibit a larger transition intensity for the forbidden transitions, i.e., $I_f(^{13}\mathrm{C}) > I_f(^{1}\mathrm{H})$ if one assumes the same magnetic field and identical hyperfine coupling parameters.

Nuclear frequency spectra can be simulated by calculating the resonance frequencies and transitions intensities (allowed or forbidden) of all orientations. The transition intensities are then weighted by $sin\theta$ and each resonance frequency is further convoluted with a Gaussian, accounting for an inhomogeneous line broadening. Summing over all orientations then yields the nuclear frequency spectra for a disordered $S = 1/2$, $I = 1/2$ system.

Figure 2.5 shows that disordered nuclear frequency spectra can be divided into three regimes - the weak coupling regime, the strong coupling regime and the cancellation regime. In the weak coupling regime ($|A_{eff}| < 2\omega_I$), the two signals of the two nuclear transitions are centered around the nuclear Larmor frequency ω_I, and split by the effective hyperfine coupling A_{eff}, which is a combination of a_{iso} and T. Depending on whether a_{iso} is smaller or larger than T, the nuclear frequency spectra in the weak coupling regime will look different. This is exemplified by the two nuclear frequency spectra at the bottom of Figure 2.5 (left), where the Pake doublets either overlap or do not overlap. For nuclear frequency spectra of the forbidden transitions, the difference between $a_{iso} > T$ and $a_{iso} < T$ is not pronounced. This is because for forbidden transitions the Pake doublets become distorted, i.e., for $\theta = 45°$ the forbidden transitions have a maximum transition probability and for $\theta = 0°, 90°$ the transition probability becomes zero. For allowed transitions, the transition probability is close to one for all orientations, thus resulting in a typical Pake pattern. At Q-band, the weak coupling condition is fulfilled for most ligand nuclei coordinating to Mn^{2+} ions, e.g., ^{1}H, ^{31}P, ^{13}C, ^{14}N, ^{15}N.

The strong coupling regime is met when $|A_{eff}| > 2\omega_I$. The two signals of the two nuclear transitions are then centered around half of the effective hyperfine

coupling A_{eff} and split by twice the Larmor frequency ω_I. Nuclear frequency spectra of the ^{55}Mn nucleus typically lie in the strong coupling regime.

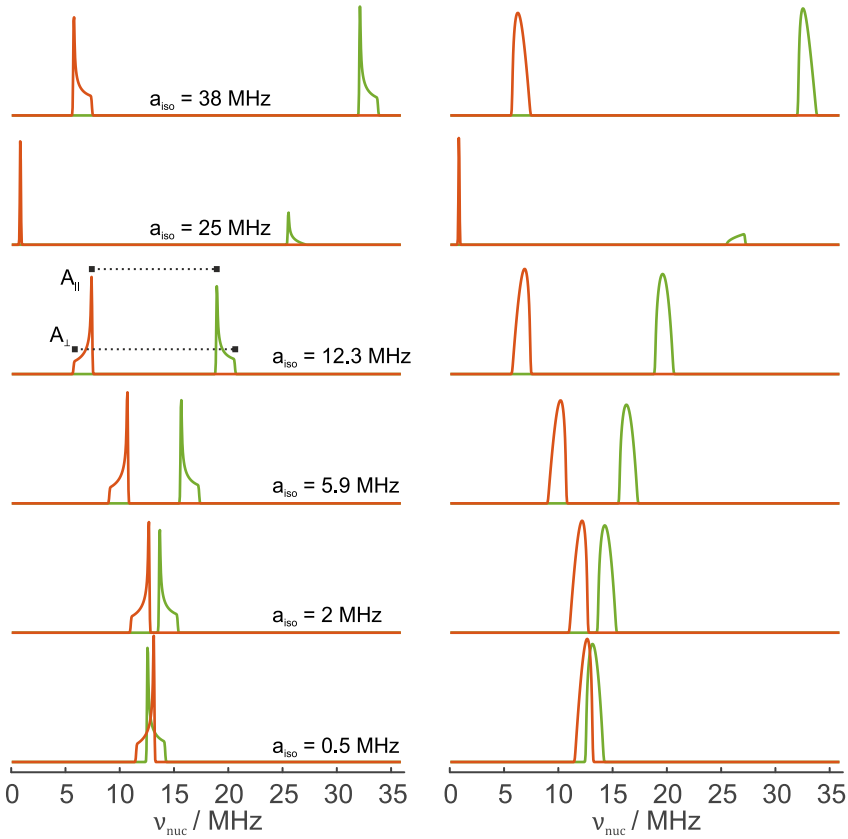

Figure 2.5: Simulated disordered nuclear frequency spectra for different combinations of the isotropic and dipolar hyperfine coupling constants a_{iso} and T. a_{iso} was varied and a dipolar component of $T = 1.1$ MHz and a nuclear Larmor frequency of $\nu_I = 12.85$ MHz was used. A FWHM of 0.1 MHz was used for the Gaussian line broadening. The left side shows nuclear frequency spectra when allowed NMR transitions are excited ($\Delta m_I = \pm 1$). The right side shows nuclear frequency spectra when forbidden transitions are excited (Δm_I, $\Delta m_S = \pm 1$). Red powder spectra correspond to nuclear transitions in the α electron spin manifold, green powder spectra correspond to nuclear transitions in the β electron spin manifold (ω_{12} and ω_{34} in Figure 2.4A). If the SNR and the ENDOR line width permits, the principal values of the hyperfine tensor can be extracted from nuclear frequency spectra when allowed NMR transitions were exited.

In the cancellation regime, the hyperfine field cancels the nuclear Zeeman field ($|A_{eff}| = 2\omega_I$). Then, nuclear frequencies in one electron spin manifold become independent of the angle θ. This yields a narrow, dispersion-free signal

close to a nuclear frequency of zero. Nuclear frequencies in the other electron spin manifold remain a function of θ (Figure 2.5, second row from the top).

Nucleus	I	Abundance / %	g_n	ν_I at 1.2 T / MHz
^{1}H	1/2	99.9885	5.5857	51.09
^{2}H	1	0.0115	0.8574	7.84
^{13}C	1/2	1.07	1.4048	12.85
^{14}N	1	99.632	0.4038	3.69
^{15}N	1/2	0.368	-0.5664	5.18
^{17}O	5/2	0.038	-0.7575	6.92
^{23}Na	3/2	100	1.4783	13.52
^{31}P	1/2	100	2.2632	20.70
^{35}Cl	3/2	75.78	0.5479	5.01
^{37}Cl	3/2	24.22	0.4561	4.17
^{39}K	3/2	93.258	0.2610	2.39
^{41}K	3/2	6.730	0.1432	1.31
^{55}Mn	5/2	100	1.3813	12.64

Table 2.1: List of NMR-active nuclei relevant for the work presented within this thesis.

Table 2.1 show a list of NMR-active nuclei that are relevant for the work presented in this thesis. The last column shows the nuclear Larmor frequencies at Q-band frequencies (1.2 T, 34 GHz). As the Larmor frequency is proportional to the applied magnetic field, higher magnetic fields give a better spectral resolution for different nuclear species. For example, the Larmor frequencies of ^{23}Na and ^{13}C have a difference of only $\Delta\nu = 0.7$ MHz at Q-band frequencies, which would make it a challenging task to entangle these two nuclei at Q-band with pulsed ENDOR or EDNMR techniques. At higher magnetic fields, such as J-band (9.4 T, 263 GHz), the difference of the Larmor frequencies increases to $\Delta\nu = 5$ MHz. Although ^{55}Mn has a similar Larmor frequency to ^{23}Na and ^{13}C, ^{55}Mn will not interfere with weakly coupled ^{23}Na and ^{13}C ligand nuclei, since the ^{55}Mn nucleus is strongly coupled to the Mn^{2+} electron spin and nuclear ^{55}Mn signals therefore resonate at nuclear frequencies of $\nu_{nuc} > 100$ MHz at Q-band frequencies.

2.5 Pulsed Hyperfine Techniques

The previous section described the underlying theory of nuclear frequency spectra. The following part describes different characteristics of pulsed populations-transfer hyperfine techniques to obtain nuclear frequency spectra by either exciting allowed NMR or forbidden transitions. Firstly, conventional and (well) established one-dimensional hyperfine methods are described. Secondly, more sophisticated and comparatively new two-dimensional population-transfer pulsed hyperfine techniques are detailed. The work presented in this thesis did not utilize coherence-transfer hyperfine techniques such as electron spin echo envelope modulation (ESEEM) and hyperfine sublevel correlation spectroscopy (HYSCORE). These experiments are therefore not further mentioned in this section, although they play an important role in pulsed EPR applications [65].

2.5.1 Pulsed ENDOR

ENDOR was the first method to investigate hyperfine couplings - CW-ENDOR was published by George Feher in 1956 [66]. Nowadays, CW-ENDOR has been replaced by pulsed ENDOR techniques. Pulsed ENDOR features a better spectral resolution than CW-ENDOR and therefore also allows to observe weakly coupled ligand nuclei. In addition, pulsed ENDOR does not rely on a critical ratio between electron spin and nuclear spin relaxation rates. As a consequence, pulsed ENDOR tolerates a more flexible temperature range, since relaxation rates do strongly depend on the temperature. Pulsed ENDOR is also less susceptible to baseline distortions and signal artifacts, which is due to the fact that pulses are turned off during signal acquisition. Finally, pulsed ENDOR offers the advantage that pulses enable for a more sophisticated manipulation of spins and the hyperfine coupling.

Today, two pulsed ENDOR methods exist, which are complementary in its application. The Mims ENDOR sequence, first proposed by William Mims in 1965, is best suited for rather small hyperfine couplings ($A_{eff} \lessapprox 2\,\mathrm{MHz}$) [67]. In 1974, Roy Davies published a second pulsed ENDOR experiment, subsequently dubbed Davies ENDOR, which is best suited for large hyperfine couplings [68].

Despite the differences, the principle of Mims and Davies ENDOR is identical: A MW channel (detection channel) is used to monitor the intensity of an allowed EPR transition (ω_{13} or ω_{24} in Figure 2.4A). In a second channel, the frequency of a radio frequency (RF) pulse is varied systematically and every time the RF pulse is on-resonance with a nuclear transition (ω_{12} or ω_{34} in Figure 2.4A), nuclear spin population is transferred to the less-populated nuclear spin manifold. The transfer of nuclear spin population is observed as an increase or decrease of the intensity of the spin echo in the MW channel.

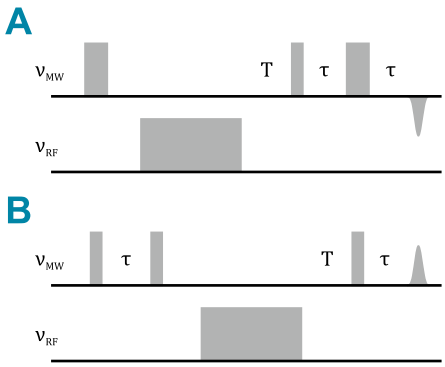

Figure 2.6: Davies ENDOR (A) and Mims ENDOR (B) pulse sequences. In both experiments, the frequency of the RF pulse is varied systematically. The spin echo is therefore monitored as a function of the RF. In Davies ENDOR, the detection channel consists of a selective π pulse and a Hahn echo sequence. In Mims ENDOR, the detection channel consists of a non-selective stimulated echo sequence.

A Davies ENDOR experiment (Figure 2.6A) starts with a selective π pulse, that inverts the population of only one of the EPR transitions shown in Figure 2.4A. A single transition operator, i.e., acting only on transition (13), can be expressed as follows [38, p. 125]:

$$S_x^{(13)} = S_x I^\alpha = \frac{1}{2} S_x + S_x I_z. \tag{2.31}$$

Single transition operators can be stripped down into a linear combination of the operators S_x and $2S_xI_z$, as was shown by Sørensen et al. [69]. Expressed as rotations, which makes it possible to calculate the density operator σ using product operator formalism, this yields [69]

$$\sigma(t_i) \xrightarrow{-\frac{1}{2}S_y} \xrightarrow{\frac{\beta}{2}S_z} \xrightarrow{\pm\frac{\beta}{2}2S_zI_z} \xrightarrow{\frac{1}{2}S_y} \sigma(t_f), \tag{2.32}$$

where $\sigma(t_i)$ describes the density operator before the selective pulse, and $\sigma(t_f)$ describes the density operator after the selective pulse. Using Equation 2.32, it is possible to calculate the density operator at any time t during a Davies ENDOR experiment.

The first MW pulse ($\pi S_x I^\alpha$) creates $2S_zI_z$ magnetization (Figure 2.7). In a next step, a selective RF pulse ($\beta_{RF}S^\alpha I_x$) acts on the spin system. If the pulse is perfectly on-resonance with an allowed NMR transition ($\beta_{RF} = \pi$), this creates longitudinal nuclear magnetization (I_z). If the pulse is off-resonance ($\beta_{RF} = 0$), the net magnetization obviously stays as before ($2S_zI_z$). At the end, the Hahn echo sequence transforms the $2S_zI_z$ magnetization with two successive applications of Equation 2.32 into transverse $-S_y$ magnetization. For an on-resonance RF pulse, the Hahn echo sequence and its product operators have no effect on the I_z magnetization. In such a case, zero echo intensity is detected.

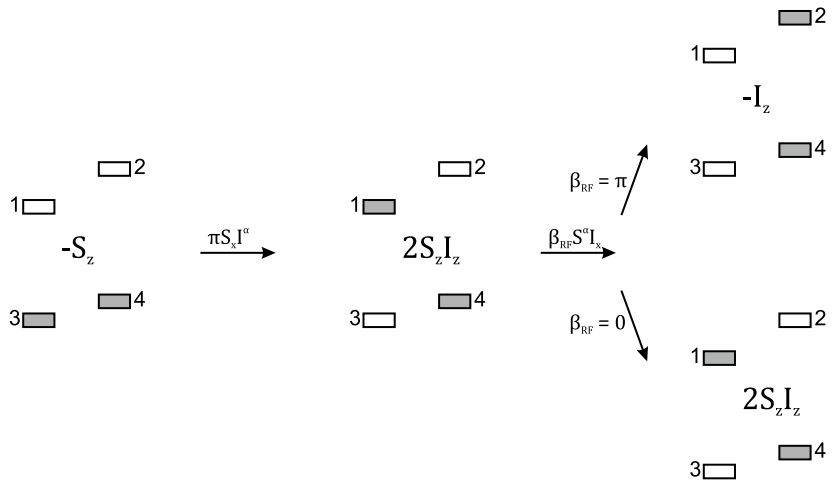

Figure 2.7: Evolution of spin population during a Davies ENDOR experiment for the model system that was introduced in Section 2.4.

An general ENDOR efficiency can be defined, which is a function of the echo intensity for an on-resonance and off-resonance RF pulse, respectively:

$$F_{ENDOR} = \frac{V_{echo}\,(on) - V_{echo}\,(off)}{2V_{echo}\,(off)}, \tag{2.33}$$

where V_{echo} describes the echo intensity. For hyperfine couplings of $A_{eff} \gtrapprox 2\,\mathrm{MHz}$, an inversion pulse can be considered selective if a pulse length of 100 ns or longer is used. For smaller hyperfine couplings, the length of the inversion pulse must be increased in order to maintain its selectivity. Increasing the length of the MW pulse, however, strongly affects the SNR since less spins are excited. Therefore, Davies ENDOR is not well suited to investigate small hyperfine couplings.

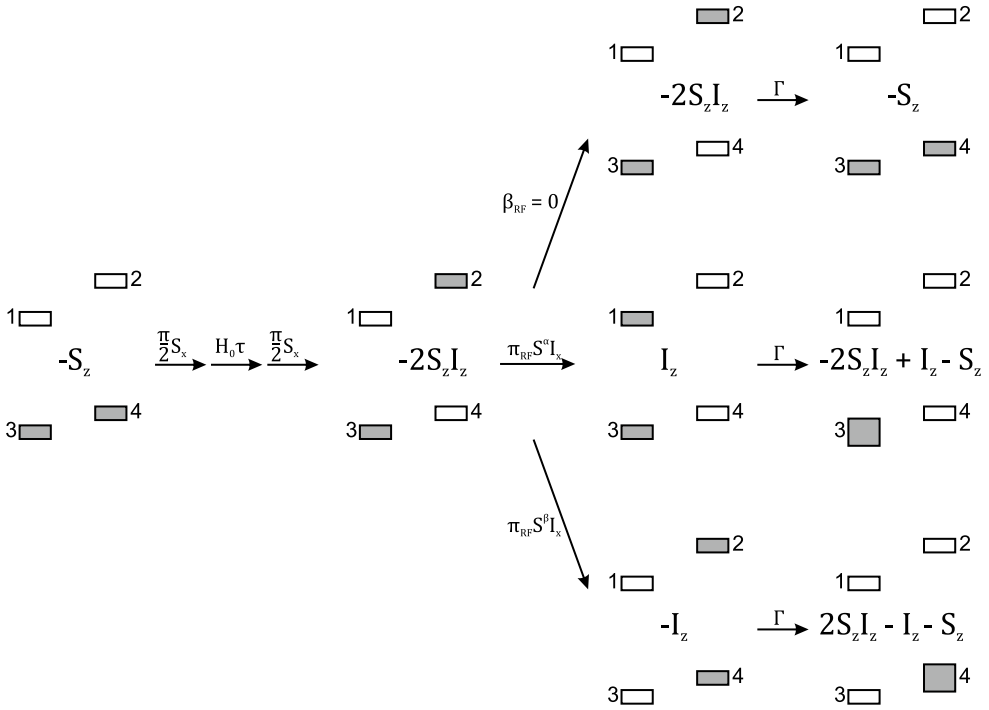

Figure 2.8: Evolution of spin population during a Mims ENDOR experiment for the model system that was introduced in Section 2.4. Γ indicates longitudinal relaxation processes, that can become significant if the interpulse delay T between the RF pulse and the third $\frac{\pi}{2}$ pulse gets increased.

The method of choice for detecting small hyperfine couplings is the Mims ENDOR technique (Figure 2.6B). A Mims ENDOR experiment starts by applying two non-selective $\frac{\pi}{2}$ pulses, which are separated by an interpulse delay

τ. Application of product operator formalism for the two $\frac{\pi}{2}$ pulses yields four magnetization operators, namely S_z, $-2S_xI_z$, $-S_x$ and $-2S_zI_z$. The first term typically "survives" the time during which the RF pulse is applied, it is, however, not affected by the RF pulse. Therefore, the S_z term does not need to be considered for detection with the stimulated Hahn echo. The second and third term ideally decay during application of the RF pulse due to electron transverse relaxation processes. The fourth term is identical to the spin operator that was created in a Davies ENDOR experiment (besides the sign).

Application of a perfectly on-resonance and selective RF pulse ($\pi S^{\alpha}I_x$) on $-2S_zI_z$ magnetization yields only I_z magnetization (Figure 2.8), which cannot be detected by the third MW pulse. Subsequently, an on-resonance RF pulse yields zero echo intensity. A perfectly off-resonance RF pulse ($\beta_{RF} = 0$) does not alter the $-2S_zI_z$ magnetization (Figure 2.8). The third $\frac{\pi}{2}$ pulse transforms the longitudinal 2-spin product operator into antiphase magnetization (S_yI_z), which evolves into detectable S_y magnetization during the second interpulse delay τ (positive stimulated Hahn echo).

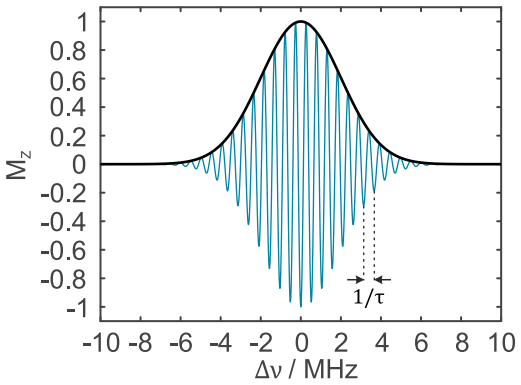

Figure 2.9: Polarization grating across a narrow EPR line after the second $\frac{\pi}{2}$ pulse of a stimulated echo sequence, i.e., a Mims ENDOR experiment.

Due to the interpulse delays in a Mims ENDOR sequence, the product operators shown in Figure 2.8 become modulated by the factors $cos\left(\frac{a_{iso}}{2}\tau\right)$, $sin\left(\frac{a_{iso}}{2}\tau\right)$, $cos\left(\Omega_S\tau\right)$ and $sin\left(\Omega_S\tau\right)$. As a consequence, the first two $\frac{\pi}{2}$ pulses create a polarization grating, of which the mesh size is defined by the interpulse delay τ (Figure 2.9). For large τ values, the individual spin packets in the

transverse plane have more time to accumulate a phase ϕ. Hence, this yields a tighter mesh size. If a spin packet vector is completely aligned along the x-axis after the first interpulse delay, the second $\frac{\pi}{2}$ pulse (coming from the x direction) has no effect on this particular spin packet. These spin packets consequently describe the zero crossings in the polarization grating.

If the RF pulse excites a nuclear transition of a spin packet, of which the effective hyperfine coupling A_{eff} is equal to $A_{eff} = \frac{n}{\tau}$ with $n = 0, 1, 2, ...$ (A_{eff} in MHz, τ in us), this "shifts" the polarization grating by exactly one oscillation along the x-axis. In such a case, the polarization grating after the RF pulse is identical to the polarization grating before the RF pulse. Therefore, the ENDOR efficiency F_{ENDOR} will be zero, even if the RF pulse is perfectly on-resonance with a nuclear transition. For Mims ENDOR, F_{ENDOR} is defined as

$$F_{Mims}\left(a_{iso}, \tau\right) = \frac{1}{2} sin^2\left(a_{iso}\tau\pi\right). \tag{2.34}$$

Plotting of Equation 2.34 yields the Mims ENDOR blind spot function, from which Mims ENDOR intensity minima (blind spots) and maxima can be read out. Figure 2.10A shows that for small hyperfine couplings long τ values have to be used. Long τ values can, however, compromise the SNR due to transverse relaxation. For large hyperfine couplings, short τ values have to be used. At Q-band frequencies the length of protection gates, prevents the use of τ values lower than 100 ns. In an intermediate regime, Mims ENDOR spectra with different τ values can be summed with the goal of averaging out the blind spots.

As already mentioned, a prerequisite for a successful Davies ENDOR experiment is a selective inversion pulse. If the pulse is not selective, the population of both EPR transitions is inverted and S_z magnetization is created, which is not affected by the RF pulse. For a given pulse length t_p of the inversion pulse, small hyperfine couplings will be partially suppressed if $a_{iso}t_p = \eta_S \lessapprox 1$ (units in MHz and µs, respectively), where η_S is the Davies ENDOR selectivity parameter [70]. The intensity inside this suppression hole is described by [71]

$$F_{Davies}\left(a_{iso}, t_p\right) \propto \frac{1.4 a_{iso} t_p}{0.7^2 + \left(a_{iso}t_p\right)^2}. \tag{2.35}$$

Figure 2.10B shows Equation 2.35 plotted as a function of the hyperfine coupling constant a_{iso}. For shorter time lengths of the inversion pulse, the central hole gets broader and more hyperfine couplings are suppressed. Vice versa, a long inversion pulse suppresses only a rather small range of hyperfine couplings. The ability to suppress certain hyperfine couplings by controlling the length of the inversion pulse is sometimes referred to as hyperfine contrast selectivity.

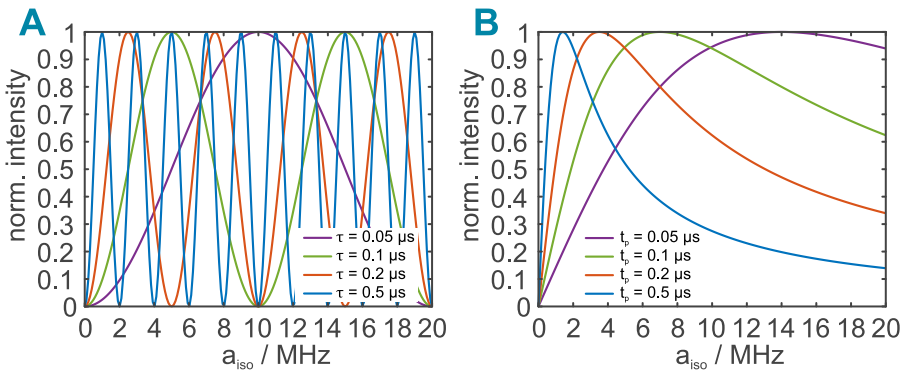

Figure 2.10: Blind spot (intensity) functions for Mims ENDOR (A) and Davies ENDOR (B) as a function of the hyperfine coupling a_{iso}. The Mims ENDOR blind spot function is shown for different τ values, the Davies ENDOR blind spot function is shown for different pulse lengths t_p of the inversion pulse.

Since the publication of the original Davies and Mims ENDOR sequence, several other and more sophisticated ENDOR techniques have been published, that allow for a more thourough investigation and manipulation the hyperfine coupling. A description of these techniques is, however, beyond the scope of this work. For further reference, the reader is referred to the monograph by Jeschke and Schweiger [38, ch. 12]. Only two ENDOR modifications will be briefly explained, since these experiments were used in one publication that is part of this cumulative thesis (Section 3.2).

With the original Davies and Mims ENDOR sequences, it is typically not possible to extract information about the sign of the principal values of $\boldsymbol{A}$. A remedy is to perform ENDOR experiments on the outer electron transitions of paramagnetic spin centers with $S > 1/2$, i.e., Mn^{2+}. For a high-spin system with $S > 1/2$ and an isotropic hyperfine coupling, Equation 2.28A and Equation 2.28B simplify in a first approximation to

$$\omega_{m_S} = |m_S a_{iso} - \omega_I| \,. \tag{2.36}$$

Equation 2.36 shows, that nuclear frequencies are only centered symmetrically around the nuclear Larmor frequency, if the central electron transition is excited ($|m_S = \pm 1/2, m_I\rangle \leftrightarrow |\mp 1/2, m_I\rangle$). If an outer electron transition is excited, the nuclear frequencies appear on either the left-hand side or the right-hand side of the nuclear Larmor frequency [72]. Since the sign of the Larmor frequency ω_I and the electron spin magnetic quantum number m_S are known, the nuclear frequencies can be used to calculate the sign of the isotropic hyperfine coupling. For Mn^{2+} systems, outer electron transitions are excited if the magnetic field is set to the low field or high field edge of the Mn^{2+} EPR spectrum. Due to the strong Boltzmann polarization at cryogenic temperatures, mainly outer electron transitions with $m_S = -5/2$ and $m_S = -3/2$ are excited at these magnetic field positions.

For rather small hyperfine interactions, it can be sometimes difficult to determine magnitude and sign of the dipolar and the isotropic contribution. Especially when large parts of the powder spectrum appear close to the nuclear Larmor frequency and are therefore obscured by the central Mims ENDOR blind spot, it can be a cumbersome process to entangle the dipolar and the isotropic part. A good example are the simulated nuclear frequency spectra with $T = 1.1\,\mathrm{MHz}$, $a_{iso} = 2\,\mathrm{MHz}$ and $T = 1.1\,\mathrm{MHz}$, $a_{iso} = 0.5\,\mathrm{MHz}$ in Figure 2.5, which would look almost identical after convolution with a Mims ENDOR blind spot function. If the SNR permits, ENDOR on outer electron transitions is able to distinguish between these two cases. For $a_{iso} > T$, the Pake patterns of both nuclear transitions will completely appear on either the right-hand side or left-hand side of the nuclear Larmor frequency. For $a_{iso} < T$, the powder spectrum will still be asymmetric with respect to the nuclear Larmor frequency. However, the Pake patterns are now no longer confined to only one side of the nuclear frequency spectrum. For example, parts of the “shoulder” of the Pake pattern would appear on the left-hand side of the spectrum, whereas the “horn” of the Pake pattern would appear on the right-hand side of the spectrum.

Another possibility to distinguish the nuclear transition in the $|m_S = \beta\rangle$ manifold from the nuclear transition in the $|m_S = \alpha\rangle$ manifold is to perform a variable mixing time Mims ENDOR (VMT Mims ENDOR) experiment. In such an experiment, the time T (mixing time, $T = t_{mix}$) between the RF pulse and the third $\frac{\pi}{2}$ pulse in a Mims ENDOR sequence is varied. At longer mixing times and strong Boltzmann polarizations, longitudinal relaxation results in different ENDOR efficiencies for nuclear spin transitions in the $|m_S = \beta\rangle$ or $|m_S = \alpha\rangle$ manifold. In extreme cases, the signal of one nuclear transition can become positive, whereas the signal of the other nuclear transition remains negative [73].

The underlying mechanism of VMT Mims ENDOR is schematically shown in the last column of Figure 2.8. If the RF pulse is perfectly off-resonance, longitudinal electron spin relaxation Γ starts to transform $-2S_zI_z$ into thermal equilibrium $-S_z$ magnetization:

$$\sigma_{off}\left(t_{mix}\right) = -2S_zI_ze^{-\Gamma t_{mix}} - S_z\left(1 - e^{-\Gamma t_{mix}}\right), \tag{2.37}$$

whereby it was assumed for simplicity that $sin\left(\Omega_S\tau\right) = 1$ and $sin\left(\frac{a_{iso}}{2}\tau\right) = 1$ to maximize the initial $-2S_zI_z$ spin operator. $\sigma_{off}\left(t_{mix}\right)$ describes the density operator for an off-resonance RF pulse after the time t_{mix}. If the RF pulse is on-resonance with the $|m_S = \alpha\rangle$ manifold (middle row in Figure 2.8), longitudinal relaxation starts to transform I_z magnetization into a sum of I_z, $-2S_zI_z$ and $-S_z$ magnetization:

$$\sigma_{\pi S^{\alpha}I_x}\left(t_{mix}\right) = I_z - 2S_zI_z\left(1 - e^{-\Gamma t_{mix}}\right) - S_z\left(1 - e^{-\Gamma t_{mix}}\right). \tag{2.38}$$

If the RF pulse is on-resonance with the $|m_S = \beta\rangle$ manifold (bottom row in Figure 2.8), longitudinal relaxation starts to transform $-I_z$ magnetization into a sum of $-I_z$, $2S_zI_z$ and $-S_z$ magnetization:

$$\begin{aligned}\sigma_{\pi S^{\beta}I_x}\left(t_{mix}\right) &= -I_z + 2S_zI_z\left(1 - e^{-\Gamma t_{mix}}\right) - S_z\left(1 - e^{-\Gamma t_{mix}}\right) \\ &= -I_z - 2S_zI_z\left(e^{-\Gamma t_{mix}} - 1\right) - S_z\left(1 - e^{-\Gamma t_{mix}}\right).\end{aligned} \tag{2.39}$$

The sign of the $2S_zI_z$ spin operator can be changed by changing the sign of the relaxation term. For detection of the stimulated echo, only the $-2S_zI_z$ terms

of Equation 2.37, 2.38 and 2.39 have to be considered, since the $-S_z$ term will not be refocused by a single $\frac{\pi}{2}$ pulse (in reality the sine terms are not 1). The density operator at the time of the stimulated Hahn echo is then given by:

$$\sigma_{off}\left(echo\right) = -S_y e^{-\Gamma t_{mix}}, \tag{2.40A}$$

$$\sigma_{\pi S^{\alpha} I_x}\left(echo\right) = -S_y \left(1 - e^{-\Gamma t_{mix}}\right), \tag{2.40B}$$

$$\sigma_{\pi S^{\beta} I_x}\left(echo\right) = -S_y \left(e^{-\Gamma t_{mix}} - 1\right). \tag{2.40C}$$

The ENDOR efficiencies of the different nuclear transitions can be compared to each other by using Equation 2.33. Since in this case the denominator can become zero because of relaxation, it is useful to define the denominator in Equation 2.33 for VMT Mims ENDOR purposes as $V_{echo}\left(off, t_{mix} = 0\right)$. The ENDOR efficiency in the electron $|m_S = \alpha\rangle$ manifold then becomes $F^{\alpha}_{VMT} = \frac{1}{2}\left(2e^{-\Gamma t_{mix}} - 1\right)$. The ENDOR efficiency in the electron $|m_S = \beta\rangle$ manifold becomes $F^{\beta}_{VMT} = \frac{1}{2}$. F^{β}_{VMT} therefore stays constant or, in other words, the decrease of F^{β}_{VMT} is identical to the decrease of stimulated Hahn echo intensity for the off-resonance case because of longitudinal relaxation. For F^{α}_{VMT}, the ENDOR efficiency becomes positive for short t_{mix} times (stimulated Hahn echo increases) and negative for long t_{mix} times (stimulated Hahn echo decreases). The abovementioned theory neglects longitudinal cross relaxation. In addition, it is assumed that longitudinal electron spin relaxation occurs faster than longitudinal nuclear spin relaxation.

For a meaningful VMT Mims ENDOR experiment, ENDOR spectra with several t_{mix} should be recorded. If spin polarization is sufficient, the nuclear transition in the $|m_S = \alpha\rangle$ manifold should be easy to identify since the intensity should change. The nuclear frequency of the nuclear transition in the $|m_S = \alpha\rangle$ manifold with respect to the nuclear Larmor frequency (left-hand side or ride-hand side) can then be used to calculate the sign of the isotropic hyperfine coupling.

2.5.2 ELDOR-detected NMR

The EDNMR technique was first described by the group of Arthur Schweiger in 1994 [36]. EDNMR utilizes two MW channels, of which one operates at a fixed frequency and the other at a variable frequency. The requirement of two MW channels is the reason why EDNMR, already published in 1994, rose to prominence only in the mid 2000s, since only then EPR spectrometers with two MW sources became commercially available.

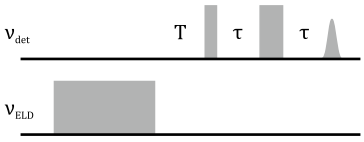

Figure 2.11: EDNMR pulse sequence. The integrated Hahn echo intensity is monitored as a function of the frequency of the ELDOR pulse.

The EDNMR pulse sequence consists of a Hahn echo detection sequence (Figure 2.11). The second MW channel contains a single, typically long and weakly powered MW pulse (electron-electron double resonance (ELDOR) pulse). The frequency of the ELDOR pulse is varied systematically around the frequency of the detection channel.

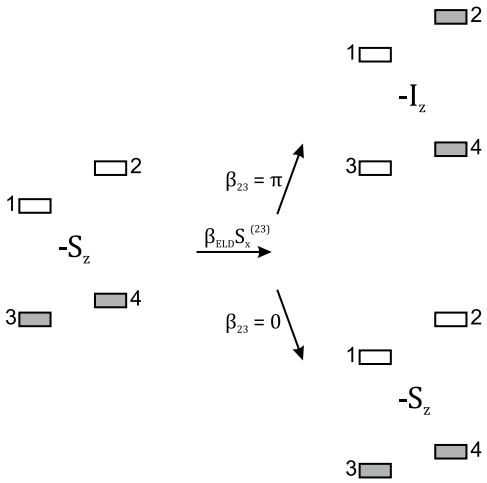

Figure 2.12: Evolution of spin population during an EDNMR experiment for the model system that was introduced in Section 2.4.

Everytime the frequency of the ELDOR pulse is on-resonance with a "forbidden" transition (Δm_S, $\Delta m_I = \pm 1$), population is moved from the ground state to the excited state. The transfer of population is observed as a loss of Hahn echo intensity in the detection channel. In an EDNMR experiment, the integrated Hahn echo intensity is typically plotted as a function of $\nu_{ELD} - \nu_{det}$, which yields the nuclear frequency spectrum.

Selective excitation of the double quantum transition (23) in Figure 2.4A is described by the single spin operator $S_x^{(23)} = \frac{1}{2}\left(S^+I^- + S^-I^+\right) = S_xI_x + S_yI_y$ [69]. Application to thermal equilibrium $-S_z$ magnetization yields (Figure 2.12)

$$\begin{aligned}
\sigma(0) = -S_z &\xrightarrow{\frac{\beta_{ELD}}{2} 2S_xI_x} \\
&- cos\left(\frac{\beta_{ELD}}{2}\right) S_z + sin\left(\frac{\beta_{ELD}}{2}\right) 2S_yIx \xrightarrow{\frac{\beta_{ELD}}{2} 2S_yI_y} \\
&- cos\left(\frac{\beta_{ELD}}{2}\right)^2 S_z - cos\left(\frac{\beta_{ELD}}{2}\right) sin\left(\frac{\beta_{ELD}}{2}\right) 2S_xI_y \\
&+ sin\left(\frac{\beta_{ELD}}{2}\right) cos\left(\frac{\beta_{ELD}}{2}\right) 2S_yI_x - sin\left(\frac{\beta_{ELD}}{2}\right)^2 I_z,
\end{aligned} \tag{2.41}$$

whereby for the subsequent Hahn echo detection sequence only the S_z component is relevant. Other terms will not be refocused into detectable in-phase magnetization. The Hahn echo intensity is therefore proportional to $\frac{1}{2}\left(1 + cos\left(\beta_{ELD}\right)\right)$. The biggest EDNMR effect occurs when the ELDOR pulse has an effective flip angle of $\beta_{23} = \pi$ on the forbidden transition and inverts the population. The effective flip angle can be defined as

$$\beta_{23} = \omega_{ELD} t_{ELD} \sqrt{I_{23}} = \beta_{ELD} \sqrt{I_{23}}. \tag{2.42}$$

In Equation 2.42, β_{ELD} describes the nominal flip angle of the ELDOR pulse on an allowed EPR transition, and I_{23} describes the transition probability connecting energy levels 2 and 3 in Figure 2.4A. As a general formula, the transition probability I_{ij} is given by Fermi's golden rule ($I_{ij} = \langle \phi_i \,|\, \mathcal{H}_1 \,|\, \phi_j \rangle^2$). For the 2-spin model system presented in Section 2.4, Equation 2.30A and Equation 2.30B can be used to calculate the transition probabilities. In most cases, the

transition probability of forbidden transitions is rather small. By increasing the value of the product of $\omega_{ELD}t_{ELD}$ it is, however, possible to achieve a sufficient flip angle for the forbidden transition. In most cases, a large t_{ELD} is chosen over a large ω_{ELD}, since a too high amplitude of the ELDOR pulse can lead to power broadening of the EDNMR lines.

The depth of the hole, that an ELDOR pulse burns into the EPR spectrum can be quantified by the hole-depth parameter h [36]:

$$h = 1 - I_a cos\left(\beta_{ELD}\sqrt{I_f}\right) - I_f cos\left(\beta_{ELD}\sqrt{I_a}\right), \tag{2.43}$$

where I_a corresponds to the transition probability of the observed and allowed EPR transition. Equation 2.43 shows that an EDNMR signal can be a sum of two contributions. The ELDOR pulse can pump a forbidden transition, which is then monitored by the detection pulses. If, however, the frequency offset between allowed and forbidden transitions is small and the inhomogeneous EPR line width is large, the ELDOR pulse can also pump an allowed EPR transition (second term in Equation 2.43). The detection sequence then monitors a forbidden transition.

The magnitude of the inhomogeneous EPR line width in relation to the hyperfine coupling also affect the appearance of an EDNMR spectrum. Figure 2.13A highlights the two allowed EPR transitions of the 2-spin model system that was introduced in Section 2.4. Schematic EDNMR spectra of both allowed EPR transitions are shown in Figure 2.13B. The signal in the middle occurs when the frequency of the ELDOR pulse approaches the frequency of the observed EPR transition and is called the central blind spot. When the hyperfine coupling is larger than the inhomogeneous EPR line width and resolved in the EPR spectrum, only one allowed EPR transition (either ω_{13} or ω_{24}) will be excited by the detection pulses. In such a case, the EDNMR spectrum will be asymmetric with respect to the central blind spot, i.e., only the green or red spectrum presented in Figure 2.13B will be recorded ("hyperfine-selective"). If the inhomogeneous EPR line width is larger than the hyperfine coupling, two different allowed EPR transitions (ω_{13} and ω_{24}) of two spin packets will overlap. In such a case, the detection sequence will simultaneously excite both allowed EPR transitions

shown in Figure 2.13A and the resulting EDNMR spectrum will be symmetric with respect to the central blind spot and a sum of the individual EDNMR spectra presented in Figure 2.13B ("hyperfine-unselective"). Ligand nuclei, i.e., ^{1}H of H_2O coordinating to Mn^{2+}, typically possess a relatively small hyperfine coupling and therefore yield "hyperfine-unselective" EDNMR spectra. If the hyperfine couplings are too small to be resolved with EDNMR, only a single signal will be observed on each side of the EDNMR spectrum for one nucleus.

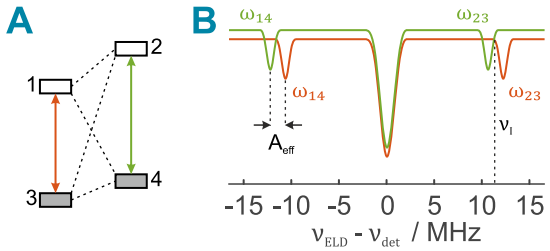

Figure 2.13: A) Energy level diagram of the 2-spin model system that was introduced in Section 2.4. The two different allowed EPR transitions are highlighted. B) Schematic EDNMR spectra of the two different allowed EPR transitions. If the hyperfine coupling is small in comparison to the inhomogeneous EPR line width, the sum of both EDNMR spectra will be recorded.

A crucial parameter in EDNMR experiments is the width $\Delta\nu_{1/2}$ of the central blind spot, since a too broad blind spot can obscure EDNMR signals - especially those of low-γ nuclei. The width of the central blind spot is of less concern when EDNMR experiments are performed at higher magnetic fields (W-band, 94 GHz), as here nuclear frequencies of weakly coupled nuclei are further separated from the central blind spot. At frequencies such as Q-band (34 GHz), experimental parameters such as the length of the ELDOR pulse, the amplitude of the ELDOR pulse and the length of the detection pulses need to be carefully chosen. Optimization of those parameters for Q-band EDNMR measurements is a key component of one publication that is part of this cumulative work (Section 3.1). Therefore, only a brief summary will be given in this section.

The width of the central blind spot can be significantly decreased by using soft detection pulses, although this comes at the expense of a reduced SNR. Physically, softer detection pulses reduce the spectral overlap between ELDOR and detection

pulses when the frequency of the ELDOR pulse approaches the frequency of the detection channel. The length of the ELDOR pulse does not affect the width of the central blind spot as much as the detection pulses. However, use of Gaussian-shaped ELDOR pulses results in a narrowing of the central blind spot, especially at its flanks. For rectangular ELDOR pulses, the full width at half maximum (FWHM) of the central blind spot is directly related to the amplitude ω_{ELD} of the ELDOR pulse by $\Delta\nu_{1/2} = \omega_{ELD}/\pi$, if $\omega_{ELD}t_{ELD} \gg 1$ ($\Delta\nu_{1/2}$ in Hz and ω_{ELD} in rad s^{-1}) [74]. It should be noted, however, that at Q-band frequencies, unresolved and obscured nuclear frequencies can lead to an artificial broadening of the central blind spot. In such cases, it is better to measure ω_{ELD} with nutation experiments at zero frequency.

The resolution of EDNMR experiments is limited by the homogeneous EPR line width, which is the inverse of the phase memory time T_m. For $d5$ transition metal ions at Q-band frequencies, T_m is on the order of approximately 2 µs, which limits the resolution of EDNMR experiments on transition metal ions to approximately 0.5 MHz. For ENDOR techniques, the resolution is determined by the longitudinal electron spin or nuclear spin relaxation time T_{1e} and T_{1n} (depending on which is shorter). For $d5$ transition metal ions at Q-band frequencies, T_{1e} is on the order of approximately 1 ms, which corresponds to a maximum resolution of 1 kHz. As a consequence, the resolution of EDNMR is worse than the resolution of ENDOR. Additional shortcomings of EDNMR are that resonances of low-γ nuclei can be obscured by the central blind spot, and that the appearance of multi quantum (MQ) signals (Section 3.1) and an overlap of different nuclear species (Section 3.2) can hamper a meaningful analysis of EDNMR spectra. Advantages of EDNMR over ENDOR include a drastically increased sensitivity, the absence of any blind spots (besides the central blind spot) and the possibility to observe different nuclear species in a single EDNMR experiment. In an ENDOR experiment, the RF pulse must be specifically tuned to every nuclear species with nutation experiments.

2.5.3 2D ELDOR-detected NMR and THYCOS

Although widely used, conventional ENDOR techniques and the EDNMR experiment have its limitations. For example, more sophisticated hyperfine experiments are needed if nuclear frequency spectra are too congested for a meaningful analysis or if it is required to correlate different nuclear spins to the same electron spin. In such a case, two-dimensional hyperfine methods are valuable. In this context, two-dimensional means that the echo intensity is monitored as a function of two variables. Two-dimensional hyperfine data are typically plotted as a two-dimensional contour plot of a three-dimensional "surface".

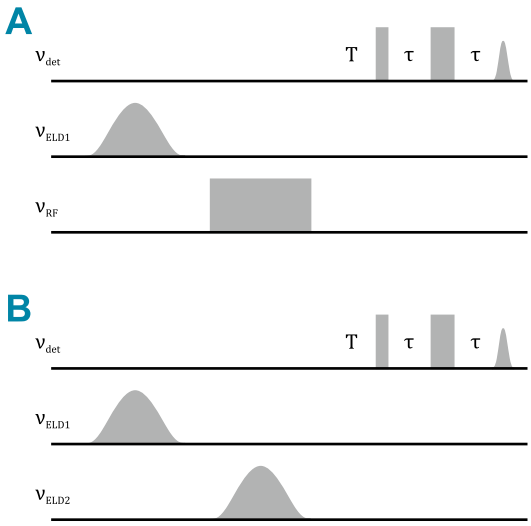

Figure 2.14: THYCOS (A) and 2D EDNMR (B) pulse sequences. In both cases, Gaussian-shaped ELDOR pulses are depicted.

The first two-dimensional hyperfine spectroscopy experiment was HYSCORE, which is a descendant of a three-pulse ESEEM experiment. In HYSCORE, of which the original pulse sequence was published in 1986 [75], the echo is monitored as a function of two interpulse delay times τ_1 and τ_2. Just as ESEEM, HYSCORE is a coherence-transfer technique. Therefore, HYSCORE will not be further described in this work. In 1987, Mehring et al. reported a ENDOR triple resonance (TRIPLE) experiment, in which the two RF pulses are used instead of one [76]. The frequencies of the RF pulses are varied independently, hence the observed signal becomes a function of the two RF pulses. A modification

of the pulsed TRIPLE sequence and a combination of ENDOR and EDNMR is the THYCOS experiment [34]. In THYCOS, the first RF pulse is replaced by a highly selective ELDOR pulse (Figure 2.14A). In theory, the frequencies of the ELDOR pulse and the RF pulse are varied systematically around the frequencies of interest. In practice, however, the frequency of the ELDOR pulse is kept constant and set on-resonance with a forbidden transition, while the frequency of the RF pulse is varied. THYCOS is therefore a highly selective Davies ENDOR experiment - if the ELDOR pulse is off-resonance to any transition, only a baseline will be recorded as a RF pulse will have no effect on thermal equilibrium $-S_z$ magnetization.

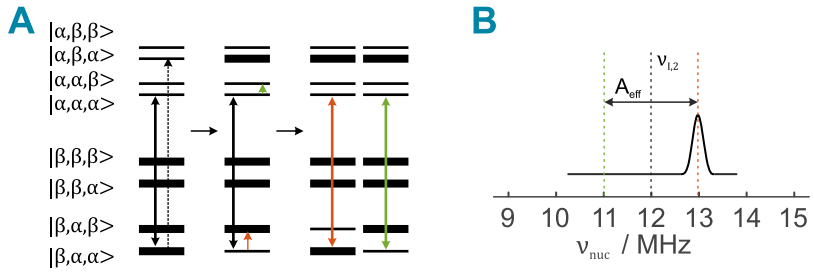

Figure 2.15: A) Evolution of spin population during THYCOS and energy ladder diagram of a 3-spin model system with $S = 1/2$, $I_1 = 1/2$ and $I_2 = 1/2$ (g_n, $a_{iso} > 0$). Coupling between the two nuclear spins I_1 and I_2 is neglected. Thick solid lines depict the observed allowed EPR transition. The dashed black line highlights the forbidden transition that is on-resonance with the ELDOR pulse. Colored thin solid lines depict allowed NMR transitions on-resonance with the RF pulse. B) Expected THYCOS spectrum.

THYCOS spectra can be understood by looking at a 3-spin model system, consisting of one electron spin with $S = 1/2$ and two nuclear spins with $I_1 = 1/2$ and $I_2 = 1/2$. The resulting energy ladder diagram is depicted in Figure 2.15A (g_n, $a_{iso} > 0$). If the detection channel is set to monitor the intensity of the allowed EPR transition $|m_S = \beta, m_{I,1} = \alpha, m_{I,2} = \alpha\rangle \leftrightarrow |\alpha, \alpha, \alpha\rangle$, only one forbidden transition associated with nucleus I_1 exists ($|\beta, \alpha, \alpha\rangle \leftrightarrow |\alpha, \beta, \alpha\rangle$) that has a larger energy than the observed allowed EPR transitions. After the population of this transition has been inverted by the ELDOR pulse, the RF pulse can excite two allowed NMR transitions of nucleus I_2 that are connected with the observed allowed EPR transition. If the RF pulse is on-resonance with

transition $|\alpha,\alpha,\alpha\rangle \leftrightarrow |\alpha,\alpha,\beta\rangle$ no population will be transferred, simply because both energy levels are equally populated. If transition $|\beta,\alpha,\alpha\rangle \leftrightarrow |\beta,\alpha,\beta\rangle$ is affected by the RF pulse, population will be transferred to the ground state. The detection sequence will now monitor zero echo intensity if the RF pulse was on-resonance with transition $|\alpha,\alpha,\alpha\rangle \leftrightarrow |\alpha,\alpha,\beta\rangle$ (green thick solid arrow in Figure 2.15A). A positive Hahn echo will be recorded if the RF pulse was on-resonance with transition $|\beta,\alpha,\alpha\rangle \leftrightarrow |\beta,\alpha,\beta\rangle$ (red thick solid arrow in Figure 2.15A).

Figure 2.15B shows the expected THYCOS spectrum for the abovementioned transition-excitation-scheme. No THYCOS signal is obtained if the RF pulse excites a nuclear transition of nucleus I_2, that lies in the same electron spin manifold that was also used for excitation of a nuclear transition of nucleus I_1 by the ELDOR pulse ($|m_S = \alpha\rangle$ in Figure 2.15). A positive THYCOS signal is obtained if the RF pulse excites the nuclear transition of nucleus I_2 that lies in the $|m_S = \beta\rangle$ manifold. This relation can be used to determine the sign of the hyperfine coupling [77, 78].

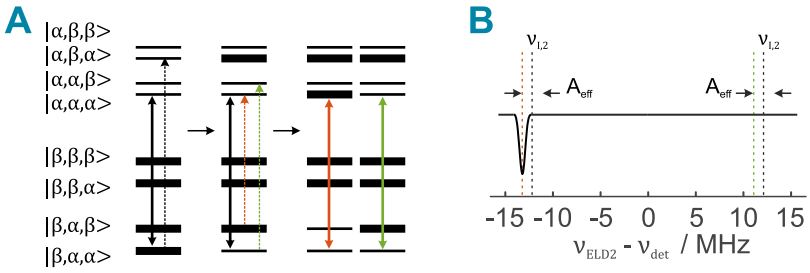

Figure 2.16: A) Evolution of spin population during 2D EDNMR and energy ladder diagram of a 3-spin model system with $S = 1/2$, $I_1 = 1/2$ and $I_2 = 1/2$ (g_n, $a_{iso} > 0$). Coupling between the two nuclear spins I_1 and I_2 is neglected. Thick solid lines depict the observed allowed EPR transition. The dashed black line highlights the forbidden transition that is on-resonance with the first ELDOR pulse. Colored dashed lines depict forbidden transitions on-resonance with the second ELDOR pulse. B) Expected 2D EDNMR spectrum.

Figure 2.14B shows the 2D EDNMR pulse sequence [35]. In comparison to THYCOS, the RF pulse gets replaced by a second ELDOR pulse. Thus, the Hahn echo is monitored as a function of the frequencies of the two ELDOR pulses. The first step of evolution of spin population for a 2D EDNMR is identical to a

THYCOS pulse sequence (Figure 2.16A). In a second step, the second ELDOR pulse can excite two forbidden transitions of nucleus I_2 that are connected to the observed allowed EPR transition. If transition $|\beta,\alpha,\alpha\rangle \leftrightarrow |\alpha,\alpha,\beta\rangle$ is excited by the second ELDOR pulse, no population will be transferred. Excitation of transition $|\beta,\alpha,\beta\rangle \leftrightarrow |\alpha,\alpha,\alpha\rangle$ by the second ELDOR pulse, however, inverts the spin population. The Hahn echo sequence will record zero intensity if transition $|\beta,\alpha,\alpha\rangle \leftrightarrow |\alpha,\alpha,\beta\rangle$ was excited by the second ELDOR pulse. A negative 2D EDNMR signal will be observed upon excitation of transition $|\beta,\alpha,\beta\rangle \leftrightarrow |\alpha,\alpha,\alpha\rangle$ by the second ELDOR pulse.

The expected 2D EDNMR spectrum is shown in Figure 2.16B. The information content is very similar to the THYCOS spectrum presented in Figure 2.15B. The biggest difference is that the signal, which corresponds to excitation of the nuclear transition of nucleus I_2 in the $|m_S = \beta\rangle$ manifold, is negative and not positive as in THYCOS (Figure 2.15B). One has to bear in mind that in reality long and weakly powered ELDOR pulses act as saturation-pulses and not as inversion-pulses. In addition, a forbidden transition will never be completely saturated. As a consequence, considerable Hahn echo intensity will be detected if the first ELDOR pulse is off-resonance and the second ELDOR pulse is on-resonance (and vice versa). These 1D EDNMR signals will have a stronger intensity than the 2D EDNMR signals. A background correction procedure is therefore required to remove the stronger 1D EDNMR signals. In such a protocol, every data vector along the $\Delta\nu_1$ domain of primary 2D EDNMR data $(\Delta\nu_1, \Delta\nu_2)$ is divided by the mean value of the two vectors along the $\Delta\nu_1$ domain with the biggest $\Delta\nu_2$ offsets. This first step removes all 1D EDNMR signals in the $\Delta\nu_1$ domain. In a second step, the background corrected data matrix is used for a background correction in the $\Delta\nu_2$ domain.

2D EDNMR is typically more sensitive than THYCOS. Therefore, it is feasible to record a complete 2D EDNMR spectrum if the concentration if high enough. If a high resolution is desired or if the concentration is low, specific 2D EDNMR slices can be recorded. Then, two 2D EDNMR slices are required. One, where both ELDOR pulses are on-resonance with the desired forbidden transitions (the frequency in one domain is kept fixed, whereas the frequency in the other domain varied). The second slice is needed for background correction

and should therefore contain only 1D EDNMR signals (the ELDOR pulse of the fixed frequency-domain should be off-resonance to any transition). Normally, it is not feasible to record complete THYCOS spectra, even for highly concentrated samples. In virtually every situation it is therefore appropriate to record a single THYCOS slice instead of a complete THYCOS spectrum.

Although THYCOS is superior to 2D EDNMR in terms of sensitivity, it offers a better resolution than 2D EDNMR (just as ENDOR offers a better resolution than 1D EDNMR). Moreover, the background correction of 2D EDNMR can introduce uncertainties in signal assignment if the SNR is not sufficient. Especially 2D EDNMR signals close to the central blind spot can become difficult to analyze and assign. In general, signal assignment and interpretation for 2D EDNMR is not as straightforward as for THYCOS. For a more detailed discussion, including problems in signal assignment and the choice of experimental parameters, the reader is referred to Section 3.2. Application of THYCOS and 2D EDNMR to a TC-aptamer and analysis and interpretation of the obtained data is a focal point of Section 3.2 and its related publication.

2.6 PELDOR with Rigid Nitroxide Spin Labels

2.6.1 4-pulse PELDOR

PDS describes an array of techniques that probe the dipolar coupling of weakly coupled electron spins (Section 2.1.4). The primary use of PDS is the determination of intramolecular distances between two paramagnetic spin centers. The PELDOR technique (sometimes also called double electron-electron resonance (DEER) spectroscopy) is currently the most used PDS pulse sequence [79, 80].

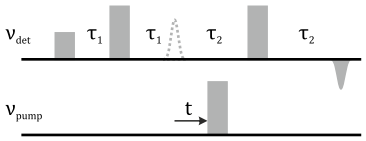

Figure 2.17: 4-pulse PELDOR pulse sequence. The refocused Hahn echo is monitored as a function of the interpulse delay time t.

With the 4-pulse sequence, PELDOR is able to measure distances in the range of 1.5 to 8 nm [81]. Under exceptional circumstances (sparse spin-labeling, deuterated solvent and biomolecule), intramolecular distance up to 16 nm could be measured [11]. In PELDOR, a refocused Hahn echo sequence at frequency ν_{det} is used to monitor the intensity of an allowed EPR transition (referred to as "detection spins" or "observer spins"). A π pulse in a second MW channel is used to invert the population of spins that are on-resonance with frequency ν_{pump} ("pump spins"). A certain minimum frequency offset of $\Delta\nu = \nu_{det} - \nu_{pump}$ is needed to ensure that each channel acts selectively on either the detection spins or the pump spins. In PELDOR, the time t before the pump pulse is incremented. As a consequence, the refocused Hahn echo gets modulated by the dipolar coupling frequency ν_{dd}. If one assumes that the pump pulse is applied at the time of the Hahn echo (or later), the Hahn echo sequence $(\frac{\pi}{2} - \tau_1 - \pi - \tau_1)$ generates $-S_y$ coherence on the observer spin ($-S_{y,1}$). If one neglects the dephasing due to different electron spin offsets (it refocuses after the time $2\tau_1 + 2\tau_2$), the dipolar coupling evolves during time t. After the time t the pump pulse inverts the population of the pump spins:

$$\begin{aligned}\sigma\left(2\tau_1\right) = -S_{y,1} &\xrightarrow{\nu_{dd} t S_{z,1} S_{z,2}} -cos\left(\frac{\nu_{dd} t}{2}\right) S_{y,1} + sin\left(\frac{\nu_{dd} t}{2}\right) 2S_{x,1}S_{z,2} \\ &\xrightarrow{\pi S_{x,2}} -cos\left(\frac{\nu_{dd} t}{2}\right) S_{y,1} - sin\left(\frac{\nu_{dd} t}{2}\right) 2S_{x,1}S_{z,2} = \sigma\left(2\tau_1 + t\right).\end{aligned} \tag{2.44}$$

During the time $\tau_2 - t$, the dipolar coupling is again allowed to evolve:

$$\begin{aligned}&\sigma\left(2\tau_1 + t\right) \xrightarrow{\nu_{dd}(\tau_2 - t) S_{z,1} S_{z,2}} \\ &- cos\left(\frac{\nu_{dd} t}{2}\right)\left\{cos\left(\frac{\nu_{dd}(\tau_2 - t)}{2}\right) S_{y,1} - sin\left(\frac{\nu_{dd}(\tau_2 - t)}{2}\right) 2S_{x,1}S_{z,2}\right\} \\ &- sin\left(\frac{\nu_{dd} t}{2}\right)\left\{cos\left(\frac{\nu_{dd}(\tau_2 - t)}{2}\right) 2S_{x,1}S_{z,2} + sin\left(\frac{\nu_{dd}(\tau_2 - t)}{2}\right) S_{y,1}\right\} \\ &\quad = -cos\left(\frac{\nu_{dd}(\tau_2 - 2t)}{2}\right) S_{y,1} + sin\left(\frac{\nu_{dd}(\tau_2 - 2t)}{2}\right) 2S_{x,1}S_{z,2} \\ &\quad = \sigma\left(2\tau_1 + \tau_2\right),\end{aligned} \tag{2.45}$$

whereby the last transformation of Equation 2.45 is due to the cosine and

sine addition formulae ($cos(\alpha \pm \beta) = cos\alpha cos\beta \mp sin\alpha sin\beta$, $sin(\alpha \pm \beta) = sin\alpha cos\beta \pm sin\beta sin\alpha$). In a next step, the third detection pulse inverts the spin population of the observer spins. Afterwards, the dipolar coupling ν_{dd} evolves during the time τ_2:

$$\begin{aligned}
&\sigma\left(2\tau_1+\tau_2\right) \xrightarrow{\pi S_{x,1}} \\
&cos\left(\frac{\nu_{dd}(\tau_2-2t)}{2}\right) S_{y,1} + sin\left(\frac{\nu_{dd}(\tau_2-2t)}{2}\right) 2S_{x,1}S_{z,2} \xrightarrow{\nu_{dd}\tau_2 S_{z,1}S_{z,2}} \\
&\quad cos\left(\frac{\nu_{dd}(\tau_2-2t)}{2}\right)\left\{cos\left(\frac{\nu_{dd}\tau_2}{2}\right) S_{y,1} - sin\left(\frac{\nu_{dd}\tau_2}{2}\right) 2S_{x,1}S_{z,2}\right\} \\
&+ sin\left(\frac{\nu_{dd}(\tau_2-2t)}{2}\right)\left\{cos\left(\frac{\nu_{dd}\tau_2}{2}\right) 2S_{x,1}S_{z,2} + sin\left(\frac{\nu_{dd}\tau_2}{2}\right) S_{y,1}\right\} \\
&\quad = cos\left(\frac{\nu_{dd}2t}{2}\right) S_{y,1} - sin\left(\frac{\nu_{dd}2t}{2}\right) 2S_{x,1}S_{z,2} = \sigma\left(2\tau_1+2\tau_2\right).
\end{aligned} \tag{2.46}$$

Application of trigonometric addition formulae (last line of Equation 2.46, $cos(\alpha \pm \beta) = cos\alpha cos\beta \mp sin\alpha sin\beta$, $sin(\alpha \pm \beta) = sin\alpha cos\beta \pm sin\beta sin\alpha$) yields detectable in-phase S_y magnetization for the detection spins, which no longer depends on τ_2, but only on t and ν_{dd}. The detected refocused Hahn echo therefore oscillates with $cos(\nu_{dd}t)$ if time t before the pump pulse gets incremented.

In almost all applications, the primary PELDOR signal is a product of two components:

$$V(t) = F(t) \times B(t), \tag{2.47}$$

where $F(t)$ contains the intramolecular dipolar interaction. $B(t)$ describes the intermolecular dipolar coupling and is sometimes referred to as the "background" function. Typically, the dipolar oscillations in $F(t)$ are dampened out at a certain time point (t_{const}). From this point on, $F(t)$ is a constant value. If the maximum dipolar evolution time t_{max} is larger than t_{const}, the time between t_{max} and t_{const} can be used to fit the intermolecular background function $B(t)$. $B(t)$ can be modeled by a stretched exponential decay function [82, 83]:

$$B(t) = e^{-(kt)^{d/3}}, \tag{2.48}$$

where d describes the spatial homogeneity of the background function. For a homogeneous distribution in three-dimensional space, d is equal to 3 and Equation 2.48 becomes a monoexponetial decay function. k is a decay rate constant and is defined as [82, 83]

$$k = c\lambda \frac{8\pi^2 \beta_e g_{det} g_{pump}}{9\sqrt{3}\hbar}, \tag{2.49}$$

where c is the local concentration of the sample and λ describes the fraction of spins excited by the pump pulse ("spin flip probability"). A highly concentrated sample therefore yields a strongly decaying background function. Since a strongly decaying background function can compromise the SNR, PELDOR samples typically have a concentration of 100 µM.

In Section 2.1.4, it was discussed that the electron dipole-dipole interaction is anisotropic and depends on the angle θ. The intramolecular PELDOR signal is therefore the weighted sum off all orientations for a given distance r. In addition, the distance r is in most cased subjected to a distribution, i.e., a Gaussian. Mathematically, such a function can be expressed as

$$S(t) = \int_r exp\left\{ -\frac{(r-r_0)^2}{2\left(\frac{FWHM}{2\sqrt{2ln2}}\right)^2} \right\} S_0 \int_0^{\pi/2} cos\left(\nu_{dd}\left(3cos^2\theta - 1\right)t\right) sin\theta d\theta dr. \tag{2.50}$$

In Equation 2.48 and Equation 2.49, it was already shown that the fraction of spins that are excited by the pump pulse affects the decay rate of the background function. For obvious reasons, λ also affect the intramolecular signal. The intramolecular PELDOR signal for a given distance distribution, considering the spin flip probability λ, is given by [84]:

$$F(t) = 1 - \lambda + \lambda S(t). \tag{2.51}$$

Equation 2.51 shows that larger λ values lead to a bigger difference between the maximum signal intensity and the signal intensity at t_{max} (better SNR). For example, if no pump spins are excited that are dipolar coupled to the observer spins, λ is zero and Equation 2.51 becomes $F(t) = 1$.

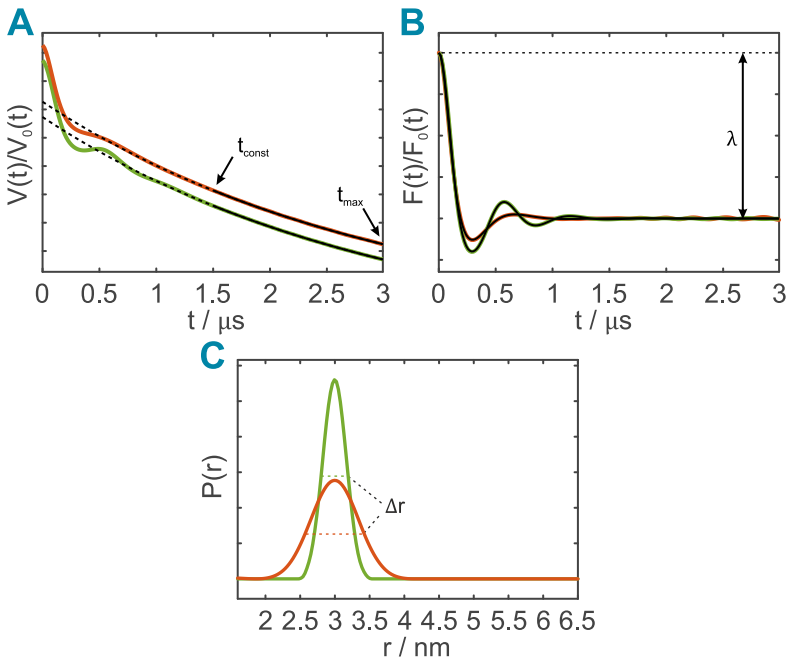

Figure 2.18: Simulated PELDOR data for a Gaussian distance distribution centered at $r = 3\,\text{nm}$. A FWHM of either 0.4 nm (green) and 0.8 nm (orange) was used. A) Primary PELDOR data. The fitted background function is shown in black. The solid black line shows the region used for fitting. B) Background-corrected PELDOR data. The Tikhonov fit is shown in black. C) Distance distribution obtained after Tikhonov regularization. PELDOR data were simulated with a home-written MATLAB script, background correction and Tikhonov regularization was performed with the MATLAB toolbox DeerAnalysis [85].

Figure 2.18 shows the data processing of PELDOR data, with primary (raw) PELDOR data (Figure 2.18A), background-corrected PELDOR data (Figure 2.18B) and the distance probability function $P(r)$ (Figure 2.18C). Obtaining $P(r)$ is an inverse problem, since the effect (recorded PELDOR time trace) is used to "back-calculate" the cause (distance probability function $P(r)$). Solving an inverse problem is difficult (ill-posed problem), since the back-calculation is sensitive to many parameters, i.e., the SNR. The solution of an inverse problem can be stabilized by applying regularization procedures. For PELDOR, Tikhonov regularization with a second-derivative regularization operator is currently the most commonly applied regularization procedure:

$$P_\alpha = \underset{P\geq 0}{\operatorname{argmin}} \left(\|S(t) - K(t,r)P(r)\|^2 + \alpha \|LP(r)\|^2 \right). \tag{2.52}$$

Equation 2.52 is minimized for every α value under the condition that P_α is positive. The first term of Equation 2.52 is a least-squares term, where $S(t)$ represents the experimental intramolecular PELDOR signal. The product (Fredholm integral) of a kernel function $K(t,r)$ and a model distance distribution $P(r)$ gives a simulated intramolecular PELDOR signal. The second term penalizes unwanted properties of the model distance distribution $P(r)$. L is the regularization operator, i.e., $L = \frac{d^2}{dr^2}$, and defines what properties of $P(r)$ are to be penalized. α is the regularization parameter, and weights the penalizing term. If the value of α is too high, the distance distribution is "oversmoothed" and narrow features of the actual distance distribution might become obscured. If the value of α is too low, $P(r)$ is insufficiently penalized, and the first term in Equation 2.52 might fit noise as a dipolar oscillation.

Consequently, the correct choice of α is crucial for a correct analysis of PELDOR data. The most widely used selection method for the regularization parameter is based on the L-curve criterion. In a L-curve, the decadic logarithm of the least-squares term is plotted as a function of the decadic logarithm of the penalizing term for every α value. For an ideal data set, the plotted function should be L-shaped and the optimal α value is the one that corresponds to the "kink" of the L-shaped plot. Recent publications suggest the use of other α selection methods than the L-curve criterion (Akaike information criterion or generalized cross validation) or the use of neural networks [86–88].

As already mentioned at the beginning of this section, detection and pump pulses are irradiated with a frequency offset ($\Delta\nu = \nu_{pump} - \nu_{det}$). Typically, the frequency (magnetic field) of the pump pulse is chosen so that it coincides with the maximum intensity of the nitroxide EPR spectrum (Figure 2.1). At Q-band, the detection frequency is decreased by $|\Delta\nu|$. Hence, detection is performed on the right-hand side of the maximum of the Q-band nitroxide EPR spectrum. At X-band, the detection frequency is typically increased by $|\Delta\nu|$ and as a consequence, detection is performed on the left-hand side of the maximum of

the X-band nitroxide EPR spectrum. Typical frequency offsets lie in the range of $|40 - 90\,\mathrm{MHz}|$.

If in a PELDOR experiment only the distance is of interest, pulse lengths are chosen so that as much spins as possible are excited while avoiding spectral overlap of detection and pump pulse excitation profiles. Typical PELDOR pulse lengths at X- and Q-band frequencies are in the range of 20 ns. If orientation selection (OS) is desired, softer (longer) pulses may be used. Gaussian-shaped pulses are known to increase the fidelity of PELDOR data, as the use of Gaussian-shaped pulses reduce the residual "2+1" signal at the end of PELDOR time traces [89]. The "2+1" artifact is a consequence of minor spectral overlap of detection and pump pulses, which sometimes cannot be avoided with rectangular pulses.

Depending on the ratio of τ_1 and τ_2 and the use of a coherent or incoherent pump pulse source, different phase cycle schemes are required for PELDOR [90]. If a significant amount of the sample is deuterated (glassing agent, buffer, biomolecule), a τ_1-averaging cycle to suppress ^{2}H ESEEM modulations is recommended [91]. Often, the use of shaped broadband pump pulses alone, or in combination with more elaborated PELDOR pulse schemes helps to increase the maximum dipolar evolution time and sensitivity of PELDOR [47, ch. 21]. It should be noted that the outlined theory involving product operator formalism and Tikhonov regularization is only valid if multi-spin systems, high-spin systems, OS, exchange coupling and differential relaxation can be neglected.

The experimental difference between maximum signal intensity and the signal intensity at the maximum dipolar evolution time t_{max} for background-corrected PELDOR data is often referred to as modulation depth Δ. For an isolated 2-spin system without OS, the spin flip probability λ is the same as the modulation depth Δ. Multi-spin and/or high-spin systems, however, introduce terms in the Hamiltonian that increase the modulation depth, so that $\Delta > \lambda$ [84].

2.6.2 Advantages of Rigid Spin Labels

As the name suggests, rigid spin labels are attached in a very rigid manner to the biomolecule of interest. For nucleic acids, rigid spin labels are typically connected via two covalent bonds to the nucleobase. A frequently used rigid nitroxide spin label for nucleic acids is the Ç (for DNA) and Çm spin label (for RNA, Figure 1.3C). As can be inferred from Figure 1.3C, the absence of any free rotating bond severely limits the internal degree of freedom of Çm. This stands in contrast to flexible nitroxide spin labels (such as MTSL), where the spin label is connected via a flexible and free rotating tether to the biomolecule of interest.

As a consequence of the rigidity, PELDOR in combination with rigid spin labels can be used to directly investigate the conformational flexibility of the spin-labeled secondary structure elements. RNA helices with a high degree of conformational freedom will yield a broad distance distribution and strongly dampened dipolar oscillations in the time domain (orange lines in Figure 2.18). Vice versa, RNA helices with a low degree of conformational freedom will give a narrow distance distribution with pronounced dipolar oscillations (green lines in Figure 2.18). Flexible spin labels should not be used to relate the width of the distance distribution Δr to the conformational flexibility of the spin-labeled secondary structure, since it is not known if the width Δr is mainly caused by the spin label itself or by the secondary structure element.

Under certain experimental conditions, rigid spin labels can produce PELDOR time traces that show OS. OS can alter the oscillation pattern and the spin flip probability function λ and is caused by selective excitation of specific g tensor and/or ^{14}N hyperfine tensor components. For strong OS, distance analysis using Tikhonov regularization is no longer reliable and therefore not recommended.

In order to understand OS, it is necessary to introduce different coordinate frames. The dipolar frame defines the orientation of the dipolar tensor with respect to the external magnetic field (laboratory frame). Per definition, the dipolar distance vector r is always aligned along the z-axis of the dipolar frame. The molecular frames of nitroxide 1 and 2 describe the orientations of nitroxide 1 and 2. Per definition, the x-axis is aligned along the NO bond and the z-axis is the out-of-plane normal and aligned with the $2p_z$ orbital of nitrogen.

For disordered samples, it is common practice to use the g tensor coordinate frame as the molecular frame. To a very good approximation, the g tensor and the ^{14}N hyperfine tensor are collinear [39]. The dipolar frame is related to the laboratory frame by the polar angles θ and ϕ. The molecular frames are related to the dipolar frame by two sets of Euler angles ($\alpha_{1/2}$, $\beta_{1/2}$ and $\gamma_{1/2}$). Per definition, α_1 is always 0°. A schematic representation of a nitroxide spin pair with the aforementioned coordinate frames is shown in Figure 2.19A.

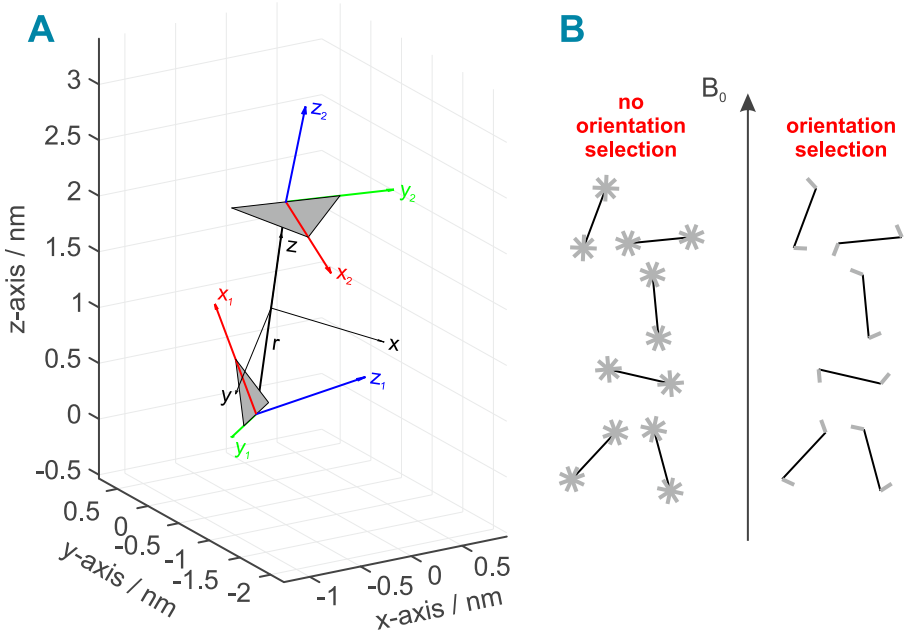

Figure 2.19: A) Nitroxide spin pair with a randomly chosen orientation with respect to the laboratory frame. The dipolar coordinate frame and the dipolar distance vector are shown as black arrows and lines. The molecular coordinate frames of nitroxide 1 and 2 are shown as red ($x_{1/2}$-axis), green ($y_{1/2}$-axis) and blue ($z_{1/2}$-axis) arrows. B) Schematic visualization of the physical origin of OS. If OS exists, specific orientations in a spin pair are correlated and more probable.

The physical origin behind OS is depicted schematically in Figure 2.19B. In the case of no OS, all orientations are randomly and uniformly distributed in space. If, for example, a X-band PELDOR time trace with an offset of $\Delta\nu = -90\,\mathrm{MHz}$ is recorded, the detection pulses mainly excite the A_z component of the detection spins (Figure 2.1A). The frequency of the pump pulse is typically on-resonance with the maximum of the X-band nitroxide EPR spectrum, and therefore the

pump pulse excites all possible orientations (to a good approximation). In case of no OS, the A_z component of the detection spins interacts via dipolar coupling with *all* possible orientations of the pump spins. If OS is present, the A_z component of the detection spins *only* interacts with a very specific orientation of the pump spins, although the pump pulse still excites all possible orientations. The specific orientation of the pump spins that is interacting with the detection spins is determined by the (rigid) geometry of the spin-labeled biomolecule.

Mathematically speaking, OS means that the spin flip probability λ becomes a function of the resonance frequencies of the detection and pump spins, the two set of Euler angles and the polar angle θ. If one omits a distance distribution for sake of clarity and only assumes a single distance r, the intramolecular PELDOR signal in case of OS is given by [92]:

$$F(t) = S_0 \int_0^{\pi/2} \lambda\left(\nu_{det}, \nu_{pump}, \xi_1, \xi_2, \theta\right) \times \left[cos\left(\nu_{dd}\left(3cos^2\theta - 1\right)t\right) - 1\right] sin\theta d\theta, \tag{2.53}$$

whereby $\xi_1 \equiv (\alpha_1, \beta_1, \gamma_1)$ and $\xi_2 \equiv (\alpha_2, \beta_2, \gamma_2)$. For this work it is sufficient to realize that λ becomes a function of the excited orientations of the detection and pump spins. A derivation of an analytical expression of $\lambda\left(\nu_{det}, \nu_{pump}, \xi_1, \xi_2, \theta\right)$ is beyond the scope of this work, however, the reader is referred to several literature reports for further reading and a complete derivation of $\lambda\left(\nu_{det}, \nu_{pump}, \xi_1, \xi_2, \theta\right)$ [93–95].

In order to extract the information content of OS (ξ_1 and ξ_2), one typically records several X-band PELDOR time traces with different offsets ranging from -40 to -90 MHz in steps of 10 MHz. The frequency of the pump pulse is kept constant, whereas the frequency of the detection pulses is changed. The recorded and background-corrected PELDOR time traces can be simulated with iterative fitting algorithms and programs that calculate PELDOR data based on a density operator formalism approach [96]. Figure 2.20 shows simulated orientation-selective X-band PELDOR data for different offsets and two different orientations. The first orientation ($\xi_1 = (0°, 20°, 0°)$, $\xi_2 = (20°, 10°, 0°)$, $r = 3$ nm, Figure 2.20A) shows clear OS for the modulation depth and the oscillation pattern.

For the second orientation ($\xi_1 = (0°, 50°, 0°)$, $\xi_2 = (80°, 40°, 0°)$, $r = 3\,\mathrm{nm}$, Figure 2.20B), however, no clear sign of OS can be detected. The oscillation pattern and the modulation depth seem to be constant for different offsets. Figure 2.20 shows, that OS can be difficult to detect for certain orientations. It is therefore recommended to cross-validate X-band OS PELDOR with high frequency PELDOR data or other methods of structural biology.

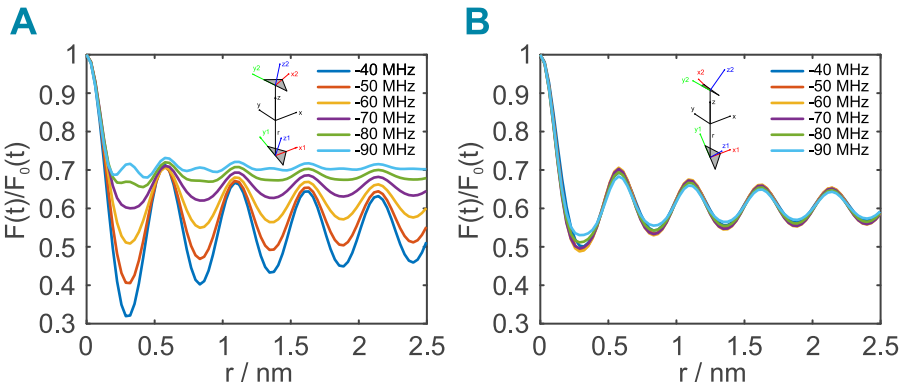

Figure 2.20: Simulation of orientation-selective X-band PELDOR time traces using a density operator formalism approach [96]. Two different orientations were simulated. A) $\xi_1 = (0°, 20°, 0°)$ and $\xi_2 = (20°, 10°, 0°)$. B) $\xi_1 = (0°, 50°, 0°)$ and $\xi_2 = (80°, 40°, 0°)$. All other parameters were identical. In both cases a single distance of $r = 3\,\mathrm{nm}$ was used.

X-band PELDOR experiments are not able to resolve the in-plane Euler angles γ_1 and γ_2. For elucidation of these angles, PELDOR experiments at higher frequencies (G-band, 180 GHz) are necessary [97]. In addition, orientation-selective PELDOR cannot differentiate between a 180° symmetry of the A_z components. In other words, PELDOR cannot resolve if $A_{z,1}$ and $A_{z,2}$ point in the same direction ($\varphi \leq 90°$) or in the opposite direction ($\varphi \geq 90°$). φ is the arccosine of the dot product of $A_{z,1}$ and $A_{z,2}$ and referred to as the bend angle. Furthermore, X-band PELDOR allows to make only relative statements, as both spin labels are indistinguishable and yield identical nitroxide EPR spectra [98]. As a consequence, simulations with an exchanged set of Euler angles for nitroxide 1 and nitroxide 2 will look identical. OS is largely eliminated when traces of all offsets are summed. Q-band PELDOR time traces are not well suited to investigate OS. This is because the anisotropy of the ^{14}N hyperfine interaction

and the anisotropy of the g tensor have similar spectral magnitudes (Figure 2.1B). The rather strong overlap of the different spin Hamiltonian components makes it difficult to excite specific orientations with the detection pulses or the pump pulse. Still, OS at Q-band frequencies can be observed for very rigid systems in combination with very selective detection and pump pulses [99].

Chapter 3

Results and Discussion

The experimental part of this thesis consists of four sections. The first three sections (Section 3.1, 3.2 and 3.3) are based on findings that were previously published in peer-review journals. Therefore, each of these sections contains a short motivation, a summary of the most important results and a brief discussion and conclusion. Section 3.4 contains unpublished data and consequently serves as an outlook for potential future experiments.

Section 3.1 deals with the verification of the feasibility of EDNMR at Q-band frequencies (34 GHz) by applying EDNMR on Mn^{2+} model complexes. Based on the results of Section 3.1, two-dimensional hyperfine spectroscopy (2D EDNMR and THYCOS) is then used to study the metal-mediated ligand binding of a TC-aptamer (Section 3.2). The influence of the divalent metal ion concentration on the conformational flexibility of the TC-aptamer in the presence and absence of the ligand is studied with PELDOR in combination with rigid spin labels (Section 3.3). Section 3.4 presents first Mn^{2+}-nitroxide PELDOR experiments on the TC-aptamer at different Mn^{2+} concentrations with the goal of investigating the affinities of the additional divalent metal ion binding sites.

3.1 ELDOR-detected NMR at Q-band

EDNMR is typically performed at W-band frequencies (94 GHz). This is because at higher microwave frequencies (magnetic fields), nuclear transitions of weakly

coupled ligand nuclei resonate at higher nuclear frequencies. Especially low-γ nuclei like ^{14}N and ^{15}N are therefore easier to detect with EDNMR since they are no longer obscured by the central blind spot. Another reason for performing EDNMR at W-band rather than Q-band is that the spectral resolution between different nuclear spin species increases at higher frequencies.

Despite these disadvantages, Q-band EDNMR has advantages over W-band EDNMR. Firstly, Equation 2.30B shows that forbidden transitions will have an intrinsically larger transition probability I_f at Q-band frequencies compared to W-band frequencies. The transition probability dictates the EDNMR intensity h (hole-depth parameter) of an EDNMR signal alongside with the nominal flip angle β_{ELD} of the ELDOR pulse (Equation 2.43). Secondly, Q-band EPR spectrometers have a wider commercial availability than W-band EPR spectrometers. In addition, Bruker Q-band EPR spectrometers come with an built-in arbitrary waveform generator (AWG) which allows the use of shaped microwave pulses. Shaped microwave pulses, i.e., Gaussian-shaped, will narrow down the width of central blind spot since the spectral overlap of detection pulses and the ELDOR pulse is reduced. Thirdly, the Bruker EN 5170 D2 Q-band probehead is rather robust and shows a good reproducibility of the blind spot profile. An identical resonator bandwidth profile is important for comparing EDNMR intensities of different samples, as the bandwidth profile dictates the effective B_1 field and therefore also the flip angle of the ELDOR pulse.

In order to unravel the potential of Q-band EDNMR, EDNMR at Q-band was applied to several Mn^{2+} model complexes. Namely these model complexes where the hexaaqua complex (either without any isotope labeling or with ^{17}O-labeling) and the Mn-DOTA complex (either without any isotope labeling or with ^{13}C-labeling). Before performing EDNMR on these samples, experimental EDNMR parameters at Q-band were optimized on the manganese hexaaqua complex. It was found that the width of the central blind spot is optimized by using very soft detection pulses ($t_p = 400\,\text{ns}$) and weakly powered ELDOR pulses. For the aforementioned Mn^{2+} model complexes, it was found that an ELDOR pulse amplitude of $\omega_{ELD} = 1.2 \times 10^7\,\text{rad}\,\text{s}^{-1}$ yields a sufficiently narrow central blind spot ($\Delta\nu_{1/2} = 4.4\,\text{MHz}$) while maintaining a reasonable ^{1}H EDNMR signal intensity.

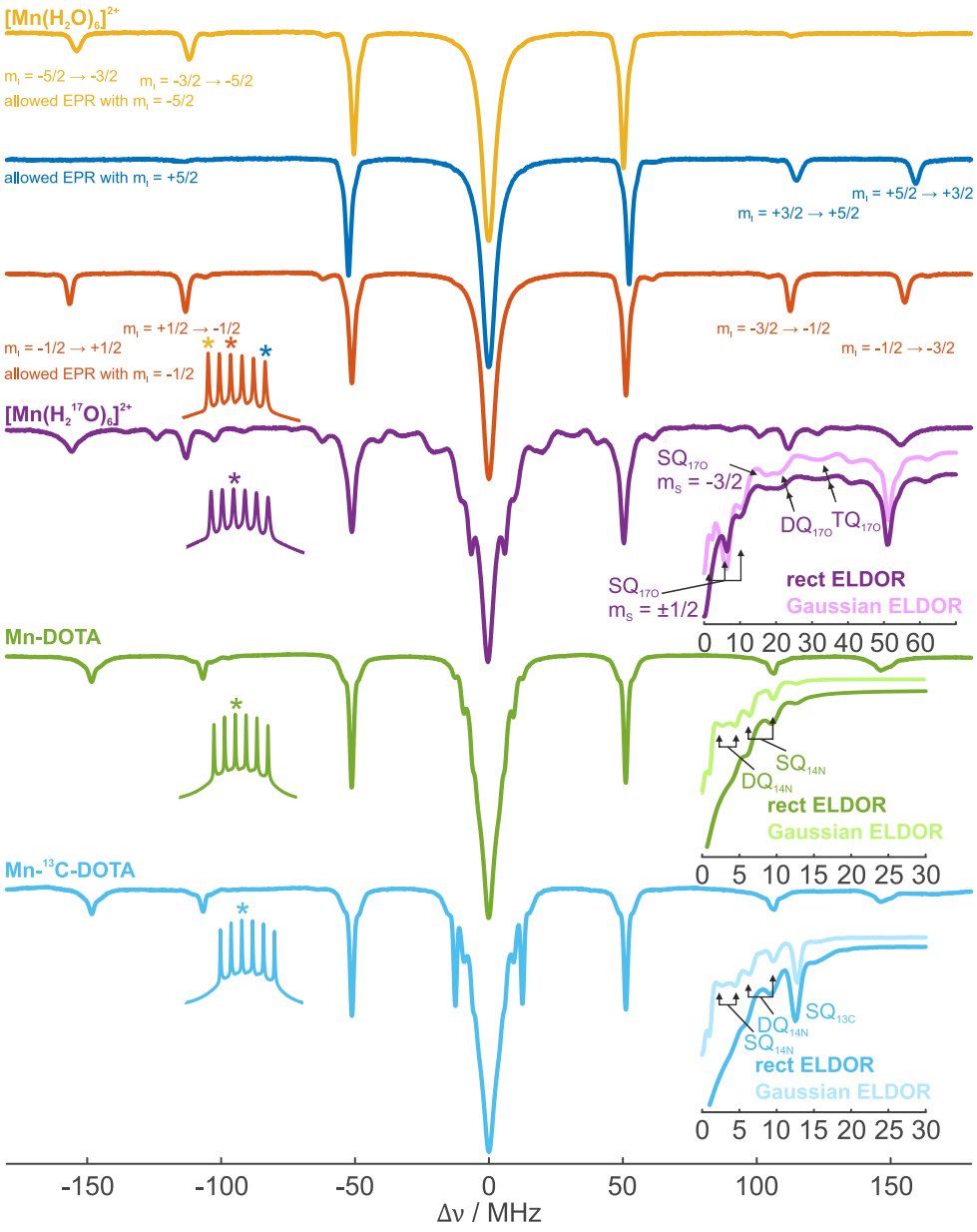

Figure 3.1: Q-band EDNMR spectra of Mn^{2+} model complexes. For the hexaaqua complex, EDNMR spectra are shown for three different magnetic field positions (yellow, blue and red spectra). For the ^{17}O-labeled hexaaqua complex (purple), Mn-DOTA (green) and Mn-^{13}C-DOTA (light blue) only one magnetic field position is shown.

The length of the ELDOR pulse had a rather small impact on the width of the central blind spot, however, it had a strong influence on the line width

of EDNMR signals. For too short ELDOR pulses, an artificial broadening of the EDNMR lines was observed. An ELDOR pulse length of $t_p = 9000\,\text{ns}$ in combination with a broad Hahn echo detection window ($> 1200\,\text{ns}$) yielded EDNMR line widths that were identical to line widths observed with ENDOR. For the abovenamed values of ω_{ELD} and t_p, the empirically postulated blind spot width formula by Nalepa et al. was fulfilled ($\Delta\nu_{1/2} = \omega_{ELD}/\pi$) [74]. The use of Gaussian-shaped ELDOR pulses led to a significant narrowing of the blind spot at its flanks. The use of Gaussian-shaped detection pulses did not improve the width of the central blind spot.

Figure 3.1 shows Q-band EDNMR spectra of the aforementioned Mn^{2+} model complexes. The nuclear frequencies of the strongly coupled ^{55}Mn nucleus ($I = 5/2$) resonate at approximately $\pm 115\,\text{MHz}$ and $\pm 155\,\text{MHz}$. Depending on which nuclear ^{55}Mn transition is excited, the ^{55}Mn EDNMR spectrum is either symmetric or asymmetric with respect to the central blind spot. Interestingly, the splitting $\Delta\nu$ between two ^{55}Mn EDNMR signals is $\Delta\nu \approx 44\,\text{MHz}$ and therefore larger than the expected first-order expression for strongly coupled nuclei of $\Delta\nu = 2\nu_{55Mn} \approx 26\,\text{MHz}$. Sturgeon et al. could show that, due to the large ^{55}Mn hyperfine coupling and the large Mn^{2+} electron spin, it is necessary to use perturbation theory up to third-order to adequately describe the nuclear ^{55}Mn frequencies [100]. A careful investigation of the exact ^{55}Mn EDNMR resonance frequencies at different magnetic fields (the six hyperfine lines of the "central" electron transition) also allows to draw conclusions about the ^{55}Mn quadrupole tensor, although for such studies single crystals are preferred over a frozen solution [50].

For all Mn^{2+} model complexes, nuclear frequencies of weakly coupled ^{1}H nuclei resonate at approximately $\pm 51\,\text{MHz}$. The ^{1}H EDNMR signal of the Mn-DOTA compounds (green and light blue spectra in Figure 3.1) is significantly narrower than the ^{1}H EDNMR signals of the hexaaqua complexes (yellow, blue, red and purple EDNMR spectra). This shows that, although EDNMR does not resolve a Pake doublet and the hyperfine tensor, it is still possible to confine the range of the hyperfine coupling constant with EDNMR at Q-band frequencies.

For the Mn-DOTA complexes (green and light blue EDNMR spectra in Figure 3.1) and the ^{17}O-labeled hexaaqua complex (purple EDNMR spectrum in Figure

3.1), additional signals appear close to the central blind spot. These signals can be sufficiently separated from the central blind spot by using weakly powered and Gaussian-shaped ELDOR pulses. As a consequence, ^{14}N single quantum (SQ) ($\Delta m_S = \pm 1$, $\Delta m_I = \pm 1$) and double quantum (DQ) ($\Delta m_S = \pm 1$, $\Delta m_I = \pm 2$) EDNMR signals become visible for the Mn-DOTA complexes. The extracted effective ^{14}N hyperfine coupling of 1.7 MHz matches the value reported previously [48].

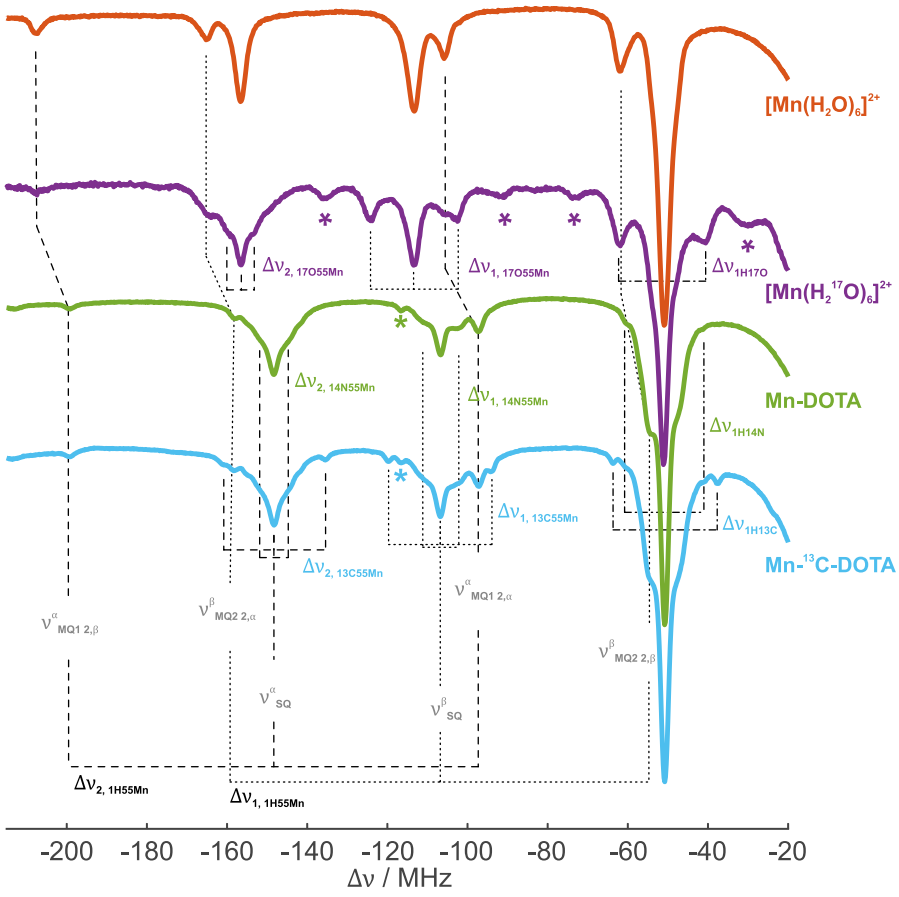

Figure 3.2: ^{55}Mn and ^{1}H region of Q-band EDNMR spectra of Mn^{2+} model complexes using a highly powered ELDOR pulse ($\omega_{ELD} = 8.2 \times 10^7\,\mathrm{rad\,s^{-1}}$). An increase of the power of the ELDOR pulse results in a stronger intensity of MQ EDNMR signals ($\Delta m_S = \pm 1$, $\Delta m_{I,1} = \pm 1$, $\Delta m_{I,2} = \pm 1$).

For the ^{17}O-labeled hexaaqua complex, the signal pattern close to central blind spot features first and second coordination sphere ^{17}O SQ EDNMR signals

originating from the central electron spin manifold. Due to the relatively large ^{17}O isotropic hyperfine coupling, ^{17}O SQ EDNMR signals from the outer electron spin manifold $m_S = -3/2$ are also resolved. In addition, ^{17}O DQ and triple quantum (TQ) ($\Delta m_S = \pm 1$, $\Delta m_I = \pm 3$) EDNMR signals become visible. The surprisingly strong intensity of these signals is attributed to the fact that Mn^{2+}-coupled ^{17}O is close to the cancellation condition at Q-band frequencies.

Application of EDNMR pulses with higher power ($\omega_{ELD} = 8.2 \times 10^7\,\mathrm{rad\,s^{-1}}$) leads to the appearance of additional signals across the EDNMR spectrum (Figure 3.2). These signals can be assigned to combination frequencies, which is the EPR-analogue of a two-photon excitation in optical spectroscopy. In the present study, these signals are referred to as MQ EDNMR signals, as the projection of two different nuclei change their projection ($\Delta m_S = \pm 1$, $\Delta m_{I,1} = \pm 1$, $\Delta m_{I,2} = \pm 1$). Assuming a model spin system consisting of an unpaired electron spin $S = 1/2$ and two nuclear spins $I_1 = 1/2$ and $I_2 = 1/2$, a simple spin ladder diagram and an isotropic spin Hamiltonian can be used to calculate the expected combination frequencies:

$$\nu^{\alpha}_{MQ2|2,\beta} = \nu^{\alpha}_{SQ} - \nu_{I,2} + A_2/2, \tag{3.1A}$$
$$\nu^{\beta}_{MQ1|2,\beta} = \nu^{\beta}_{SQ} + \nu_{I,2} + A_2/2, \tag{3.1B}$$
$$\nu^{\alpha}_{MQ2|2,\alpha} = \nu^{\alpha}_{SQ} + \nu_{I,2} - A_2/2, \tag{3.1C}$$
$$\nu^{\beta}_{MQ1|2,\alpha} = \nu^{\beta}_{SQ} - \nu_{I,2} - A_2/2. \tag{3.1D}$$

In Equations 3.1, ν^{α}_{SQ} and ν^{β}_{SQ} describe SQ EDNMR signals of nucleus I_1, i.e., $-115\,\mathrm{MHz}$ and $-155\,\mathrm{MHz}$ for ^{55}Mn as shown in Figure 3.2. The nomenclature of a MQ EDNMR signal as shown for example in Equation 3.1A ($\nu^{\alpha}_{MQ2|2,\beta}$) is to be understood as follows: The $_{2,\beta}$ in the denominator shows that this MQ signal is connected to an allowed EPR transition with $|m_{I,2} = \beta\rangle$. The $^{\alpha}$ in the numerator shows that the MQ EDNMR signal $\nu^{\alpha}_{MQ2|2,\beta}$ belongs to a pair of MQ signals that are centered around the SQ ν^{α}_{SQ} EDNMR signal of nucleus I_1. The $_{MQ2}$ in the denominator labels two MQ EDNMR signals that are centered around a given SQ EDNMR signal. Equations 3.1 show that two MQ EDNMR signals ($\nu^{\beta}_{MQ1|2,\beta}$ and $\nu^{\beta}_{MQ1|2,\alpha}$) are centered around ν^{β}_{SQ} and split by $2\nu_{I,2} + A_2$, whereas

two MQ EDNMR signals ($\nu^{\alpha}_{MQ2|2,\alpha}$ and $\nu^{\alpha}_{MQ2|2,\beta}$) are centered around ν^{α}_{SQ} and split by $2\nu_{I,2} - A_2$ (see also Figure 3.2):

$$\Delta\nu_{1I1,I2} = \nu^{\beta}_{MQ1|2,\beta} - \nu^{\beta}_{MQ1|2,\alpha} = 2\nu_{I,2} + A_2, \tag{3.2A}$$

$$\Delta\nu_{2I1,I2} = \nu^{\alpha}_{MQ2|2,\alpha} - \nu^{\alpha}_{MQ2|2,\beta} = 2\nu_{I,2} - A_2. \tag{3.2B}$$

Once the combination frequencies have been assigned to the correct nuclei, the frequencies can be used to calculate the effective hyperfine coupling. For example, the additive splitting (Equation 3.2A) of MQ EDNMR signals involving ^{14}N and ^{55}Mn nuclei yields a splitting of 8.6 MHz. As the ^{14}N Larmor frequency is known (Table 2.1), the effective ^{14}N hyperfine coupling can be calculated to 1.2 MHz, which is in agreement with the already published values [48].

The work presented in this section could show that EDNMR at Q-band is a valuable and very sensitive technique to investigate hyperfine couplings. It was possible to extract the effective ^{14}N hyperfine coupling, which would not have been possible with Q-band ENDOR. However, care has to be taken when using highly powered ELDOR pulses, i.e., in cases of poor ligand binding or low concentrations, since the appearance of DQ, TQ and MQ EDNMR signals can severely hamper signal assignment and data analysis. In addition, the low spectral resolution of nuclear Larmor frequencies at Q-band can be problematic, i.e., if the sample contains ^{13}C and ^{23}Na.

3.2 Two-dimensional Hyperfine Spectroscopy on a Tetracycline Aptamer

Once a protocol for EDNMR at Q-band had been established, EDNMR and other hyperfine techniques were used to study the binding of TC to its aptamer. Although the TC-aptamer features a very high affinity towards its ligand at high divalent metal ions concentrations (K_d = 800 pM at 10 mM Mg^{2+}), the affinity is known to decrease at lower and more physiological divalent metal ion concentrations. So far, ligand binding was not yet spectroscopically investigated on an atomistic level but instead on a more macroscopic scale [29, 30]. In

order to directly observe the ligand binding center with pulsed EPR (hyperfine) spectroscopy, diamagnetic Mg^{2+} was substituted by paramagnetic Mn^{2+}. ^{13}C-labeled TC was used as a selective isotope marker. X-ray crystallography data showed that TC coordinates via its $O11$ and $O12$ oxygen atoms to the divalent metal ion. The distance of the metal ion to the oxygen-adjacent carbon atoms is 0.31 nm in both cases. Using the PDA (Equation 2.9), this yields an expected ^{13}C dipolar hyperfine coupling of 0.65 MHz. The divalent metal ion in the binding pocket is further stabilized by two water molecules. A *pro*-R_p oxygen of the phosphate backbone occupies the fifth coordination site. The distance of the divalent metal ion to the phosphorous atom is 0.33 nm, which yields an expected ^{31}P dipolar hyperfine coupling of 1.08 MHz.

Similar ^{13}C-Mn^{2+} and ^{31}P-Mn^{2+} hyperfine coupling values were already observed and reported in literature [35, 101, 102]. Therefore, the hyperfine couplings in the TC-aptamer should be readily observable with hyperfine spectroscopy. All measurements presented in this chapter were performed on samples with equimolar concentrations (1 mM) of the RNA, Mn^{2+} and TC (if present).

^{31}P Davies ENDOR experiments on samples with i) TC-aptamer and Mn^{2+}, ii) TC-aptamer, Mn^{2+} and TC and iii) TC-aptamer, Mn^{2+} and ^{13}C-labeled TC yielded three essentially identical ^{31}P Davies ENDOR spectra. All spectra featured a rather isotropic looking hyperfine splitting with an isotropic ^{31}P hyperfine coupling of $\approx$ 4 MHz ("inner" hyperfine coupling). In addition, a larger hyperfine coupling with an isotropic ^{31}P hyperfine coupling of $\approx$ 9.5 MHz was visible for all three samples ("outer" hyperfine coupling). The outer hyperfine coupling had a reduced intensity in comparison to the inner hyperfine coupling ($\approx$ 30 %). For the outer hyperfine coupling a clear Pake pattern was visible.

The inner hyperfine coupling $A_{31P}(1)$ could be simulated with a combination of four ^{31}P hyperfine tensors, for the outer hyperfine coupling $A_{31P}(2)$ a single ^{31}P hyperfine tensor was sufficient (Table 3.1). The distances shown in Table 3.1 are in agreement with those from the X-ray structure, however, the distances could not be assigned to specific Mn^{2+} binding sites. It is known from a combined ENDOR and density functional theory (DFT) study, that several ^{31}P hyperfine tensors are sometimes needed to describe a single Mn^{2+} binding site [103]. ^{13}C Mims ENDOR was used to investigate the interaction of ^{13}C-labeled TC with

Mn^{2+}. Since it is known that TC also forms a free Mn-TC complex [104], a ^{13}C Mims ENDOR spectrum of a sample containing ^{13}C-labeled TC and Mn^{2+} was compared to the ^{13}C Mims ENDOR spectrum of a sample containing TC-aptamer, Mn^{2+} and ^{13}C-labeled TC. Both spectra looked identical and were characterized by a larger ^{13}C hyperfine coupling which shape was smeared out by the Mims ENDOR blind spot function. A smaller hyperfine coupling close to the ^{13}C Larmor frequency was visible in both cases. EDNMR experiments were in agreement with ^{31}P Davies and ^{13}C Mims ENDOR experiments.

	a_{iso} / MHz	T / MHz	ρ / MHz	r / nm
$A_{31P}(1)$ i	3.75	0.90	-0.35	0.33
$A_{31P}(1)$ ii	4.70	0.85	-0.25	0.34
$A_{31P}(1)$ iii	4.80	0.80	-0.55	0.34
$A_{31P}(1)$ iv	2.85	0.90	-0.35	0.33
$A_{31P}(2)$	9.55	1.05	-	0.31

Table 3.1: Hyperfine tensors that were needed to simulate ^{31}P Davies ENDOR spectra of the TC-aptamer. The ratio of the four rhombic hyperfine tensors for $A_{31P}(1)$ was $1 : 1 : 1 : 0.2$.

Although Davies and Mims ENDOR experiments show that TC interacts with Mn^{2+} at lower divalent metal ion concentrations, one-dimensional hyperfine spectroscopy cannot determine if TC interacts with the TC-aptamer at these concentrations or if TC forms a separate Mn-TC complex and some Mn^{2+} binds to the RNA. In addition, it is not possible to assign the two ^{31}P hyperfine couplings to the different divalent metal ion binding sites of the TC-aptamer. Two-dimensional hyperfine spectroscopy (2D EDNMR and THYCOS) was used to answer these questions.

Figure 3.3 shows 2D EDNMR spectra of samples containing RNA, Mn^{2+} and either TC (Figure 3.3A) or ^{13}C-labeled TC (Figure 3.3B). In both cases, the plus-plus quadrants are mainly comprised of positive self-correlation signals on the diagonal that resemble the respective 1D EDNMR spectrum. The minus-plus quadrant of the sample with unlabeled TC (Figure 3.3A) is characterized by negative cross peaks between the two different ^{31}P nuclear spin manifolds of the inner hyperfine coupling. These cross peaks are also visible for the sample

with ^{13}C-labeled TC (Figure 3.3B). In addition, the minus-plus quadrant of the ^{13}C-labeled sample features a signal at the ^{13}C Larmor frequency. Due to the small ^{13}C hyperfine coupling and a strong spectral overlap of the two ^{13}C nuclear spin manifolds, only one single signal can be seen.

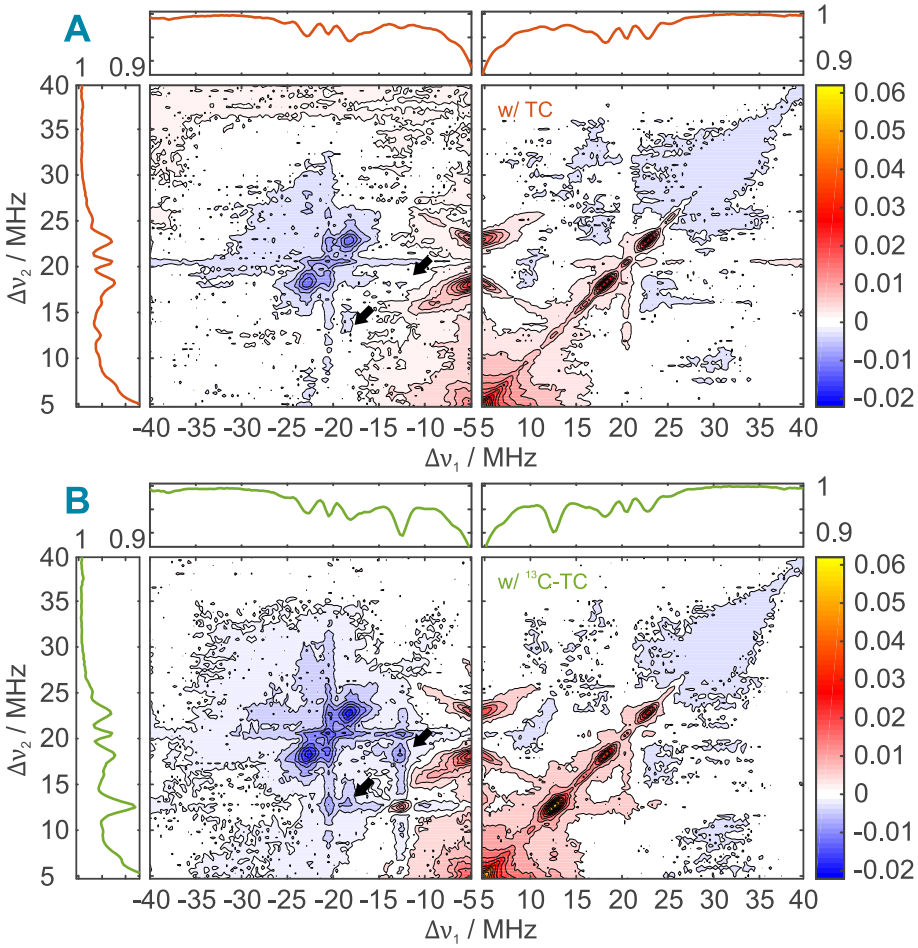

Figure 3.3: Background-corrected Q-band 2D EDNMR spectra. A) TC-aptamer with Mn^{2+} and TC, B) TC-aptamer with Mn^{2+} and ^{13}C-labeled TC. Strips to the left and above the 2D EDNMR spectra show 1D EDNMR spectra that are free of any correlation signals. Black arrows label expected frequency offsets for ^{13}C-^{31}P correlation signals.

The most striking difference of the ^{13}C-labeled TC sample in comparison to the unlabeled TC sample are, however, the appearance of ^{13}C-^{31}P cross peaks for the inner hyperfine coupling (black arrows in Figure 3.3).

Interestingly, the 2D EDNMR spectrum only shows a cross peak for the low-frequency signal of the inner ^{31}P hyperfine coupling, however, a cross peak for the high-frequency signal of the inner ^{31}P hyperfine coupling could be observed when chosen 2D EDNMR slices with a higher resolution and a better SNR were recorded.

In order to substantiate the 2D EDNMR results, Q-band THYCOS was performed on the two aforementioned samples. For THYCOS, the RF pulse was used to sample the ^{31}P region, whereas the ELDOR pulse was either set off-resonance to any transition or on-resonance with the expected frequency offset for a ^{13}C EDNMR signal. As expected, no THYCOS signal can be detected for the sample with unlabeled TC (red THYCOS spectra in Figure 3.4), irrespective of whether the ELDOR pulse is off-resonance (35 MHz) or on-resonance with an expected ^{13}C EDNMR signal (12.7 MHz). For the sample with ^{13}C-labeled TC (green THYCOS spectra in Figure 3.4), however, clear THYCOS signals are visible for the inner ^{31}P hyperfine coupling if the ELDOR pulse is on-resonance with a ^{13}C EDNMR signal. Hence, THYCOS experiments confirm the results obtained with 2D EDNMR.

If the frequency offset of the ELDOR pulse is moved away from the center frequency of the ^{13}C EDNMR signal, the high-frequency THYCOS signal of the inner ^{31}P hyperfine coupling disappears. Since the sign of the isotropic ^{31}P hyperfine coupling is known to be positive [103], the asymmetry of the THYCOS signal intensities can be used to determine the sign of the isotropic ^{13}C hyperfine coupling, which has to be positive as well. ^{13}C VMT Mims ENDOR and ^{13}C Mims ENDOR performed on the outer electron transition and DFT calculations yielded results that are in agreement with determination of the sign of the isotropic ^{13}C hyperfine coupling based on THYCOS data.

The work presented in this section could show that 2D EDNMR and THYCOS at Q-band are useful techniques to investigate ternary paramagnetic transition metal complexes on an atomistic level. It could be shown that TC interacts via Mn^{2+} with the TC-aptamer at divalent metal ion concentrations of 1 mM. Out of the two ^{31}P hyperfine couplings observed with ^{31}P Davies ENDOR, only the inner hyperfine couplings shows clear correlation signals to ^{13}C-labeled TC. This hypothesis is in agreement with EDNMR-monitored freeze-thaw cycles on

a sample with ^{13}C-labeled TC. After several freeze-thaw cycles, it was observed that the intensity of the outer ^{31}P hyperfine coupling increased, whereas the intensity of the inner ^{31}P hyperfine coupling decreased. At the same time, the intensity of the ^{13}C EDNMR signal decreased as well. Since it is known that double stranded RNA (dsRNA) degrades partially into single stranded RNA (ssRNA) after several freeze-thaw cycles in the presence of transition metal ions, the outer ^{31}P hyperfine coupling is most likely caused by ssRNA. Interestingly, the ssRNA Mn^{2+} binding sites seem to have a lower K_d value than the free Mn-TC complex, since the ^{13}C EDNMR intensity decreases.

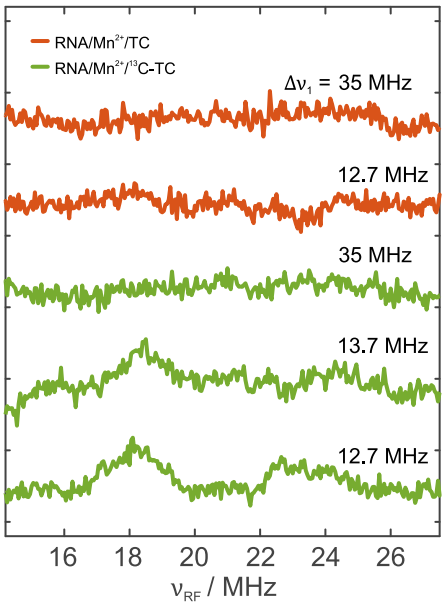

Figure 3.4: Q-band THYCOS spectra. Red: TC-aptamer with Mn^{2+} and TC, green: TC-aptamer with Mn^{2+} and ^{13}C-labeled TC. The RF pulse was used to sample the ^{31}P region, whereas the frequency offset $\Delta\nu_1$ of the ELDOR pulse was kept fixed at either 12.7 MHz, 13.7 MHz (^{13}C region) or 35.0 MHz (off-resonance).

2D EDNMR is much more sensitive than THYCOS, however, 2D EDNMR is inferior to THYCOS in terms of resolution. If the SNR permits, it is therefore advisable to acquire a THYCOS spectrum after a 2D EDNMR spectrum has been recorded. Some 2D EDNMR signals and the sign of these signals are not fully understood, i.e., the positive and "cross-like" signals in Figure 3.3 centered around the zero frequency of $\Delta\nu_1$. For a complete understanding of

these signals, a more systematic study is required. Based on the results presented in this chapter it is not possible to say how much TC actually binds to the RNA. Monitoring the intensity of ^{13}C-^{31}P correlation signals in a TC-titration series should, however, give insight into this question. It could be shown that Q-band 2D EDNMR and THYCOS are valuable tools to study other biochemically relevant ternary metal complexes, i.e., Mg^{2+}/Mn^{2+} mediated ATP-hydrolysis in membrane transporters.

3.3 Influence of Mg^{2+} on a Tetracycline Aptamer Monitored with PELDOR

In the previous section, it was shown that one- and two-dimensional hyperfine spectroscopy are suitable techniques to study the local geometry ($r \lessapprox 0.5\,\text{nm}$) of paramagnetic metal centers and ligand binding. In this section, it is shown that distance distributions obtained with PELDOR spectroscopy can be used to sample global conformational spaces of the TC-aptamer. More specifically, the shape of the distance distribution was used to investigate the conformational flexibility of nitroxide-labeled helices $P1$ and $P2$ (Figure 1.3A) for different Mg^{2+} concentrations in the absence and presence of the ligand TC. Hence, the results presented in this study are complementary to the hyperfine results presented in Section 3.2, which focused on studying more local interactions. No paramagnetic Mn^{2+} was used in this study since rigid nitroxide radicals were used as EPR spin probes (Çm spin label, Figure 1.3C, Section 2.6). Figure 3.5A shows background-corrected Q-band PELDOR time traces and distance distributions of the TC-aptamer at different Mg^{2+} concentrations in the presence of TC. At Mg^{2+} concentrations of 3 mM, a distance distribution centered at 3.8 nm with a rather narrow width of $\Delta r = 0.4\,\text{nm}$ was obtained. This distance matches exactly the expected distance of the crystal structure (Figure 1.3A). At Mg^{2+} concentrations of 3 mM and in the presence of TC, the TC-aptamer therefore adopt its folded tertiary structure with a very low degree of conformational flexibility.

At intermediate Mg^{2+} concentrations of 0.2 to 1.2 mM, the width of the distance distribution centered at 3.8 nm increases only slightly. At the same

time, a somewhat undefined distance distribution at smaller distances ($\approx 2.5\,nm$) increases upon decreasing Mg^{2+} concentrations. These distances are assigned to an ensemble of unfolded and metastable TC-aptamer structures. Hence, at intermediate Mg^{2+} concentrations an equilibrium between the ensemble of unfolded TC-aptamer structures and the folded tertiary structure exists. In the presence of TC, this equilibrium lies mainly on the side of the folded tertiary structure.

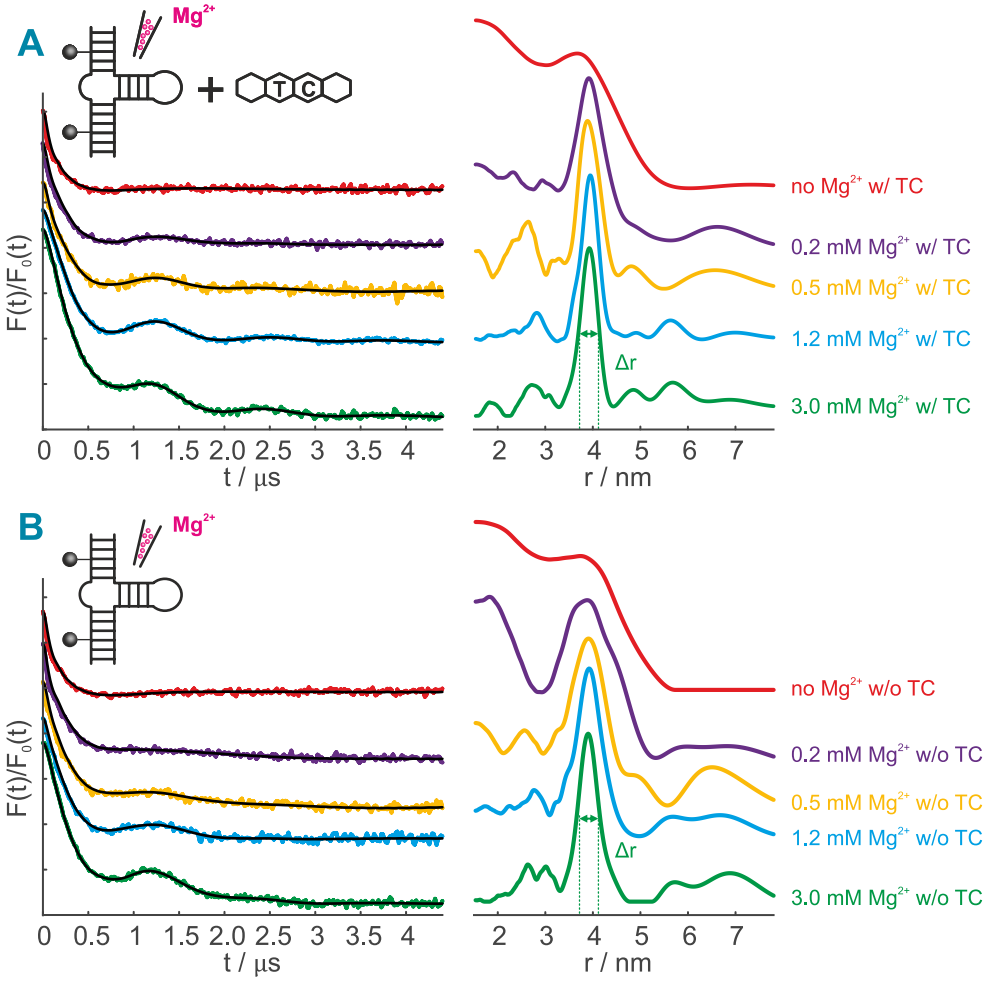

Figure 3.5: Background-corrected Q-band PELDOR time traces (left) and distance distributions (right) of the TC-aptamer at different Mg^{2+} concentrations in the presence (A) or absence (B) of the ligand TC. Tikhonov regularization was performed using the MATLAB toolbox DeerAnalysis [85].

Without Mg^{2+}, no more dipolar oscillations are visible in the PELDOR time traces. As a consequence, the distance distribution is broad and undefined with a maximum probability at 2 nm. In the absence of Mg^{2+}, the TC-aptamer therefore cannot adopt a stable tertiary structure, which is expected since it is generally known that Mg^{2+} is needed to induce folding of nucleic acids.

In the absence of TC, the PELDOR time trace and distance distribution at 3 mM Mg^{2+} look identical to the data at 3 mM Mg^{2+} but in the presence of TC. Therefore, at 3 mM Mg^{2+}, TC does not seem to be the major factor for folding of the TC-aptamer. At intermediate Mg^{2+} concentrations of 0.2 to 1.2 mM, distance distributions in the absence of TC are always broader than the corresponding distance distribution in the presence of TC. In accordance with this observation, the rather broad distance distribution at smaller distances increases more strongly in the absence of TC with decreasing Mg^{2+} concentrations. Without TC, the aforementioned equilibrium is characterized by a larger fraction of the ensemble of metastable unfolded TC-aptamer structures. Also, the fraction of the folded tertiary structure exhibits a larger conformational flexibility in the absence of TC than in the presence of TC. Not surprisingly, the PELDOR data in the absence of Mg^{2+} and TC are identical to data without Mg^{2+} but in the presence of TC.

The distance distributions at 3 mM Mg^{2+} feature a small but significant probability for larger distances, which decrease with decreasing Mg^{2+} concentrations. Furthermore, the modulation depth Δ exceeds the expected value of $\Delta = 0.25$ for an isolated 2-spin system (Figure 3.6). These observations are indicative for helical end-to-end stacking of two nucleic acid molecules [105]. The presence of multi-spin systems is known to increase the modulation depth Δ beyond the value for an isolated 2-spin system [84]. To test if the larger distances and the increased modulation depths are due to helical end-to-end stacking, two TC-aptamer constructs with overhanging ends were synthesized (construct II and construct III in Figure 3.6A). As expected, the modulations depths and the probability of longer distances decreased for these constructs. Interestingly, construct II (cytidine overhang) completely prevented stacking, whereas small evidence of stacking could be still observed for construct III (guanine overhang). This is, however, reasonable, as guanine exhibits a larger aromatic system, which should facilitate helical end-to-end stacking via π-π interactions.

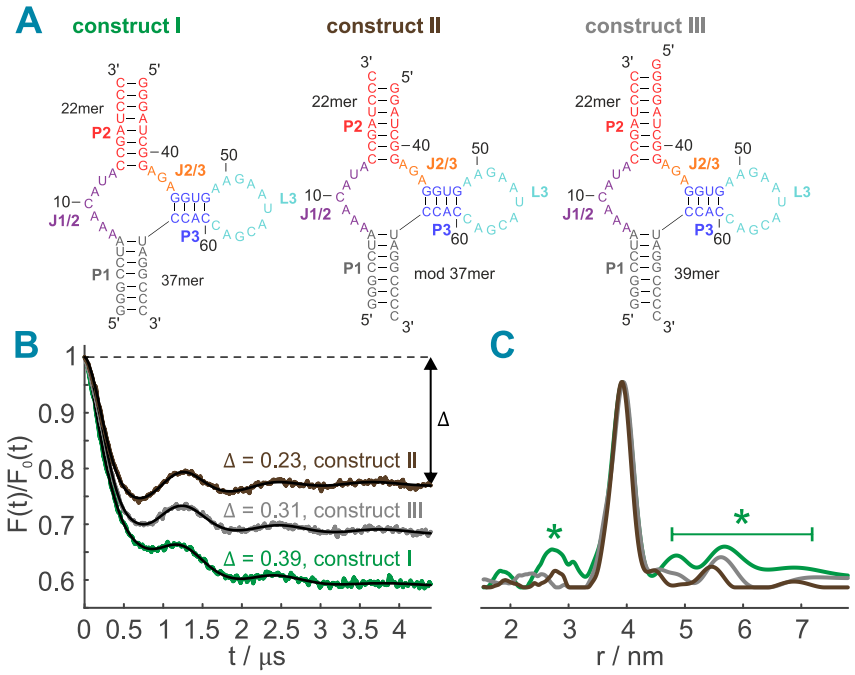

Figure 3.6: Q-band PELDOR of different TC-aptamer constructs. A) Different secondary structures of the TC-aptamer. Spin labels were always introduced at $C3$ and $C15$. B) Background-corrected Q-band PELDOR time traces of the different TC-aptamer constructs shown in A) in the presence of TC and with 3 mM Mg^{2+}. The different modulation depths Δ are indicated. C) Distance distributions obtained after Tikhonov regularization using the MATLAB toolbox DeerAnalysis [85]. Asterisks label distances due to helical end-to-end stacking.

Although the main mean distance in Figure 3.5 and Figure 3.6 at high Mg^{2+} concentrations matches the distance from the crystal structure, it does not necessarily mean that the relative orientation of the two helices in frozen solution is the same as in the crystal structure. The correct orientation of the nitroxide-labeled helices could be validated by performing orientation selective PELDOR at X-band frequencies on a TC-aptamer sample containing TC and 3 mM Mg^{2+}. Figure 3.7A shows the corresponding background-corrected X-band PELDOR time traces for different offsets $\Delta\nu$. Different dipolar oscillations and modulation depths for the different offsets are a clear sign of OS.

In a next step, different orientations, defined by the Euler angles β_1, α_2 and β_2 were used to simulate the experimental X-band PELDOR time traces shown

in Figure 3.7A. A set of Euler angles β_1, α_2 and β_2 can also be transformed into the bend angle φ. Figure 3.7B shows that the orientation with the best root-mean-square deviation (RMSD) exhibits a bend angle of $\varphi = 106°$, which is in very good agreement with the bend angle extracted from the crystal structure ($\varphi = 118°$). The helical orientation that was sampled with PELDOR therefore resembles the helical orientation from the crystal structure. As already mentioned in Section 2.6, orientation selective PELDOR cannot deduce if the two A_z vectors of the nitroxide molecular frames point in the same ($\varphi < 90°$) or in the opposite ($\varphi > 90°$) direction. Due to information from the crystal structure it was assumed that $\varphi > 90°$.

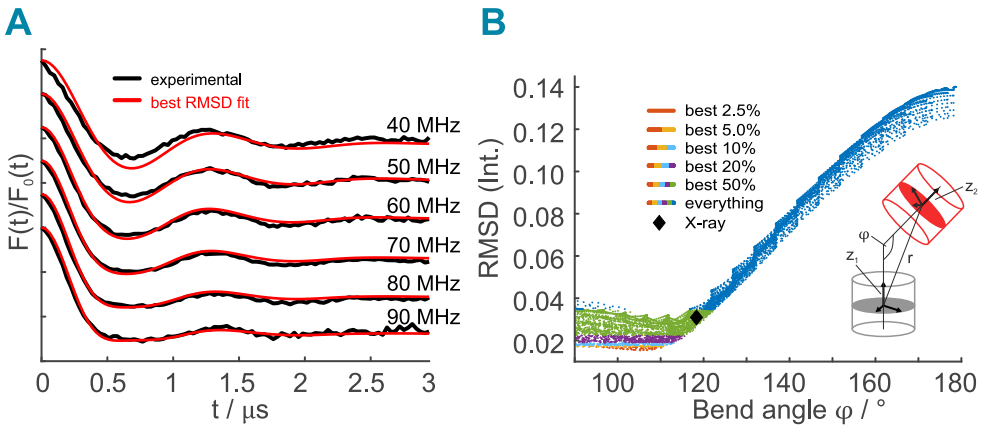

Figure 3.7: A) Background-corrected X-band PELDOR time traces of the TC-aptamer (construct II in Figure 3.6) in the presence of TC and at 3 mM Mg^{2+} at different offsets. PELDOR simulations with Euler angles that yielded the best RMSD are shown in red. B) RMSD of PELDOR simulations with different sets of Euler angles as a function of the helical bend angle φ. The helical bend angle of the crystal structure with its RMSD is shown as a black diamond.

The work presented in this section could show that PELDOR with rigid spin labels can be used to directly study the conformational flexibility of certain secondary structure motifs. The PELDOR data are complementary to a recent fluorescence, ITC and melting-curve study, in which a two-step binding model was proposed [30]. Whereas the work by Reuss et al. uses thermodynamic and kinetic parameters to investigate the TC-aptamer and its folding on a macroscopic scale, the present PELDOR study resembles a more quantitative approach by using

distance distributions to investigate specific secondary structure elements. For future experiments, PELDOR at higher frequencies could help to resolve the in-plane Euler angles γ_1 and γ_2. Additional labeling positions could be used to study the conformational flexibility and rearrangement of other secondary structure motifs, i.e., loop $L3$ (Figure 1.3A).

3.4 Mn^{2+}-nitroxide PELDOR on a Tetracycline Aptamer

In Section 3.2, it was shown that two-dimensional hyperfine spectroscopy in combination with ^{13}C-labeled TC is a valuable technique to study the Mn^{2+} ion in the ligand binding pocket. A similar approach to study the additional divalent metal ion binding sites (Figure 1.3A) of the TC-aptamer would require the introduction of specific isotope markers by ^{13}C-labeling of single nucleotides. Such an undertaking would be rather time-consuming, inefficient and very expensive. A more efficient approach is substitution of diamagnetic Mg^{2+} by paramagnetic Mn^{2+} in combination with a singly nitroxide-labeled TC-aptamer. By performing Mn^{2+}-nitroxide PELDOR experiments at different Mn^{2+} concentrations in the presence and absence of TC, the probabilities of the extracted distance distributions and a comparison with the distances from the crystal structures should give insight into the affinities of the additional divalent metal ion binding sites.

Figure 3.8A (left) shows the crystal structure of a singly nitroxide TC-aptamer used for first Mn^{2+}-nitroxide PELDOR studies. A semi-rigid E-TU nitroxide spin label was used [106], since the synthesis of E-TU is less demanding than the synthesis of Çm and observation of OS was not important for this study. Figure 3.8B and Figure 3.8C show background-corrected Mn^{2+}-nitroxide PELDOR time traces and distance distributions with or without TC for different Mn^{2+} concentrations. The inset of Figure 3.8B shows a typical Mn^{2+}-nitroxide field-sweep EPR spectrum, optimized for detecting the Mn^{2+} electron spin. Since the results of this section are preliminary and not published, the following paragraph states the experimental parameters used for the Mn^{2+}-nitroxide PELDOR measurements. The results are discussed in the ensuing paragraph.

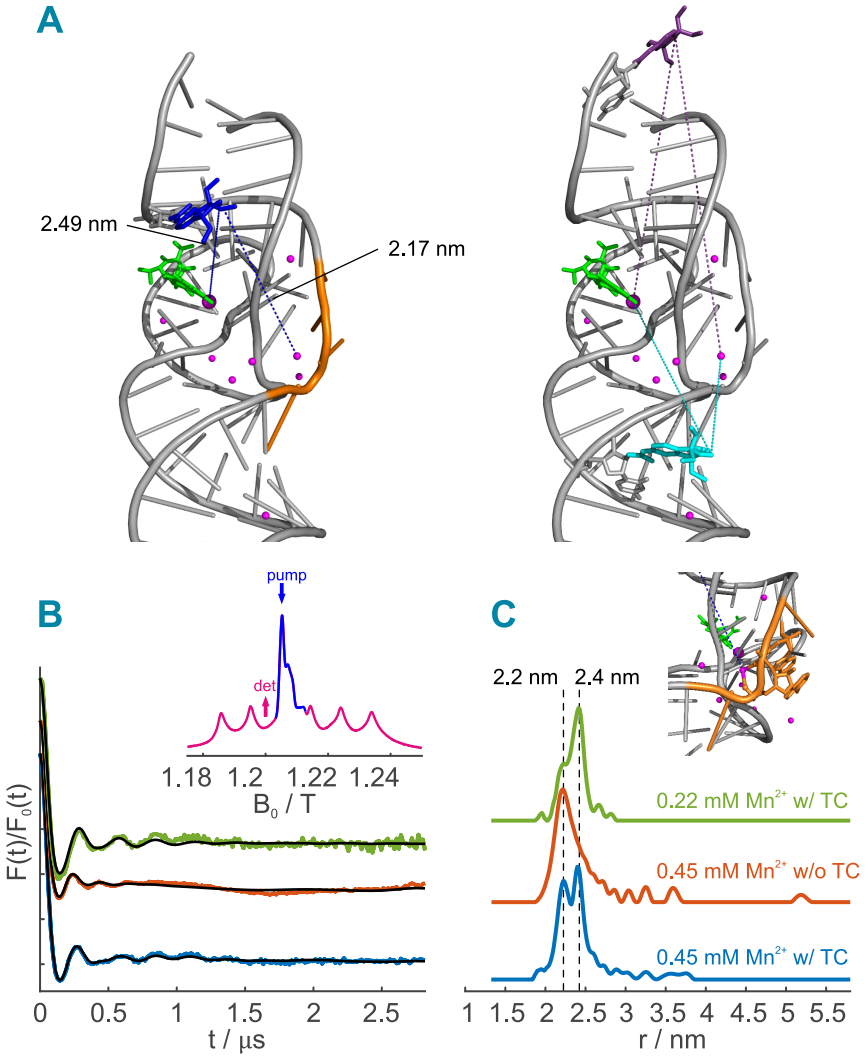

Figure 3.8: A) Singly nitroxide-labeled TC-aptamer with different labeling positions - left: $C15$ (blue), right: $C3$ (cyan), $U18$ (purple). B) Background-corrected Q-band Mn^{2+}-nitroxide PELDOR time traces of labeling position $C15$ at different Mn^{2+} concentrations with or without TC. C) Distance data obtained after Tikhonov regularization using the MATLAB toobox DeerAnalysis [85]. The insets show an EPR spectrum of the singly-labeled TC-aptamer with Mn^{2+} and TC (left) and a close-up shot of the $AAAA$-motif (right).

The frequency of the pump pulse was chosen so that ν_{pump} coincided with the maximum of the nitroxide spectrum. A frequency offset of $\Delta\nu = \nu_{pump} - \nu_{det} = -80\,\text{MHz}$ was used, which corresponds to a detection of the outer electron spin

transitions of the Mn^{2+} electron spin. All PELDOR experiments spectra were recorded at 5 K, since this temperature is the optimal choice in terms of SNR when detecting Mn^{2+} electron spins. Gaussian-shaped pulses were used to further decrease a potential spectral overlap of detection and pump pulses. Detection pulses had a length of 32 ns, the amplitude of the pump pulse was optimized for a pump pulse length of 25 ns. No deuterated glassing agent was used, since deuteration did not lead to a prolongation of the phase memory time of the Mn^{2+} electron spin. τ values of $\tau_1 = 272$ ns and $\tau_2 = 3000$ ns and a shot repetition time of 5 ms were used. No τ averaging was employed and the echo was integrated 45 ns around its maximum. 248 points along the x-axis with a time increment of 12 ns were collected. A 16-step phase cycle ($x[x][x_p]x$) was used to suppress unwanted coherence pathways [90].

The distance distribution of a sample with 0.45 mM Mn^{2+} and 0.15 mM TC-aptamer in the presence of TC yielded two distances at 2.2 and 2.4 nm (blue data in Figure 3.8B and Figure 3.8C). In the absence of TC, the signal at 2.4 nm disappeared (red data in Figure 3.8B and Figure 3.8C). A sample with reduced Mn^{2+} concentration (0.22 mM) but in the presence of TC revealed again a distance at 2.4 nm (green data in Figure 3.8B and Figure 3.8C). For 0.22 mM Mn^{2+}, however, the distance at 2.2 nm had a significantly decreased probability. Interestingly, the decrease in probability was approximately identical to the decrease in Mn^{2+} concentration ($\approx 50\,\%$).

A comparison to the crystal structure reveals that the experimental distance of 2.4 nm matches the crystal structure distance between E-TU and the Mn^{2+} ion in the ligand binding pocket (Figure 3.8A). This is reasonable, as the distance of 2.4 nm disappears in the absence of TC. The experimental distance of 2.2 nm agrees very well with the crystal structure distance between E-TU and a Mn^{2+} close to the *AAAA*-motif. Interestingly, this *AAAA*-Mn^{2+} ion is the only resolved Mn^{2+} ion in the crystal structure that is directly coordinated by two oxygen atoms. In addition, the backbone of the *AAAA*-motif is characterized by a rather unusual "u-turn". Therefore, the *AAAA*-Mn^{2+} ion most likely acts as a bridging and counter ion that stabilized the "u-turn". In the absence of the positively charged Mn^{2+} ion, RNA backbones in such a close proximity probably would not be stable. These observations suggest that the *AAAA*-Mn^{2+} ion has the highest

affinity of all additional divalent metal ion binding sites. Assuming that the affinity of the Mn^{2+} ion in the ligand binding center (TC-Mn^{2+} ion) is higher than the affinity of the *AAAA*-Mn^{2+} ion, it is also reasonable that the distance at 2.2 nm has a lower probability at lower Mn^{2+} concentrations: At lower Mn^{2+} concentrations, less Mn^{2+} is left that can occupy the additional binding sites.

	TC-Mn^{2+} / nm	*AAAA*-Mn^{2+} / nm	$\lvert\Delta r\rvert$ / nm
*C*15 PELDOR	2.4	2.2	0.2
*C*15 X-ray	2.49	2.17	0.32
*C*3 X-ray	3.15	1.79	1.36
*U*18 X-ray	3.14	3.63	0.49

Table 3.2: Experimental PELDOR and crystal structure distance of an E-TU spin label at position *C*15 to different Mn^{2+} ions. The predicted crystal structure distances for E-TU spin labels at position *C*3 and *U*18 are also shown. Δr describes the difference between the two Mn^{2+}-E-TU distances (TC-Mn^{2+} and *AAAA*-Mn^{2+}).

To underline the hypothesis of the *AAAA*-Mn^{2+} ion, it is planned to synthesize two singly nitroxide-labeled TC-aptamer constructs with different labeling positions (Figure 3.8A, right). For these labeling positions (*C*3 and *U*18), the crystal structure predicts a bigger difference for the distance from E-TU to the TC-Mn^{2+} ion and the distance from E-TU to the *AAAA*-Mn^{2+} ion (Table 3.2). Although the PELDOR time traces presented in Figure 3.8B already exhibit a significantly different dipolar oscillation pattern upon careful investigation, one could argue that distances of 2.2 and 2.4 nm are rather close together and are therefore a SNR or regularization artifact. Distance data from three independent E-TU labeling positions would also allow for a trilateration of the different Mn^{2+} binding sites. The coordinates of the Mn^{2+} ions obtained by trilateration could then be compared to the coordinates of the crystal structure, which could lead to refinement of the crystal structure [107]. In addition, the relaxation induced dipolar modulation enhancement (RIDME) technique could help to increase the SNR of the Mn^{2+}-nitroxide time traces. Mn^{2+}-Mn^{2+} PELDOR could help to gain further insight into the additional divalent metal ion binding sites.

Chapter 4

Summary and Outlook

In this work, different pulsed EPR techniques were used to characterize several structural and biochemical aspects of a TC-aptamer. Different one- and two-dimensional pulsed EPR hyperfine methods were used to investigate the ligand binding and the local geometry of the ligand binding center. More precisely, hyperfine spectroscopy probed hyperfine interactions that corresponded to an electron-nuclear-spin distance of up to $r = 0.5\,\mathrm{nm}$. PELDOR spectroscopy at different MW frequencies, on the other hand, was used to investigate global conformational rearrangements upon ligand binding and the influence of Mg^{2+} on the conformational flexibility of the TC-aptamer. In this study, PELDOR spectroscopy relied on detecting interactions that corresponded to an electron-electron-spin distance of up to $r = 5\,\mathrm{nm}$. Comparison of hyperfine and PELDOR spectroscopy shows that these techniques yield very complementary data in terms of distance-sensitive interactions and structural information. In fact, a combination of these two techniques is in most cases crucial for obtaining a "complete picture" of the structure and function of a biomolecule - as was shown in this work in case of the TC-aptamer. In this work, application of hyperfine and PELDOR spectroscopy included state-of-the art pulse schemes and spin labels.

The hyperfine project of this work, for example, relied on the EDNMR technique (Section 3.1). EDNMR is a relatively new pulsed hyperfine method, which gained significant popularity only in the mid 2000s. In comparison to ENDOR, EDNMR features a high sensitivity and the ability to sample all nuclear

species at the same time. In previous studies, EDNMR was mainly applied at high MW frequencies (W-band, 94 GHz), since at high MW frequencies nuclear resonances are better separated from the central blind spot. Therefore, the first goal of the hyperfine project was to verify the feasibility of EDNMR at Q-band frequencies (34 GHz). As a consequence, EDNMR at Q-band was applied to a series of Mn^{2+} model compounds. The use of Gaussian-shaped ELDOR pulses and soft detection pulses (t_p = 400 ns) led to a significant narrowing of the central blind spot, which enabled the detection of ^{14}N SQ and DQ EDNMR signals. Separation of the ^{14}N SQ EDNMR signals from zero frequency was only $\approx$ 3.5 MHz; an observation of such low-frequency signals with Q-band ENDOR would be impossible. At Q-band, EDNMR was found to be even more sensitive than at W-band, since transition probabilities of forbidden transitions increases with lower magnetic fields. However, the use of high-powered ELDOR pulses can lead to the appearance of various nuclear combination frequencies, which can hamper data analysis and signal assignment.

Once the feasibility of Q-band EDNMR had been verified, EDNMR was used to study the ligand binding of a TC-aptamer (Section 3.2). Although it is known that the TC-aptamer binds its ligand at high divalent metal ion concentrations with high affinity, it is also known that the affinity decreases for lower and more physiological divalent metal ion concentrations. In addition, ligand binding was so far not investigated with spectroscopic methods on an atomistic level. One-dimensional hyperfine spectroscopy (EDNMR and ENDOR) on a Mg^{2+}/Mn^{2+} substituted TC-aptamer in combination with ^{13}C-labeled TC yielded two distinct ^{31}P hyperfine couplings from the RNA backbone and ^{13}C hyperfine couplings from ^{13}C-labeled TC. From these data alone, however, it cannot be deduced if TC interacts via Mn^{2+} to the TC-aptamer, since it is known that TC also forms a free Mn-TC complex. Two-dimensional population transfer hyperfine experiments (2D EDNMR and THYCOS) were used to investigate the formation of a ternary RNA-Mn^{2+}-TC complex. In contrast to one-dimensional hyperfine spectroscopy, 2D EDNMR and THYCOS can correlate different nuclear spins, i.e., ^{13}C and ^{31}P, to the same electron spin, i.e., Mn^{2+}. Since 2D EDNMR and THYCOS are only recently published pulsed hyperfine schemes that were thus far not used at Q-band frequencies, experimental 2D EDNMR and THYCOS parameters at Q-

band were first optimized on Mn^{2+} model compounds. Afterwards, 2D EDNMR and THYCOS were used to study the ligand binding of the TC-aptamer. The formation of the ternary RNA-Mn^{2+}-TC complex at physiological divalent metal ion concentrations could be confirmed by observation of ^{13}C-^{31}P 2D EDNMR and THYCOS correlation signals for the "inner" ^{31}P hyperfine coupling.

2D EDNMR is superior to THYCOS in terms of sensitivity, however, 2D EDNMR is inferior to THYCOS in terms of resolution. In addition, signal assignment and interpretation seems to be more straightforward for the THYCOS technique. Here, a more systematic experimental 2D EDNMR study on model systems, accompanied by density matrix simulations, is needed.

The PELDOR project of this thesis relied for most parts on the unique properties of the recently developed Çm spin label (Section 3.3). With flexible spin labels, most of the PELDOR could not have been obtained. Despite the challenging synthesis of Çm, its rigidity and low degree of internal freedom yield very narrow distance distributions and pronounced OS that can be used to study the relative orientation of two spin labels and spin-labeled helices. The strong OS at X-band frequencies (9.4 GHz) was used to show that the orientation of the spin-labeled helices in frozen solution is very similar to the orientation found in the crystal structure. In addition, Q-band PELDOR showed that at high Mg^{2+} concentrations (3 mM), the TC-aptamer adopts its folded tertiary structure already in the absence of TC. At Mg^{2+} concentrations of 0.2 to 1.2 mM, TC was found to be the limiting factor for RNA folding and a reduced conformational flexibility. In such a Mg^{2+} intermediate regime, distance distributions of samples without TC always had a broader distance width (higher conformational flexibility) than the corresponding samples in the presence of TC. The results of the PELDOR experiments are complementary to a recent fluorescence, ITC and melting-curve study by Reuss et al. [30]. Whereas Reuss et al. investigated the TC-aptamer on a macroscopic scale, PELDOR studied specific secondary structure elements and looked on the TC-aptamer on a more quantitative and atomistic level.

Regarding future pulsed hyperfine experiments on the TC-aptamer, monitoring the intensity of ^{13}C-^{31}P 2D EDNMR and THYCOS signals in a TC-titration study could help to determine how much TC actually binds to the TC-aptamer

at physiological divalent metal ion concentrations. Since the 2D EDNMR and THYCOS experiments presented in this thesis were performed at only one TC concentration, no conclusion can be drawn on how much TC binds to the TC-aptamer. The 2D EDNMR and THYCOS results of the TC-aptamer also demonstrated the potential of these relatively new two-dimensional hyperfine techniques. Therefore, 2D EDNMR and THYCOS will be useful experiments to investigate other ternary paramagnetic metal complexes in biochemistry, if no prior knowledge about the binding model is available.

PELDOR measurements on a doubly nitroxide-labeled TC-aptamer with different labeling positions would help to investigate the conformational rearrangement and flexibility of other secondary structure elements. Performing PELDOR at higher magnetic fields (G-band, 180 GHz) would help to resolve the in-plane Euler angles γ_1 and γ_2, which would give additional angular information. PELDOR on a singly nitroxide-labeled and Mg^{2+}/Mn^{2+}-substituted TC-aptamer can be used to study the affinity of the additional divalent metal ion binding sites (Section 3.4). First Mn^{2+}-nitroxide PELDOR measurements at different Mn^{2+} concentrations in the presence and absence of TC, and a comparison of the experimental distances to the distances from the crystal structure suggest that the Mn^{2+} ion at the *AAAA*-motif has the highest affinity of all additional binding sites. However, more labeling positions should be tested to underline this hypothesis. If enough independent labeling positions exist, a trilateration procedure can be used to localize the binding sites of the metal ions with EPR spectroscopy. Such an approach could be used to refine the resolution of the crystal structure. RIDME spectroscopy could help to increase the SNR of the dipolar oscillations. Mn^{2+}-Mn^{2+} PELDOR at different Mn^{2+} concentrations with and without TC could give more insight into the affinities of the additional divalent metal ion binding sites. Mn^{2+}-nitroxide PELDOR data would be an excellent candidate for molecular dynamics (MD) benchmark studies to verify new RNA and Mn^{2+} force fields.

Chapter 5

German Summary

In den letzten Jahren haben Aptamare vermehrt für Aufmerksamkeit in den Wissenschaftsgemeinden der Chemie, Biochemie, Medizin und Biophysik gesorgt. Aptamere beschreiben meist kleinere doppelsträngige Desoxyribonukleinsäure- (DNA) oder Ribonukleinsäuremoleküle (RNA), die ein bestimmtes kleineres Molekül mit hoher Affinität binden. Nur selten überschreiten Aptamere dabei eine Größe von über 100 Nukleobasen. Ein mögliches Anwendungsgebiet von Aptameren ist das Gebiet der künstlichen Riboswitches. Hierunter versteht man RNA-Sequenzen in den untranslatierten Regionen von *messenger* RNA (mRNA), die ein kleineres Molekül binden und durch die dadurch induzierte Konformationsänderung die Genexpression regulieren.

Ein interessanter Vertreter der Klasse der RNA-Aptamere ist das Tetrazyklin-bindende Aptamer (TC-Aptamer) [20], das einige besondere Eigenschaften aufweist. So besitzt das TC-Aptamer eine sehr hohe Affinität zu seinem Liganden, dem Antibiotikum Tetrazyklin (TC). Die Dissoziationskonstante beträgt bei einer Mg^{2+} Konzentration von 10 mM $K_d = 800$ pM [22]. Außerdem wurde bewiesen, dass das TC-Aptamer auch in vivo seine Funktion als künstlicher Riboswitch beibehält [24]. Dies ist insofern besonders, da die meisten Aptamere über eine in vitro Prozedur, genannt *systematic evolution of igands by exponential enrichment* (SELEX), ausgewählt werden, in lebenden Zellen jedoch meist ihre Funktion verlieren. Des Weiteren besitzt TC eine nicht-toxische Wirkung auf Zellen [27].

Aufgrund dieser Tatsachen ist es nicht verwunderlich, dass eine Kristallstruktur des TC-Aptamers im ligandengebundenden Zustand bereits veröffentlicht

wurde [28]. Aus der Kristallstruktur geht hervor, dass TC über ein zweiwertiges Mg^{2+}-Ion mit der RNA wechselwirkt. Die Tertiärstruktur des TC-Aptamers besteht aus 3 Helizes, die über eine Schleife und zwei Knotenpunkte miteinander verbunden sind. Weitere Mg^{2+}-Ionen werden an den großen Furchen der drei Helizes gebunden. Obwohl eine Kristallstruktur ein hochauflösendes dreidimensionales Abbild liefert, ist sie dennoch eine statische Methode und verrät wenig über dynamische Fragen der Strukturbiologie. Zum Beispiel gibt die Kristallstruktur des TC-Aptamers keinen Aufschluss über den Faltungsprozess und die Abhängigkeit der Ligandenbindung von der Mg^{2+} Konzentration.

In dieser Arbeit wurde ein TC-Aptamer mit Techniken der gepulsten Elektronenspinresonanz-Spektroskopie (ESR-Spektroskopie) untersucht. Die ESR-Spektroskopie beruht auf der Detektion von ungepaarten Elektronenspins und deren Interaktion mit anderen Elektronenspins, Kernspins oder dem externen Magnetfeld. Für Biomoleküle wie DNAs, RNAs oder Proteine werden ungepaarte Elektronenspins meist in Form von stabilen Nitroxidradikalen in das Molekül eingeführt. In manchen Fällen binden Biomoleküle auch paramagnetische Übergangsmetalle wie Fe^{3+}, Mn^{2+}, Co^{2+}, Ni^{3+} und Cu^{2+}. In wiederum anderen Fällen kann aufgrund ähnlicher Eigenschaften in der Koordinationschemie diamagnetisches Mg^{2+} mit paramagnetischem Mn^{2+} ersetzt werden.

Die moderne gepulste ESR-Spektroskopie kann in zwei Teilgebiete aufgeteilt werden. Die Hyperfein-Spektroskopie detektiert die Wechselwirkung zwischen gekoppelten Elektronen- und Kernspins und ist sensitiv für Interaktionen die einem Elektronen-Kernspin-Abstand von maximal 1 nm entsprechen. Die gepulste dipolare Spektroskopie - *pulsed dipolar spectroscopy* (PDS) - detektiert Wechselwirkungen zwischen schwach gekoppelten Elektronenspins und ist sensitiv für Interaktionen die einem maximalen Elektronen-Elektronenspin-Abstand von 8 nm entsprechen. Beide Techniken (Hyperfein-Spektroskopie und PDS) wurden in vorliegender Arbeit verwendet um verschiedene strukturbiologische Aspekte des TC-Aptamers zu untersuchen.

Das Ziel der Hyperfein-Spektroskopie Experimente war es, die Bindung des Liganden TC zum TC-Aptamer bei niedrigeren und somit physiologischen divalenten Metallionen Konzentrationen zu untersuchen. Das TC-Aptamer wurde mittels *electron-nuclear double resonance* (ENDOR) und *electron-electron double*

resonance detected NMR (EDNMR) untersucht. Da es sich bei EDNMR um eine verhältnismäßig neue Methode der Hyperfein-Spektroskopie handelt [36], die zudem selten bei Q-band Frequenzen (34 GHz) angewandt wurde, wurde das Potential von EDNMR bei Q-band Frequenzen zuerst an Mn^{2+} Modellkomplexen untersucht. Es wurde herausgefunden, dass eine Verwendung von gaußförmigen ELDOR Pulsen und sehr weichen Detektionspulsen ($t_p = 400$ ns) zu einer deutlichen Verringerungen der spektralen Breite des zentralen *blind spots* führen, sodass ^{14}N *single quantum* (SQ) und *double quantum* (DQ) EDNMR Signale detektiert werden konnten. ^{14}N SQ EDNMR Signale waren nur ≈ 3.5 MHz von der Nullfrequenz entfernt, was eine Detektion von diesen Signalen mit Q-band ENDOR in der Praxis unmöglich macht. Die intrinsisch bereits sehr sensitive EDNMR Technik wies bei Q-band Frequenzen eine nochmals erhöhte Sensitivität im Vergleich zu W-band Frequenzen (94 GHz) auf. Dies ist durch eine größere Übergangswahrscheinlichkeit von verbotenen Übergängen bei niedrigeren Mikrowellenfrequenzen zu erklären. Bei einem Einsatz von ELDOR Pulsen mit erhöhter Leistung können Kombinationsfrequenzen erheblich an Intensität gewinnen, was eine Auswertung der Spektren erschweren kann. DQ und sogar *triple quantum* (DQ) EDNMR Signale von *high-spin* Kernen wie ^{2}H, ^{14}N und ^{17}O besitzen bei Q-band Frequenzen ebenfalls eine hohe Übergangswahrscheinlichkeit. Koppeln mehrere dieser Kerne zum detektieren Eleketronenspin, kann dies zu einem überfüllten und schwer zu analysierendem EDNMR Spektrum führen. Nichtsdestotrotz erwies sich Q-band EDNMR als eine sehr nützliche und sensitive Methode zum Detektieren von Hyperfein-Wechselwirkungen.

Am TC-Aptamer wurden Hyperfein-Experimente an drei unterschiedlichen Proben durchgeführt. Hierfür wurde diamagnetisches Mg^{2+} mit paramagnetischem Mn^{2+} substituiert und ^{13}C gelabeltes TC verwendet. Zum einen wurde das TC-Aptamer mit Mn^{2+} in Abwesenheit von TC untersucht, zum anderen wurde das TC-Aptamer mit Mn^{2+} und entweder ^{13}C-gelabeltem oder ungelabeltem TC untersucht. ^{31}P Davies ENDOR Experimente ergaben nahezu identische Spektren für alle drei Proben. Alle Spektren bestanden aus einer “kleinen” ^{31}P Hyperfeinkopplung mit $a_{iso} = 4.5$ MHz und einer “größeren” Hyperfeinkopplug mit $a_{iso} = 9$ MHz. Die ^{31}P Hyperfeinkopplungen konnten durch Wechselwirkung von Mn^{2+} mit dem negativ geladenen Phosphatrückgrat der RNA erklärt werden.

Die zwei ^{31}P Hyperfeinkopplungen konnten mittels eindimensionaler Hyperfein-Spektroskopie jedoch keiner bestimmten Bindungsstelle zugewiesen werden. Die Probe mit ^{13}C gelabeltem TC wurde auch mit ^{13}C Mims ENDOR untersucht. Da es bekannt ist, dass TC auch einen freien Mn-TC Komplex bildet [104], wurde auch ein ^{13}C Mims ENDOR Spektrum des freien Mn-^{13}C-TC Komplexes aufgenommen. Beide ^{13}C Mims ENDOR Spektren waren nahezu identisch. EDNMR Experimente lieferten identische Information wie die ENDOR Experimente. Aus den ENDOR und EDNMR Experimenten konnte somit kein Rückschluss gezogen werden, ob bei niedrigeren divalenten Metallionen Konzentrationen TC über ein Mn^{2+}-Ion mit der RNA wechselwirkt, oder ob hauptsächlich der freie Mn-TC Komplex vorliegt.

Daher wurden Methoden der zweidimensionalen Hyperfein-Spektroskopie verwendet, um unterschiedliche Kernspins (^{13}C von TC, ^{31}P von der RNA) zu demselben Elektronenspin (Mn^{2+}) zu korrelieren. Als Methoden kamen hierfür 2D-EDNMR und *triple hyperfine correlation spectroscopy* (THYCOS) zum Einsatz. Da beide Techniken noch selten genutzt und erst vor kurzem publiziert wurden [34, 35], wurden experimentelle 2D-EDNMR und THYCOS Parameter bei Q-band Frequenzen zuerst an Mn^{2+} Modellsystem getestet und optimiert. Nach einer erfolgreichen Optimierung wurden TC-Aptamer Proben mit gelabeltem ^{13}C-TC und ungelabeltem TC mit 2D-EDNMR und THYCOS untersucht. Während bei der ungelabelten TC-Aptamer Probe keine ^{13}C-^{31}P Kreuzsignale zu sehen waren, wies die TC-Aptamer Probe mit ^{13}C-gelabeltem TC deutliche ^{13}C-^{31}P 2D-EDNMR und THYCOS Kreuzsignale für die innere ^{31}P Hyperfein Kopplung auf. Die Ausbildung des ternären RNA-Mn^{2+}-TC Komplexes konnte somit bestätigt werden. Bei einem Vergleich der 2D-EDNMR und TYCOS Daten stellte sich heraus, dass 2D-EDNMR über eine größere Sensitivität als THYCOS verfügt. Dafür besitzt 2D-EDNMR eine schlechtere Auflösung als THYCOS.

Das Ziel der PDS Experimente war es, konformelle Änderungen des TC-Aptamers bei Ligandenbindung und die konformelle Flexibilität in Abhängigkeit von der Mg^{2+} Konzentration zu untersuchen. Als PDS Technik kam ausschließlich die *pulsed electron-electron double resonance* (PELDOR) Spektroskopie zum Einsatz. Für Experimente mittels PELDOR Spektroskopie wurde das TC-Aptamer mit zwei Nitroxidradikalen gelabelt. Als Nitroxidradikal kam hierbei das Çm

Spin Label zum Einsatz. Das Çm Spin Label besitzt den großen Vorteil, dass es über zwei kovalente und somit rigide Bindungen mit der RNA verbunden ist und über einen sehr niedrigen Grad an interner Flexibilität verfügt. Somit kann über die Breite der Abstandsverteilung ein direkter Rückschluss auf die konformelle Flexibilität der gelabelten RNA gezogen werden. Des Weiteren weist das Çm Spin Label eine starke Orientierungsselektion (OS) auf. OS kann benutzt werden um, neben reinen Abstandsinformationen, auch Winkelinformationen zwischen zwei Nitroxid Spin Labeln zu erhalten. Q-band PELDOR Experimente am TC-Aptamer lieferten das Ergebnis, dass das TC-Aptamer bei hohen Mg^{2+} Konzentrationen (3 mM) in seinem gefalteten Zustand vorliegt, unabhängig von der Tatsache ob der Ligand TC zugegen ist oder nicht. Bei mittleren Mg^{2+} Konzentrationen ist der Ligand jedoch eine treibende Kraft um das TC-Aptamer zu falten und die Tertiärstruktur zu stabilisieren. So waren bei Konzentrationen von 0.2 bis 1.2 mM Mg^{2+} die Abstandsverteilungen von Proben ohne TC immer breiter als die Abstandsverteilungen von Proben mit gleicher Mg^{2+} Konzentration, jedoch in Anwesenheit von TC. Bei hohen Mg^{2+} Konzentrationen (3 mM) waren die Abstandsverteilungen in An- und Abwesenheit von TC identisch. Orientierungsselektives X-band PELDOR wurde benutzt um die relative Orientierung der gelabelten Helizes zueinander zu untersuchen. Dabei wurde festgestellt, dass die Orientierung in gefrorener Lösung der Orientierung der Kristallstruktur entspricht.

Die Q-band PELDOR Ergebnisse an dem TC-Aptamer sind komplementär zu einer kürzlich veröffentlichten Fluoreszenz-, Isothermen Titrationskalometrie- und Schmelzkurvenstudie [30]. Reuss et al. konnten zeigen, dass die Bindung von TC nach einem 2-stufigen Bindungsmodell abläuft, und dass das TC-Aptamer bei hohen Mg^{2+} Konzentrationen und in Abwesenheit von TC bereits in seiner fast endgültigen Tertiärstruktur vorliegt. Während die Ergebnisse der Studie von Reuss et al. auf thermodynamischen und kinetischen Parameter beruhen, untersucht PELDOR gezielte Sekundärstrukturen quantitativ auf einer atomistischen Ebene.

In der Zukunft könnten 2D-EDNMR und THYCOS Experimente bei verschiedenen TC Konzentrationen benutzt werden, um festzustellen wieviel TC bei physiologischen divalenten Metallionen Konzentrationen mit dem TC-Aptamer

bindet. Da in vorliegender Arbeit 2D-EDNMR und THYCOS Experimente nur bei einer TC Konzentration durchgeführt wurden, konnte über die Quantität der Ligandenbindung keine Aussage getroffen werden. Die erfolgreiche Anwendung von 2D-EDNMR und THYCOS in dieser Studie lässt den Schluss zu, dass diese Methoden auch für die Untersuchung von anderen ternären Metallkomplexen in der Biochemie von großem Nutzen sein können. PELDOR Mg^{2+} Titrationen könnten mit anderen Labelingpositionen wiederholt werden. Dies würde Aufschluss über konformelle Änderungen und Flexibilitäten von anderen Sekundärstrukturelementen geben. PELDOR Experimente bei höheren Magnetfeldern könnten helfen die *in-plane* Eulerwinkel γ_1 und γ_2 aufzulösen, woraus weitere Winkelinformationen gewonnen werden können.

In ersten Mn^{2+}-Nitroxid PELDOR Experimenten wurden ein einfach Nitroxid gelabelter TC-Aptamer und Substitution von diamagnetischem Mg^{2+} mit paramagnetischem Mn^{2+} dazu genutzt, um die Affinität der zusätzlichen divalenten Metallionenbindungsstellen zu untersuchen. Mn^{2+}-Nitroxid PELDOR Messungen bei verschiedenen Mn^{2+} Konzentrationen in An- und Abwesenheit des Liganden ergaben, dass das Mn^{2+}-Ion in der Nähe der *AAAA*-Sequenz die höchste Affinität von allen zusätzlichen Bindungsstellen besitzt. Jedoch sind weitere Labelingpositionen notwendig um diese Hypothese zu untermauern. Sollten die zusätzlichen Labelingpositionen die erwarteten Abstandsverteilungen liefern, können die verschiedenen Abstandsverteilungen benutzt werden um über Trilateration die Metallionenbindungsstellen mittels EPR zu lokalisieren. Dies könnte die Auflösung der Kristallstruktur zu verbessern. *Relaxation induced dipolar modulation enhancement* (RIDME) Experimente könnten helfen das Signal-zu-Rausch Verhältnis der dipolaren Mn^{2+}-Nitroxid Oszillationen zu verbessern. Mn^{2+}-Mn^{2+} PELDOR Experimente bei verschiedenen Mn^{2+} Konzentrationen in An- und Abwesenheit von TC könnten weitere unterstützende Daten liefern um die Affinitäten der zusätzlichen Metallionenbindungsstellen zu bestimmen. Die Ergebnisse der Mn^{2+}-Nitroxid PELDOR Experimente wären außerdem hervorragend für *molecular dynamics* (MD) Benchmark Studien geeignet, um das Potential von neuen RNA und Mn^{2+} Kraftfeldern zu verifizieren.

References

(1) Fuertig, B.; Richter, C.; Woehnert, J.; Schwalbe, H. NMR spectroscopy of RNA. *ChemBioChem* **2003**, *4*, 936–962, DOI: 10.1002/cbic.200300700.

(2) Yu, H. Extending the size limit of protein nuclear magnetic resonance. *Proc. Natl. Acad. Sci.* **1999**, *96*, 332–334, DOI: 10.1073/pnas.96.2.332.

(3) Cheng, Y.; Grigorieff, N.; Penczek, P. A.; Walz, T. A primer to single-particle cryo-electron microscopy. *Cell* **2015**, *161*, 438–449, DOI: 10.1016/j.cell.2015.03.050.

(4) Liu, Y.; Gonen, S.; Gonen, T.; Yeates, T. O. Near-atomic cryo-EM imaging of a small protein displayed on a designed scaffolding system. *Proc. Natl. Acad. Sci.* **2018**, *115*, 3362–3367, DOI: 10.1073/pnas.1718825115.

(5) Murata, K.; Wolf, M. Cryo-electron microscopy for structural analysis of dynamic biological macromolecules. *Biochim. Biophys. Acta - Gen. Subj.* **2018**, *1862*, 324–334, DOI: 10.1016/j.bbagen.2017.07.020.

(6) Liko, I.; Allison, T. M.; Hopper, J. T.; Robinson, C. V. Mass spectrometry guided structural biology. *Curr. Opin. Struct. Biol.* **2016**, *40*, 136–144, DOI: 10.1016/j.sbi.2016.09.008.

(7) Svergun, D. I.; Koch, M. H. J. Small-angle scattering studies of biological macromolecules in solution. *Reports Prog. Phys.* **2003**, *66*, 1735–1782, DOI: 10.1088/0034-4885/66/10/R05.

(8) Akbey, Ü.; Oschkinat, H. Structural biology applications of solid state MAS DNP NMR. *J. Magn. Reson.* **2016**, *269*, 213–224, DOI: 10.1016/j.jmr.2016.04.003.

(9) Piston, D. W.; Kremers, G.-J. Fluorescent protein FRET: the good, the bad and the ugly. *Trends Biochem. Sci.* **2007**, *32*, 407–414, DOI: 10.1016/j.tibs.2007.08.003.

(10) Jeschke, G. The contribution of modern EPR to structural biology. *Emerg. Top. Life Sci.* **2018**, *2*, 9–18, DOI: 10.1042/ETLS20170143.

(11) Schmidt, T.; Waelti, M. A.; Baber, J. L.; Hustedt, E. J.; Clore, G. M. Long distance measurements up to 160 Å in the GroEL tetradecamer using Q-band DEER EPR spectroscopy. *Angew. Chem. Int. Ed.* **2016**, *55*, 15905–15909, DOI: 10.1002/anie.201609617.

(12) Zaenker, P. P.; Jeschke, G.; Goldfarb, D. Distance measurements between paramagnetic centers and a planar object by matrix Mims electron nuclear double resonance. *J. Chem. Phys.* **2005**, *122*, 024515.1–024515.11, DOI: 10.1063/1.1828435.

(13) Horton, T. E.; Clardy, D. R.; DeRose, V. J. Electron paramagnetic resonance spectroscopic measurement of Mn^{2+} binding affinities to the hammerhead ribozyme and correlation with cleavage activity. *Biochemistry* **1998**, *37*, 18094–18101, DOI: 10.1021/bi981425p.

(14) Endeward, B.; Marko, A.; Denysenkov, V. P.; Sigurdsson, S. T.; Prisner, T. F. Advanced EPR methods for studying conformational dynamics of nucleic acids. *Methods Enzymol.* **2015**, *564*, 403–425, DOI: 10.1016/bs.mie.2015.06.007.

(15) Cekan, P.; Smith, A. L.; Barhate, N.; Robinson, B. H.; Sigurdsson, S. T. Rigid spin-labeled nucleoside Ç: a nonperturbing EPR probe of nucleic acid conformation. *Nucleic Acids Res.* **2008**, *36*, 5946–5954, DOI: 10.1093/nar/gkn562.

(16) Höbartner, C.; Sicoli, G.; Wachowius, F.; Gophane, D. B.; Sigurdsson, S. T. Synthesis and characterization of RNA containing a rigid and nonperturbing cytidine-derived spin label. *J. Org. Chem.* **2012**, *77*, 7749–7754, DOI: 10.1021/jo301227w.

(17) Reverdatto, S.; Burz, D.; Shekhtman, A. Peptide aptamers: development and applications. *Curr. Top. Med. Chem.* **2015**, *15*, 1082–1101, DOI: 10.2174/1568026615666150413153143.

(18) Tuerk, C.; Gold, L. Systematic evolution of ligands by exponential enrichment: RNA ligands to bacteriophage T4 DNA polymerase. *Science* **1990**, *249*, 505–510, DOI: 10.1126/science.2200121.

(19) Ellington, A. D.; Szostak, J. W. In vitro selection of RNA molecules that bind specific ligands. *Nature* **1990**, *346*, 818–822, DOI: 10.1038/346818a0.

(20) Berens, C.; Thain, A.; Schroeder, R. A tetracycline-binding RNA aptamer. *Bioorg. Med. Chem.* **2001**, *9*, 2549–2556, DOI: 10.1016/S0968-0896(01)00063-3.

(21) Hanson, S.; Bauer, G.; Fink, B.; Suess, B. Molecular analysis of a synthetic tetracycline-binding riboswitch. *RNA* **2005**, *11*, 503–11, DOI: 10.1261/rna.7251305.

(22) Muller, M.; Weigand, J. E.; Weichenrieder, O.; Suess, B. Thermodynamic characterization of an engineered tetracycline-binding riboswitch. *Nucleic Acids Res.* **2006**, *34*, 2607–2617, DOI: 10.1093/nar/gkl347.

(23) Hanson, S.; Berthelot, K.; Fink, B.; McCarthy, J. E.; Suess, B. Tetracycline-aptamer-mediated translational regulation in yeast. *Mol. Microbiol.* **2003**, *49*, 1627–1637, DOI: 10.1046/j.1365-2958.2003.03656.x.

(24) Weigand, J. E.; Suess, B. Tetracycline aptamer-controlled regulation of pre-mRNA splicing in yeast. *Nucleic Acids Res.* **2007**, *35*, 4179–4185, DOI: 10.1093/nar/gkm425.

(25) Kötter, P.; Weigand, J. E.; Meyer, B.; Entian, K.-D.; Suess, B. A fast and efficient translational control system for conditional expression of yeast genes. *Nucleic Acids Res.* **2009**, *37*, e120.1–e120.7, DOI: 10.1093/nar/gkp578.

(26) Vogel, M.; Weigand, J. E.; Kluge, B.; Grez, M.; Suess, B. A small, portable RNA device for the control of exon skipping in mammalian cells. *Nucleic Acids Res.* **2018**, *46*, e48.1–e48.12, DOI: 10.1093/nar/gky062.

(27) Chopra, I.; Roberts, M. Tetracycline antibiotics: mode of action, applications, molecular biology, and epidemiology of bacterial resistance. *Microbiol. Mol. Biol. Rev.* **2001**, *65*, 232–260, DOI: 10.1128/MMBR.65.2.232-260.2001.

(28) Xiao, H.; Edwards, T. E.; Ferré-D'Amaré, A. R. Structural basis for specific, high-affinity tetracycline binding by an in vitro evolved aptamer and artificial riboswitch. *Chem. Biol.* **2008**, *15*, 1125–1137, DOI: 10.1016/j.chembiol.2008.09.004.

(29) Förster, U.; Weigand, J. E.; Trojanowski, P.; Suess, B.; Wachtveitl, J. Conformational dynamics of the tetracycline-binding aptamer. *Nucleic Acids Res.* **2012**, *40*, 1807–1817, DOI: 10.1093/nar/gkr835.

(30) Reuss, A. J.; Vogel, M.; Weigand, J. E.; Suess, B.; Wachtveitl, J. Tetracycline determines the conformation of its aptamer at physiological magnesium concentrations. *Biophys. J.* **2014**, *107*, 2962–2971, DOI: 10.1016/j.bpj.2014.11.001.

(31) Wunnicke, D.; Strohbach, D.; Weigand, J. E.; Appel, B.; Feresin, E.; Suess, B.; Muller, S.; Steinhoff, H.-J. Ligand-induced conformational capture of a synthetic tetracycline riboswitch revealed by pulse EPR. *RNA* **2011**, *17*, 182–188, DOI: 10.1261/rna.2222811.

(32) Lambs, L.; Venturim, M.; Révérend, B. D.-L.; Kozlowski, H.; Berthon, G. Metal ion tetracycline interactions in biological fluids. *J. Inorg. Biochem.* **1988**, *33*, 193–209, DOI: 10.1016/0162-0134(88)80049-7.

(33) Aladin, V.; Vogel, M.; Binder, R.; Burghardt, I.; Suess, B.; Corzilius, B. Complex formation of the tetracycline-binding aptamer investigated by specific cross-relaxation under DNP. *Angew. Chem. Int. Ed.* **2019**, *58*, 4863–4868, DOI: 10.1002/anie.201811941.

(34) Potapov, A.; Epel, B.; Goldfarb, D. A triple resonance hyperfine sublevel correlation experiment for assignment of electron-nuclear double resonance lines. *J. Chem. Phys.* **2008**, *128*, 052320.1–052320.10, DOI: 10.1063/1.2833584.

(35) Kaminker, I.; Sushenko, A.; Potapov, A.; Daube, S.; Akabayov, B.; Sagi, I.; Goldfarb, D. Probing conformational variations at the ATPase site of the RNA helicase DbpA by high-field electron-nuclear double resonance spectroscopy. *J. Am. Chem. Soc.* **2011**, *133*, 15514–15523, DOI: 10.1021/ja204291d.

(36) Schosseler, P.; Wacker, T.; Schweiger, A. Pulsed ELDOR detected NMR. *Chem. Phys. Lett.* **1994**, *224*, 319–324, DOI: 10.1016/0009-2614(94)00548-6.

(37) Abragam, A.; Pryce, M. L. H. Theory of the nuclear hyperfine structure of paramagnetic resonance spectra in crystals. *Proc. Roy. Soc. London.* **1951**, *205*, 135–153, DOI: 10.1098/rspa.1951.0022.

(38) Schweiger, A.; Jeschke, G., *Principles of pulse electron paramagnetic resonance*, 1st ed.; Oxford University Press: Oxford, 2001.

(39) Budil, D. E.; Earle, K. A.; Freed, J. H. Full determination of the rotational diffusion tensor by electron paramagnetic resonance at 250 GHz. *J. Phys. Chem.* **1993**, *97*, 1294–1303, DOI: 10.1021/j100109a009.

(40) Fuchs, M. R. A high-field/high-frequency electron paramagnetic resonance spectrometer., PhD Thesis, Free University of Berlin, 1999.

(41) McGarvey, B. R. The isotropic hyperfine interaction. *J. Phys. Chem.* **1967**, *71*, 51–66, DOI: 10.1021/j100860a007.

(42) Goodman, B.; Raynor, J. In *Adv. Inorg. Chem. Radiochem.* Emeléus, H. J., Sharpe, G. H., Eds.; Academic Press: Cambridge, 1970; Vol. 13, pp 135–362, DOI: 10.1016/S0065-2792(08)60336-2.

(43) Morton, J.; Preston, K. Atomic parameters for paramagnetic resonance data. *J. Magn. Reson.* **1978**, *30*, 577–582, DOI: 10.1016/0022-2364(78)90284-6.

(44) Abragam, A.; Bleaney, B., *Electron paramagnetic resonance of transition ions*, 1st ed.; Oxford University Press: Oxford, 1970.

(45) King, G. J.; Miller, B. S. Paramagnetic resonance of Mn^{2+} in NaN_3, KN_3, and RbN_3. *J. Chem. Phys.* **1964**, *41*, 28–40, DOI: 10.1063/1.1725637.

(46) Markham, G. D.; Nageswara Rao, B.; Reed, G. H. Analysis of EPR powder pattern lineshapes for Mn(II) including third-order perturbation corrections. Applications to Mn(II) complexes with enzymes. *J. Magn. Reson.* **1979**, *33*, 595–602, DOI: 10.1016/0022-2364(79)90171-9.

(47) *EPR spectroscopy fundamentals and methods*, 1st ed.; Goldfarb, D., Stoll, S., Eds.; John Wiley & Sons: Hoboken, 2018.

(48) Keller, K.; Zalibera, M.; Qi, M.; Koch, V.; Wegner, J.; Hintz, H.; Godt, A.; Jeschke, G.; Savitsky, A.; Yulikov, M. EPR characterization of Mn^{2+} complexes for distance determination with pulsed dipolar spectroscopy. *Phys. Chem. Chem. Phys.* **2016**, *18*, 25120–25135, DOI: 10.1039/C6CP04884F.

(49) Baute, D.; Goldfarb, D. The ^{17}O hyperfine interaction in $V_{17}O(H_2{}^{17}O)_5{}^{2+}$ and $Mn(H_2{}^{17}O)_6{}^{2+}$ determined by high field ENDOR aided by DFT calculations. *J. Phys. Chem. A* **2005**, *109*, 7865–7871, DOI: 10.1021/jp052132q.

(50) Narasimhulu, K. V.; Carmieli, R.; Goldfarb, D. Single crystal ^{55}Mn ENDOR of concanavalin A: detection of two Mn^{2+} sites with different ^{55}Mn quadrupole tensors. *J. Am. Chem. Soc.* **2007**, *129*, 5391–5402, DOI: 10.1021/ja0662826.

(51) Hustedt, E. J.; Beth, A. H. In *Biol. Magn. Reson.* Berliner, L. J., Eaton, G. R., Eaton, S. S., Eds., 1st ed.; Plenum Press: New York, 2002; Vol. 19, pp 155–184, DOI: 10.1007/0-306-47109-4_3.

(52) Potapov, A.; Song, Y.; Meade, T.; Goldfarb, D.; Astashkin, A.; Raitsimring, A. Distance measurements in model bis-Gd(III) complexes with flexible "bridge". Emulation of biological molecules having flexible structure with Gd(III) labels attached. *J. Magn. Reson.* **2010**, *205*, 38–49, DOI: 10.1016/j.jmr.2010.03.019.

(53) Demay-Drouhard, P.; Ching, H. V.; Akhmetzyanov, D.; Guillot, R.; Tabares, L. C.; Bertrand, H. C.; Policar, C. A bis-manganese(II)-DOTA complex for pulsed dipolar spectroscopy. *ChemPhysChem* **2016**, *17*, 2066–2078, DOI: 10.1002/cphc.201600234.

(54) Yulikov, M.; Lueders, P.; Farooq Warsi, M.; Chechik, V.; Jeschke, G. Distance measurements in Au nanoparticles functionalized with nitroxide radicals and Gd^{3+}–DTPA chelate complexes. *Phys. Chem. Chem. Phys.* **2012**, *14*, 10732, DOI: 10.1039/c2cp40282c.

(55) Abdullin, D.; Matsuoka, H.; Yulikov, M.; Fleck, N.; Klein, C.; Spicher, S.; Hagelueken, G.; Grimme, S.; Lützen, A.; Schiemann, O. Pulsed EPR dipolar spectroscopy under the breakdown of the high-field approximation: the high-spin iron(III) case. *Chem. – A Eur. J.* **2019**, 8820–8828, DOI: 10.1002/chem.201900977.

(56) Burghaus, O.; Plato, M.; Rohrer, M.; Moebius, K.; MacMillan, F.; Lubitz, W. 3-mm high-field EPR on semiquinone radical anions $Q^{\bullet-}$ related to photosynthesis and on the primary donor $P^{\bullet+}$ and acceptor $QA^{\bullet-}$ in reaction centers of Rhodobacter sphaeroides R-26. *J. Phys. Chem.* **2005**, *97*, 7639–7647, DOI: 10.1021/j100131a037.

(57) Stoll, S.; Schweiger, A. EasySpin, a comprehensive software package for spectral simulation and analysis in EPR. *J. Magn. Reson.* **2006**, *178*, 42–55, DOI: 10.1016/j.jmr.2005.08.013.

(58) Plato, M.; Steinhoff, H. J.; Wegener, C.; Törring, J. T.; Savitsky, A.; Möbius, K. Molecular orbital study of polarity and hydrogen bonding effects on the g and hyperfine tensors of site directed NO spin labelled bacteriorhodopsin. *Mol. Phys.* **2002**, *100*, 3711–3721, DOI: 10.1080/00268970210166246.

(59) Steinhoff, H. J.; Savitsky, A.; Wegener, C.; Pfeiffer, M.; Plato, M.; Möbius, K. High-field EPR studies of the structure and conformational changes of site-directed spin labeled bacteriorhodopsin. *Biochim. Biophys. Acta* **2000**, *1457*, 253–262, DOI: 10.1016/S0005-2728(00)00106-7.

(60) Bloembergen, N.; Morgan, L. O. Proton relaxation times in paramagnetic solutions. Effects of electron spin relaxation. *J. Chem. Phys.* **1961**, *34*, 842–850, DOI: 10.1063/1.1731684.

(61) Cohn, M.; Townsend, J. A study of manganous complexes by paramagnetic resonance absorption. *Nature* **1954**, *173*, 1090–1091, DOI: 10.1038/1731090b0.

(62) *Electron spin relaxation in liquids*, 1st ed.; Muus, L. T., Atkins, P. W., Eds.; Plenum Press: New York, 1971, DOI: 10.1016/0022-2364(73)90263-1.

(63) Meirovitch, E.; Poupko, R. Line shape studies of the electron spin resonance spectra of manganese protein complexes. *J. Phys. Chem.* **1978**, *82*, 1920–1925, DOI: 10.1021/j100506a013.

(64) Stich, A.; Lahiri, S.; Yeagle, G.; Dicus, M.; Brynda, M.; Gunn, A.; Aznar, C.; DeRose, V. J.; Britt, R. D. Multifrequency pulsed EPR studies of biologically relevant manganese(II) complexes. *Appl. Magn. Reson.* **2007**, *341*, 321–341.

(65) Dikanov, S. A.; Tsvetkov, Y. D., *Electron spin echo envelope modulation (ESEEM) spectroscopy*, 1st ed.; CRC Press: Boca Ranton, 1992.

(66) Feher, G. Observation of nuclear magnetic resonances via the electron spin resonance line. *Phys. Rev.* **1956**, *103*, 834–835, DOI: 10.1103/PhysRev.103.834.

(67) Mims, W. B. Pulsed electron nuclear double resonance methodology. *Proc. R. Soc. Lond. A. Math. Phys. Sci.* **1965**, *91*, 1481–1505.

(68) Davies, E. R. A new pulse endor technique. *Phys. Lett. A* **1974**, *47*, 1–2, DOI: 10.1016/0375-9601(74)90078-4.

(69) Sørensen, O.; Eich, G.; Levitt, M.; Bodenhausen, G.; Ernst, R. Product operator formalism for the description of NMR pulse experiments. *Prog. Nucl. Magn. Reson. Spectrosc.* **1984**, *16*, 163–192, DOI: 10.1016/0079-6565(84)80005-9.

(70) Fan, C.; Doan, P. E.; Davoust, C. E.; Hoffman, B. M. Quantitative studies of davies pulsed ENDOR. *J. Magn. Reson.* **1992**, *98*, 62–72, DOI: 10.1016/0022-2364(92)90109-K.

(71) Doan, P. E.; Lees, N. S.; Shanmugam, M.; Hoffman, B. M. Simulating suppression effects in pulsed ENDOR, and the hole in the middle of Mims and Davies ENDOR spectra. *Appl. Magn. Reson.* **2010**, *37*, 763–779, DOI: 10.1007/s00723-009-0083-6.

(72) Epel, B.; Manikandan, P.; Kroneck, P. M. H.; Goldfarb, D. High-field ENDOR and the sign of the hyperfine coupling. *Appl. Magn. Reson.* **2001**, *21*, 287–297, DOI: 10.1007/BF03162408.

(73) Bennebroek, M.; Schmidt, J. Pulsed ENDOR spectroscopy at large thermal spin polarizations and the absolute sign of the hyperfine interaction. *J. Magn. Reson.* **1997**, *128*, 199–206, DOI: 10.1006/jmre.1997.1234.

(74) Nalepa, A.; Möbius, K.; Lubitz, W.; Savitsky, A. High-field ELDOR-detected NMR study of a nitroxide radical in disordered solids: Towards characterization of heterogeneity of microenvironments in spin-labeled systems. *J. Magn. Reson.* **2014**, *242*, 203–213, DOI: 10.1016/j.jmr.2014.02.026.

(75) Höfer, P.; Grupp, A.; Nebenführ, H.; Mehring, M. Hyperfine sublevel correlation (HYSCORE) spectroscopy: a 2D ESR investigation of the squaric acid radical. *Chem. Phys. Lett.* **1986**, *132*, 279–282, DOI: 10.1016/0009-2614(86)80124-5.

(76) Mehring, M.; Höfer, P.; Grupp, A. Pulsed electron nuclear double and triple resonance schemes. *Berichte der Bunsengesellschaft für Phys. Chemie* **1987**, *91*, 1132–1137, DOI: 10.1002/bbpc.19870911111.

(77) Potapov, A.; Pecht, I.; Goldfarb, D. Resolving ligand hyperfine couplings of type 1 and 2 Cu(II) in ascorbate oxidase by high field pulse EPR correlation spectroscopy. *Phys. Chem. Chem. Phys.* **2010**, *12*, 62–65, DOI: 10.1039/B919069D.

(78) Litvinov, A.; Feintuch, A.; Un, S.; Goldfarb, D. Triple resonance EPR spectroscopy determines the Mn2+ coordination to ATP. *J. Magn. Reson.* **2018**, *294*, 143–152, DOI: 10.1016/j.jmr.2018.07.007.

(79) Schmidt, R. R.; Martin, R. E.; Pannier, M.; Diederich, F.; Gramlich, V. Determination of end-to-end distances in a deries of TEMPO diradicals of up to 2.8 nm length with a new four-pulse double electron electron resonance experiment. *Angew. Chem. Int. Ed.* **1998**, *37*, 2834–2837, DOI: 10.1002/(SICI)1521-3773(19981102)37.

(80) Pannier, M.; Veit, S.; Godt, A.; Jeschke, G.; Spiess, H. Dead-time free measurement of dipole-dipole interactions between electron spins. *J. Magn. Reson.* **2000**, *142*, 331–340, DOI: 10.1006/jmre.1999.1944.

(81) Schiemann, O.; Prisner, T. F. Long-range distance determinations in biomacromolecules by EPR spectroscopy. *Q. Rev. Biophys.* **2007**, *40*, 1–53, DOI: 10.1017/S003358350700460X.

(82) Milov, A. D.; Salikhov, K. M.; Shchirov, M. D. Use of the double resonance in electron spin echo method for the study of paramagnetic center spatial distribution in solids. *Fiz. Tverd. Tela* **1981**, *23*, 975–982.

(83) Milov, A. D.; Ponomarev, A. B.; Tsvetkov, Y. D. Electron-electron double resonance in electron spin echo: model biradical systems and the sensitized photolysis of decalin. *Chem. Phys. Lett.* **1984**, *110*, 67–72, DOI: 10.1016/0009-2614(84)80148-7.

(84) Von Hagens, T.; Polyhach, Y.; Sajid, M.; Godt, A.; Jeschke, G. Suppression of ghost distances in multiple-spin double electron-electron resonance. *Phys. Chem. Chem. Phys.* **2013**, *15*, 5854, DOI: 10.1039/c3cp44462g.

(85) Jeschke, G.; Chechik, V.; Ionita, P.; Godt, A.; Zimmermann, H.; Banham, J.; Timmel, C. R.; Hilger, D.; Jung, H. DeerAnalysis2006—a comprehensive software package for analyzing pulsed ELDOR data. *Appl. Magn. Reson.* **2006**, *30*, 473–498, DOI: 10.1007/BF03166213.

(86) Edwards, T. H.; Stoll, S. Optimal tikhonov regularization for DEER spectroscopy. *J. Magn. Reson.* **2018**, *288*, 58–68, DOI: 10.1016/j.jmr.2018.01.021.

(87) Worswick, S. G.; Spencer, J. A.; Jeschke, G.; Kuprov, I. Deep neural network processing of DEER data. *Sci. Adv.* **2018**, *4*, 1–18, DOI: 10.1126/sciadv.aat5218.

(88) Fábregas Ibáñez, L.; Jeschke, G. General regularization framework for DEER spectroscopy. *J. Magn. Reson.* **2019**, *300*, 28–40, DOI: 10.1016/j.jmr.2019.01.008.

(89) Teucher, M.; Bordignon, E. Improved signal fidelity in 4-pulse DEER with gaussian pulses. *J. Magn. Reson.* **2018**, *296*, 103–111, DOI: 10.1016/j.jmr.2018.09.003.

(90) Tait, C. E.; Stoll, S. Coherent pump pulses in double electron electron resonance spectroscopy. *Phys. Chem. Chem. Phys.* **2016**, *18*, 18470–18485, DOI: 10.1039/C6CP03555H.

(91) Polyhach, Y.; Bordignon, E.; Tschaggelar, R.; Gandra, S.; Godt, A.; Jeschke, G. High sensitivity and versatility of the DEER experiment on nitroxide radical pairs at Q-band frequencies. *Phys. Chem. Chem. Phys.* **2012**, *14*, 10762–10773, DOI: 10.1039/c2cp41520h.

(92) Marko, A.; Margraf, D.; Cekan, P.; Sigurdsson, S. T.; Schiemann, O.; Prisner, T. F. Analytical method to determine the orientation of rigid spin labels in DNA. *Phys. Rev. E* **2010**, *81*, 021911, DOI: 10.1103/PhysRevE.81.021911.

(93) Larsen, R. G.; Singel, D. J. Double electron–electron resonance spin–echo modulation: spectroscopic measurement of electron spin pair separations in orientationally disordered solids. *J. Chem. Phys.* **1993**, *98*, 5134–5146, DOI: 10.1063/1.464916.

(94) Milov, A. D.; Maryasov, A. G.; Tsvetkov, Y. D. Pulsed electron double resonance (PELDOR) and its applications in free-radicals research. *Appl. Magn. Reson.* **1998**, *15*, 107–143, DOI: 10.1007/BF03161886.

(95) Marko, A.; Margraf, D.; Yu, H.; Mu, Y.; Stock, G.; Prisner, T. Molecular orientation studies by pulsed electron-electron double resonance experiments. *J. Chem. Phys.* **2009**, *130*, 064102.1–064102.9, DOI: 10.1063/1.3073040.

(96) Marko, A.; Prisner, T. F. An algorithm to analyze PELDOR data of rigid spin label pairs. *Phys. Chem. Chem. Phys.* **2013**, *15*, 619–627, DOI: 10.1039/C2CP42942J.

(97) Grytz, C. M.; Kazemi, S.; Marko, A.; Cekan, P.; Güntert, P.; Sigurdsson, S. T.; Prisner, T. F. Determination of helix orientations in a flexible DNA by multi-frequency EPR spectroscopy. *Phys. Chem. Chem. Phys.* **2017**, *19*, 29801–29811, DOI: 10.1039/C7CP04997H.

(98) Abé, C.; Klose, D.; Dietrich, F.; Ziegler, W. H.; Polyhach, Y.; Jeschke, G.; Steinhoff, H.-J. Orientation selective DEER measurements on vinculin tail at X-band frequencies reveal spin label orientations. *J. Magn. Reson.* **2012**, *216*, 53–61, DOI: 10.1016/j.jmr.2011.12.024.

(99) Erlenbach, N.; Endeward, B.; Schöps, P.; Gophane, D. B.; Sigurdsson, S. T.; Prisner, T. F. Flexibilities of isoindoline-derived spin labels for nucleic acids by orientation selective PELDOR. *Phys. Chem. Chem. Phys.* **2016**, *18*, 16196–16201, DOI: 10.1039/C6CP02475K.

(100) Sturgeon, B. E.; Ball, J. A.; Randall, D. W.; Britt, R. D. ^{55}Mn electron spin echo ENDOR of Mn^{2+} complexes. *J. Phys. Chem.* **1994**, *98*, 12871–12883, DOI: 10.1021/j100100a012.

(101) Schiemann, O.; Carmieli, R.; Goldfarb, D. W-band ^{31}P-ENDOR on the high-affinity Mn^{2+} binding site in the minimal and tertiary stabilized hammerhead ribozymes. *Appl. Magn. Reson.* **2007**, *31*, 543–552, DOI: 10.1007/BF03166601.

(102) Stull, J. A.; Stich, T. A.; Service, R. J.; Debus, R. J.; Mandal, S. K.; Armstrong, W. H.; Britt, R. D. ^{13}C ENDOR reveals that the D1 polypeptide C-terminus is directly bound to Mn in the photosystem II oxygen evolving complex. *J. Am. Chem. Soc.* **2010**, *132*, 446–447, DOI: 10.1021/ja908688t.

(103) Un, S.; Bruch, E. M. How bonding in manganous phosphates affects their Mn(II)-31P hyperfine interactions. *Inorg. Chem.* **2015**, *54*, 10422–10428, DOI: 10.1021/acs.inorgchem.5b01864.

(104) Albert, A.; Rees, C. W. Avidity of the tetracyclines for the cations of metals. *Nature* **1956**, *177*, 433–434, DOI: 10.1038/177433a0.

(105) Erlenbach, N.; Grünewald, C.; Krstic, B.; Heckel, A.; Prisner, T. F. End-to-end stacking of small dsRNA. *RNA* **2019**, *25*, 239–246, DOI: 10.1261/rna.068130.118.

(106) Saha, S.; Jagtap, A. P.; Sigurdsson, S. T. Site-directed spin labeling of 2'-amino groups in RNA with isoindoline nitroxides that are resistant to reduction. *Chem. Commun.* **2015**, *51*, 13142–13145, DOI: 10.1039/C5CC05014F.

(107) Abdullin, D.; Florin, N.; Hagelueken, G.; Schiemann, O. EPR-based approach for the localization of paramagnetic metal ions in biomolecules. *Angew. Chem. Int. Ed.* **2015**, *54*, 1827–1831, DOI: 10.1002/anie.201410396.

Curriculum Vitae

Thilo Hetzke
Bergweg 55
61440 Oberursel
Phone: +49 173 340 1059
Email: hetzke@prisner.de
Date of birth: 30.06.1988
Place of birth: Frankfurt am Main

Education

06/2015 - 2019 PhD in Chemistry, Research Group of Prof Prisner
Goethe University, Frankfurt
Thesis Title: "PELDOR and Hyperfine Spectroscopy as Complementary Tools to Investigate a Tetracycline-binding RNA Aptamer"

04/2013 - 05/2015 Master of Science in Chemistry (1.1)
Goethe University, Frankfurt

04/2009 - 03/2013 Bachelor of Science in Chemistry (1.7)
Goethe University, Frankfurt

09/2003 - 07/2007 Abitur, University Entrance Diploma (2.1)
Immanuel Kant Gymnasium, Kelkheim

Academic Teachers

N. Auner, M. Bamberger, M. Braun, B. Brutschy, G. Bruls, A. Dreuw, G. Eckert, E. Egert, J. Engels, C. Glaubitz, J. Glinnemann, M. Göbel, A. Heckel, M. Heilemann, R. Hegger, M. Holthausen, D. Klapper, B. Kolbesen, H.W. Lerner, G. Manolikakes, S. Metz, T. Prisner, M. Rehan, C. Richter, U. Scheffer, M. Schmidt, R. Schmidt, W. Schubert, H. Schwalbe, G. Stock, A. Terfort, M. Wagner

Author Contributions

Hetzke, **T.**; Bowen, A. M.; Prisner, T. F. ELDOR-detected NMR at Q-band. *Appl. Magn. Reson.* **2017**, *48*, 1375–1397.

T.H. and A.M.B. performed pulsed EPR measurements. T.H. synthesized the ^{13}C-labeled DOTA compound, analyzed all experimental data and wrote the manuscript. A.M.B. and T.F.P. supervised the experiments. All authors discussed the results and commented on the manuscript.

Saha, S.; **Hetzke**, **T.**; Prisner, T. F.; Sigurdsson, S. T. Noncovalent spin-labeling of RNA: the aptamer approach. *Chem. Commun.* **2018**, *54*, 11749–11752.

T.H. performed all pulsed and some CW EPR measurements, analyzed all pulsed and some CW EPR data and simulated CW EPR spectra. S.S. synthesized the E-TU spin label, performed RNA solid-phase synthesis, purified the RNA, performed fluorescence spectroscopy experiments and some CW EPR experiments. S.S. and S.T.S. wrote the manuscript. S.T.S. conceived the study and was in charge of overall direction and planning. All authors discussed the results and commented on the manuscript.

Hetzke, **T.**; Vogel, M.; Gophane, D. B.; Weigand, J. E.; Suess, B.; Sigurdsson, S. T.; Prisner, T. F. Influence of Mg 2+ on the conformational flexibility of a tetracycline aptamer. *RNA* **2019**, *25*, 158–167.

T.H. performed all pulsed EPR measurements at X-band and Q-band frequencies, analyzed all experimental EPR and PELDOR database data, simulated

orientation-selective X-band PELDOR data and wrote the manuscript. M.V. performed in vitro transcription of the RNA, ITC measurements and RNA hybridization and purification. D.G. synthesized the Çm spin label and performed the solid-phase synthesis. J.E.W., B.S., S.T.S. and T.F.P. planned and supervised the study. M.V., J.E.W., B.S., S.T.S. and T.F.P. provided critical feedback and helped shape the final manuscript.

Hetzke, **T.**; Bowen, A. M.; Vogel, M.; Gauger, M.; Suess, B.; Prisner, T. F. Binding of tetracycline to its aptamer determined by 2D-correlated Mn2+ hyperfine spectroscopy. *J. Magn. Reson.* **2019**, *303*, 105–114.

T.H. performed all pulsed EPR measurements, analyzed all EDNMR, ^{31}P Davies ENDOR, THYCOS and 2D EDNMR data, performed ^{31}P Davies ENDOR simulations and wrote the manuscript. A.M.B. had the initial idea of performing 2D EDNMR experiments. M.V. performed in vitro transcription and purification of the RNA. M.G. assisted in acquisition of ^{13}C Mims ENDOR experiments, analyzed and simulated ^{13}C Mims ENDOR data and performed DFT calculations. T.F.P. supervised the research. A.M.B., M.V., B.S. and T.F.P. provided critical feedback and helped shape the final manuscript.

List of Conference Presentations

Oral presentations given by the author:

1. "Pulsed hyperfine spectroscopy of Mn^{2+} coordination spheres"

   Institute Seminar of the Institute for Physical and Theoretical Chemistry, Hirschegg, Austria, 2016

2. "Investigation of a Tetracycline-binding RNA aptamer using ELDOR-detected NMR"

   Asia-Pacific EPR/ESR Symposium 2016, Irkutsk, Russia, 2016

3. "Investigation of a Tetracycline-binding RNA aptamer using pulsed EPR spectroscopy"

   IRTG902 Winter School 2016, Hirschegg, Austria, 2016

4. "Investigating the influence of Mg^{2+} concentration on a Tetracycline-binding RNA aptamer using EPR spectroscopy"

   Group Seminar of the Group of Prof Wolfgang Lubitz, Mühlheim, Germany, 2016

5. "Two-dimensional ELDOR-detected NMR as a useful tool for correlating ^{13}C and ^{31}P nuclear spins to paramagnetic Mn^{2+} ions in a Tetracycline-binding RNA aptamer"

   The 50th Annual International Meeting of the ESR Spectroscopy Group of the Royal Society of Chemistry, Oxford, United Kingdom, 2017

6. "Influence of Mg^{2+} on a Tetracycline-binding RNA aptamer studied by PELDOR spectroscopy"

IRTG902 Sumnmer School 2018, Altglashütten, Germany, 2018

7. "2D-correlated hyperfine spectroscopy on a Tetracycline-binding RNA aptamer"

   Institute Seminar of the Institute for Physical and Theoretical Chemistry, Hirschegg, Austria, 2018

8. "Mn^{2+}-binding of a TC-aptamer studied by pulsed EPR spectroscopy"

   10th Biomolecular Magnetic Resonance Center Symposium, Bad Homburg, Germany, 2018

9. "2D-correlated hyperfine spectroscopy on Mn^{2+} complexes at Q-band frequencies"

   SPP1601 Young Researchers Workshop 2018, Schmitten, Germany, 2018

10. "2D-correlated Hyperfine Spectroscopy on a Tetracycline-binding RNA aptamer"

    59th Annual Rocky Mountain Conference on Magnetic Resonance, Snowbird, United States of America, 2018

11. "Influence of Mg^{2+} on the conformational flexibility of a Tetracycline aptamer"

    CRC902 Symposium 2018 - Understanding RNA-based Regulation in Cells, Frankfurt, Germany, 2018

12. "Binding of tetracycline to its aptamer determined by 2D-correlated Mn^{2+} hyperfine spectroscopy"

    XIth Conference of European Federation of EPR Groups, Bratislava, Slovakia, 2019

13. "Pulsed EPR spectroscopy on a TC-aptamer"

    IPTC Symposium 2019, Frankfurt, Germany, 2019

Poster presentations given by the author:

1. "ELDOR-detected NMR of Manganese Coordination Spheres at Q-band"

   The 37th Discussion Meeting of the GDCh-Division of Magnetic Resonance (FGMR), Darmstadt, Germany, 2015

2. "Investigation the influence of Mg^{2+} concentration on a Tetracycline-binding RNA aptamer using PELDOR spectroscopy"

   Ringberg Meeting: Connecting EPR, ssNMR and DNP for the study of complex biomolecules, Kreuth, Germany, 2016

3. "Investigation of conformational dynamics and its dependence on M^{2+} of a Tetracycline-binding RNA aptamer by using pulsed EPR spectroscopy"

   The 22nd Annual Meeting of the RNA Society, Prague, Czech Republic, 2017

Publications for Cumulative Dissertation

Appl Magn Reson (2017) 48:1375–1397
DOI 10.1007/s00723-017-0927-4

Applied Magnetic Resonance

ORIGINAL PAPER

ELDOR-detected NMR at Q-Band

Thilo Hetzke[1] · Alice M. Bowen[1,2] · Thomas F. Prisner[1]

Received: 28 June 2017 / Revised: 14 August 2017 / Published online: 29 August 2017

Abstract In recent years, electron–electron double resonance detected nuclear magnetic resonance (EDNMR) has gained considerable attention as a pulsed electron paramagnetic resonance technique to probe hyperfine interactions. Most experiments published so far were performed at W-band frequencies or higher, as at lower frequencies detection of weakly coupled low-γ nuclei is hampered by the presence of a central blind spot, which occurs at zero frequency. In this article we show that EDNMR measurements and a meaningful data analysis is indeed possible at intermediate microwave frequencies (Q-band, 34 GHz), once experimental parameters have been optimized. With highly selective detection pulses and Gaussian shaped electron–electron double resonance (ELDOR) pulses it is possible to detect low-γ nuclei coupled to paramagnetic Mn^{2+}. Weakly coupled ^{14}N resonances, which are separated from the zero frequency by only 2.8 MHz, were readily detected. In systems where different spin active nuclei are coupled to the electron spin, particular care has to be taken when using higher powered ELDOR pulses, as combination frequencies from the two nuclei ($\Delta m_S = \pm 1$, $\Delta m_{I,1} = \pm 1$, $\Delta m_{I,2} = \pm 1$) can lead to severe line broadening and complicated EDNMR spectra. We also compare the EDNMR spectra of ^{13}C-labeled Mn–DOTA to ^{13}C-Mims electron–nuclear double resonance to get a better insight into the similarities and differences in the results of the two techniques for ^{13}C hyperfine coupling.

✉ Thomas F. Prisner
prisner@chemie.uni-frankfurt.de

[1] Institute of Physical and Theoretical Chemistry and Center of Biomolecular Magnetic Resonance, Goethe University Frankfurt, Frankfurt Am Main, Germany

[2] Department of Chemistry, Center for Advanced Electron Spin Resonance (CAESR), University of Oxford, Oxford, UK

1 Introduction

Electron–electron double resonance detected nuclear magnetic resonance (ELDOR-detected NMR or just EDNMR) is a technique of pulsed electron paramagnetic resonance (EPR) spectroscopy to measure hyperfine couplings of paramagnetic spin centers to nearby spin-active nuclei. First proposed by the group of Arthur Schweiger in 1994 [1], it took approximately ten more years until it found further scientific applications and became a useful tool for research [2–4].

As the technique has gained wider applications several EDNMR review articles have been published, describing the experiment in detail [5–8]. In this article, we will, therefore, only give a short introduction to EDNMR. A more detailed theoretical description can be found in the aforementioned references. A typical EDNMR pulse sequence consists of two microwave channels, a detection channel (ν_{det}) and an ELDOR channel (ν_{ELD}). The detection channel consists of a Hahn-echo sequence and is operated at a fixed frequency to monitor the intensity of an allowed EPR transition. The second microwave channel consists of a single, typically long microwave pulse referred to as ELDOR or high-turning angle (HTA) pulse. ν_{ELD} of the ELDOR pulse is normally swept symmetrically around ν_{det}. Every time the ELDOR pulse hits a formally forbidden transition of the type $\Delta m_S = \pm 1$, $\Delta m_I = \pm 1$ (or for high-spin nuclei also $\Delta m_I = \pm 2$, ± 3, etc.) population from the lower state is transferred to an excited state. The removal of population from the lower state of the allowed transition manifests itself as a reduction of intensity of the integrated spin echo in ν_{det}, as the population difference of the allowed transition is reduced. As ν_{ELD} approaches ν_{det}, the ELDOR pulse saturates the detected EPR transition. As a consequence, the integrated intensity drops to zero at $\Delta\nu = \nu_{ELD} - \nu_{det} = 0$. This is commonly referred to as the central blind spot. The unit of $\Delta\nu$ is typically given in MHz. Weakly coupled ligand nuclei resonate at their respective Larmor frequency ν_I, with individual peaks split by the hyperfine coupling constant A_I. These nuclei yield a symmetric EDNMR spectrum with respect to the central blind spot, as allowed EPR transitions in all nuclear spin manifolds are excited simultaneously. Strongly coupled nuclei resonate at $A_I/2$ with peaks being split by $2\nu_I$ to first order. The EDNMR spectrum may be asymmetric with respect to the central blind spot, if the allowed EPR transitions in the different nuclear manifolds can be selectively excited, as demonstrated here for various Mn^{2+} complexes.

The central blind spot is the reason why most of the currently published EDNMR studies have been performed at high microwave frequencies (W-band, 95 GHz and 3393 mT for $g = 2$). At these field strengths weakly coupled nuclei, especially those of low-γ nuclei, have sufficiently high Larmor frequencies such that they are no longer obscured by the central blind spot of the experiment. Examples include work by Jeschke and Spiess [2], work by Sun Un et al. on Mn^{2+} systems [9–11], work by the Goldfarb lab [12–15], the Lubitz lab [4, 16, 17] and the van Doorslaer lab [18–20].

To the authors' knowledge, only few EDNMR studies at lower microwave frequencies have so far been reported. Examples include ^{1}H-EDNMR at X-band [3],

strongly coupled ^{61}Ni-EDNMR at Q-band [21], strongly coupled ^{14}N-EDNMR at Q-band [22] and a Q-band EDNMR study on copper single crystals [23]. All these studies, however, exclude the investigation of weakly coupled low-γ nuclei such as ^{14}N at these lower microwave frequencies and field strengths. In this work, it is shown that useful information can be extracted from Q-band EDNMR data of Mn^{2+} model systems, even for low-γ nuclei such as ^{14}N and ^{17}O, once the experimental parameters have been carefully optimized.

2 Q-band EDNMR versus High-Field EDNMR

High-field EDNMR comes with two major advantages the first one being that weakly coupled low-γ nuclei are well separated from the central blind spot. For example, the biologically relevant ^{14}N nucleus resonates at 10.2 MHz at W-band frequencies, this means that weakly coupled ^{14}N nuclei will only overlap slightly with the Lorentzian-shaped central blind spot function, which has a FWHM (full width half maximum) of typically 6 MHz [5]. Second, different nuclei are better resolved from one another. At W-band, the frequency difference between ^{23}Na ($\nu_{23Na} = 37.8$ MHz) and ^{13}C ($\nu_{13C} = 35.9$ MHz) is 1.9 MHz, whereas at Q-band, the frequency difference is reduced to 0.7 MHz ($\nu_{23Na} = 13.5$ MHz, $\nu_{13C} = 12.8$ -MHz). Although the resolution of EDNMR at Q-band is accurate enough to tell if predominantly ^{23}Na or ^{13}C is present in the sample, it is difficult to give a 'quantitative' answer, as it is impossible to separate ^{23}Na and ^{13}C signals. Although ^{23}Na and ^{13}C signals are still not fully separated at W-band, the larger separation facilitates a more quantitative treatment [10]. All Larmor frequencies given in this article are based on $g = 2$ and $\nu_0 = 33.5$ GHz, $B_0 = 1200$ mT and $\nu_0 = 94.0$ GHz, $B_0 = 3360$ mT for Q- and W-band, respectively, unless calculated with reference to a specific example data set shown in a figure.

In contrast, an advantage of Q-band EDNMR over high-field EDNMR is that forbidden transitions have an intrinsically higher transition probability (I_f) at Q-band as I_f is inversely proportional to the square of the Larmor frequency ν_I [1]:

$$I_a = \frac{\left|\nu_I^2 - \frac{1}{4}\left(\nu_\alpha - \nu_\beta\right)^2\right|}{\nu_\alpha \nu_\beta}, \tag{1}$$

and

$$I_f = \frac{\left|\nu_I^2 - \frac{1}{4}\left(\nu_\alpha + \nu_\beta\right)^2\right|}{\nu_\alpha \nu_\beta}, \tag{2}$$

where I_a and I_f describe the transition probabilities of allowed and forbidden transitions, ν_I describes the nuclear Larmor frequency and ν_α and ν_β the nuclear transitions in the different electron spin manifolds. I_f dictates the EDNMR intensity h alongside with the nominal flip angle of the ELDOR pulse:

$$h = 1 - I_a \cos\left(\beta_0 \sqrt{I_f}\right) - I_f \cos\left(\beta_0 \sqrt{I_a}\right), \tag{3}$$

with $\beta_f = \omega_{ELD} t_{ELD} \sqrt{I_f} = \beta_0 \sqrt{I_f}$. v_α and v_β are defined as:

$$|v_\alpha| = \left[(v_I + A)^2 + \left(\frac{1}{2} B\right)^2 \right]^{1/2}, \tag{4}$$

and

$$|v_\beta| = \left[(v_I - A)^2 + \left(\frac{1}{2} B\right)^2 \right]^{1/2}, \tag{5}$$

where A describes the secular part of the hyperfine coupling and contains the isotropic (a_{iso}) as well as the dipolar hyperfine interaction (T). B describes the pseudosecular part of the hyperfine coupling and contains only the dipolar contribution of the hyperfine interaction [24]. Equations (1), (2), (4) and (5) are only valid for an $S = 1/2$, $I = 1/2$ spin system. For high-spin systems, the zero-field and quadrupole interactions lead to an additional level mixing of the spin states and, therefore, to an increase in I_f. These high-spin terms are also inversely proportional to v_I^2. As a consequence, their impact on I_f is larger at smaller magnetic fields [25, 26]. For spin-1/2 nuclei such as ^{15}N and ^{31}P, which are known to have relatively small pseudosecular contributions to the hyperfine interaction Hamiltonian in Mn^{2+}-coupled systems [27, 28], I_f can become rather small, especially at higher fields.

Another important aspect of EDNMR is its reproducibility, to allow comparison of different samples (e.g., different incubation times for ABC transporters with Mn^{2+}/ATP to investigate the transport cycle [29]). Reproducibility for EDNMR data is in large parts dictated by the effective B_1 field of the ELDOR pulse. This varies with the pulse frequency as it depends on the bandwidth profile of the resonator used. In our experiments, we have found that the Bruker EN 5170 D2 probehead is a robust resonator, which is easy to tune and gives similar bandwidth profiles for samples in similar solvent systems. An automatized nutation experiment with good resolution to probe the resonator bandwidth is routinely performed in under 10 min.

A further advantage of Q-band EDNMR is more of a practical nature: Q-band spectrometers are more widespread than W-band spectrometers. Additionally modern commercial Q-band spectrometers can be purchased with built-in AWG systems, this offers the possibility to easily use Gaussian shaped ELDOR pulses, which somewhat reduces the problem of the central blind spot (see Sect. 4.1).

3 Methods

3.1 Sample Preparation

For the Mn^{2+} hexaaqua complexes, an appropriate amount of $MnCl_2 \cdot 4H_2O$ (Sigma-Aldrich) was dissolved in ddH_2O to yield a 40 mM stock solution. An aliquot of the

stock solution was then further diluted with ddH_2O or $H_2^{17}O$ (Nukem Isotopes, >70% w/w isotope purity) to yield 4 mM Mn^{2+} solutions. Small amounts were then mixed with methanol (50%, v/v) as glassing agent to yield a final 2 mM Mn^{2+} solution.

For Mn–DOTA complexes, an appropriate amount of DOTA (Strem Chemicals) or ^{13}C-labeled DOTA was dissolved in a 100 mM buffered triethanolamine solution at pH 7.5 to yield a 4 mM DOTA solution. $Mn(ClO_4)_2{\cdot}4H_2O$ (Sigma-Aldrich) was then added to yield an equimolar Mn^{2+}/DOTA solution. Complete formation of the Mn–DOTA complex was verified with X-band CW-EPR at room temperature. In case of Mims electron–nuclear double resonance (ENDOR) experiments, the matrix was deuterated by lyophilisation and redissolution in D_2O. For pulsed EPR measurements, glycerol (or deuterated glycerol) was added as a glassing agent (50%, v/v) to yield a 2 mM Mn–DOTA solution.

3.2 Synthesis of ^{13}C-DOTA

^{13}C-DOTA was synthesized as reported earlier [30, 31]. 0.25 g of cyclen (1.45 mmol) was dissolved in 2.5 mL of ddH_2O. The solution was gently heated to facilitate complete dissolution. The alkaline solution was then neutralized with 2 mM hydrochloric acid. In a separate flask, 1 g of 1,2-^{13}C-bromoacetic acid (7.20 mmol) was dissolved in 2.5 mL of ddH_2O. The solution was then cooled with an ice bath and neutralized with sodium hydroxide in such a way that a temperature of 5 °C was not exceeded. The two solutions were then mixed together and the temperature was elevated to 80 °C. Concentrated sodium hydroxide was added to maintain pH 13. After the reaction was complete, the solution was acidified to pH 2.5, upon which precipitation occurred. The white precipitate was isolated, washed with ethanol and recrystallized twice in ddH_2O.

^{1}H NMR, 250 MHz, D_2O, δ (ppm): 3.78 (s, br, 8H, acetate), 3.28 (s, br, 16H, cyclen ring). MS (ESI +) *m/z*: [M + H] + Calcd for C8^{13}C8H28N4O8 413.36; found 413.24, [M + Na] + Calcd for C8^{13}C8H28N4O8 435.35; found 435.24.

3.3 EPR Spectroscopy and Data Analysis

Pulsed EPR measurements were performed at Q-band on a Bruker E580 spectrometer with an EN 5170 D2 ENDOR probehead. The spectrometer was equipped with either a Bruker AmpQ 10 W solid-state amplifier or a 150 W traveling-wave tube (Applied Systems Engineering Inc.) for microwave amplification. EDNMR experiments were performed either in a 'conservative' manner using microwave pulse-forming units and an external SuperQ-FTu ELDOR source for probe and pump frequencies, respectively, or using a Bruker SpinJet-AWG. In all pulsed experiments the temperature was kept at 5 K using a continuous-flow helium cryostat (CF935) and an ITC 502 temperature control unit, both from Oxford Instruments.

RF frequencies were generated from a Bruker DICE-II system and amplified with an externally blanked 2 kW Dressler amplifier (LPA 10020 LF). A 30 MHz low-pass filter (RF Limited DF-3000) was used to cut off higher harmonics. The RF was

connected via a Noise Suppressor to the resonator and terminated on the other side with a 50 Ω load.

Echo-detected field-swept experiments were performed using the standard Hahn-echo sequence $t_p/2 - \tau - t_p - \tau$ echo ($t_p = 40$ ns, $\tau = 400$ ns). Unless otherwise stated, EDNMR experiments where performed using a $t_{ELD} - T - t_p/2 - \tau - t_p - \tau$ echo sequence with $t_{ELD} = 9000$ ns, $T = 8000$ ns, $t_p = 800$ ns, $\tau = 1800$ ns. The integration width of the echo was set to 800 ns, centered around the maximum of the spin echo. No transients were collected. The shot repetition time was set to 3000 µs with 20–50 shots per point. The sweep width of the frequency of the ELDOR pulse was 440 MHz with a frequency increment of 0.2 MHz, symmetrically placed around the detection frequency. The detection frequency (ν_{det}) was chosen to be equal to the frequency of the central dip feature of the resonator bandwidth profile, such that the variation in ELDOR amplitude is approximately symmetric about ν_{det}. Amplitudes of ELDOR pulses were extracted from nutation experiments at the detection frequency with subsequent Fourier transformation. Mims ENDOR experiments were performed using the $t_p - \tau - t_p - t_{RF} - T - t_p - \tau$ echo pulse sequence with $t_p = 20$ ns, $t_{RF} = 27{,}500$ µs and $T = 5500$ µs. The length of the RF pulse was optimized by nutation experiments of the RF pulse close to ν_{13C}. τ values were incremented in steps of 50 ns from 300 to 2000 ns. The RF sweep width of 6 MHz started at 9.9 MHz with a frequency increment of 10 kHz. The shot repetition time was set to 60 ms with 1 shot per point. The random acquisition mode was used to minimize baseline artifacts [32]. The ENDOR-efficiency was calculated to $\varepsilon(\tau, \nu_{RF}) = (I_{RF}–I_0)/I_0$, where I_0 is an average value of an off-resonant frequency range. The resonator bandwidth for all pulsed EPR experiments was approximately 100 MHz.

Density functional theory (DFT) calculations were performed using the ORCA 4.0 package [33]. The PBE0 hybrid functional with a 6 − 31 + G(d, p) basis set were used for calculation of EPR parameters of the Mn–DOTA complex [34]. The C-PCM solvation model (water as a solvent) was used to obtain more accurate information about a_{iso} [35]. Similar settings were recently used by Un and Bruch in a hyperfine coupling benchmark study of Mn^{2+} systems [11]. The geometry of the crystal structure of Mn–DOTA was used as a starting point for DFT calculations [36].

4 Results

The following section is ordered as follows: Sect. 4.1 deals with the optimization of important experimental parameters to obtain Q-band EDNMR spectra with a sufficient narrow width of the central blind spot. Section 4.2 then deals with Q-band EDNMR spectra of different Mn^{2+} systems, namely the hexaaqua complex, the ^{17}O-labeled hexaaqua complex, Mn–DOTA and Mn–^{13}C-DOTA. Section 4.3 is dedicated to the investigation and explanation of combination frequencies, which appear when using higher powered ELDOR pulses. Section 4.4 compares EDNMR to the Mims ENDOR technique with the aim of getting a better insight into the ^{13}C hyperfine coupling of Mn–^{13}C-DOTA.

In terms of nomenclature in this paper, a sq EDNMR transition describes a transition in which the projection of both the electron spin and the nuclear spin is changed ($\Delta m_S = \pm 1$, $\Delta m_I = \pm 1$). Consequently, dq and tq describe double and triple quantum transitions in which $\Delta m_S = \pm 1$, $\Delta m_I = \pm 2$ and ± 3. Transitions in which two different nuclei change their projection (e.g., ^{1}H and ^{55}Mn) are denoted as mq transitions [$\Delta m_S = \pm 1$, $\Delta m_{I,1} = \pm 1$, $\Delta m_{I,2} = \pm 1$ (or ± 2, etc., for high-spin nuclei)] and also called combination frequencies.

4.1 Optimization of Experimental EDNMR Parameters

As already detailed in the previous section, the central blind spot plays a crucial role in EDNMR experiments at Q-band. An important step in setting up a Q-band EDNMR experiment is, therefore, the optimization of the width of the central blind spot; making it narrow enough so as not to obscure signals from any low-γ nuclei present while at the same time using an ELDOR pulse of sufficient power to excite the formally forbidden electron and nuclear transitions. Figure 1 shows a series of EDNMR spectra of $[Mn(H_2O)_6]^{2+}$ with different pulse lengths, amplitudes and shapes for the detection and/or the ELDOR channel. h denotes the hole-depth parameter of the central blind spot, and $\Delta\nu_{1/2}$ the full width at half maximum of the central blind spot. The only nuclei visible are proton signals appearing at ca. ± 51 MHz. The first three spectra were recorded with 50–100 ns detection pulses and 1000, 4500 and 9000 ns long ELDOR pulses, respectively, with an identical microwave amplitude ω_{ELD}. As expected, h and the intensity of the proton signals increases with stronger ELDOR pulses. All three spectra are characterized by an excessive line broadening of the proton signals and the central blind spot caused by relatively unselective detection pulses and a short echo integration window, which is the most important factor in determining the resolution of detectable EDNMR signals [8].

The 4th, 5th and 6th spectra were recorded with highly selective 400–800 ns detection pulses, and 9000 ns long ELDOR pulses with different microwave amplitudes. With strong ELDOR pulses ($\omega_{ELD} = 5.0 \times 10^7$ rad s^{-1}) an almost-complete saturation of the allowed EPR transition as well as the forbidden proton transition is possible. Although spectra recorded with highly powered ELDOR pulses are characterized by a broad central blind spot, which renders detection of low-γ nuclei difficult, the line shape of proton signals is much better resolved in comparison to the first three spectra. The proton line shape did not change when using ELDOR pulses of shorter length than 9000 ns with 400–800 ns detection pulses, indicating that any magnetization transfer artifact from the 9000 ns long ELDOR pulse can be neglected [8].

The signals appearing at approximately ± 60 MHz in the 4th and 5th spectra are part of ^{55}Mn-^{1}H combination frequencies, which are discussed in detail in Sect. 4.4.

The influence of the length of the detection pulses and the echo integration window on EDNMR is best visible when comparing the 3rd spectrum to the 6th spectrum in which all experimental settings are identical except for the length of the detection pulses and the echo integration window; the shorter detection pulses and integration window leads to a broadening in the detected proton signals.

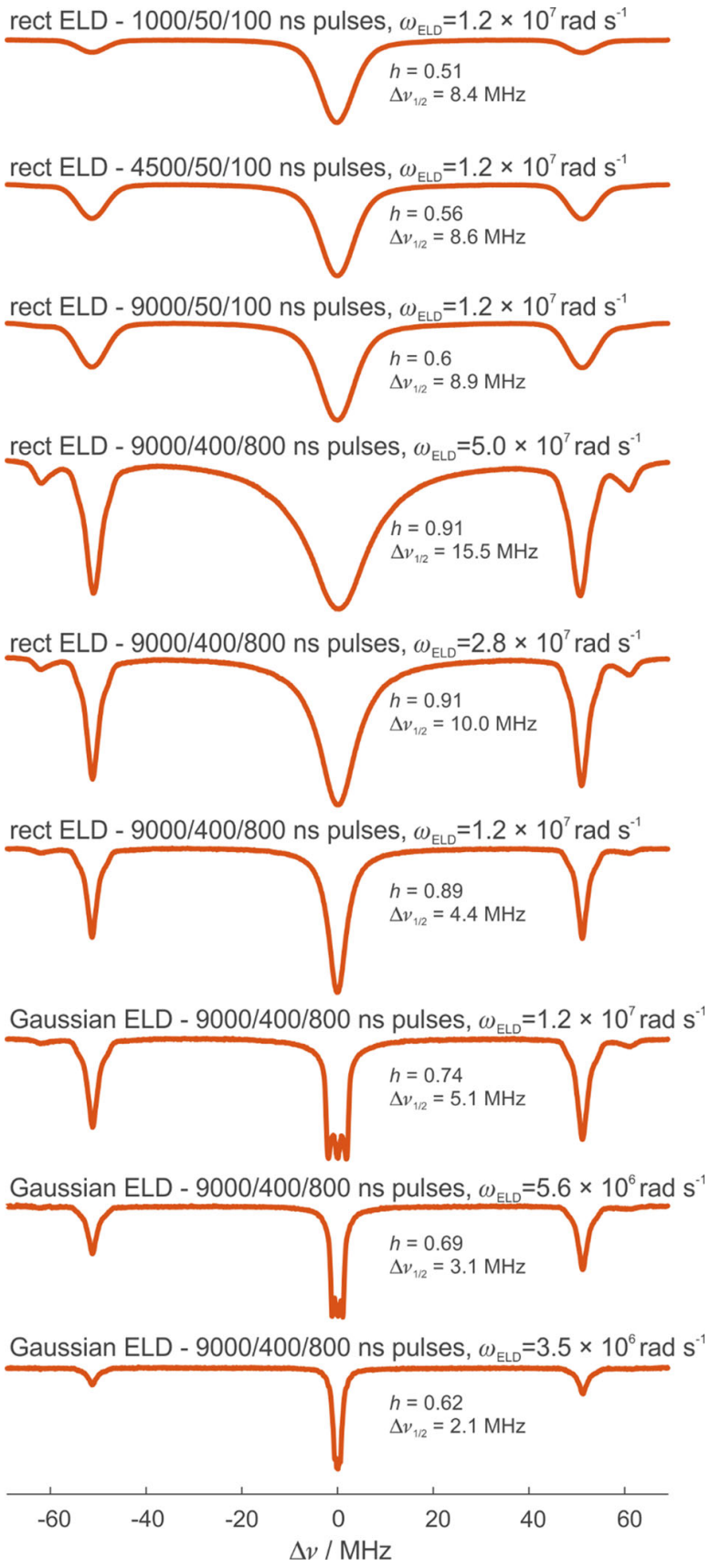
rect ELD - 1000/50/100 ns pulses, ω_{ELD}=1.2 × 10^7 rad s^{-1}
h = 0.51
$\Delta\nu_{1/2}$ = 8.4 MHz
rect ELD - 4500/50/100 ns pulses, ω_{ELD}=1.2 × 10^7 rad s^{-1}
h = 0.56
$\Delta\nu_{1/2}$ = 8.6 MHz
rect ELD - 9000/50/100 ns pulses, ω_{ELD}=1.2 × 10^7 rad s^{-1}
h = 0.6
$\Delta\nu_{1/2}$ = 8.9 MHz
rect ELD - 9000/400/800 ns pulses, ω_{ELD}=5.0 × 10^7 rad s^{-1}
h = 0.91
$\Delta\nu_{1/2}$ = 15.5 MHz
rect ELD - 9000/400/800 ns pulses, ω_{ELD}=2.8 × 10^7 rad s^{-1}
h = 0.91
$\Delta\nu_{1/2}$ = 10.0 MHz
rect ELD - 9000/400/800 ns pulses, ω_{ELD}=1.2 × 10^7 rad s^{-1}
h = 0.89
$\Delta\nu_{1/2}$ = 4.4 MHz
Gaussian ELD - 9000/400/800 ns pulses, ω_{ELD}=1.2 × 10^7 rad s^{-1}
h = 0.74
$\Delta\nu_{1/2}$ = 5.1 MHz
Gaussian ELD - 9000/400/800 ns pulses, ω_{ELD}=5.6 × 10^6 rad s^{-1}
h = 0.69
$\Delta\nu_{1/2}$ = 3.1 MHz
Gaussian ELD - 9000/400/800 ns pulses, ω_{ELD}=3.5 × 10^6 rad s^{-1}
h = 0.62
$\Delta\nu_{1/2}$ = 2.1 MHz
-60
-40
-20
0
20
40
60
$\Delta\nu$ / MHz

◀**Fig. 1** ELDOR-detected NMR spectra of $[Mn(H_2O)_6]^{2+}$ recorded at Q-band frequencies ($\nu_0 = 33.855$ GHz) and 5 K with different pulse lengths, shapes and amplitudes. The magnetic field was selected to be at the position of the 3rd hyperfine peak ($B_0 = 1206$ mT). ω_{ELD} is the amplitude (strength) of the ELDOR pulse, h denotes the hole-depth parameter and $\Delta\nu_{1/2}$ the full width at half maximum of the central blind spot. In all cases the strength of the detection pulses was selected to yield a maximum echo intensity. ^{1}H signals are centered around $|\pm\nu_{1H}| = 51.3$ MHz. For more experimental details see Sect. 3.3

Consequently, Q-band EDNMR is always a compromise between the signal-to-noise ratio and the width of the central blind spot. For our Q-band studies, the most convenient setup consisted of a 9000–400–800 ns pulse scheme with $\omega_{ELD} = 1.2 \times 10^7$ rad s^{-1}. In case of low concentrations (e.g., membrane proteins), it may be better to use 200–400 ns detection pulses, as the line broadening of the proton signals and the central blind spot was seen to be minimal in our studies. The shape of the central blind spot for rectangular ELDOR pulses was a pure Lorentzian as expected [17], with minor deviations stemming from a non-symmetric resonator profile.

As previously demonstrated in the original hole-burning EPR techniques by the group of Arthur Schweiger (FT-detected NMR and ELDOR-detected NMR) [1, 37], the use of Gaussian shaped ELDOR pulses leads to a considerable narrowing of the central blind spot, especially at its flanks, while retaining the intensity of the forbidden proton transitions (6th and 7th spectrum in Fig. 1). The FWHM of the central blind spot can be reduced even further (8th and 9th spectrum in Fig. 1) by reducing the power of the ELDOR pulse. For $\omega_{ELD} = 3.5 \times 10^6$ rad s^{-1}, however, the intensities of the forbidden transitions become rather small, especially as proton signals typically give the most intense EDNMR signals. The 'trident'-like feature close to ν_0, which is visible in the 7th, 8th and partially in the 9th spectrum of Fig. 1, must not be mistaken as a real signal. It is rather an artifact stemming from an imperfect Gaussian line shape of the ELDOR pulse. These artifacts can be distinguished from possible real signals by reducing the ELDOR amplitude and carefully monitoring the frequency of the observed signal. Upon reducing the ELDOR amplitude from $\omega_{ELD} = 1.2 \times 10^7$ rad s^{-1} to $\omega_{ELD} = 5.9 \times 10^6$ rad s^{-1} the outer 'triplet signal' maxima move from ± 1.9 to ± 1.1 MHz (7th and 8th spectrum in Fig. 1). If the 'triplet signal' would be real, one would expect a slight increase in frequency (if any), as at lower ELDOR powers the signals will convolute less with the narrower blind spot function. The use of Gaussian shaped detection pulses did not yield improved EDNMR spectra in terms of the FWHM of the central blind spot in comparison to rectangular detection pulses.

4.2 Q-band EDNMR Spectra of Mn^{2+} Complexes

Figure 2 shows a series of Q-band EDNMR spectra of different Mn^{2+} complexes; namely the hexaaqua complex ($[Mn(H_2O)_6]^{2+}$), the ^{17}O-labeled hexaaqua complex ($[Mn(H_2^{17}O)_6]^{2+}$), the Mn–DOTA complex and the ^{13}C-labeled Mn–DOTA complex. The echo-detected field-swept spectra (EDFS) of all four compounds are shown as insets on the left-hand side of each EDNMR spectrum with asterisks denoting the magnetic field positions for EDNMR experiments. Not surprisingly,

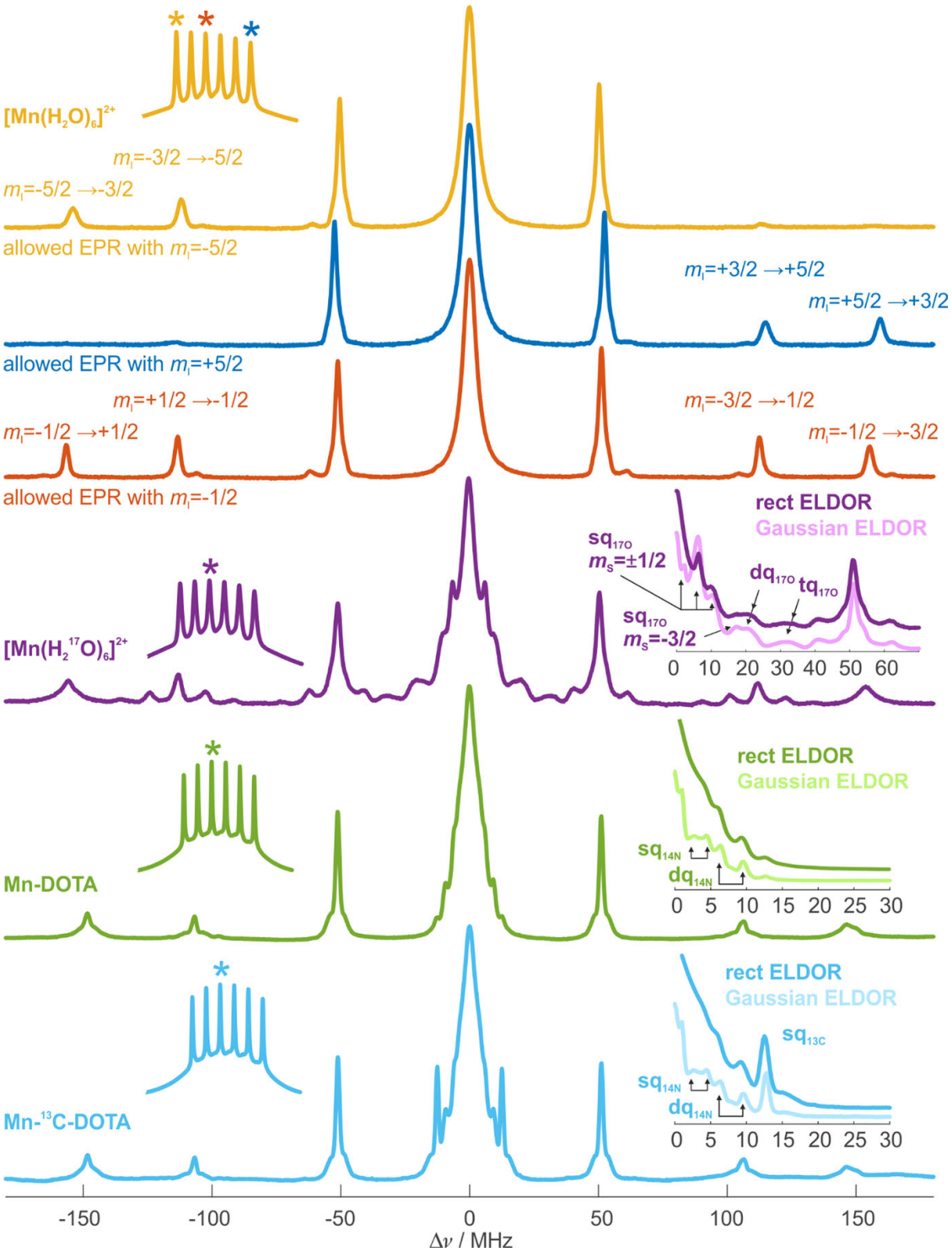

Fig. 2 Spectra from the top of figure: Q-band EDNMR of $[Mn(H_2O)_6]^{2+}$ at different magnetic fields (1st, 3rd and 6th hyperfine peak), $[Mn(H_2^{17}O)_6]^{2+}$, Mn–DOTA and Mn-^{13}C-DOTA (3rd hyperfine peak). Spectra were normalized to [0,1] and inverted. Echo-detected field-swept spectra are shown as *insets* on the *left* and expansions of the blind spot region with rectangular ($\omega_{ELD} = 1.2 \times 10^7$ rad s^{-1}) or Gaussian shaped ELDOR pulses ($\omega_{ELD} = 6.0 \times 10^6$ rad s^{-}1, *pale color*) are show as *insets* on the *right*. For the hexaaqua complex, forbidden transitions are labeled for different allowed EPR transitions ($\Delta m_S = \pm 1$ is omitted for sake of clarity). Strongly coupled ^{55}Mn signals appear around ±150 and ±110 MHz, whereas weakly coupled protons are centered around $|\pm\nu_{1H}| = 51$ MHz. Larmor frequencies of other relevant nuclei: $\nu_{17O} = 6.9$ MHz, $I = 5/2$; $\nu_{14N} = 3.7$ MHz, $I = 1$; $\nu_{13C} = 12.8$ MHz, $I = 1/2$ (color figure online)

the ^{17}O-labeled hexaaqua shows the broadest EDFS spectrum due to unresolved ^{17}O hyperfine couplings with FWHM = 2.4 mT for the 3rd hyperfine peak, whereas FWHM = 1.6 mT for the unlabeled hexaaqua complex. The EDFS of Mn–DOTA complexes are characterized by a smaller FWHM of 0.9 mT, which is expected, as the Mn–DOTA complexes have a smaller zero-field splitting compared to the hexaaqua complex [38].

The EDNMR spectra of the unlabeled hexaaqua complex were recorded at three different magnetic field positions (1st, 3rd and 6th hyperfine peak). Signals of the strongly coupled ^{55}Mn nucleus ($\nu_{55\mathrm{Mn}}$ = 12.7 MHz, $I = 5/2$) appear at approximately ±155 and ±115 MHz, respectively. As expected, the two signals at the right hand side and the left hand side of the EDNMR spectrum are centered at $|a_{\mathrm{iso}}|/2$, which yields an isotropic ^{55}Mn hyperfine coupling of $|a_{\mathrm{iso}}| = 269$ MHz. It should be noted that the isotropic hyperfine coupling of ^{55}Mn is known to be negative [39]. Throughout this article, absolute values are given for the hyperfine coupling as EDNMR spectra are not sensitive to the sign of the isotropic hyperfine coupling. If the magnetic field is set to one of the outer hyperfine peaks (yellow/1st or blue/2nd EDNMR spectra in Fig. 2), the EDNMR spectra become asymmetric with respect to the ^{55}Mn resonances. For outer hyperfine transitions, each allowed EPR transition ($\Delta m_{\mathrm{S}} = \pm 1$, $m_{\mathrm{I}} = -5/2$ or $\Delta m_{\mathrm{S}} = \pm 1$, $m_{\mathrm{I}} = +5/2$, yellow/1st and blue/2nd spectra in Fig. 2, respectively) is connected to two forbidden EDNMR transitions only. If the magnetic field is on resonant with one of the four inner hyperfine peaks, each allowed EPR transition is connected to four forbidden ^{55}Mn EDNMR transitions (red/3rd spectrum in Fig. 2). For a distinct labeling of the different forbidden transitions, the reader is referred to Fig. 2.

The splitting between the two ^{55}Mn resonances on each side of the EDNMR spectra is larger than the expected first order expression of $\Delta\nu = 2\nu_{55\mathrm{Mn}} = 26$ MHz for a strongly coupled ^{55}Mn nucleus. Sturgeon et al. used perturbation up to the third order to evaluate the splitting in their ^{55}Mn X-band ENDOR spectra [40]. As proposed in their study, the deviation of the splitting from $\Delta\nu = 2\nu_{55\mathrm{Mn}}$ decreases with higher microwave frequencies from 70% at Q-band ($\Delta\nu = 44$ MHz, as observed in this study) to 10% at W-band ($\Delta\nu = 77$ MHz where $\Delta\nu = 2\nu_{55\mathrm{Mn}} = 70$ MHz, Cox et al. [5]). In addition, the quadrupole interaction of the ^{55}Mn nucleus is also known to affect the position of the ^{55}Mn lines slightly [41].

In contrast to strongly coupled ^{55}Mn nuclei, weakly coupled ^{1}H nuclei, observed as signals at ca. ±51 MHz, are not subject to asymmetries depending on the magnetic field positions. This is because the hyperfine coupling of weakly coupled ^{1}H nuclei is smaller than the inhomogeneous EPR linewidth. As a consequence, the detection pulses excite both allowed EPR transitions simultaneously (e.g., $\Delta m_{\mathrm{S}} = \pm 1$, $m_{\mathrm{I}} = -1/2$ and $\Delta m_{\mathrm{S}} = \pm 1$, $m_{\mathrm{I}} = +1/2$), thus making the ^{1}H EDNMR spectrum symmetric around the central blind spot at all field positions.

The EDNMR spectrum of the ^{17}O-labeled hexaaqua complex in Fig. 2 (purple/4th spectrum) shows a more complex spectrum than the hexaaqua complex. Although the resonance frequencies of the ^{55}Mn sq EDNMR transitions at ±155 and ±115 MHz remain unchanged, many satellite transitions appear on both sides of the spectrum at the expense of ^{55}Mn sq signal intensity. A more detailed explanation is

given in Sect. 4.4 of this article. Additional signals close to the blind spot region belong to resonances from the ^{17}O nucleus ($\nu_{17O} = 6.9$ MHz, $I = 5/2$). The advantage of using a Gaussian shaped ELDOR pulse over a rectangular ELDOR pulse is illustrated in the inset, showing a close-up of the blind spot region of the ^{17}O-labeled hexaaqua complex. An intense signal close to ν_{17O} at 6.3 MHz, originating from 2nd shell ^{17}O nuclei, is visible in both cases. The deviation from ν_{17O} is most likely caused by a convolution with the function of the central blind spot. The signal at 9.9 MHz originates from 1st coordination sphere ^{17}O nuclei in the $m_S = -1/2$ manifold. The splitting to the matrix line is 3.7 MHz, which is half the ^{17}O hyperfine coupling reported in previous studies ($|a_{iso}| = 7.5$ MHz) [5, 42, 43]. The EDNMR signals of 1st coordination sphere ^{17}O nuclei in the $m_S = +1/2$ manifold are expected at approximately 2.5 MHz and are not resolved due to severe overlap with the blind spot. Although a 'signal' is visible at 2.3 MHz for Gaussian shaped ELDOR pulses, it is not possible to conclusively say if this is an actual signal of the ^{17}O nuclei or rather an artifact caused by Gaussian shaped ELDOR pulses, which is also visible in Fig. 1. The signals in the range around 20 MHz are difficult to analyze with rectangular ELDOR pulses. With Gaussian shaped ELDOR pulses it is clear however that two signals can be clearly distinguished. The first signal resonates at 17.3 MHz and stems from ^{17}O nuclear transitions in the $m_S = -3/2$ manifold. The signal at 20.3 MHz is assigned to a ^{17}O nuclear double quantum transition ($\Delta m_I = \pm 2$). To first order, double quantum resonances are centered at $2\nu_{17O}$ and split by $2A_{17O}$. The second double quantum signal is expected at approximately 7 MHz and therefore is most likely obscured by the more intense sq signals. The broad signal at 31.0 MHz is finally assigned to a ^{17}O nuclear triple quantum transition ($\Delta m_I = \pm 3$). Here, signals are expected to be centered at $3\nu_{17O}$ and split by $3A_{17O}$.

The surprisingly large intensity of nuclear double and even triple quantum transitions can be explained by evaluating the different contributions to the spin Hamiltonian. Firstly, ^{17}O is a high-spin nuclei with a relatively large quadrupole interaction of $e^2qQ/h = 7$ MHz and $\eta = 1$ [43]. This leads to larger off-diagonal elements in the spin Hamiltonian and therefore an increased level mixing of nuclear spin states and an increased transitions probability, I_f. This effect is increased at Q-band frequencies, as the quadrupole interaction, the principal values of the hyperfine tensor and the nuclear Zeeman interaction have very similar magnitudes [44, 45].

The last two spectra show Q-band EDNMR spectra of a Mn–DOTA complex, either unlabeled or partially ^{13}C-labeled (see Sect. 3.2 for more experimental details). Due to the smaller ^{55}Mn hyperfine coupling of $|a_{iso}| = 255$ MHz of Mn–DOTA, the ^{55}Mn resonances are centered around a slighter smaller frequency value. The signals at ±150 and ±110 MHz are broader than the ^{55}Mn signals of the hexaaqua complex, which is due to unresolved ^{55}Mn-^{14}N combination signals (see Sect. 4.3). The width of the proton signals of Mn–DOTA at ±51 MHz are clearly smaller than the proton signals of the hexaaqua complex, which is in agreement with ^{1}H-ENDOR [28]. The insets reveal many signals close to the blind spot region for both complexes. The signals at 2.7 and 4.4 MHz have been identified as sq EDNMR transitions of the ^{14}N nucleus ($\nu_{14N} = 3.7$ MHz, $I = 1$), as they are centered around the ν_{14N} Larmor frequency and split by 1.7 MHz, which is similar to reported values

for A_{14N} in Mn–DOTA systems [28, 38]. The signals appearing at 6.4 and 9.6 MHz are consequently assigned to ^{14}N dq EDNMR transitions. The peak at 12.8 MHz belongs to a sq transition of ^{13}C nuclei ($\nu_{13C} = 12.8$ MHz, $I = 1/2$). Interestingly, a signal with a much smaller intensity is also visible in the unlabeled sample at the same frequency. We assign this feature to natural abundance ^{13}C, which is plausible as firstly EDNMR is known to be sensitive enough to detect natural abundance ^{13}C [10], and secondly Mn–DOTA offers a very carbon rich environment. Q-band EDNMR was not able to resolve the rather large and recently reported ^{14}N quadrupole interaction ($e^2qQ/h = 4.5$ MHz) [28]. Just as in the case of ^{17}O, the ^{14}N quadrupole interaction is of comparable magnitude to the nuclear Zeeman interaction and the hyperfine interaction leading to strong mixing of nuclear spin states, which results in an increased forbidden transition probability, I_f.

4.3 Combination frequencies

Some nuclei exhibit a relatively small forbidden transition probability, I_f. ^{31}P ($\nu_{31P} = 20.8$ MHz, $I = 1/2$) for example, is a spin-1/2 nuclei with a reasonably large isotropic hyperfine coupling constant and a small dipolar hyperfine contribution for weakly coupled ligand ^{31}P nuclei in Mn^{2+} systems [11, 27]. Both features lead to a smaller I_f, which is disadvantageous for detecting these interactions using EDNMR. In some cases, especially at lower concentrations or in cases of poor ligand binding, it is therefore useful to use higher-powered ELDOR pulses to increase the intensity of the signals observed. Higher-powered ELDOR pulses, however, also lead to the appearance of combination frequencies involving the simultaneous excitation of two different nuclei ($\Delta m_S = \pm 1$, $\Delta m_{I,1} = \pm 1$, $\Delta m_{I,2} = \pm 1$). Combination frequencies have previously been observed at W-band frequencies [5, 8]. At Q-band, combination frequencies will be intrinsically more intense, as $I_f \propto 1/\nu_I^2$. In addition, more weakly coupled nuclear will approach the 'cancelation condition'; $A_I = 2\nu_I$. In this section we therefore include a more in-depth explanation of combination frequencies at Q-band, with reference to the systems presented in Fig. 2.

Figure 3 shows a spin-ladder diagram of an unpaired electron with $S = 1/2$ coupled to two nuclei with $I_1 = 1/2$ and $I_2 = 1/2$. In the diagram the first nuclei is strongly coupled with $A_1 < 0$ and $\gamma_{N,1} > 0$, in the same way that we have already seen for the central nuclear transition of ^{55}Mn. The second nucleus is weakly coupled with $A_2 > 0$ and $\gamma_{N,2} > 0$, as observed for a proton coupled to Mn^{2+} in all of the systems shown in Fig. 2. In such a case the spin Hamiltonian is defined as:

$$\mathcal{H} = \beta_e \mathcal{B}\}\mathcal{S}/h - \beta_{N,1} g_{N,1} \mathcal{B}\mathcal{S}/h + \mathcal{S}\mathcal{A}_1\mathcal{I}_1 - \beta_{N,2} g_{N,2} \mathcal{B}\mathcal{S}/h + \mathcal{S}\mathcal{A}_2\mathcal{I}_2. \quad (6)$$

Assuming the high-field approximation is valid for electron and nuclear Zeeman interactions, the frequencies of the allowed EPR transitions are given by:

$$\nu_{EPR\,|\,2,\beta} = E_{\alpha\beta\beta} - E_{\beta\beta\beta} = \nu_S + A_1/2 - A_2/2, \quad (7)$$

$$\nu_{EPR\,|\,2,\alpha} = E_{\alpha\beta\alpha} - E_{\beta\beta\alpha} = \nu_S + A_1/2 + A_2/2, \quad (8)$$

ν_S describes the Larmor frequency of the electron. In accordance with Fig. 3 two allowed EPR transitions are found, as for the strongly coupled nucleus I_1 only the

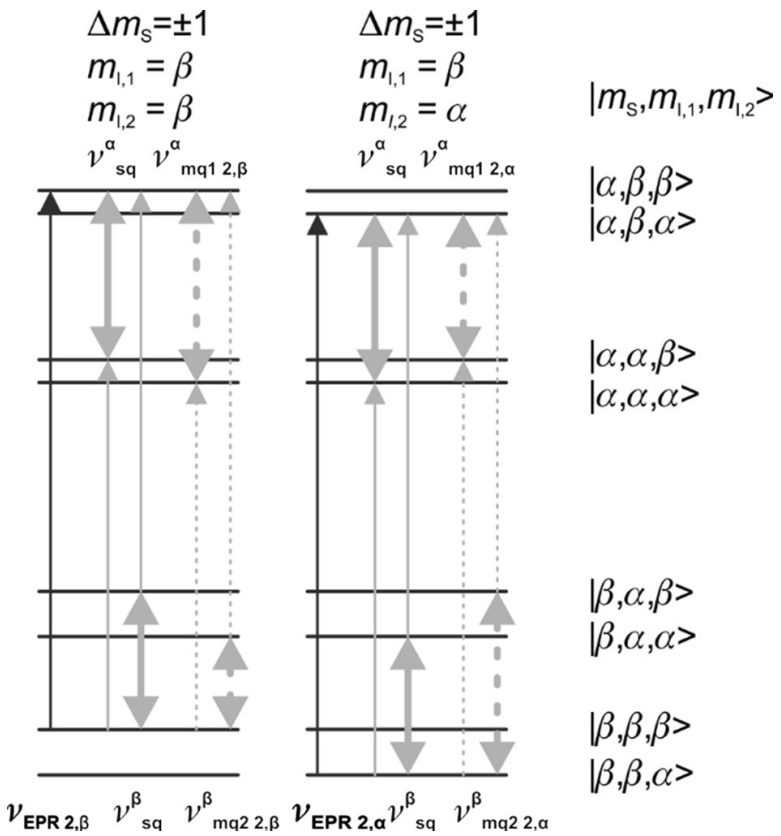

Fig. 3 Spin-ladder energy diagram of $S = 1/2$ coupled to two nuclei with $I_1 = 1/2$ and $I_2 = 1/2$. The first nuclei is strongly coupled ($A_1 < 0$ and $\gamma_{N,1} > 0$). As a consequence, a selective excitation of the allowed EPR transition with $\Delta m_S = \pm 1$, $\Delta m_{I,1} = \beta$ is possible. The second nuclei is weakly coupled with $A_2 > 0$ and $\gamma_{N,2} > 0$. Therefore, both allowed EPR transitions are excited simultaneously. *Black lines* allowed EPR transitions with either $m_{I,1} = \beta$, $m_{I,2} = \beta$ (*left*) or $m_{I,1} = \beta$, $m_{I,2} = \alpha$ (*right*). *Solid gray lines* EDNMR sq transitions with $\Delta m_S = \pm 1$, $\Delta m_{I,1} = \pm 1$ and $\Delta m_{I,2} = 0$. *Dotted gray lines* EDNMR mq transitions with $\Delta m_S = \pm 1$, $\Delta m_{I,1} = \pm 1$ and $\Delta m_{I,2} = \pm 1$. For all types of *lines*: *Thin lines* correspond to electronic transition frequencies (ca. 34 GHz at Q-band) whereas *bold lines* correspond to nuclear frequencies (MHz)

allowed EPR transition with $m_{I,1} = \beta$ is considered. In the following text, subscripted expressions describe the 'type' of transitions (EPR, sq, or mq) and to which allowed EPR transitions they are connected ($m_{I,2} = \beta$ or $m_{I,2} = \alpha$, see Fig. 3). Superscripted expressions describe the electron spin manifold from which the nuclear frequencies stem. For forbidden transitions of the type $\Delta m_S = \pm 1$, $\Delta m_{I,1} = \pm 1$ one finds:

$$\nu_{sq1\,|\,2,\beta} = E_{\alpha\alpha\beta} - E_{\beta\beta\beta} = \nu_S - \nu_{I,1} - A_2/2, \tag{9}$$

$$\nu_{sq2\,|\,2,\beta} = E_{\alpha\beta\beta} - E_{\beta\alpha\beta} = \nu_S + \nu_{I,1} - A_2/2, \tag{10}$$

$$\nu_{sq1\,|\,2,\alpha} = E_{\alpha\alpha\alpha} - E_{\beta\beta\alpha} = \nu_S - \nu_{I,1} + A_2/2, \tag{11}$$

$$\nu_{sq2\,|\,2,\alpha} = E_{\alpha\beta\alpha} - E_{\beta\alpha\alpha} = \nu_S + \nu_{I,1} + A_2/2. \tag{12}$$

Forbidden transitions of the type $\Delta m_S = \pm 1$, $\Delta m_{I,1} = \pm 1$, $\Delta m_{I,2} = \pm 1$ yield:

$$\nu_{mq1\,|\,2,\beta} = E_{\alpha\alpha\alpha} - E_{\beta\beta\beta} = \nu_S - \nu_{I,1} - \nu_{I,2}, \tag{13}$$

$$\nu_{\mathrm{mq2\,|\,2,}\beta} = E_{\alpha\beta\beta} - E_{\beta\alpha\alpha} = \nu_{\mathrm{S}} + \nu_{\mathrm{I,1}} + \nu_{\mathrm{I,2}}, \tag{14}$$

$$\nu_{\mathrm{mq1\,|\,2,}\alpha} = E_{\alpha\alpha\beta} - E_{\beta\beta\alpha} = \nu_{\mathrm{S}} - \nu_{\mathrm{I,1}} + \nu_{\mathrm{I,2}}, \tag{15}$$

$$\nu_{\mathrm{mq2\,|\,2,}\alpha} = E_{\alpha\beta\alpha} - E_{\beta\alpha\beta} = \nu_{\mathrm{S}} + \nu_{\mathrm{I,1}} - \nu_{\mathrm{I,2}}. \tag{16}$$

To find the nuclear/EDNMR frequencies, the frequencies of the corresponding allowed EPR transitions must be subtracted from the different forbidden transitions defined above:

$$\nu_{\mathrm{sq}}^{\alpha} = \nu_{\mathrm{sq1\,|\,2,}\beta} - \nu_{\mathrm{EPR\,|\,2,}\beta} = \nu_{\mathrm{sq1\,|\,2,}\alpha} - \nu_{\mathrm{EPR\,|\,2,}\alpha} = -\nu_{\mathrm{I,1}} - A_1/2, \tag{17}$$

$$\nu_{\mathrm{sq}}^{\beta} = \nu_{\mathrm{sq2\,|\,2,}\beta} - \nu_{\mathrm{EPR\,|\,2,}\beta} = \nu_{\mathrm{sq2\,|\,2,}\alpha} - \nu_{\mathrm{EPR\,|\,2,}\alpha} = \nu_{\mathrm{I,1}} - A_1/2. \tag{18}$$

These frequencies reflect the familiar strong coupling regime. However, in the case of Mn^{2+} these expressions are not valid as the large hyperfine coupling and the high-spin system mandate the use of higher order terms [40]. Nevertheless, they can be used to gain a more complete understanding of the combination peaks. The EDNMR frequencies of the combination peaks can be calculated by:

$$\begin{aligned}\nu_{\mathrm{mq1\,|\,2,}\beta}^{\alpha} = \nu_{\mathrm{mq1\,|\,2,}\beta} - \nu_{\mathrm{EPR\,|\,2,}\beta} &= -\nu_{\mathrm{I,1}} - A_1/2 - \nu_{\mathrm{I,2}} + A_2/2 \\ &= \nu_{\mathrm{sq}}^{\alpha} - \nu_{\mathrm{I,2}} + A_2/2,\end{aligned} \tag{19}$$

$$\begin{aligned}\nu_{\mathrm{mq2\,|\,2,}\beta}^{\beta} = \nu_{\mathrm{mq2\,|\,2,}\beta} - \nu_{\mathrm{EPR\,|\,2,}\beta} &= \nu_{\mathrm{I,1}} - A_1/2 + \nu_{\mathrm{I,2}} + A_2/2 \\ &= \nu_{\mathrm{sq}}^{\beta} + \nu_{\mathrm{I,2}} + A_2/2,\end{aligned} \tag{20}$$

$$\begin{aligned}\nu_{\mathrm{mq1\,|\,2,}\alpha}^{\alpha} = \nu_{\mathrm{mq1\,|\,2,}\alpha} - \nu_{\mathrm{EPR\,|\,2,}\alpha} &= -\nu_{\mathrm{I,1}} - A_1/2 + \nu_{\mathrm{I,2}} - A_2/2 \\ &= \nu_{\mathrm{sq}}^{\alpha} + \nu_{\mathrm{I,2}} - A_2/2,\end{aligned} \tag{21}$$

$$\begin{aligned}\nu_{\mathrm{mq2\,|\,2,}\alpha}^{\beta} = \nu_{\mathrm{mq2\,|\,2,}\alpha} - \nu_{\mathrm{EPR\,|\,2,}\alpha} &= \nu_{\mathrm{I,1}} - A_1/2 - \nu_{\mathrm{I,2}} - A_2/2 \\ &= \nu_{\mathrm{sq}}^{\beta} - \nu_{\mathrm{I,2}} - A_2/2.\end{aligned} \tag{22}$$

Equations (19–22) show that two combination frequencies are centered around each sq EDNMR transition, although it should be noted that these two combination frequencies are connected to different allowed EPR transitions ($\nu_{\mathrm{EPR|2,}\alpha}$ or $\nu_{\mathrm{EPR|2,}\beta}$). The combination frequencies of Eqs. (19) and (21) are centered around the sq EDNMR transition $\nu_{\mathrm{sq}}^{\alpha}$ and split by $2\nu_{\mathrm{I,2}} - A_2$. Combination frequencies of Eqs. (20) and (22) are centered around $\nu_{\mathrm{sq}}^{\beta}$ and split by $2\nu_{\mathrm{I,2}} + A_2$:

$$\Delta\nu_{1\,\mathrm{I1,I2}} = \nu_{\mathrm{mq2\,|\,2,}\beta}^{\beta} - \nu_{\mathrm{mq2\,|\,2,}\alpha}^{\beta} = 2\nu_{\mathrm{I,2}} + A_2, \tag{23}$$

$$\Delta\nu_{2\mathrm{I1,I2}} = \nu_{\mathrm{mq1\,|\,2,}\alpha}^{\alpha} - \nu_{\mathrm{mq1\,|\,2,}\beta}^{\alpha} = 2\nu_{\mathrm{I,2}} - A_2. \tag{24}$$

Figure 4 shows a series of Mn^{2+} Q-band EDNMR spectra recorded using higher powered ELDOR pulses to allow the combination frequencies of the type $\Delta m_{\mathrm{S}} = \pm 1$, $\Delta m_{\mathrm{I,1}} = \pm 1$, $\Delta m_{\mathrm{I,2}} = \pm 1$ or even $\Delta m_{\mathrm{S}} = \pm 1$, $\Delta m_{\mathrm{I,1}} = \pm 1$, $\Delta m_{\mathrm{I,2}} = \pm 2$ to be resolved. Only the left-hand side with the magnetic field set to the 3rd hyperfine peak is shown; here the $\Delta m_{\mathrm{S}} = \pm 1$, $m_{55\mathrm{Mn}} = -1/2 \leftrightarrow +1/2$ transitions are excited, which exhibit a narrower linewidth than the outer ^{55}Mn nuclear spin manifolds [25, 26]. For the unlabeled hexaaqua complex, four distinct

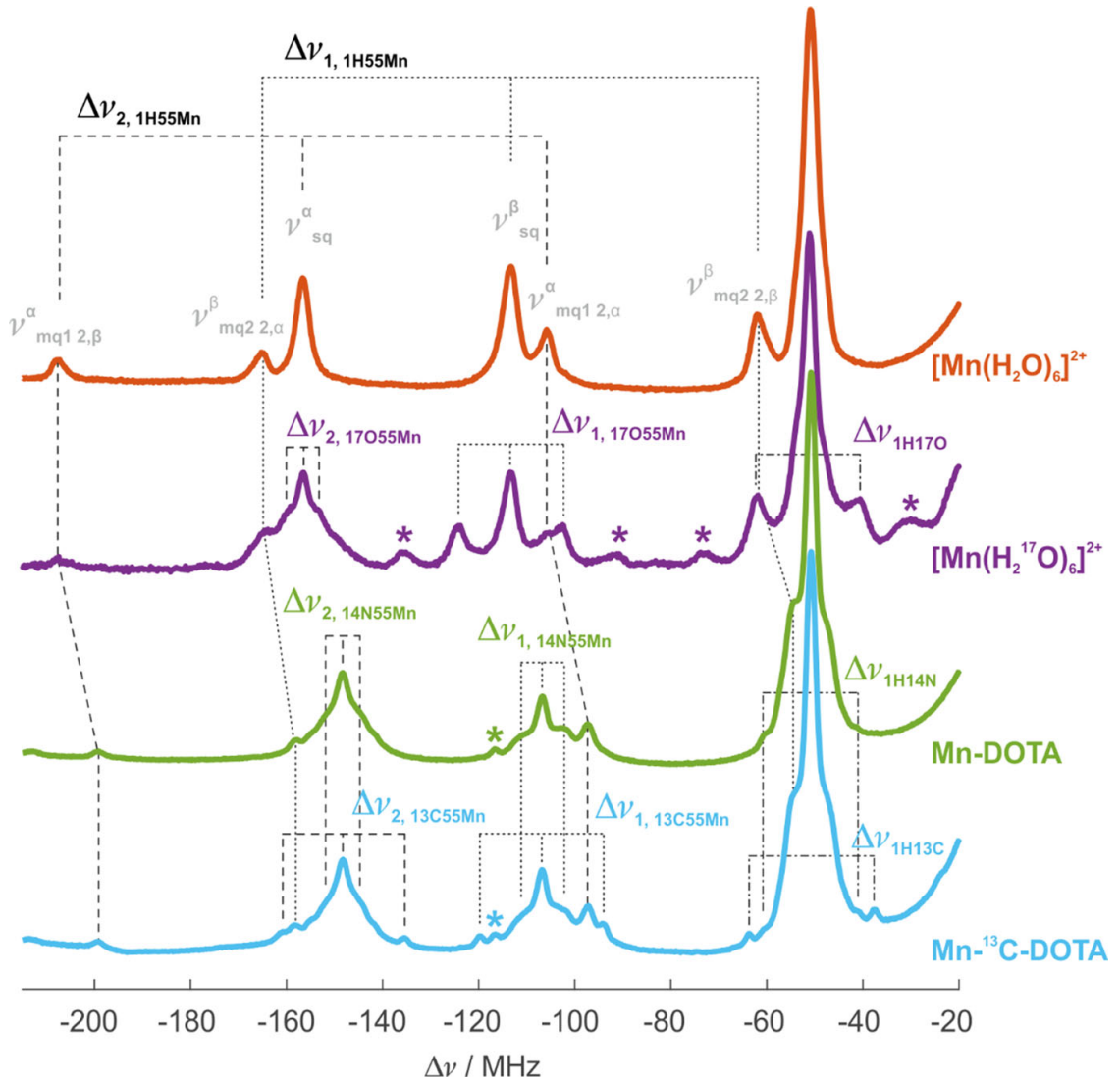

Fig. 4 Q-band *left-hand side* EDNMR spectra of $[Mn(H_2O)_6]^{2+}$ (*orange*), $[Mn(H_2^{17}O)_6]^{2+}$ (*purple*), Mn–DOTA (*green*) and Mn-^{13}C-DOTA (*blue*) with higher-powered ELDOR pulses ($\omega_{ELD} = 8.2 \times 10^7$ rad s^{-1}) to resolve various combination frequencies. ^{55}Mn signals appear around -150 and -110 MHz, whereas weakly coupled protons are centered around $-\nu_{1H} = -51$ MHz. Various combination frequencies of ^{1}H, ^{13}C, ^{14}N and ^{17}O with ^{55}Mn are visible, which are centered around one of the ^{55}Mn sq signals. *Dotted lines* combination frequencies centered around the ^{55}Mn signal at -110 MHz (ν^{β}_{sq}). *Dashed lines* combination frequencies centered around the ^{55}Mn signal at -150 MHz (ν^{α}_{sq}). *Dash-dotted line* combination frequencies of ^{13}C, ^{14}N and ^{17}O with ^{1}H, centered around $-\nu_{1H} = -51$ MHz. The expressions above the EDNMR spectrum of $[Mn(H_2O)_6]^{2+}$ correspond to transitions shown in Fig. 3 and the analytical expressions given in Eqs. (19)–(24), although the analytical expressions do not take into account high-spin effects and higher order effects that are necessary to account for the large ^{55}Mn hyperfine coupling [40]. *Asterisks* denote combination frequencies of the type $\Delta m_S = \pm 1$, $\Delta m_{I,1} = \pm 1$, $\Delta m_{I,2} = \pm 2$. Larmor frequencies of other relevant nuclei: $\nu_{17O} = 6.9$ MHz, $I = 5/2$; $\nu_{14N} = 3.7$ MHz, $I = 1$; $\nu_{13C} = 12.8$ MHz, $I = 1/2$ (color figure online)

additional signals are visible which correspond to the four combination frequencies given in Eqs. (19)–(22) and which are drawn in Fig. 3. The signals marked with $\Delta\nu_{1,\,1H55Mn}$ are centered almost perfectly around the ^{55}Mn sq transition at -113.3 MHz (the experimentally measured center between the signals was: $\tilde{\nu}_{1,\,1H55Mn} = 113.4$ MHz, with a frequency separation between the peaks of: $\Delta\nu_{1,1H55Mn} = 103.0$ MHz). From this point on $\tilde{\nu}$ notates the experimentally

measured center frequency between two peaks and $\Delta\nu$ the frequency separation (splitting) between them. The signals marked with $\Delta\nu_{2,\ 1H55Mn}$, on the other hand, are centered around the ^{55}Mn sq transition at -156.6 MHz ($\tilde{\nu}_{2,\ 1H55Mn} = -156.6$ MHz, $\Delta\nu_{2,\ 1H55Mn} = 101.6$ MHz).

As predicted by Eqs. (19–22), the splitting of $\Delta\nu_{1,\ 1H55Mn}$ is slightly larger, which is due to additive hyperfine coupling. The difference of ca. 2 MHz between $\Delta\nu_{1,\ 1H55Mn}$ and $\Delta\nu_{2,\ 1H55Mn}$ is not an error of the experiment. Indeed, it was reproduced with different samples at high accuracy. ^{1}H-^{55}Mn combination frequencies are also visible in all other samples, although they shift to smaller frequencies for Mn–DOTA complexes, as here $|a_{iso}|$ gets smaller and correspondingly the ^{55}Mn sq peaks shift to smaller absolute frequencies (-148.3 and -106.7 MHz). For Mn–DOTA complexes it was found that: $\tilde{\nu}_{1,\ 1H55Mn} = -106.0$ MHz, $\Delta\nu_{1,\ 1H55Mn} = 103.8$ MHz and $\tilde{\nu}_{2,\ 1H55Mn} = -148.3$ MHz, $\Delta\nu_{2,\ 1H55Mn} = 102.0$ MHz.

It should be noted, that ^{1}H-^{55}Mn combination frequencies are also centered around the ^{1}H sq peaks. Equations (19–22) show that two combination frequencies which are centered around one sq transition are connected to different allowed EPR transitions ($\nu_{EPR|2,\alpha}$ or $\nu_{EPR|2,\beta}$). Therefore, combination frequencies centered around a ^{1}H sq line must be connected to allowed EPR transitions within different nuclear ^{55}Mn spin manifolds. As the ^{55}Mn nucleus is, however, strongly coupled, only one allowed EPR transition within a specific nuclear ^{55}Mn spin manifold can be excited at a time (e.g., $m_{I,1} = \beta$ for the theoretical model presented in this section). As a consequence, only 'one half' of the combination frequencies that are centered around a ^{1}H sq line are excited. The 'second half' will get excited once the allowed EPR transition in the other nuclear spin manifold of the strongly coupled nuclei gets excited (e.g., $m_{I,1} = \alpha$. For Mn^{2+} this corresponds to moving the magnetic field from the third to the fourth hyperfine peak).

Due to strong level mixing of nuclear spin states, the ^{17}O-labeled hexaaqua complex is characterized by very intense ^{17}O-^{55}Mn and ^{1}H-^{17}O combination frequencies. For ^{17}O-^{55}Mn, only the splitting with the additive hyperfine coupling centered around -113.3 MHz is clearly resolved ($\Delta\nu_{1,\ 17O55Mn} = 21.7$ MHz, $\tilde{\nu}_{1,\ 17O55Mn} = -113.4$ MHz). The splitting with the subtractive hyperfine coupling is not clearly visible, but rather leads to a broadening of the ^{55}Mn sq peak at -156.4 MHz. ^{1}H-^{17}O combination peaks are centered around the proton signal at -51.3 MHz ($\Delta\nu_{1H17O} = 20.6$ MHz, $\tilde{\nu}_{1H17O} = -50.9$ MHz). As one of the ^{1}H-^{17}O combination signals overlaps with a ^{1}H-^{55}Mn signal, this may lead to some uncertainties in the exact frequency determination. ^{17}O $\Delta\nu$ values are, however, in very good agreement with the theoretical value of $2\nu_{17O} + A_{17O} = 21.3$ MHz.

The EDNMR spectrum of Mn–DOTA exhibits combination signals from ^{1}H-^{55}Mn, ^{14}N-^{55}Mn and ^{1}H-^{14}N. Due to the small ^{14}N Larmor frequency ($\nu_{14N} = 3.7$ MHz, $I = 1$), the ^{14}N-^{55}Mn and ^{1}H-^{14}N combination signals are not clearly resolved and lead to an apparent line broadening of the ^{55}Mn sq signals (and to some extent to broadening of the ^{1}H signals). The signals of the splitting with the additive hyperfine coupling can be roughly estimated to $\Delta\nu_{1,\ 14N55Mn} = 8.6$ MHz, $\tilde{\nu}_{1,\ 14N55Mn} = -106.7$ MHz. The experimental splitting is in good agreement with the expected value of $2\nu_{14N} + A_{14N} = 9.1$ MHz. Upon closer investigation, two

satellites signals, centered around the proton signal at −50.8 MHz become visible. We attribute these satellites signals to combinations frequencies of the type $\Delta m_S = \pm 1$, $\Delta m_{I,1} = \pm 1$, $\Delta m_{I,2} = \pm 2$ as they agree well with the expected value of $4\nu_{14N} + 2A_{14N} = 18.2$ MHz ($\Delta\nu_{1H14N} = 19.0$ MHz, $\tilde{\nu}_{1H14N} = -50.9$ MHz).

In the EDNMR spectrum of Mn-^{13}C-DOTA, ^{13}C-^{55}Mn and ^{1}H-^{13}C combination frequencies are clearly visible. As the Larmor frequency of ^{13}C is relatively large, the additive ($\Delta\nu_{1,\ 13C55Mn}$) and subtractive splitting ($\Delta\nu_{2,\ 13C55Mn}$) are both clearly resolved. The additive splitting is centered around the ^{55}Mn sq transition at −106.9 MHz ($\Delta\nu_{1,\ 13C55Mn} = 25.8$ MHz, $\tilde{\nu}_{1,\ 17O55Mn} = -106.9$ MHz), whereas the subtractive splitting is centered around the ^{55}Mn sq transition at −148.3 MHz ($\Delta\nu_{2,\ 13C55Mn} = 25.2$ MHz, $\tilde{\nu}_{2,\ 17O55Mn} = -148.2$ MHz). ^{1}H-^{13}C combination frequencies are centered around the proton signals at −50.8 MHz ($\Delta\nu_{1H13C} = 26.0$ MHz, $\tilde{\nu}_{1H13C} = -50.7$ MHz).

Signals marked with an asterisk were assigned to transitions of the type $\Delta m_S = \pm 1$, $\Delta m_{I,1} = \pm 1$ and $\Delta m_{I,2} = \pm 2$. All these signals match the expected value of $4\nu_I + 2A_I$ rather well.

4.4 EDNMR versus Mims ENDOR at Q-band

^{1}H and ^{14}N hyperfine interactions of Gd-DOTA and Mn–DOTA were recently investigated with pulsed ENDOR studies at W-band frequencies to draw conclusions about the electron spin delocalization over ligand nuclei [28, 46]. In the following section, we evaluate the ^{13}C-hyperfine interaction of Mn-^{13}C-DOTA using Mims ENDOR with variable tau (τ) values and an EDNMR experiment.

Figure 5 shows a series of Mims ENDOR spectra with different τ values compared to a Q-band ^{13}C-EDNMR spectrum. Although EDNMR is more sensitive than ENDOR, information about the spectral line shape is lost in EDNMR, as the canonical orientations (the turning points of the Pake pattern) exhibit a zero transition probability for the forbidden transitions. The disadvantage of Mims ENDOR are blind spots that are defined by an oscillatory function of the type $\sin^2(\pi A\tau)$, where A is the hyperfine coupling and τ is the first delay time used in the Mims ENDOR pulse sequence. The Mims ENDOR spectrum collected with $\tau = 500$ ns is characterized by a rather broad central blind spot. Other blind spots do not distort the intense signals of the nuclear frequencies in the two central electron spin manifolds. As a consequence, the flanks of the signals at ±0.3 MHz are reminiscent as edges of a smeared out ENDOR Pake pattern. The signal at −1 MHz is attributed to nuclear transitions associated with the outer $m_S = -3/2$ electron spin manifold. Upon increasing τ, more intensity starts to build up around $\nu_{nuc} - \nu_{13C} = 0$ MHz. Information about the spectral line shape is, however, lost, as now the periodic blind spots are closer together with increasing τ.

To support our experimental results, we performed DFT calculations on a Mn–DOTA complex (see Sect. 3.3 for more details). The calculations yielded small hyperfine couplings, dominated by a dipolar hyperfine coupling of $T = 0.50$–0.65 MHz and an isotropic contribution close to zero (see Fig. 5 right and legend for more information). The deviations from an axial hyperfine tensor were rather small ($\rho \approx 0.05$, ρ denotes the rhombic component of the hyperfine

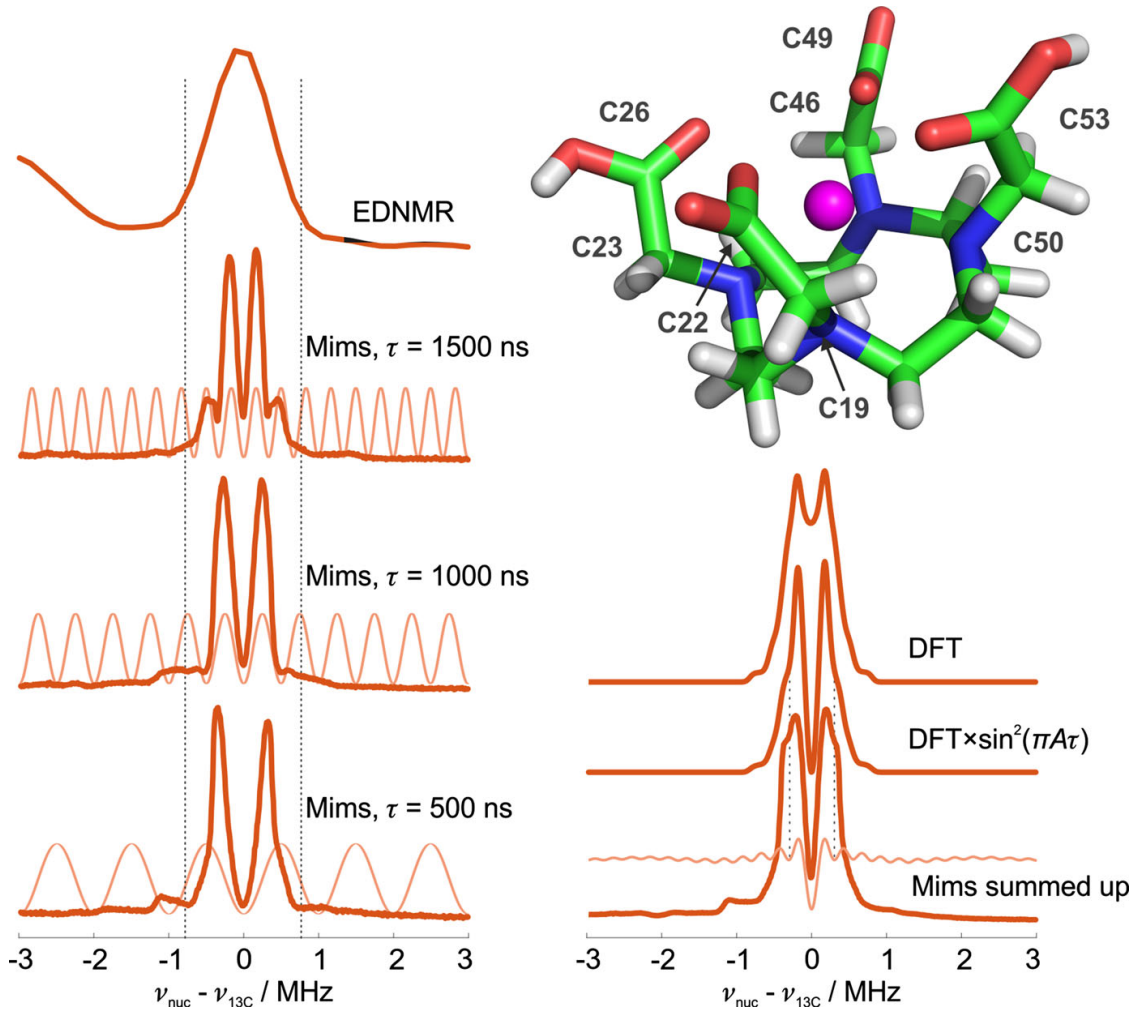

Fig. 5 *Left* Comparison of the ^{13}C region of a Q-band EDNMR spectrum of Mn-^{13}C-DOTA with ^{13}C-Mims ENDOR recorded on the same compound using different τ values. Mims ENDOR blind spot functions of the type $\sin^2(\pi A\tau) = \sin^2(\pi(2(\nu_{\mathrm{nuc}} - \nu_{13\mathrm{C}}))\tau)$ are represented as *pale lines*. *Top right* Crystal structure of Mn–DOTA [36]. The ^{13}C-labeled carbon atoms as used in this study are marked. *Bottom right* Simulated ENDOR spectrum ($S = 1/2$) using the EasySpin toolbox [47] with parameters obtained from DFT calculations on the crystal structure (*top trace*) compared with a summed Mims ENDOR versus tau (τ) experiment (*bottom trace*). The *spectrum* in the *middle* represents the simulated spectrum multiplied with the sum of the Mims blind spot functions used in the Mims ENDOR vs tau experiment. The 'dent' in the experimentally recorded Mims ENDOR spectrum at ±0.25 MHz comes from incomplete averaging of the blind spots. The sum of the Mims ENDOR blind spot functions are plotted as a *pale line*. Hyperfine values obtained from DFT calculations ($[a_{\mathrm{iso}}, T]$) for the labeled ^{13}C positions are: C19,C46 [−0.13, 0.65], C22, C49 [0.24, 0.79], C23, C50 [−0.05, 0.58], C26, C53 [0.09, 0.50] (color figure online)

tensor). Based on the hyperfine values obtained from DFT calculations an ENDOR spectrum was simulated using the EasySpin toolbox [47] (top spectra on the right side of Fig. 5). The simulated ENDOR spectrum was compared to the sum of the experimentally recorded ENDOR spectra (bottom trace of Fig. 5). The sum of the experimental ENDOR spectra contains artifacts from an incomplete blind spot averaging, as can be seen when examining the sum of the Mims ENDOR blind spot functions (pale lines in Fig. 5). In addition, the sum of the experimental ENDOR spectra also contains a central blind spot. To compare the experimental data to the simulated data the calculated DFT spectrum was multiplied with the sum of the

Mims ENDOR blind spot functions corresponding to the experimental data sets measured. The resulting spectrum is shown as the middle spectrum in Fig. 5 on the right side. The line shape is now much more akin to the sum of the experimentally recorded spectra shown at the bottom right of Fig. 5.

It should be noted that multiplication of the sum of the Mims blind spot functions (suppression function) with the calculated DFT spectrum is a simplified assumption: The suppression function is always zero at center frequency and so will be the new function after multiplication. This is, however, clearly not correct when looking at the sum of the experimentally recorded Mims ENDOR with different τ values, shown as the bottom right trace in Fig. 5.

5 Discussion

Q-band EDNMR has proven to be a useful technique for detecting nuclear frequencies within Manganese(II) systems and will also be applicable to many other spin active systems. Some points are, however, important to know when recording Q-band EDNMR spectra for low-γ nuclei. Firstly; the use of Gaussian ELDOR pulses is very beneficial, as it leads to a narrowing of the central blind spot while maintaining a similar intensity of the forbidden transitions (6th and 7th spectra in Fig. 1). Secondly, soft detection pulses should be used to further minimize the width of the central blind spot. In this way, the problem of low-γ nuclei being obscured by the central blind spot can be alleviated to some extent.

A problem that is, however, harder to mitigate, is the decreased resolution between nuclear Larmor frequencies of different nuclei at Q-band fields and frequencies. Here, the only solution is a careful planning of sample preparation to remove any nuclei that might overlap with the desired region of study (e.g., substitution of ^{23}Na buffer components with ^{40}K when investigating ^{13}C resonances with Q-band EDNMR).

In addition a very complicated spectrum is expected when ^{14}N and ^{17}O are present at the same time. Both nuclei have a small Larmor frequency ($\nu_{14N} = 3.7$ MHz and $\nu_{17O} = 6.9$ MHz) but relatively large quadrupole interactions, which leads to intense dq, tq and mq transitions, that are very difficult to disentangle and interpret accurately due to severe overlap of different signals. For ^{14}N and ^{17}O, combination frequencies are visible, even when using relatively low powered ELDOR pulses. In addition, care has to be taken when analysing the line width of sq transitions, as the sq peaks may be broadened by combination frequencies (e.g., ^{55}Mn).

Certain aspects, such as a low concentration or small binding affinity may mandate the use of higher powered ELDOR pulses to increase the EDNMR signal observed. At Q-band frequencies, this can lead to the appearance of relatively intense combination frequencies, which can easily be misinterpreted as sq signals of other nuclei. Using the first order expressions given in Eqs. (19–24), we were able to assign all additional signals when using higher powered ELDOR pulses for the four systems studied in this work. In addition, combination frequencies can give an estimation of the magnitude of the hyperfine coupling if analyzed correctly. It is

noted, that the first order equations in Sect. 4.3 do not reflect a correct physical description as they lack the pseudosecular part of the hyperfine coupling and high-spin interactions from the Mn^{2+} electron and ^{55}Mn nuclear spin. However, they still proved useful in identifying the different combination frequencies present. The underlying physical mechanism for the appearance of the fairly intense combination frequencies remains unknown. It is noted, that for most systems with g-values in the region of $g = 2$, Q-band EDNMR is most likely the useful lower limit in terms of microwave frequencies when investigating low-γ nuclei ($\nu_{14N} = 1.1$ MHz at X-band). For these systems at X-band, the blind spot separation and the resolution of nuclear Larmor frequencies will get significantly worse. Furthermore, even more intense dq, tq and even mq are expected for some nuclei; for example, for ^{14}N and ^{17}O the cancelation condition is perfectly fulfilled for certain orientations.

The acquisition time for each EDNMR spectra shown in this work was around 20 min. To achieve a similar signal-to-noise for sub-mM samples (e.g., 0.2 mM), the acquisition time would be around 2000 min ($\approx$30 h). The acquisition time can be reduced using less selective detection pulses and by constraining the frequency range to one side of the EDNMR spectrum of the nuclei of interest. Therefore, EDNMR spectra for a 0.2 mM sample with a good signal-to-noise ratio and a sufficient resolution are obtainable in $\approx$3 h.

Complete characterization of the ^{13}C hyperfine coupling of Mn-^{13}C-DOTA with Mims ENDOR was difficult, as the hyperfine couplings are rather small and most of the intensity occurs around ν_0. In addition, Mims ENDOR spectra could not be freed completely of the central blind spot, even with the collection and summation of data using different τ values. The experimentally recorded summed Mims versus tau spectrum is, however, in good agreement with the blind spot corrected EasySpin simulation using EPR parameters obtained from DFT calculations on the crystal structure of the complex: The maxima at $\pm$0.2 MHz coincide. So does the width of simulated and experimental spectrum and the shape at the flanks of the two intense signals at $\pm$0.5 MHz. As expected, the electron spin delocalization over ^{13}C ligand nuclei is, therefore, negligibly small. The two small features in the simulated spectra at $\pm$0.75 MHz could not be identified in the experimental spectrum, but may not be observed due to incomplete cancelation of the experimental blind spots. The width of the EDNMR spectrum and the Mims ENDOR spectrum with $\tau = 500$ ns is also very similar, indicating that (1) EDNMR can be used to constrain the magnitude of the hyperfine coupling constant if (2) the EDNMR linewidth is not broadened by to short detection pulses, too highly powered ELDOR pulses, or magnetization transfer artifacts due to too long ELDOR pulses (see Fig. 1).

6 Conclusion

Q-band EDNMR has been shown to be a valuable method to detect nuclear frequencies of low-γ with nuclear frequencies of 2.6 MHz upwards. Although the principal values of the hyperfine tensor could not be determined due to vanishingly small transition probabilities at the canonical orientations, estimations of the magnitude of the hyperfine coupling could be determined from dq (^{14}N) or resolved

sq (^{17}O) splittings. For our Mn^{2+} systems, highly selective detection pulses (400–800 or 200–400 ns) and an ELDOR pulse with an amplitude of $\omega_{ELD} \approx 1.0 \times 10^7$ rad s^{-1} gave the best results in terms of balancing signal intensity with a narrow central blind spot. An advantage of Q-band EDNMR over higher frequencies is its high sensitivity, as the transition probability of the forbidden transitions upon which the technique relies is intrinsically higher than at higher microwave frequencies. This can be a particular advantage when performing 2D-experiments such as THYCOS [12] or 2D-EDNMR [14], e.g., between ^{13}C and ^{31}P.

Acknowledgements This work was supported by the Deutsche Forschungsgemeinschaft (CRC 902—Molecular Principles of RNA-based Regulation). AMB acknowledges the Goethe International (GOIN) postdoctoral fellowship program and the Royal Society—EPSRC Dorothy Hodgkin fellowship program for generous support. We are grateful to Prof. Christiane Timmel and Dr William Myers at the Centre of Advanced Electron Spin Resonance (CAESR), Oxford University for access to their facilities for some of the aforementioned experiments.

References

1. P. Schosseler, T. Wacker, A. Schweiger, Chem. Phys. Lett. **224**, 319 (1994)
2. G. Jeschke, H.W. Spiess, Chem. Phys. Lett. **293**, 9 (1998)
3. H. Mino, T. Ono, Appl. Magn. Reson. **23**, 571 (2003)
4. L. Kulik, B. Epel, J. Messinger, W. Lubitz, Photosynth. Res. **84**, 347 (2005)
5. N. Cox, W. Lubitz, A. Savitsky, Mol. Phys. **111**, 2788 (2013)
6. N. Cox, A. Nalepa, M. E. Pandelia, W. Lubitz, A. Savitsky, in *Methods Enzymol.*, 1st edn. (Elsevier Inc., 2015), pp. 211–249
7. D. Goldfarb, eMagRes **6**, 101 (2017)
8. N. Cox, A. Nalepa, W. Lubitz, A. Savitsky, J. Magn. Reson. **280**, 63 (2017)
9. S. Un, Inorg. Chem. **52**, 3803 (2013)
10. E.M. Bruch, M.T. Warner, S. Thomine, L.C. Tabares, S. Un, J. Phys. Chem. B **119**, 13515 (2015)
11. S. Un, E.M. Bruch, Inorg. Chem. **54**, 10422 (2015)
12. A. Potapov, B. Epel, D. Goldfarb, J. Chem. Phys. **128**, 052320/1–052320/10 (2008)
13. M. Florent, I. Kaminker, V. Nagarajan, D. Goldfarb, J. Magn. Reson. **210**, 192 (2011)
14. I. Kaminker, T.D. Wilson, M.G. Savelieff, Y. Hovav, H. Zimmermann, Y. Lu, D. Goldfarb, J. Magn. Reson. **240**, 77 (2014)
15. M. Ramirez Cohen, N. Mendelman, M. Radoul, T.D. Wilson, M.G. Savelieff, H. Zimmermann, I. Kaminker, A. Feintuch, Y. Lu, D. Goldfarb, Inorg. Chem. **56**, 6163 (2017)
16. L. Rapatskiy, N. Cox, A. Savitsky, W.M. Ames, J. Sander, M.M. Nowaczyk, M. Rögner, A. Boussac, F. Neese, J. Messinger, W. Lubitz, J. Am. Chem. Soc. **134**, 16619 (2012)
17. A. Nalepa, K. Möbius, W. Lubitz, A. Savitsky, J. Magn. Reson. **242**, 203 (2014)
18. M. Fittipaldi, I. García-Rubio, F. Trandafir, I. Gromov, A. Schweiger, A. Bouwen, S. Van Doorslaer, J. Phys. Chem. B **112**, 3859 (2008)
19. S. Zamani, V. Meynen, A.-M. Hanu, M. Mertens, E. Popovici, S. Van Doorslaer, P. Cool, Phys. Chem. Chem. Phys. **11**, 5823 (2009)
20. N.V. Nagy, S. Van Doorslaer, T. Szabó-Plánka, S. Van Rompaey, A. Hamza, F. Fülöp, G.K. Tóth, A. Rockenbauer, Inorg. Chem. **51**, 1386 (2012)
21. M. Flores, A.G. Agrawal, M. Van Gastel, W. Gärtner, W. Lubitz, J. Am. Chem. Soc. **130**, 2402 (2008)
22. S. Van Doorslaer, E. Vinck, Phys. Chem. Chem. Phys. **9**, 4620 (2007)
23. A. Aliabadi, R. Zaripov, K. Salikhov, V. Voronkova, E. Vavilova, M.A. Abdulmalic, T. Rueffer, B. Buechner, V. Kataev, J. Phys. Chem. B **119**, 13762 (2015)
24. A. Schweiger, G. Jeschke, *Principles of Pulse Electron Paramagnetic Resonance* (Oxford University Press, Oxford, 2001)

25. B. Bleaney, R.S. Rubins, Proc. Phys. Soc. **77**, 103 (1961)
26. E. Meirovitch, R. Poupko, J. Phys. Chem. **82**, 1920 (1978)
27. O. Schiemann, R. Carmieli, D. Goldfarb, Appl. Magn. Reson. **31**, 543 (2007)
28. K. Keller, M. Zalibera, M. Qi, V. Koch, J. Wegner, H. Hintz, A. Godt, G. Jeschke, A. Savitsky, M. Yulikov, Phys. Chem. Chem. Phys. **18**, 25120 (2016)
29. A. Collauto, S. Mishra, A. Litvinov, H.S. Mchaourab, D. Goldfarb, Structure **25**, 1264 (2017)
30. J.F. Desreux, Inorg. Chem. **19**, 1319 (1980)
31. L. Lumata, M. Merritt, C. Malloy, A.D. Sherry, Z. Kovács, Appl. Magn. Reson. **43**, 69 (2012)
32. B. Epel, D. Arieli, D. Baute, D. Goldfarb, J. Magn. Reson. **164**, 78 (2003)
33. F. Neese, Wiley interdiscip. Rev. Comput. Mol. Sci. **2**, 73 (2012)
34. C. Adamo, V. Barone, J. Chem. Phys. **110**, 6158 (1999)
35. V. Barone, M. Cossi, J. Phys. Chem. A **102**, 1995 (1998)
36. S. Wang, T.D. Westmoreland, Inorg. Chem. **48**, 719 (2009)
37. T. Wacker, G.A. Sierra, A. Schweiger, Isr. J. Chem. **32**, 305 (1992)
38. H.Y. Vincent Ching, P. Demay-Drouhard, H.C. Bertrand, C. Policar, L.C. Tabares, S. Un, Phys. Chem. Chem. Phys. **17**, 23368 (2015)
39. S. Sinnecker, F. Neese, L. Noodleman, W. Lubitz, J. Am. Chem. Soc. **126**, 2613 (2004)
40. B.E. Sturgeon, J.A. Ball, D.W. Randall, R.D. Britt, J. Phys. Chem. **98**, 12871 (1994)
41. P. Manikandan, R. Carmieli, T. Shane, A.J. Kalb, D. Goldfarb, J. Am. Chem. Soc. **122**, 3488 (2000)
42. X. Tan, M. Bernardo, H. Thomann, C.P. Scholes, J. Chem. Phys. **102**, 2675 (1995)
43. D. Baute, D. Goldfarb, J. Phys. Chem. A **109**, 7865 (2005)
44. F.E. Mabbs, D. Collison, *Electron Paramagnetic Resonance of d Transition Metal Compounds*. Studies in Inorganic Chemistry series, Chap. 6 (Elsevier, 1992), pp. 189–217
45. H.L. Flanagan, D.J. Singel, J. Chem. Phys. **87**, 5605–5616 (1987)
46. A. Collauto, A. Feintuch, M. Qi, A. Godt, T. Meade, D. Goldfarb, J. Magn. Reson. **263**, 156 (2016)
47. S. Stoll, A. Schweiger, J. Magn. Reson. **178**, 42 (2006)

Journal of Magnetic Resonance 303 (2019) 105–114

Contents lists available at ScienceDirect

Journal of Magnetic Resonance

journal homepage: www.elsevier.com/locate/jmr

Binding of tetracycline to its aptamer determined by 2D-correlated Mn^{2+} hyperfine spectroscopy

Thilo Hetzke [a], Alice M. Bowen [b], Marc Vogel [c], Maximilian Gauger [a], Beatrix Suess [c], Thomas F. Prisner [a,*]

[a] Institute of Physical and Theoretical Chemistry and Center of Biomolecular Magnetic Resonance, Goethe University Frankfurt, Frankfurt am Main, Germany
[b] Center for Advanced Electron Spin Resonance (CAESR), Inorganic Chemistry Laboratory, Department of Chemistry, University of Oxford, Oxford, United Kingdom
[c] Department of Biology, Technical University of Darmstadt, Darmstadt, Germany

ARTICLE INFO

Article history:
Received 13 March 2019
Revised 16 April 2019
Accepted 17 April 2019

Keywords:
Tetracycline aptamer
Metal binding
Mn^{2+} ions
Hyperfine spectroscopy
2D ELDOR-detected NMR
THYCOS

ABSTRACT

The tetracycline-binding RNA aptamer (TC-aptamer) binds its cognate ligand the antibiotic tetracycline (TC) via a Mg^{2+} or Mn^{2+} ion with high affinity at high divalent metal ion concentrations ($K_D = 800$ pM, $\geqslant 10$ mM). These concentrations lie above the physiological divalent metal ion concentration of ca. 1 mM and it is known from literature, that the binding affinity decreases upon decreasing the divalent metal ion concentration. This work uses a Mn^{2+} concentration of 1 mM and 1D-hyperfine experiments reveal two pronounced ^{31}P couplings from the RNA besides the ^{13}C signal of ^{13}C-labeled TC. From these 1D-hyperfine data alone, however, no conclusions can be drawn on the binding of TC. Either TC may bind via Mn^{2+} to the aptamer or TC may form a free Mn-TC complex and some Mn^{2+} also binds to the aptamer. In this work, we show using 2D-correlated hyperfine spectroscopy at Q-band frequencies (34 GHz), that the ^{13}C and ^{31}P signals can be correlated; thus arising from a single species. We use THYCOS (triple hyperfine correlation spectroscopy) and 2D ELDOR-detected NMR (2D electron electron double resonance detected NMR) for this purpose showing that they are suitable techniques to correlate two different nuclear spin species (^{13}C and ^{31}P) on two different molecules (RNA and TC) to the same electron spin (Mn^{2+}). Out of the two observed ^{31}P-hyperfine couplings, only one shows a clear correlation to ^{13}C. Although THYCOS and 2D EDNMR yield identical results, 2D EDNMR is far more sensitive. THYCOS spectra needed a time factor of $\times 20$ in comparison to 2D EDNMR to achieve a comparable signal-to-noise.

1. Introduction

RNA aptamers describe a class of typically short RNA molecules, that bind a specific small molecule with high affinity and that have potential applications in diagnostic and therapeutic medicine [1]. The tetracycline-binding RNA aptamer (TC-aptamer) was identified by SELEX (systematic evolution of ligands by exponential enrichment) by Berens et al. [2]. It is known from the crystal structure [3], that the aptamer binds its cognate ligand tetracycline (TC) via a Mg^{2+} ion. The crystal structure reveals several additional Mg^{2+} ions that are bound by the TC-aptamer. The TC-aptamer is characterized by a very high affinity toward its ligand ($K_D = 800$ pM at 10 mM Mg^{2+}) [4]. In addition, the TC-aptamer is one of only a few aptamers that are known to function *in vivo*, where it can control translation and splicing [5–7]. These aspects, paired with the non toxicity and good cell permeability of the ligand [8], make the TC-aptamer a promising artificial riboswitch.

Recent spectroscopic (fluorescence spectroscopy, time-correlated single photon counting spectroscopy and pulsed dipolar electron paramagnetic resonance (EPR) spectroscopy) and thermodynamic studies (isothermal titration calorimetry (ITC), melting curve analysis and circular dichroism spectroscopy) focused on investigating the folding kinetics, the global structure and the conformational flexibility in the presence and absence of TC and its dependence on Mg^{2+} [9–12]. In contrast to the aforementioned studies, this work directly studies the binding of the divalent metal ion in the ligand binding pocket using pulsed EPR hyperfine spectroscopy. This is achieved by replacing diamagnetic Mg^{2+} with paramagnetic Mn^{2+}, which is common practice [13–15], as Mg^{2+} and Mn^{2+} share similar coordination chemistry properties. ITC measurements of the aptamer with Mn^{2+} instead of Mg^{2+} yielded identical binding affinities (Fig. S1) at high divalent metal ion concentrations.

Fig. 1A shows the ligand binding pocket of the TC-aptamer based on the crystal structure [3]. As can be seen, TC coordinates via its *O*11 and *O*12 oxygens (Fig. 1B) to the divalent metal ion. The divalent metal ion is further stabilized by a *pro-*R_P oxygen of

* Corresponding author.
E-mail address: prisner@epr.uni-frankfurt.de (T.F. Prisner).

https://doi.org/10.1016/j.jmr.2019.04.011
1090-7807/

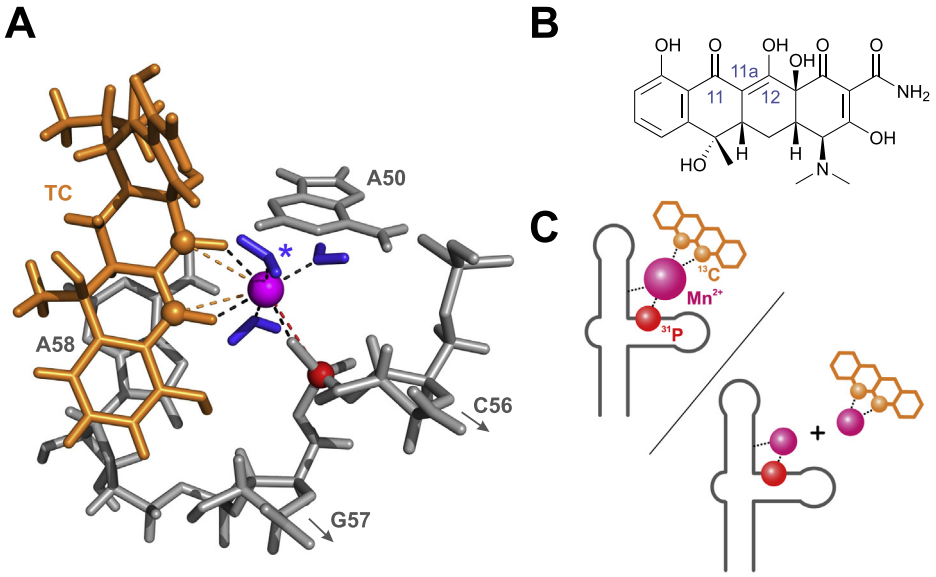

Fig. 1. (A) Ligand binding pocket of the TC-aptamer based on the crystal structure by Xiao et al. [3]. The ligand TC is shown in orange and the nucleobases, which form the binding pocket, are shown in grey (*A50*, *C56*, *G57* and *A58*). Mn^{2+} ions and water molecules are depicted in magenta and blue, respectively. The water molecule marked with an asterisk was not resolved in the crystal structure. (B) Chemical structure of the antibiotic TC. (C) Possible binding models of Mn^{2+} to the aptamer and TC. Depending on the K_D values, TC-binding might be different at an equimolar RNA/Mn^{2+}/TC concentration ratio: TC might interact with the RNA via a Mn^{2+} chelate complex (upper left) or TC might form a separate Mn-TC complex, while remaining Mn^{2+} ions still interact with the RNA (lower right). (For interpretation of the references to colour in this figure legend, the reader is referred to the web version of this article.)

the phosphate backbone of nucleobase *G*57. The crystal structure distance of the *O*11- and *O*12-adjacent carbon atoms to the divalent metal ion is 0.31 nm in both cases, whereas the crystal structure distance of the phosphorous atom to the divalent metal ion is 3.3 nm. Under the assumption that the point-dipole approximation applies, the axial (or dipolar) component T of the hyperfine tensor $\boldsymbol{A}$ is inversely proportional to r^3:

$$\boldsymbol{A} = a_{iso}\boldsymbol{1} + T\begin{pmatrix} -1 & 0 & 0 \\ 0 & -1 & 0 \\ 0 & 0 & 2 \end{pmatrix}, \tag{1a}$$

$$T = \frac{\mu_0}{4\pi h}\frac{g_e\beta_e g_n\beta_n}{r^3}. \tag{1b}$$

a_{iso} and T in Eq. (1a) describe the isotropic and axial component of the hyperfine tensor $\boldsymbol{A}$. Eq. (1b) then yields dipolar hyperfine couplings of $T_{13C} = 0.65$ MHz and $T_{31P} = 1.08$ MHz. Both carbon and phosphorous distances found in the crystal structure are very similar to previously published ^{13}C-Mn^{2+} and ^{31}P-Mn^{2+} hyperfine studies [16–19] and should therefore be readily observable with pulsed hyperfine EPR spectroscopy.

A frequently encountered problem in biochemistry is whether two different molecules *A* and *B* interact at the same time with molecule *C* or not. Examples include nucleic acid aptamers that bind via metal ions to its cognate ligand [3], metal ions that mediate the formation of protein-RNA complexes [20] or membrane proteins that interact via metal ions with an adenosine triphosphate [21]. In case of the TC-aptamer, the binding of TC via a divalent metal ion to the RNA is known to decrease at low Mg^{2+} concentrations [11]. In addition, the free Mn-TC complex [22,23] can potentially interfere with formation of a ternary RNA-Mn-TC complex (Fig. 1C). In this work, it is shown that pulsed 2D-hyperfine spectroscopy is a suitable technique to confirm formation of a ternary RNA-Mn-TC complex at equimolar RNA/Mn^{2+}/TC concentration ratios. Although similar findings can also be obtained by ITC experiments and fluorescence spectroscopy [11], 2D-hyperfine spectroscopy offers the advantage of looking at the ternary complex on an atomistic level. Consequently, 2D-hyperfine data provide a more detailed description of the investigated ternary complex, *e.g.*, which nuclei and which hyperfine coupling are incorporated in the center of the ternary complex.

2. Population-transfer 2D-correlated hyperfine spectroscopy

Pulsed hyperfine EPR spectroscopy describes a wide array of techniques that probe the hyperfine interaction of coupled electron and nuclear spins. Hyperfine spectroscopy methods such as ENDOR (electron nuclear double resonance) and ESEEM (electron spin echo envelope modulation) are often used to study paramagnetic transition metals in nucleic acids and proteins, with the goal of elucidating the local geometry of the paramagnetic cofactor [24–27,18,28,29]. Since the 2000s, the ELDOR-detected NMR technique (electron electron double resonance detected NMR, EDNMR) [30] has gained interest as a method for measuring hyperfine or even quadrupole interactions of nitroxides and paramagnetic transitions metals. Although primarily performed at W-band frequencies (94 GHz) [31–35] to increase the spectral resolution of different nuclear species and to decrease the spectral overlap of the central blindspot and resonances of low-γ nuclei, EDNMR was recently shown to be applicable at Q-band frequencies (34 GHz) as well [36,37].

One of the first pulsed 2D-hyperfine spectroscopy techniques was the TRIPLE experiment [40], in which a Davies ENDOR sequence was expanded by a second RF pulse. Another 2D-hyperfine population transfer technique is the THYCOS (triple hyperfine correlation spectroscopy) experiment [38,41,42], in which the first RF pulse gets replaced by a typically long and weakly powered ELDOR pulse (Fig. 2A). Finally, both RF pulses can be replaced by two ELDOR pulses, resulting in a 2D EDNMR experiment [39,43,42] (Fig. 2B).

THYCOS and 2D EDNMR spectra can be understood by picturing an energy ladder diagram of a 3-spin system, consisting of an electron spin with $S = 1/2$ and two nuclear spins with $I_1 = 1/2$ and $I_2 = 1/2$. If one assumes a positive nuclear g-value (*e.g.*, ^{13}C, ^{31}P, ^{1}H), a positive isotropic hyperfine coupling a_{iso} and the

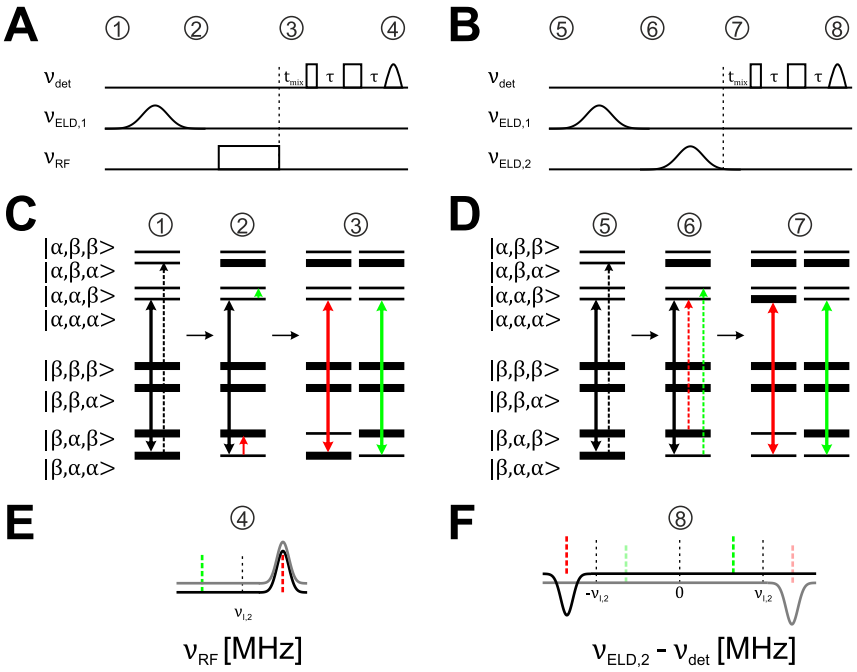

Fig. 2. (A and B) Pulse sequence of a THYCOS [38] (left) and a 2D EDNMR [39] (right) experiment. Gaussian-shaped ELDOR pulses were used to minimize the spectral overlap of detection and ELDOR pulses. (C and D) Energy ladder diagrams for a weakly coupled 8-level system, consisting of an electron spin with $S = 1/2$ and two different nuclear spins with $I_1 = 1/2$ and $I_2 = 1/2$ ($g_N, a_{iso} > 0$). Bold black arrows depict the detected allowed EPR transition, whereas the dashed black arrows (① & ⑤) depict the first ELDOR pulse, which is on-resonance with a forbidden transition of nuclei I_1. ②: For THYCOS, two allowed NMR transitions of nuclei I_2 (solid green and red arrows) are associated with the detected EPR transition. ⑥: For 2D EDNMR, two forbidden transitions of nuclei I_2 (dashed green and red arrows) are associated with the detected EPR transition. ③ & ⑦: Spin population before the echo detection sequence in THYCOS and 2D EDNMR respectively for excitation of the two nuclear transitions. (E and F) Depending on which transitions are excited, positive signals (THYCOS, dashed red line), no signals at all (2D EDNMR and THYCOS, dashed green lines) or negative signals (2D EDNMR, dashed red line) are expected. Pale dashed lines correspond to 2D EDNMR signals that stem from excitation of another allowed EPR transition ($|\beta,\alpha,\beta\rangle \leftrightarrow |\alpha,\alpha,\beta\rangle$, grey model spectra). (For interpretation of the references to colour in this figure legend, the reader is referred to the web version of this article.)

weak-coupling regime ($\nu_I > a_{iso}/2$), an energy ordering of spin levels as shown in Fig. 2C and D is expected. If ν_{det} is set to monitor the intensity of the allowed EPR transition $|\beta,\alpha,\alpha\rangle \leftrightarrow |\alpha,\alpha,\alpha\rangle$ (bold black arrows in Fig. 2C and D), only one forbidden transition ($\Delta m_S = \pm 1, \Delta m_I = \pm 1$) for nuclei I_1 exists, that has a larger resonance frequency than ν_{det} ($|\beta,\alpha,\alpha\rangle \leftrightarrow |\alpha,\beta,\alpha\rangle$, dashed black arrow in Fig. 2C and D). If one assumes that the ELDOR pulse inverts the population of the forbidden transitions of the 3-spin model system, excitation of the aforementioned forbidden transition of nucleus I_1 would lead to zero echo intensity in the detection channel.

For THYCOS, next a RF pulse is applied, the frequency of which is varied to sample the allowed NMR transitions that are associated with nucleus I_2 (green and red arrows in Fig. 2C, ②). The detected echo intensity stays at zero if transition $|\alpha,\alpha,\alpha\rangle \leftrightarrow |\alpha,\alpha,\beta\rangle$ gets excited and becomes positive if transition $|\beta,\alpha,\alpha\rangle \leftrightarrow |\beta,\alpha,\beta\rangle$ gets excited (bold green and red arrows in Fig. 2C, ③).

For 2D EDNMR, a second variable frequency ELDOR pulse is applied to probe the forbidden transitions of nucleus I_2 (dashed green and red arrows in Fig. 2D, ⑥). If the ELDOR pulse induces the transition $|\beta,\alpha,\alpha\rangle \leftrightarrow |\alpha,\alpha,\beta\rangle$ the detected echo intensity remains zero. However, the intensity becomes negative if transition $|\beta,\alpha,\beta\rangle \leftrightarrow |\alpha,\alpha,\alpha\rangle$ gets excited (bold green and red arrows in Fig. 2D, ⑦). It should be noted that in reality, long ELDOR pulses act as saturation pulses on the forbidden transitions, which may lead to slightly different signal intensities due to polarization transfer processes during the ELDOR pulse.

The expected THYCOS and 2D EDNMR model spectra are shown in Fig. 2E and F. Due to the inhomogeneous EPR linewidth, spin packets of different allowed EPR transitions have a significant spectral overlap. For this reason, the detection pulses will excite several allowed EPR transitions of the 3-spin model system simultaneously. As a consequence, the THYCOS and 2D EDNMR slices observed experimentally are a superposition of the slices of all the excited allowed EPR transitions.

Until now it has been assumed that one forbidden transition (out of two) of nucleus I_1 is excited selectively by the first ELDOR pulse (① and ⑤ in Fig. 2C and D). This is, for example, the case for the ^{31}P couplings presented in this work. If, however, the coupling is small and hence the splitting of the signals around the Larmor frequency of nucleus I_1 is small, both forbidden transitions can be excited at the same time. In such a case, more THYCOS and 2D EDNMR signals will appear (positive in THYCOS and negative in 2D EDNMR) at frequencies marked with green dashes in Fig. 2E and F.

Additionally, THYCOS and 2D EDNMR spectra will look slightly different, if the RF pulse or the second ELDOR pulse excites transitions associated with the nucleus that was excited by the first ELDOR pulse (see Fig. S2 for an explanation).

W-band THYCOS was previously used to separate different ^{1}H resonances and to determine the sign of the hyperfine coupling in a Cu(II)-L-histidine complex [38] and to assign ^{14}N resonances via ^{1}H-^{14}N THYCOS to the type 1 Cu(II) site in ascorbate oxidase (out of one type 1 Cu(II) site and one type 2 Cu(II) site) [41]. W-band 2D EDNMR and quantum chemical calculations were used to elucidate the ^{33}S-hyperfine tensor of type 1 Cu(II)-azurin, which proved difficult with a congested ^{14}N-^{33}S 1D EDNMR spectrum alone [43]. Recently, W-band $^{14/15}$N-^{31}P THYCOS was used to resolve the coordination geometry of Mn-ATP in frozen solution [42]. In this work, it is shown that ^{13}C and ^{31}P nuclei, incorporated in two different molecules (TC and RNA), can be used to correlate hyperfine signals to the same electron spin associated with a single Mn^{2+} ion.

3. Material and methods

3.1. Sample preparation

In vitro transcription was identical to a procedure published previously [11]. Before EPR measurements, the RNA was dialyzed with a buffer (100 mM triethanolamine (TEA) pH 7.5, 1 M KCl) to replace remaining Na^+ ions from the RNA purification process with K^+ ions. Amicon filters with a cut-off of 10 kDa and a sample volume of 0.5 ml were used for dialysis. The aqueous RNA solution was diluted with the buffer solution to a volume of 0.5 ml, then the solution was spun at 10,000 rpm until the solution was concentrated to a volume of 50 µl. The RNA was dialyzed four times with the buffer solution and four times with DEPC-treated MilliQ water. At Q-band, the difference between the ^{13}C- and ^{23}Na-Larmor frequency is only 0.7 MHz ($\nu_{13C} = 12.7$ MHz and $\nu_{23Na} = 13.5$ MHz). The Larmor frequency of ^{40}K (93.2% natural abundance) at Q-band frequencies is $\nu_{40K} = 2.3$ MHz. In contrast to ^{23}Na, ^{40}K should therefore not interfere with any ^{13}C or ^{31}P resonances. 1D EDNMR spectra before and after dialysis of Na^+ with K^+ are shown in the supporting information (Fig. S3). For each experiment, aliquots of the dialyzed RNA were lyophilized and dissolved in a buffer containing 2mM $Mn(ClO_4)_2$, 100 mM TEA and 1 M KCl at pH = 7.5. Depending on the sample, the buffer either contained 2 mM TC, 2 mM ^{13}C-labeled TC (Romer Labs Diagnostic) or no TC at all. 50% glycerol (v/v) was added as a glassing agent. The final RNA concentration was 1 mM. All chemicals were certified RNase free. 10 µl of the buffered RNA solutions were then transferred into 1.6 mm (outer diameter) Suprasil tubes. Samples were shock-frozen in liquid nitrogen *prior* to being inserted into the resonator.

3.2. Pulsed EPR measurements

Pulsed EPR hyperfine experiments at Q-band frequencies (33.77 GHz) were performed on a Bruker Elexsys E580 spectrometer equipped with a dielectric EN 5170 DE ENDOR probehead. The temperature was kept at 5 K using a continuous-flow helium cryostat (CF935) and an ITC 502 temperature control unit, both from Oxford Instruments. A 150 W traveling-wave tube amplifier by Applied Systems Engineering was used for microwave amplification. Pulses were created by a Bruker-manufactured arbitrary waveform generator (SpinJet AWG). For ENDOR measurements, RF frequencies were generated out of a DICE-II box and amplified by an externally blanked RF amplifier by Dressler (2 kW, LPPA 10020 LF). A low-pass filter (RF limited DF-3000) with a cutoff frequency of 30 MHz and a Bruker-supplied noise suppressor where used to avoid 3rd and 5th order ^1H harmonics and to enhance signal quality.

For ^{31}P-Davies ENDOR, the sequence $2t_p - t_{RF} - t_{mix} - t_p - \tau - 2t_p - \tau - echo$ with $t_p = 100$ ns and $\tau = 1$ µs was used. The length of the RF pulse was optimized with nutation experiments which resulted in $t_{RF} = 25$ µs for ^{31}P. The frequency of the RF pulse was varied ±9 MHz around the ^{31}P-Larmor frequency ($\nu_{31P} = 20.7$ MHz) with an increment of 50 kHz (361 points). The integration width of the echo was set to 800 ns, centered around the echo maximum. For ^{13}C-Mims ENDOR, the sequence $t_p - \tau - t_p - t_{RF} - t_{mix} - t_p - \tau - echo$ with $t_p = 10$ ns and $\tau = 320$ ns was used. The RF pulse was optimized near the ^{13}C-Larmor frequency to a length of $t_{RF} = 27.5$ µs. The echo integration width was set to 36 ns, centered around the echo maximum. The sweep width of the RF pulse was 8 MHz, centered around the ^{13}C-Larmor frequency ($\nu_{31P} = 12.7$ MHz), with a frequency increment of 25 kHz (321 points).

1D and 2D EDNMR spectra were acquired using a $(t_{ELD} - t-)t_{ELD} - t_{mix} - t_p - \tau - 2t_p - \tau - echo$ sequence, with $\tau = 1$ µs, $t_{mix} = 9$ µs and $t_p = 400$ ns. For 1D EDNMR experimemts an ELDOR pulse length of $t_{ELD} = 9$ µs was used, for 2D EDNMR experiments an ELDOR pulse length of $t_{ELD} = 40$ µs was used. For 2D EDNMR experiments, longer ELDOR pulses yielded more intense correlation signals at the cost of a slight spectral broadening. The integration width of the echo was 1400 ns for all EDNMR experiments, centered around the echo maximum. For 1D EDNMR experiments, an ELDOR sweep width of 440 MHz, starting at −220 MHz and with a frequency increment of 300 kHz, was used. For 2D EDNMR experiments where the frequency of both ELDOR pulses was varied (complete 2D EDNMR spectra), the ELDOR sweep width was decreased to 80 MHz, starting at −40 MHz and with a frequency increment of 300 kHz. For 2D EDNMR slices, where only the frequency of first ELDOR pulse was varied and the frequency of the second ELDOR pulse was kept constant, the x-axis resolution was increased to 200 kHz with an ELDOR sweep width of 54 MHz (centered symmetrically around the spectrometer frequency). A higher resolution, while maintaining a sweep width of 54 MHz, was not possible due to a limited AWG pulse sequence memory space. All EDNMR experiments utilized a shot repetition time of 3 ms, 50 shots per point and Gaussian shaped ELDOR pulses to decrease the spectral overlap with detection pulses [44,30]. All EDNMR experiments (1D and 2D) used an ELDOR amplitude of $\omega_{ELD} = 1.5 \times 10^7$ rad/s at zero frequency to allow for a comparison of EDNMR intensities of different samples. Moreover, different samples were tuned at the same spectrometer frequency in such a way, that the tuning dip looked as similar as possible.

For THYCOS experiments, the Davies ENDOR sequence was used, with the only difference being a replacement of the first inversion pulse by a 9 µs long Gaussian ELDOR pulse operating at a fixed frequency offset $\Delta\nu$. The amplitude ω_{ELD} was the same as for EDNMR experiments. The RF sweep width and x-axis resolution was identical to Davies ENDOR experiments. ENDOR and THYCOS experiments employed a shot repetition time of 50 ms and 1 shot per point. The random acquisition mode was used to avoid baseline distortions due to heating effects [45].

The ENDOR/1D EDNMR intensity was calculated to $\varepsilon(\nu_{RF/ELD}) = \frac{I_{RF/ELD\,on} - I_{RF/ELD\,off}}{I_{RF/ELD\,off}}$, where $I_{RF/ELD\,off}$ is an averaged signal range with off-resonance ELDOR or RF pulses respectively. A rolling baseline in Mims ENDOR spectra was removed by subtracting a Mims ENDOR spectrum of an unlabeled TC sample from the Mims ENDOR spectrum of the ^{13}C-labeled TC sample and multiplying the result with −1 (Fig. S8). The baseline of Davies ENDOR spectra was corrected by fitting a polynomial to the off-resonance regions of Davies ENDOR spectra. 2D EDNMR spectra were processed as described earlier [39]. 2D EDNMR slices were background-corrected by normalizing a specific slice (*e.g.*, $\Delta\nu_2 = \nu_{13C} = 12.7$ MHz) to the off-resonance intensity of a slice with an off-resonance second ELDOR pulse (*e.g.*, $\Delta\nu_2 = 40.0$ MHz). Subtraction of these two slices then yielded a background-corrected 2D EDNMR slice [42].

t_{mix} describes the time delay between mixing period and detection period. It is increased for variable-mixing-time (VMT) ENDOR experiments (Fig. S11), and kept as short as possible for ENDOR, EDNMR and THYCOS measurements. For ENDOR and THYCOS measurements, t_{mix} is chosen so that the trailing edge of the RF pulse does not interfere with the detection sequence. For EDNMR measurements, t_{mix} is chosen to allow for a decay of electron coherence, which can be created by the ELDOR pulse.

All experiments were performed on the "third" ^{55}Mn-hyperfine transition from the left of the "central" electron transition ($|m_S = -1/2, m_I = -1/2\rangle \leftrightarrow |+1/2, -1/2\rangle$).

4. Results and discussion

4.1. 1D EDNMR

Fig. 3 shows the ^{13}C and ^{31}P region of Q-band EDNMR spectra of different TC-aptamer samples (Fig. S4 contains full-range EDNMR spectra). In the absence of any TC (Fig. 3, blue spectrum), two pronounced ^{31}P-hyperfine couplings with $A_{31P}(1) = 4.8$ MHz and $A_{31P}(2) = 9.3$ MHz are visible. The small signal at the ^{13}C-Larmor frequency ($\nu_{13C} = 12.7$ MHz) is attributed to natural abundance ^{13}C, which is reasonable, as a rather carbon-rich environment is expected for RNA-coordinated Mn^{2+} ions.

The signal at 9 MHz is assigned to the high-frequency component of a hyperfine-split ^{14}N double quantum transition ($\Delta m_S = \pm 1, \Delta m_I = \pm 2$, $2\nu_{14N} = 7.4$ MHz), which is plausible, as Mn^{2+}-coupled ^{14}N nuclei exhibit a rather large quadrupole coupling [46] and therefore have an intrinsically high probability for forbidden transitions. The EDNMR spectrum in the presence of TC (Fig. 3, red spectrum) is essentially identical to the one in the absence of TC. Upon addition of ^{13}C-labeled TC (Fig. 3, green spectrum), the signal around the ^{13}C-Larmor frequency is enhanced. Besides the ^{13}C signal, however, all EDNMR spectra are very similar.

^{31}P couplings are expected for Mn^{2+}-containing RNA systems, as the negatively charged phosphate groups of the RNA backbone coordinate the positively charged Mn^{2+} ion. The difference of 4.5 MHz between the two observed phosphorous couplings is due to different values for the isotropic hyperfine coupling, a_{iso}. For a typical Mn^{2+}-^{31}P first coordination sphere distance of 0.3 nm, a dipolar hyperfine coupling, T, of 1.18 MHz is expected, which cannot explain the splitting of either 4.8 or 9.3 MHz. Interestingly, values similar to $A_{31P}(1)$ and $A_{31P}(2)$ have already been reported in literature for Mn^{2+}-containing RNA systems [25,16,17,28]. A DFT and hyperfine study on Mn^{2+}-phosphate complexes recently also revealed a considerable impact of the pH value on the magnitude of the isotropic hyperfine coupling a_{iso} [47]. Kaminker et al. attributed the larger phosphorous coupling of ≈ 9 MHz to single-stranded RNA (ssRNA) [17]. In our case, we observed an increase in intensity for the outer phosphorous coupling and a decrease in intensity for the inner phosphorous coupling after several freeze-thaw cycles (Fig. S5). The intensity of the carbon signal, originating from ^{13}C-TC, decreased as well. As it is generally known that several freeze-thaw cycles lead to degradation of RNAs and therefore to a higher percentage of shorter ssRNA fragments, these findings are in line with the results of Kaminker et al. [17].

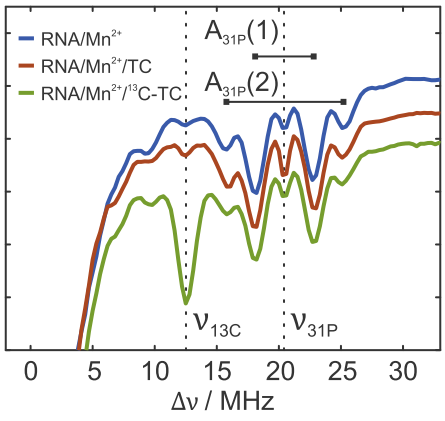

Fig. 3. Q-band 1D EDNMR spectra of different Mn^{2+} complexes. Blue: TC-aptamer with Mn^{2+}, red: TC-aptamer with Mn^{2+} and TC, green: TC-aptamer with Mn^{2+} and ^{13}C-labeled TC. Only the ^{13}C and ^{31}P regions are shown. Larmor frequencies of these nuclei are indicated with dashed lines. Two distinct ^{31}P-hyperfine couplings are visible. (For interpretation of the references to colour in this figure legend, the reader is referred to the web version of this article.)

Full-range EDNMR spectra (Fig. S4) reveal different ^{55}Mn linewidths for the samples presented in Fig. 3. Samples containing unlabelled TC and ^{13}C-labeled TC exhibit a broader ^{55}Mn linewidth than a sample containing RNA and Mn^{2+}. A different lineshape is expected as coordination of TC to Mn^{2+} should lead to a slightly different coordination geometry, e.g., a different hyperfine coupling, a different hyperfine strain and/or a different quadrupole interaction.

Although a clear ^{13}C EDNMR signal is observed (Fig. 3) and subtle differences in the ^{55}Mn EDNMR regions are visible (Fig. S4), it cannot be deduced from these spectra if TC actually coordinates to the RNA at equimolar RNA/Mn^{2+}/TC concentration regimes. For instance, it is known that TC coordinates free Mn^{2+} ions with a dissociation constant of approximately $K_D \approx 100$ μM [22,23], that could compete with the coordination of TC to the RNA.

4.2. ^{31}P-Davies ENDOR and ^{13}C-Mims ENDOR

Fig. 4A shows Q-band ^{31}P-Davies ENDOR spectra of samples whose EDNMR data were already shown in Fig. 3. All Davies ENDOR spectra are essentially identical. Whereas the outer hyperfine coupling $A_{31P}(2)$ displays the expected axial Pake doublet, an interpretation of the isotropic-looking shape of the inner hyperfine coupling $A_{31P}(1)$ is more difficult. It is known that a superposition of hyperfine couplings of different magnitudes leads to a rather isotropic-looking lineshape [47].

A simulation of experimental Davies ENDOR spectra, using the MATLAB toolbox EasySpin [48], required at least four rhombic components for $A_{31P}(1)$ and one axial component for $A_{31P}(2)$ to achieve a good agreement between experimental and simulated data (Fig. S6). The simulation yielded hyperfine coupling constants of $a_{iso}(1) =$ 2.8–4.8 MHz and $T(1) =$ 0.8–0.9 MHz for the inner hyperfine coupling, and coupling constants of $a_{iso}(2) = 9.5$ MHz and $T(2) = 1.1$ MHz for the outer hyperfine coupling (Table S1). Assuming the point-dipole approximation, the dipolar hyperfine couplings translate into ^{31}P-Mn^{2+} distances of $r =$ 0.33–0.34 nm (inner coupling) and $r = 0.31$ nm (outer coupling). Theses distances are in excellent agreement with the extracted ^{31}P-Mn^{2+} distances from the crystal structure [3]. However, the distances cannot be assigned to specific Mn^{2+} binding sites of the TC-aptamer, as the differences of the different crystal structure distances are to small (Figs. S7 and Table S1).

Fig. 4B shows Q-band ^{13}C-Mims ENDOR spectra of a sample containing the TC-aptamer, Mn^{2+} and ^{13}C-labeled TC (green spectrum) and a sample containing just Mn^{2+} and ^{13}C-labeled TC (violet spectrum). The spectrum of the free Mn-TC complex is very similar to the spectrum of the sample containing the TC-aptamer. Both spectra feature two hyperfine couplings: a larger one, whose Pake doublet shape is slightly smeared out by the Mims ENDOR blindspot function (depicted as a dashed grey line in Fig. 4B), and a smaller hyperfine coupling with a splitting of approximately 0.2 MHz. Mims ENDOR spectra with different τ values did not reveal less blindspot-distorted Mims ENDOR spectra (Fig. S9). Simulations of the Mims ENDOR spectra convoluted with a Mims ENDOR blindspot-function are presented in Fig. S9. For the outer hyperfine coupling, two different hyperfine tensors yielded equally good results (possibility one: $a_{iso,1} = 1.3$ MHz, $T_1 = 0.6$ MHz, $r_1 = 0.32$ nm, possibility two: $a_{iso,2} = 0.4$ MHz, $T_2 = 1.2$ MHz, $r_2 = 0.37$ nm). Mims ENDOR experiments with the magnetic field on-resonance with outer electron transitions [49] (Fig. S10), VMT Mims ENDOR experiments [50] (Fig. S11) and DFT-calculations (Figs. S12 and Table S2) favour possibility one ($a_{iso} > T$) over possibility two.

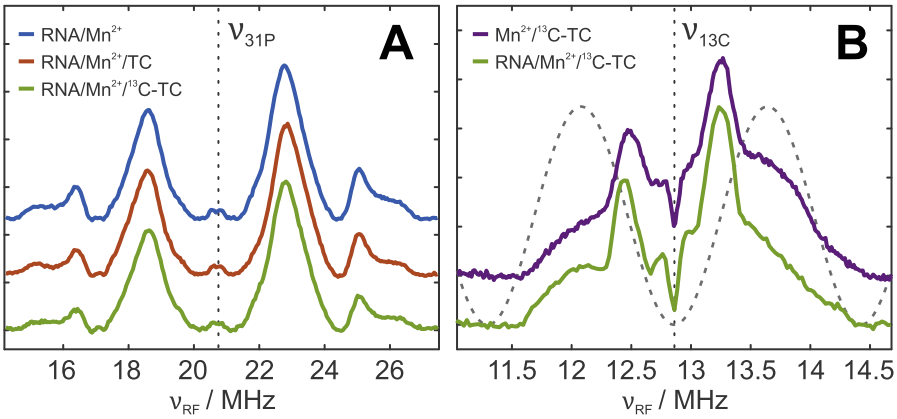

Fig. 4. (A) Q-band ^{31}P-Davies ENDOR spectra of different Mn^{2+} complexes. Blue: TC-aptamer with Mn^{2+}, red: TC-aptamer with Mn^{2+} and TC, green: TC-aptamer with Mn^{2+} and ^{13}C-labeled TC. (B) Q-band ^{13}C-Mims ENDOR spectra of different Mn^{2+} complexes. Purple: Mn^{2+} with ^{13}C-labeled TC, green: TC-aptamer with Mn^{2+} and ^{13}C-labeled TC. A τ value of 330ns was used. The Mims ENDOR blindspot function is shown as a dotted grey line. Larmor frequencies of ^{13}C and ^{31}P are indicated with dashed lines. (For interpretation of the references to colour in this figure legend, the reader is referred to the web version of this article.)

Both spectra in Fig. 4B are proof for binding of TC to Mn^{2+}, however, the binding of TC to the RNA via Mn^{2+} cannot be deduced directly from the Mims ENDOR spectra.

4.3. 2D EDNMR

In order to address the question of the binding of Mn^{2+} to the aptamer and TC we performed Q-band 2D EDNMR measurements on samples with ^{13}C-labeled TC and unlabeled TC. Whereas the labeled sample should feature ^{13}C-^{31}P cross peaks in the case of simultaneous binding of TC to the RNA via Mn^{2+}, no such signals should be present in the unlabeled sample. Fig. 5A shows the minus-plus and plus-plus quadrant of a sample containing RNA, Mn^{2+} and unlabeled TC. The minus-minus and plus-minus quadrant are not shown, as they contain redundant information. Strips to the left and above the 2D EDNMR spectrum show 1D EDNMR spectra with no correlation signals. The plus-plus quadrant is characterized by ^{31}P self-correlations signals on the diagonal. The information content is similar to a 1D EDNMR spectrum, but with a slightly higher spectral resolution.

The signals close to the central blindspot at (5.0,5.0) MHz are assigned to ^{14}N self-correlation signals. We exclude the possibility of these signals being an artifact stemming from an incomplete central blindspot removal by the background correction procedure. In such a case, the signals at (−5.0,5.0) MHz in the minus-plus quadrant should be equally intense.

The minus-plus quadrant of Fig. 5A is characterized by negative cross peaks of the two nuclear spin manifolds of the inner phosphorous coupling at (−22.9,18.1) and (−18.1,22.9) MHz. Negative cross peaks with the phosphorous matrix signal at 20.8 MHz are also visible. No cross peaks of the outer phosphorous couplings could be detected. In contrast to previous work by Kaminker et al. and Ramirez-Cohen et al. [39,43], negative cross peaks are solely confined to the minus-plus quadrant. This behavior was also observed for less complex Mn^{2+} compounds, such as Mn^{2+} with inorganic phosphate (Mn-P_i) and Mn-^{13}C-DOTA (Figs. S16 and S17).

More signals appear at (−5.0,18.1) and (−5.0,22.9) MHz in the minus-plus quadrant and at (5.0,18.1) and (5.0,22.9) MHz in the plus-plus quadrant. Originally these signals were assigned to ^{14}N-^{31}P cross peaks. However, these signals do not show up in the other frequency domain, *e.g.*, (18.1,−5.0) MHz. In addition, one would expect negative cross peaks for heteronuclear 2D EDNMR spectra (Fig. 2F). These cross peaks also have a rather unusual shape, as they point in a "cross-like" manner toward the phosphorous Larmor frequency.

Litvinov et al. attributed similar signals in a recent 2D EDNMR and THYCOS study to off-resonance effects of the ELDOR pulse [42]. In line with these findings we observed similar cross peaks for a sample containing Mn-P_i, which should not contain any ^{14}N resonances. For Mn-^{13}C-DOTA and $[Mn(H_2O)_6]^{2+}$, which contain no ^{31}P resonances, no signals due to off-resonance effects are visible for the frequency range shown in Fig. 5 (Figs. S17 and S18).

The plus-plus quadrant of a sample with ^{13}C-labeled TC (Fig. 5B) is almost identical to the 2D EDNMR spectrum with unlabeled TC, with the only difference being the large ^{13}C self-correlation signal for the labeled sample. The minus-plus quadrant of a ^{13}C-labeled sample is characterized by a positive signal at (−12.7,12.7) MHz. As the ^{13}C-hyperfine coupling is rather small, and the intensities of the different ^{13}C nuclear spin manifolds do severely overlap (Fig. 4B), one only sees a single signal at the ^{13}C-Larmor frequency (instead of two signals as seen for ^{31}P). The most striking differences between Fig. 5A and B are, however, ^{13}C-^{31}P cross peaks at (−18.1,12.7) and (−12.7,18.1) MHz. Cross peaks of ^{13}C and ^{31}P matrix signals are visible at (−20.8,12.7) and (−12.7,20.8) MHz. These cross peaks are a clear sign that TC binds to the TC-aptamer, even at 1 mM Mn^{2+}.

It should be noted, that not all signals (and their intensities) in the 2D EDNMR spectra are completely understood. It is for example unclear why ^{13}C correlation signals of ^{13}C-TC in the minus-plus quadrant are positive (Fig. 5B), whereas the ^{13}C correlation signals of Mn-^{13}C-DOTA in the minus-plus quadrant are negative (Fig. S17). Different cross-relaxation rates and magnitudes of the hyperfine coupling could be an explanation.

Surprisingly, the contour plot in Fig. 5B does not show any cross peaks for the ^{31}P coupling at 22.9 MHz at (−22.9,12.7) and (−12.7,22.9) MHz. In order to get a better insight into ^{13}C-^{31}P cross peaks, we therefore recorded 2D EDNMR slices with an increased resolution and signal-to-noise ratio. Selected 2D EDNMR slices with $\Delta\nu_2$ on-resonance with either the phosphorous nuclear spin manifold at 18.1 MHz or at 22.9 MHz are shown in Fig. 6A and B, respectively. Again, slices for a sample with ^{13}C-labeled TC (green spectra) and unlabeled TC (red spectra) are shown.

The signals at −5.0 and 5.0 MHz in Fig. 6A and B are the "cross-like" signals in Fig. 5A and B due to off-resonance effects of the first ELDOR pulse, while the second ELDOR pulse is exciting a phosphorous transition. It should be noted, that the relative intensities of these signals are reproducible (the signal at −5.0 MHz has a higher intensity than the one at 5.0 MHz if the phosphorous transition at 18.1 MHz is excited and *vice versa*). The reason for this is currently unclear.

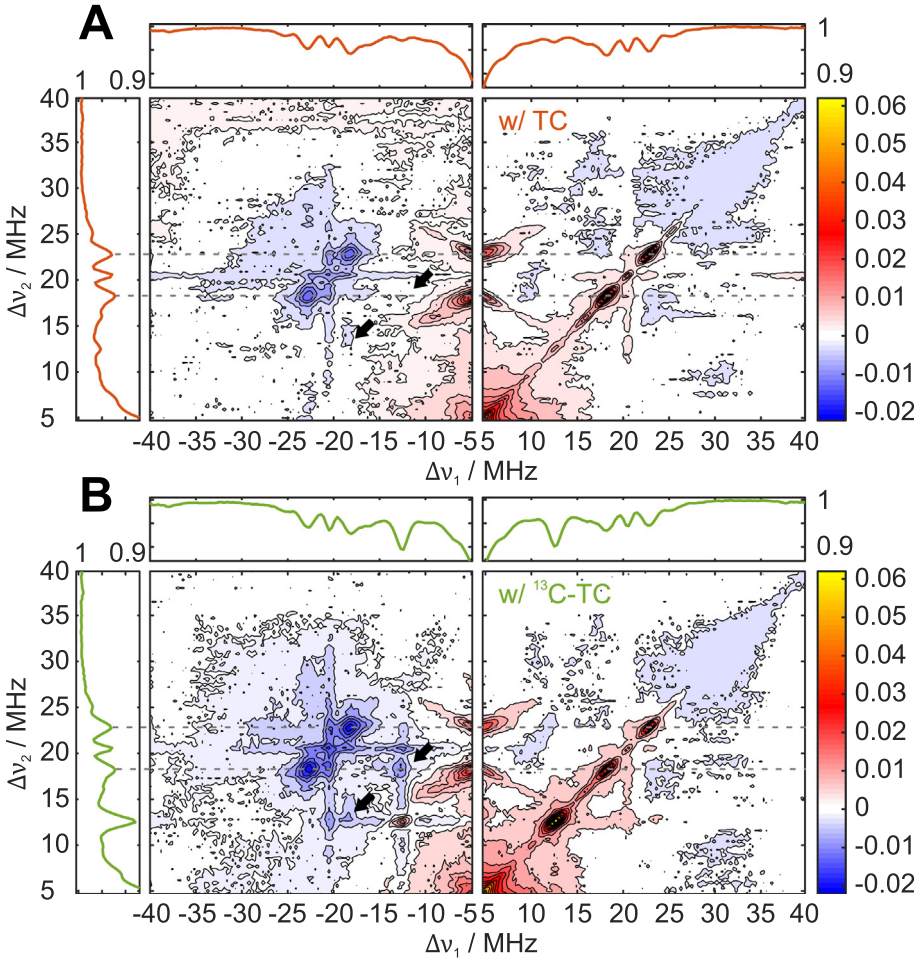

Fig. 5. Background-corrected Q-band 2D EDNMR spectra. (A) TC-aptamer with Mn^{2+} and TC, (B) TC-aptamer with Mn^{2+} and ^{13}C-labeled TC. Only the minus-plus and plus-plus quadrant are shown, as the plus-minus and minus-minus quadrant look identical. Strips to the left and above the 2D EDNMR spectrum show 1D EDNMR spectra that are free of any correlation signals. Black arrows label expected frequency offsets for ^{13}C-^{31}P correlation signals. Dotted grey lines correspond to chosen 2D EDNMR slices that were recorded with a higher resolution and a better signal-to-noise ratio (Fig. 6). Primary 2D EDNMR spectra and all four quadrants of background-corrected 2D EDNMR spectra are presented in the Supporting Information (Figs. S13–S15).

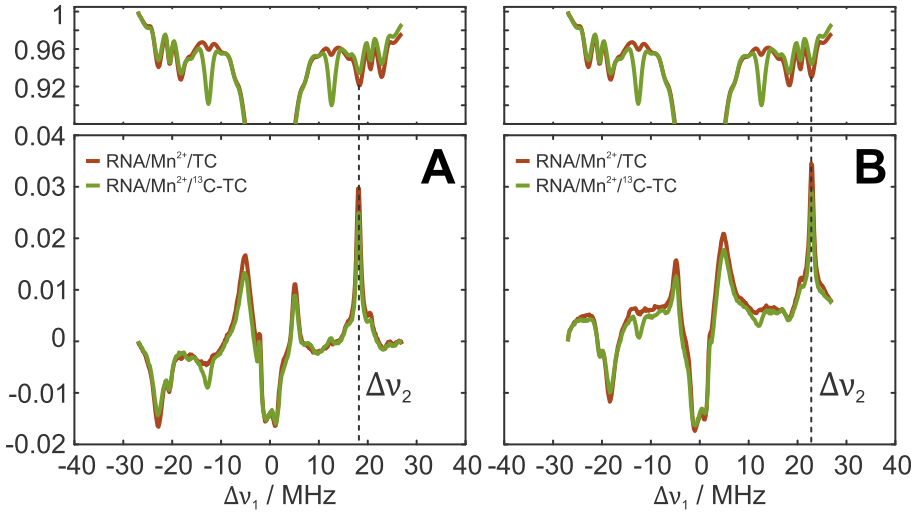

Fig. 6. Individual slices of the Q-band 2D EDNMR spectra shown in Fig. 5 recorded with higher resolution and a better signal-to-noise ratio. (A) 2D EDNMR slices with the frequency of the second ELDOR pulse set to 18.1 MHz. (B) 2D EDNMR slices with the frequency of the second ELDOR pulse set to 22.9 MHz. In both cases, the frequency of the first ELDOR pulse was varied. The slices presented in this figure correspond to horizontal slices in Fig. 5 (marked by dashed lines in Fig. 5). Red: TC-aptamer with Mn^{2+} and TC, green: TC-aptamer with Mn^{2+} and ^{13}C-labeled TC. (For interpretation of the references to colour in this figure legend, the reader is referred to the web version of this article.)

For ^{31}P, the expected signal pattern for a homonuclear 2D EDNMR is observed (Fig. S2), that is, a positive 2D EDNMR signal for the ^{31}P nuclear spin manifold that gets excited by $\Delta\nu_2$ at positive $\Delta\nu_1$ values (*e.g.*, $\Delta\nu_1 = \Delta\nu_2 = 18.1$ MHz), and a negative 2D EDNMR signal for the nuclear transition in the other electron spin manifold at negative $\Delta\nu_1$ values (*e.g.*, $\Delta\nu_1 = -22.9$ MHz).

The ^{13}C-^{31}P cross peak for a labeled sample at −12.7 MHz in Fig. 6A ($\Delta\nu_2 = 18.1$ MHz) was already clearly visible in the 2D EDNMR spectrum in Fig. 5B at (−12.7,18.1) MHz. Fig. 6B shows a clear ^{13}C-^{31}P cross peak for a labeled sample at −12.7 MHz as well ($\Delta\nu_2 = 22.9$ MHz). This cross peak at (−12.7,22.9) MHz was not visible in the complete 2D EDNMR spectrum in Fig. 5B, which is probably due to a combination of an insufficient signal-to-noise ratio and a too small number of contour levels.

Based on 2D EDNMR data alone, it is difficult to make statements about cross peaks involving the outer ^{31}P-hyperfine coupling. The ^{31}P-^{31}P cross peak at negative frequency offsets in Fig. 6B covers an area ranging from approximately −21 to −15.5 MHz. The self-correlation signal of the inner ^{31}P coupling at −18.1 MHz therefore obscures a potential correlation signal of the inner ^{31}P coupling and the outer ^{31}P coupling which should appear at −15.9 MHz.

4.4. THYCOS

To substantiate our 2D EDNMR results, we also performed THYCOS experiments. Although THYCOS is inferior to 2D EDNMR in terms of sensitivity, it offers the advantage that no background correction is needed. If the initial ELDOR pulse is off-resonance to any transition (forbidden or allowed), the RF pulse will have no effect, as the different nuclear spin levels within one electron spin manifold are almost equally populated.

Homonuclear ^{31}P-^{31}P THYCOS yielded the expected peak intensities, that is, a negative THYCOS signal for the ^{31}P nuclear spin manifold that gets excited by the ELDOR pulse, and a positive THYCOS signal for the ^{31}P nuclear spin manifold that is not getting excited by the ELDOR pulse (Fig. S19). A THYCOS effect is observed for the inner as well as for the outer ^{31}P-hyperfine coupling. However, no correlation is observed between these two hyperfine couplings.

For heteronuclear ^{13}C-^{31}P THYCOS, we irradiated the ^{13}C-EDNMR signal with the ELDOR pulse and sampled the ^{31}P region with the RF pulse. The reason for that is that the ^{13}C-EDNMR signal is larger than the ^{31}P-EDNMR signal, which should therefore give a more intense THYCOS signal. Fig. 7 shows THYCOS spectra of samples with unlabeled TC (red spectra) and ^{13}C-labeled TC (green spectra). As expected, no signal is visible for the unlabeled sample, if the ELDOR pulse is on-resonance with the ^{13}C-Larmor frequency (12.7 MHz) or if the ELDOR pulse is off-resonance with any allowed or forbidden transition (35 MHz).

For the ^{13}C-labeled sample, however, clear correlation signals are visible for the inner ^{31}P-hyperfine coupling if the ELDOR pulse is on-resonance with the ^{13}C-Larmor frequency (12.7 MHz). Therefore, the THYCOS spectra confirm the interpretation of the previous 2D EDNMR results. Due to the lower sensitivity of THYCOS, no ^{13}C-^{31}P cross peaks involving the outer ^{31}P-hyperfine coupling could be detected. The relative intensities of the THYCOS signals at 18.1 and 22.9 MHz even match the relative intensities of the 2D EDNMR signals. For both, 2D EDNMR and THYCOS, a smaller ^{13}C-^{31}P correlation signal intensity is observed if the ^{31}P transition at 22.9 MHz is excited (in comparison to the correlation signal involving the ^{31}P transition at 18.1 MHz).

Fig. 2E shows that only a single peak is expected for a heteronuclear THYCOS. As the ^{13}C-hyperfine coupling is, however, rather small, and the intensities of the different nuclear spin manifolds are known to overlap near the ^{13}C-Larmor frequency, the actual

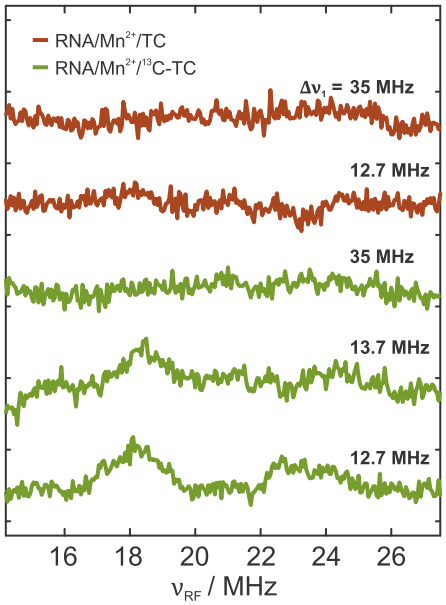

Fig. 7. Q-band THYCOS spectra of different Mn^{2+} complexes. Red: TC-aptamer with Mn^{2+} and TC, green: TC-aptamer with Mn^{2+} and ^{13}C-labeled TC. The RF pulse was used to sample the ^{31}P region, whereas the frequency offset $\Delta\nu_1$ of the ELDOR pulse was kept fixed at either 12.7 MHz, 13.7 MHz (^{13}C region) or 35.0 MHz (off-resonance). (For interpretation of the references to colour in this figure legend, the reader is referred to the web version of this article.)

THYCOS spectrum is therefore a superposition of two simultaneously excited THYCOS signals. As expected, the symmetry is lifted if the frequency offset of the ELDOR pulse is moved further away from the ^{13}C-Larmor frequency (*e.g.*, from 12.7 to 13.7 MHz, Fig. 7).

The asymmetric THYCOS spectrum recorded with $\Delta\nu_1 = 13.7$ MHz allows the determination of the sign of the ^{13}C-hyperfine coupling. As it is known that the isotropic hyperfine coupling of phosphorous is positive [42], the signal at 18.1 MHz must stem from the nuclear transition in the $|m_S = \alpha\rangle$ manifold. Positive heteronuclear THYCOS signals involve two nuclear transitions in different electron spin manifolds (Fig. 2C). The nuclear transition excited at $\Delta\nu_1 = 13.7$ MHz must therefore stem from the $|m_S = \beta\rangle$ manifold. If the nuclear transition in the $|\beta\rangle$ manifold appears at higher frequencies, the isotropic ^{13}C-hyperfine coupling must be positive (assuming $a_{iso} > T$), which is also in agreement with outer-electron transitions ENDOR studies and VMT Mims ENDOR experiments (Figs. S10 and S11).

If the ELDOR pulse is irradiated at $\Delta\nu_1$ values lower than 11.7 MHz, negative signals in the phosphorous region begin to appear (bold spectra in Fig. S20), which are reminiscent of signals due to off-resonance effects of the ELDOR pulse that where already reported by Litvinov et al. [42]. These signals start to build up around $\Delta\nu_1 \leqslant 10$ MHz, which perfectly agrees with the "cross-like" signals observed in the 2D EDNMR spectra (Fig. 5A and B). If ^{15}N-labeled RNA is used instead of nitrogen-unlabeled RNA, the negative THYCOS signals for a ^{15}N-labeled RNA are identical to the negative THYCOS signals for a nitrogen-unlabeled RNA (pale spectra in Fig. S20). This supports the idea that these signals are due to off-resonance effects and not due to ^{14}N-^{31}P correlation signals.

5. Conclusion

To the authors knowledge, this is the first time that 2D ELDOR-detected NMR and THYCOS are used to correlate ^{13}C and ^{31}P nuclei, located on two different molecules, to the same electron spin (Mn^{2+}).

2D-correlated hyperfine spectroscopy was able to show that TC binds to a TC-aptamer via a Mn^{2+} ion at physiological divalent metal ion concentrations of 1 mM. These results are in agreement with a study by Reuss et al. [11]. Although ITC experiments and fluorescence spectroscopy provide similar information by measuring thermodynamic parameters on a macroscopic scale, 2D EDNMR and THYCOS reveal complementary data on an atomistic level by directly investigating the nuclei and the electron spin incorporated in the center of the ternary complex.

Out of the two ^{31}P-hyperfine couplings, only the inner hyperfine coupling $A_{31P}(1)$ shows a clear correlation to ^{13}C-TC. Making statements about ^{13}C-^{31}P correlation signals involving the outer ^{31}P-hyperfine coupling based on 2D EDNMR and THYCOS data alone is difficult, as an insufficient resolution (2D EDNMR) or signal-to-noise ratio (THYCOS) would hamper the observation of such signals. The fact that ^{31}P-^{31}P THYCOS, however, shows clear self-correlation of the outer and the inner ^{31}P-hyperfine coupling but no correlation signals between the outer and inner ^{31}P-hyperfine coupling, underlines the hypothesis that both ^{31}P-hyperfine couplings must interact with different Mn^{2+} ions. In such a case, no ^{13}C-^{31}P correlation signals are expected that involve the outer ^{31}P-hyperfine coupling. This conclusion is in perfect agreement with the EDNMR-monitored freeze-thaw studies.

By using THYCOS, we were also able to determine the sign of the ^{13}C-hyperfine coupling of TC interacting with Mn^{2+}. Within the scope of this work, it is impossible to say how much of TC actually binds to the RNA. Monitoring the intensity of ^{13}C-^{31}P correlation signals in TC titration experiments should, however, give more insight into this question.

Although THYCOS and 2D EDNMR yield identical results, 2D EDNMR comes with the advantage of being far more sensitive. The total acquisition time of a complete 2D EDNMR spectrum was around 12 h, whereas the single 1D THYCOS spectrum recorded at $\Delta\nu_1 = 12.7$ MHz required an acquisition time of more than 24 h. The acquisition time for a complete 2D EDNMR spectrum for a less concentrated sample will be uneconomical long. However, if the nuclear species of interest is known, specific 2D EDNMR slices can be recorded, that contain the information of interest. The acquisition time for two 2D EDNMR slices (background slice and slice with nuclei of interest) was around 1 h. A shortcoming of 2D EDNMR is its reduced resolution in comparison to THYCOS, i.e., just as with 1D EDNMR signals, 2D EDNMR signals will not contain any information about the anisotropy of the hyperfine interaction. A good strategy is therefore to first perform a (complete) 2D EDNMR experiment and then record chosen THYCOS slices if the signal-to-noise ratio permits.

The implementation of non-linear frequency incrementation would help to increase the signal-to-noise ratio of 2D EDNMR data even further, as EDNMR spectra for a large part consist of baseline regions, that typically need less data points for a sufficient sampling than EDNMR signals. Such a feature is currently not implemented into Bruker spectrometers.

This study could demonstrate that THYCOS and in particular 2D EDNMR spectra or slices will be useful techniques to determine the binding of two biomolecules or small molecules/ligands to a paramagnetic transition metal, if no *prior* high-resolution knowledge about the system is available.

Acknowledgements

T.F.P. and B.S. acknowledge financial support from the Collaborative Research Center 902 – Molecular Principles of RNA-based regulation of the German Research Foundation (3214020004). A. M.B was supported by the Marie Curie GOIN program, and gratefully acknowledges her current fellowship support from the Royal Society and EPSRC for a Dorothy Hodgkin Fellowship (DH160004). We are grateful to Prof. Christiane Timmel and Dr. William Myers at the Centre of Advanced Electron Spin Resonance (CAESR), Oxford University for access to their facilities which are supported by the EPSRC (EPLO 11972/1) for some of the aforementioned experiments. We thank Dr. Björn Corzilius for useful comments on the manuscript.

Appendix A. Supplementary material

Supplementary data associated with this article can be found, in the online version, at https://doi.org/10.1016/j.jmr.2019.04.011.

References

[1] K.-M. Song, S. Lee, C. Ban, Aptamers and their biological applications, Sensors 12 (2012) 612–631, https://doi.org/10.3390/s120100612.
[2] C. Berens, A. Thain, R. Schroeder, A tetracycline-binding RNA aptamer, Bioorg. Med. Chem. 9 (2001) 2549–2556, https://doi.org/10.1016/S0968-0896(01)00063-3.
[3] H. Xiao, T.E. Edwards, A.R. Ferré-D'Amaré, Structural basis for specific, high-affinity tetracycline binding by an in vitro evolved aptamer and artificial riboswitch, Chem. Biol. 15 (2008) 1125–1137, https://doi.org/10.1016/j.chembiol.2008.09.004.
[4] M. Muller, J.E. Weigand, O. Weichenrieder, B. Suess, Thermodynamic characterization of an engineered tetracycline-binding riboswitch, Nucl. Acids Res. 34 (2006) 2607–2617, https://doi.org/10.1093/nar/gkl347.
[5] J.E. Weigand, B. Suess, Tetracycline aptamer-controlled regulation of pre-mRNA splicing in yeast, Nucl. Acids Res. 35 (2007) 4179–4185, https://doi.org/10.1093/nar/gkm425.
[6] P. Kötter, J.E. Weigand, B. Meyer, K.-D. Entian, B. Suess, A fast and efficient translational control system for conditional expression of yeast genes, Nucl. Acids Res. 37 (2009) e120.1–e120.7, https://doi.org/10.1093/nar/gkp578.
[7] M. Vogel, J.E. Weigand, B. Kluge, M. Grez, B. Suess, A small portable RNA device for the control of exon skipping in mammalian cells, Nucl. Acids Res. 46 (2018) e48.1–e48.12, https://doi.org/10.1093/nar/gky062.
[8] I. Chopra, M. Roberts, Tetracycline antibiotics: mode of action, applications, molecular biology, and epidemiology of bacterial resistance, Microbiol. Mol. Biol. Rev. 65 (2001) 232–260, https://doi.org/10.1128/MMBR.65.2.232-260.2001.
[9] D. Wunnicke, D. Strohbach, J.E. Weigand, B. Appel, E. Feresin, B. Suess, S. Muller, H.-J. Steinhoff, Ligand-induced conformational capture of a synthetic tetracycline riboswitch revealed by pulse EPR, RNA 17 (2011) 182–188, https://doi.org/10.1261/rna.2222811.
[10] U. Förster, J.E. Weigand, P. Trojanowski, B. Suess, J. Wachtveitl, Conformational dynamics of the tetracycline-binding aptamer, Nucl. Acids Res. 40 (2012) 1807–1817, https://doi.org/10.1093/nar/gkr835.
[11] A.J. Reuss, M. Vogel, J.E. Weigand, B. Suess, J. Wachtveitl, Tetracycline determines the conformation of its aptamer at physiological magnesium concentrations, Biophys. J. 107 (2014) 2962–2971, https://doi.org/10.1016/j.bpj.2014.11.001.
[12] T. Hetzke, M. Vogel, D.B. Gophane, J.E. Weigand, B. Suess, S.T. Sigurdsson, T.F. Prisner, Influence of Mg2+ on the conformational flexibility of a tetracycline aptamer, RNA 25 (2019) 158–167, https://doi.org/10.1261/rna.068684.118.
[13] J. De Vente, J. Zaagsma, The influence of the divalent cations Mn2+ and Mg2+ on the activation of particulate and digitonin-solubilized adenylate cyclase from rat fat cell membranes, Arch. Biochem. Biophys. 209 (1981) 249–255, https://doi.org/10.1016/0003-9861(81)90278-2.
[14] S.C. Dahm, O.C. Uhlenbeck, Role of divalent metal ions in the hammerhead RNA cleavage reaction, Biochemistry 30 (1991) 9464–9469, https://doi.org/10.1021/bi00103a011.
[15] T. Schweins, K. Scheffzek, R. Aßheuer, A. Wittinghofer, The role of the metal ion in the p21ras catalysed GTP-hydrolysis: Mn2+ versus Mg2+, J. Mol. Biol. 266 (1997) 847–856, https://doi.org/10.1006/jmbi.1996.0814.
[16] O. Schiemann, R. Carmieli, D. Goldfarb, W-band 31P-ENDOR on the high-affinity Mn2+ binding site in the minimal and tertiary stabilized hammerhead ribozymes, Appl. Magn. Reson. 31 (2007) 543–552, https://doi.org/10.1007/BF03166601.
[17] I. Kaminker, A. Sushenko, A. Potapov, S. Daube, B. Akabayov, I. Sagi, D. Goldfarb, Probing conformational variations at the ATPase site of the RNA helicase DbpA by high-field electron-nuclear double resonance spectroscopy, J. Am. Chem. Soc. 133 (2011) 15514–15523, https://doi.org/10.1021/ja204291d.
[18] J.A. Stull, T.A. Stich, R.J. Service, R.J. Debus, S.K. Mandal, W.H. Armstrong, R.D. Britt, 13C ENDOR reveals that the D1 polypeptide C-terminus is directly bound to Mn in the photosystem II oxygen evolving complex, J. Am. Chem. Soc. 132 (2010) 446–447, https://doi.org/10.1021/ja908688t.
[19] P.H. Oyala, T.A. Stich, J.A. Stull, F. Yu, V.L. Pecoraro, R.D. Britt, Pulse electron paramagnetic resonance studies of the interaction of methanol with the S2 state of the Mn4O5Ca cluster of photosystem II, Biochemistry 53 (2014) 7914–7928, https://doi.org/10.1021/bi501323h.
[20] T. Kumarevel, H. Mizuno, P.K.R. Kumar, Characterization of the metal ion binding site in the anti-terminator protein, HutP, of bacillus subtilis, Nucl. Acids Res. 33 (2005) 5494–5502, https://doi.org/10.1093/nar/gki868.

[21] K. Barth, S. Hank, P.E. Spindler, T.F. Prisner, R. Tampé, B. Joseph, Conformational coupling and trans-inhibition in the human antigen transporter ortholog TmrAB resolved with dipolar EPR spectroscopy, J. Am. Chem. Soc. 140 (2018) 4527–4533, https://doi.org/10.1021/jacs.7b12409.
[22] A. Albert, C.W. Rees, Avidity of the tetracyclines for the cations of metals, Nature 177 (1956) 433–434, https://doi.org/10.1038/177433a0.
[23] A. Yamaguchi, T. Udagawa, T. Sawai, Transport of divalent cations with tetracycline as mediated by the transposon Tn10-encoded tetracycline resistance protein, J. Biol. Chem. 265 (1990) 4809–4813, http://www.jbc.org/content/265/9/4809.long.
[24] S.R. Morrissey, T.E. Horton, C.V. Grant, C.G. Hoogstraten, R.D. Britt, V.J. DeRose, Mn2+-nitrogen interactions in RNA probed by electron spin-echo envelope modulation spectroscopy – application to the hammerhead ribozyme, J. Am. Chem. Soc. 121 (1999) 9215–9218, https://doi.org/10.1021/ja9921571.
[25] S.R. Morrissey, T.E. Horton, V.J. DeRose, Mn2+ sites in the hammerhead ribozyme investigated by EPR and continuous-wave Q-band ENDOR spectroscopies, J. Am. Chem. Soc. 122 (2000) 3473–3481, https://doi.org/10.1021/ja992989z.
[26] P. Manikandan, R. Carmieli, T. Shane, A.J. Kalb (Gilboa), D. Goldfarb, W-Band ENDOR investigation of the manganese-binding site of concanavalin A: determination of proton hyperfine couplings and their signs, J. Am. Chem. Soc. 122 (2000) 3488–3494, https://doi.org/10.1021/ja993395z.
[27] M. Bennati, M.M. Hertel, J. Fritscher, T.F. Prisner, N. Weiden, R. Hofweber, M. Spörner, G. Horn, H.R. Kalbitzer, High-frequency 94 GHz ENDOR characterization of the metal binding site in wild-type ras-GDP and its oncogenic mutant G12V in frozen solution, Biochemistry 45 (2006) 42–50, https://doi.org/10.1021/bi051156k.
[28] A.V. Astashkin, Y.E. Nesmelov, Mn2+ nucleotide coordination at the myosin active site as detected by pulsed electron paramagnetic resonance, J. Phys. Chem. B 116 (2012) 13655–13662, https://doi.org/10.1021/jp308423x.
[29] T.U. Nick, W. Lee, S. Koßmann, F. Neese, J. Stubbe, M. Bennati, Hydrogen bond network between amino acid radical intermediates on the proton-coupled electron transfer pathway of *E. coli* α2 ribonucleotide reductase, J. Am. Chem. Soc. 137 (2015) 289–298, https://doi.org/10.1021/ja510513z.
[30] P. Schosseler, T. Wacker, A. Schweiger, Pulsed ELDOR detected NMR, Chem. Phys. Lett. 224 (1994) 319–324, https://doi.org/10.1016/0009-2614, 94) 00548-6.
[31] L. Kulik, B. Epel, J. Messinger, W. Lubitz, Pulse EPR 55Mn-ENDOR and ELDOR-detected NMR of the S2-state of the oxygen evolving complex in photosystem II, Photosynth. Res. 84 (2005) 347–353, https://doi.org/10.1007/s11120-005-2438-7.
[32] M. Florent, I. Kaminker, V. Nagarajan, D. Goldfarb, Determination of the 14N quadrupole coupling constant of nitroxide spin probes by W-band ELDOR-detected NMR, J. Magn. Reson. 210 (2011) 192–199, https://doi.org/10.1016/j.jmr.2011.03.005.
[33] N. Cox, W. Lubitz, A. Savitsky, W-band ELDOR-detected NMR (EDNMR) spectroscopy as a versatile technique for the characterisation of transition metal-ligand interactions, Mol. Phys. 111 (2013) 2788–2808, https://doi.org/10.1080/00268976.2013.830783.
[34] E.M. Bruch, M.T. Warner, S. Thomine, L.C. Tabares, S. Un, Pulse electron double resonance detected multinuclear NMR spectra of distant and low sensitivity nuclei and its application to the structure of Mn(II) centers in organisms, J. Phys. Chem. B 119 (2015) 13515–13523, https://doi.org/10.1021/acs.jpcb.5b01624.
[35] N. Cox, A. Nalepa, W. Lubitz, A. Savitsky, ELDOR-detected NMR: a general and robust method for electron-nuclear hyperfine spectroscopy?, J Magn. Reson. 280 (2017) 63–78, https://doi.org/10.1016/j.jmr.2017.04.006.
[36] T. Hetzke, A.M. Bowen, T.F. Prisner, ELDOR-detected NMR at Q-band, Appl. Magn. Reson. 48 (2017) 1375–1397, https://doi.org/10.1007/s00723-017-0927-4.
[37] N. Wili, G. Jeschke, Chirp echo Fourier transform EPR-detected NMR, J. Magn. Reson. 289 (2018) 26–34, https://doi.org/10.1016/j.jmr.2018.02.001.
[38] A. Potapov, B. Epel, D. Goldfarb, A triple resonance hyperfine sublevel correlation experiment for assignment of electron-nuclear double resonance lines, J. Chem. Phys. 128 (2008) 052320.1–052320.10, https://doi.org/10.1063/1.2833584.
[39] I. Kaminker, T.D. Wilson, M.G. Savelieff, Y. Hovav, H. Zimmermann, Y. Lu, D. Goldfarb, Correlating nuclear frequencies by two-dimensional ELDOR-detected NMR spectroscopy, J. Magn. Reson. 240 (2014) 77–89, https://doi.org/10.1016/j.jmr.2013.12.016.
[40] M. Mehring, P. Höfer, A. Grupp, Pulsed electron nuclear double and triple resonance schemes, Berichte der Bunsengesellschaft für Phys. Chem. 91 (1987) 1132–1137, https://doi.org/10.1002/bbpc.19870911111.
[41] A. Potapov, I. Pecht, D. Goldfarb, Resolving ligand hyperfine couplings of type 1 and 2 Cu(II) in ascorbate oxidase by high field pulse EPR correlation spectroscopy, Phys. Chem. Chem. Phys. 12 (2010) 62–65, https://doi.org/10.1039/B919069D.
[42] A. Litvinov, A. Feintuch, S. Un, D. Goldfarb, Triple resonance EPR spectroscopy determines the Mn2+ coordination to ATP, J. Magn. Reson. 294 (2018) 143–152, https://doi.org/10.1016/j.jmr.2018.07.007.
[43] M. Ramirez Cohen, N. Mendelman, M. Radoul, T.D. Wilson, M.G. Savelieff, H. Zimmermann, I. Kaminker, A. Feintuch, Y. Lu, D. Goldfarb, Thiolate spin population of type I copper in azurin derived from 33S hyperfine coupling, Inorg. Chem. 56 (2017) 6163–6174, https://doi.org/10.1021/acs.inorgchem.7b00167.
[44] T. Wacker, G.A. Sierra, A. Schweiger, The concept of FID-detected hole-burning in pulsed EPR spectroscopy, Isr. J. Chem. 32 (1992) 305–322, https://doi.org/10.1002/ijch.199200038.
[45] B. Epel, D. Arieli, D. Baute, D. Goldfarb, Improving W-band pulsed ENDOR sensitivity – random acquisition and pulsed special TRIPLE, J. Magn. Reson. 164 (2003) 78–83, https://doi.org/10.1016/S1090-7807(03)00191-5.
[46] K. Keller, M. Zalibera, M. Qi, V. Koch, J. Wegner, H. Hintz, A. Godt, G. Jeschke, A. Savitsky, M. Yulikov, EPR characterization of Mn2+ complexes for distance determination with pulsed dipolar spectroscopy, Phys. Chem. Chem. Phys. 18 (2016) 25120–25135, https://doi.org/10.1039/C6CP04884F.
[47] S. Un, E.M. Bruch, How bonding in manganous phosphates affects their Mn(II)-31P hyperfine interactions, Inorg. Chem. 54 (2015) 10422–10428, https://doi.org/10.1021/acs.inorgchem.5b01864.
[48] S. Stoll, A. Schweiger, EasySpin, a comprehensive software package for spectral simulation and analysis in EPR, J. Magn. Reson. 178 (2006) 42–55, https://doi.org/10.1016/j.jmr.2005.08.013.
[49] B. Epel, P. Manikandan, P.M.H. Kroneck, D. Goldfarb, High-field ENDOR and the sign of the hyperfine coupling, Appl. Magn. Reson. 21 (2001) 287–297, https://doi.org/10.1007/BF03162408.
[50] M. Bennebroek, J. Schmidt, Pulsed ENDOR spectroscopy at large thermal spin polarizations and the absolute sign of the hyperfine interaction, J. Magn. Reson. 128 (1997) 199–206, https://doi.org/10.1006/jmre.1997.1234.

Supporting information

Binding of tetracycline to its aptamer determined by 2D-correlated Mn^{2+} hyperfine spectroscopy

Thilo Hetzke[a], Alice M Bowen[b], Marc Vogel[c], Maximilian Gauger[a], Beatrix Suess[c], Thomas F Prisner[a,*]

[a] *Institute of Physical and Theoretical Chemistry and Center of Biomolecular Magnetic Resonance, Goethe University Frankfurt, Frankfurt am Main, Germany*
[b] *Center for Advanced Electron Spin Resonance (CAESR), Inorganic Chemistry Laboratory, Department of Chemistry, University of Oxford, Oxford, United Kingdom*
[c] *Department of Biology, Technical University of Darmstadt, Darmstadt, Germany*

[*] *prisner@epr.uni-frankfurt.de*

Contents

1 ITC measurements of the TC-aptamer with Mn^{2+}

ITC measurements were performed in an iTC200 microcalorimeter (MicroCal, GE Healthcare, Chalfont St. Giles, UK) at 25 °C. The sample cell (0.2 ml) contained 6 µM TC-aptamer and the syringe contained 64 µM of TC. A 20 mM potassium phosphate buffer at pH = 7.5 with 100 mM sodium chloride and 10 mM manganese chloride was used. After preequilibration and an initial delay of 180 s, a first injection of 0.2 ml was performed, followed by 14 serial injections (2.5 ml each) with spacing of 180 s. Stirring speed was 1000 rpm. Data were recorded as differential power (DP, µW) over time (min). Afterwards, the heat associated with each titration step was integrated and plotted against the molar ratio between the titrant and the aptamer. Each binding isotherm was background-corrected for dilution effects.

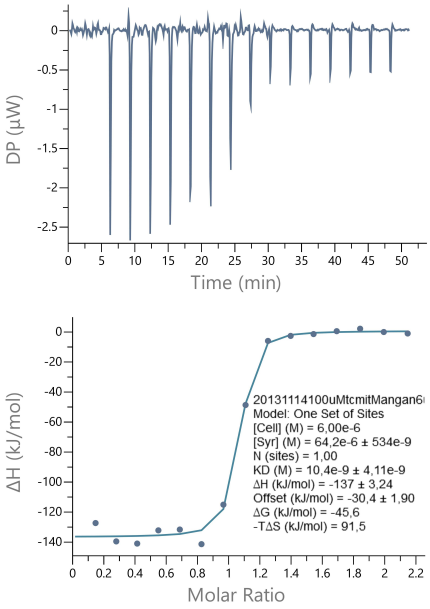

Figure S1: ITC-measurements of the TC-aptamer in the presence of 10 mM Mn^{2+}. A K_D value of 10 nM was obtained for ligand binding, which is identical to recently published results [1, 2].

2 Spin ladder diagram and model spectra for homonuclear THYCOS and 2D EDNMR

Figure S2 shows THYCOS and 2D EDNMR model spectra and the evolution of spin population when the RF pulse or the second ELDOR pulse excite the same nuclei that was already excited by the first ELDOR pulse (*e.g.*, I_1 in Figure S2). The 2D EDNMR model spectra in Figure S2 reflect the ^{31}P-^{31}P self-correlations in Figure 5 and 6 of the main manuscript.

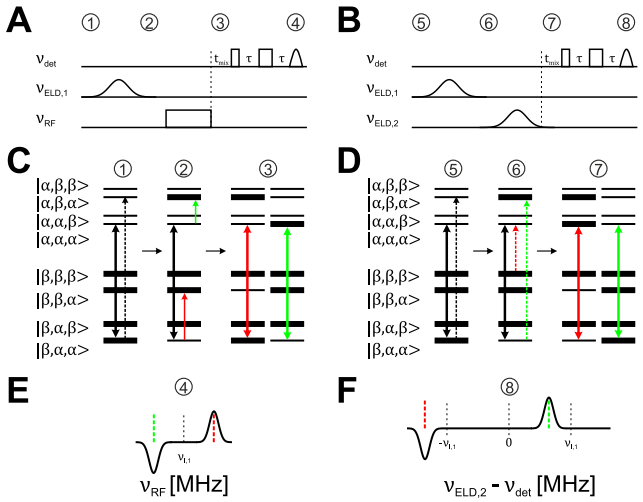

Figure S2: A and B) Pulse sequence of a THYCOS [3] (left) and a 2D EDNMR [4] (right) experiment. In both cases, Gaussian-shaped ELDOR pulses were used to minimize the spectral overlap of detection and ELDOR pulses. C and D) Energy ladder diagrams for a weakly coupled 8-level system, consisting of an electron spin with $S = 1/2$ and two different nuclear spins with $I_1 = 1/2$ and $I_2 = 1/2$ (g_N, $a_{iso} > 0$). Bold black arrows depict the detected allowed EPR transition, whereas the dashed black arrows (① & ⑤) depict the first ELDOR pulse, which is on-resonance with a forbidden transition of nuclei I_1. ②: For THYCOS, two allowed NMR transitions of nuclei I_1 (solid green and red arrows) are associated with the detected EPR transition. ⑥: For 2D EDNMR, two forbidden transitions of nuclei I_1 (dashed green and red arrows) are associated with the detected EPR transition. ③ & ⑦: Spin population before the echo detection sequence in THYCOS and 2D EDNMR respectively for excitation of the two nuclear transitions. E and F) THYCOS and 2D EDNMR model spectra. For homonuclear THYCOS and 2D EDNMR positive and negative signals are expected for both experiments.

3 Additional 1D EDNMR spectra

Figure S3 shows Q-band EDNMR data of a sample containing the TC-aptamer and Mn^{2+} before and after dialysis (Amicon 10 kDa filters) with potassium chloride (four times) and DEPC-treated MiliQ water (four times). Before ion exchange, a rather intense signal at the ^{23}Na-Larmor frequency ($\nu_{23Na} = 13.5\,\mathrm{MHz}$) is visible, that would heavily interfere with ^{13}C signals ($\nu_{13C} = 12.7\,\mathrm{MHz}$) and ^{13}C-^{31}P correlation signals. After dialysis, a small ^{13}C-carbon signal due to natural abundance ^{13}C remains visible.

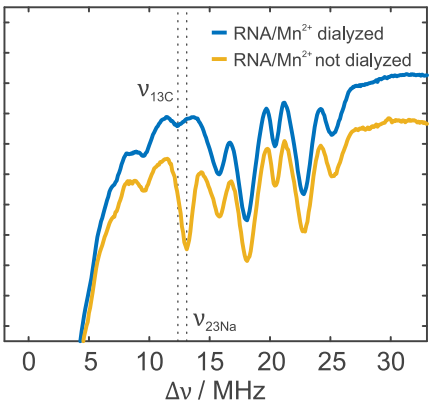

Figure S3: Q-band EDNMR spectra of a sample containing the TC-aptamer and Mn^{2+} before and after dialysis with potassium chloride and DEPC-treated MiliQ water. The Larmor frequencies of ^{13}C and ^{23}Na are depicted with dashed lines.

Figure S4 shows full-range EDNMR spectra of samples presented in Figure 3 of the main manuscript. ^{1}H resonances appear at $\Delta\nu = \pm 50.2\,\mathrm{MHz}$. EDNMR signals of the strongly-coupled ^{55}Mn nuclei ($I_{55Mn} = 5/2$) appear at $\Delta\nu = -157.0\,\mathrm{MHz}$, $\Delta\nu = -113.5\,\mathrm{MHz}$, $\Delta\nu = 113.0\,\mathrm{MHz}$ and $\Delta\nu = 155.5\,\mathrm{MHz}$. The splitting of the two ^{55}Mn signals on each side of the EDNMR spectrum is $\Delta\Delta\nu \approx 43\,\mathrm{MHz}$. The signals are centered around $\Delta\overline{\nu} \approx 135\,\mathrm{MHz}$, which is half the isotropic hyperfine coupling a_{iso}. The value of $\Delta\Delta\nu$ is larger than the expected first-order value of $2\nu_{55Mn} = 25.4\,\mathrm{MHz}$, which is due to a small electron Zeeman interaction in comparison to a large hyperfine interaction of a high spin nuclei [5].

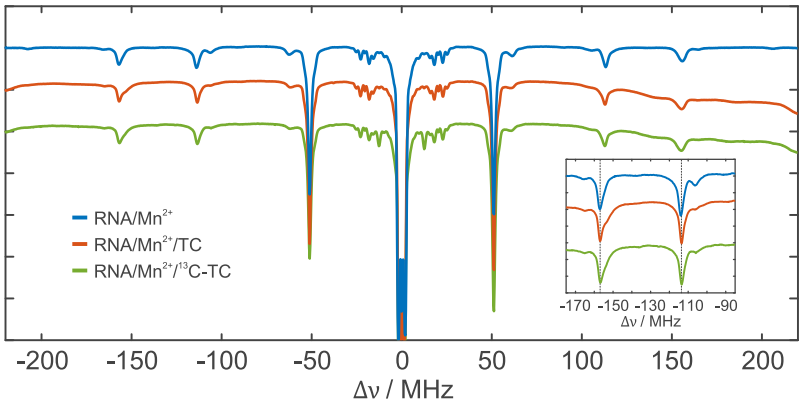

Figure S4: Full-range Q-band 1D EDNMR spectra (−220 MHz to 220 MHz) of different Mn^{2+} complexes. Blue: TC-aptamer with Mn^{2+}, red: TC-aptamer with Mn^{2+} and TC, green: TC-aptamer with Mn^{2+} and ^{13}C-labeled TC. The inset on the lower right expands the ^{55}Mn region of the full-range EDNMR spectra.

Figure S5 shows Q-band EDNMR spectra of samples with unlabeled TC (red spectra) and ^{13}C-labeled TC (green spectra) before (bold colored) and after (pale colored) three freeze-thaw cycles. The upper row shows the ^{13}C/^{31}P region, the lower row shows the ^{55}Mn region of EDNMR spectra. For both samples, an increase in intensity for the outer phosphorous coupling is observed after the freeze-thaw cycles, whereas the intensity of the inner phosphorous coupling is decreased. We therefore attribute the outer phosphorous coupling to degraded single stranded RNA (ssRNA), and the inner phosphorous coupling to intact double stranded RNA (dsRNA). The ^{13}C intensity decreases as well after the freeze-thaw cycles. This makes sense, as TC can only bind to dsRNA and not ssRNA, and the ssRNA binding sites seem to have a higher affinity toward Mn^{2+} than free TC. For both samples, the ^{55}Mn signals (especially the signals at $\Delta\nu \approx -155$ MHz) exhibit a broader linewidth after the freeze-thaw cycles. This is also expected, as Mn^{2+} ions coordinated by ssRNA are expected to have a slightly different coordination geometry compared to Mn^{2+} ions coordinated by dsRNA. Signals next to the ^{55}Mn peaks are due to ^{1}H-^{55}Mn combination frequencies [6].

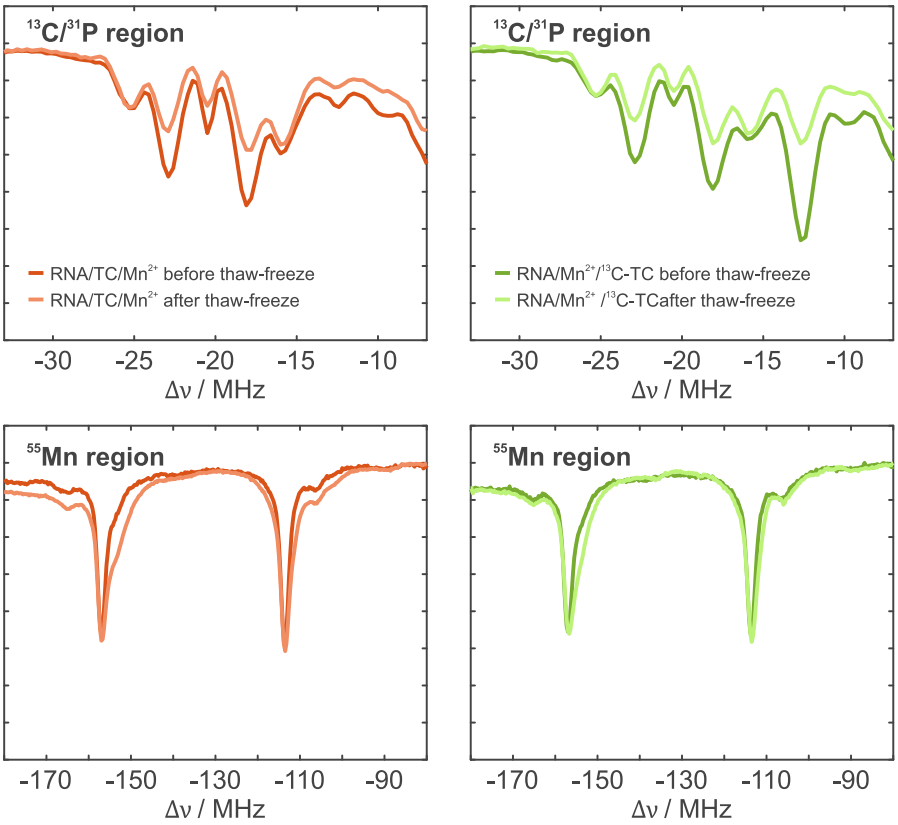

Figure S5: Q-band EDNMR spectra of different Mn^{2+} complexes before and after three freeze-thaw cycles. Red: TC-aptamer with Mn^{2+} and TC, green: TC-aptamer with Mn^{2+} and ^{13}C-labeled TC. The upper row shows the $^{13}C/^{31}P$ region, the lower row shows the ^{55}Mn region. Bold colored: before the freeze-thaw cycles, pale colored: after the freeze-thaw cycles. Spectra in the upper row are normalized to the intensity of the phosphorous signal at $\Delta\nu = -25\,\mathrm{MHz}$. Spectra in the lower row are normalized to the intensity of the manganese signal at $\Delta\nu = -155\,\mathrm{MHz}$.

4 ^{31}P-Davies ENDOR simulations and Mn^{2+} binding sites of the TC-aptamer

Figure S6 shows simulations of a ^{31}P-Davies ENDOR spectrum of a sample with TC-aptamer, Mn^{2+} and ^{13}C-labeled TC. Simulations were performed using the *salt* routine of the Matlab toolbox EasySpin [7].

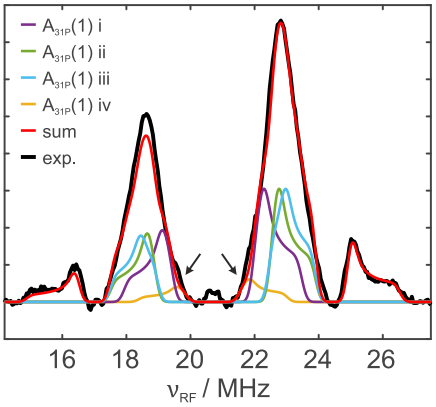

Figure S6: Simulation (red) of a ^{31}P-Davies ENDOR spectrum of a sample containing TC-aptamer, Mn^{2+} and ^{13}C-labeled TC (black). Four components were required to fit the inner hyperfine coupling. For the outer hyperfine coupling, one component was sufficient.

The outer hyperfine coupling $A_{31P}(2)$ could be fitted by assuming one axial hyperfine tensor (Table S1). For the inner hyperfine coupling $A_{31P}(1)$, four different rhombic hyperfine tensors were required (Table S1). Starting point for the 4-component fit was the 3-component fit by Un and Bruch to simulate a tridentate MnATP coordination sphere [8]. The isotropic hyperfine values by Un and Bruch had to be increased to achieve a good agreement. A fourth component was added to take into the account the flanks at 19.5 and 21.5 MHz (arrows in Figure S6). The ratio of the 4-component fit for $A_{31P}(1)$ was 1 : 1 : 1 : 0.2. A Gaussian linewidth of 0.3 MHz (full width half maximum) was used for all ^{31}P-Davies ENDOR simulations. Only the central electron transition was considered. An interpretation of the four different components is difficult, especially as the crystal structure shows 11

different Mn^{2+} binding sites (Figure S7). Although the affinities of these binding sites are not known, it can be assumed that the divalent metal ion in the binding pocket has the highest affinity out of all divalent metal ion binding sites in the presence of TC (1 in Figure S7).

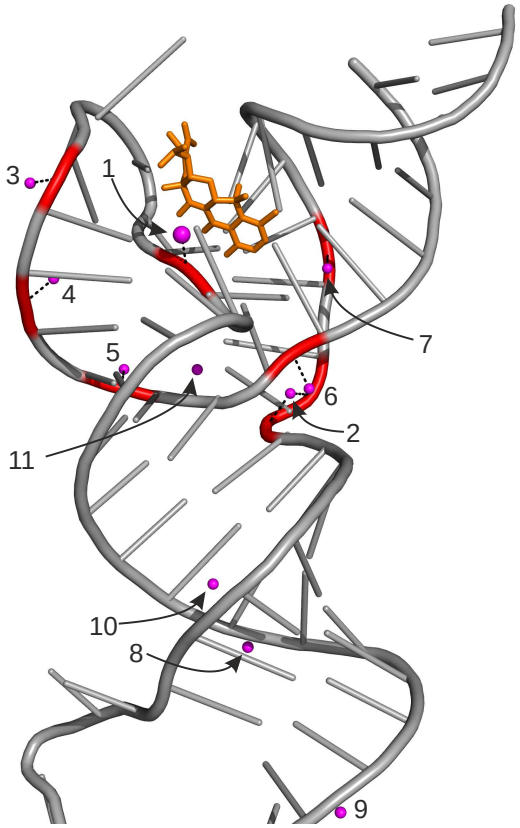

Figure S7: Stick-cartoon representation of the TC-aptamer in grey (PDB code: 3EGZ [9]) with 11 divalent metal ion binding sites (magenta). TC is shown in orange. Phosphate backbone groups that have a Mn^{2+}-^{31}P distance of $r < 0.4\,nm$ are indicated in red.

Out of the 11 divalent metal ions, 7 ions exhibit a Mn^{2+}-^{31}P distance of $r < 0.4\,nm$. Out of these 7, 4 exhibit a distance that is somewhat in agreement with the four components of $A_{31P}(1)$ (binding sites 1, 3, 4 and 6, Table S2). Still, we did not attempt to assign one of the components of the

simulation shown in Figure S6 to one of these binding sites. For example, Un and Bruch showed using experimental ENDOR data and quantum chemical DFT calculations, that even a single Mn-phosphorous binding site needs several components for an adequate fitting.

	a_{iso} / MHz	T / MHz	ρ / MHz	r / nm
$A_{31P}(1)$ i	3.75	0.90	-0.35	0.33
$A_{31P}(1)$ ii	4.70	0.85	-0.25	0.34
$A_{31P}(1)$ iii	4.80	0.80	-0.55	0.34
$A_{31P}(1)$ iv	2.85	0.90	-0.35	0.33
$A_{31P}(2)$	9.55	1.05	-	0.31
binding site 1	-	0.98	-	0.32
binding site 2	-	0.63/0.69	-	0.36/0.37
binding site 3	-	0.90	-	0.33
binding site 4	-	0.90	-	0.33
binding site 5	-	0.69	-	0.37
binding site 6	-	0.75	-	0.35
binding site 7	-	0.69	-	0.37
binding site 8	-	-	-	-
binding site 9	-	-	-	-
binding site 10	-	-	-	-
binding site 11	-	-	-	-

Table S1: Hyperfine tensors that were needed to simulate the ^{31}P-Davies ENDOR spectrum shown in Figure S6. The ratio of the four rhombic hyperfine tensors for $A_{31P}(1)$ was $1:1:1:0.2$. For comparison, ^{31}P-Mn^{2+} crystal structure distances and dipolar hyperfine couplings T assuming the point-dipole approximation of binding sites with ^{31}P-Mn^{2+} distances of $r < 0.4\,\mathrm{nm}$ are also shown.

5 ^{13}C-Mims ENDOR simulations and additional ^{13}C-Mims ENDOR spectra

The ^{13}C-Mims ENDOR spectrum of a sample containing TC-aptamer, Mn^{2+} and ^{13}C-labeled TC was background-corrected by subtracting the ^{13}C-Mims ENDOR spectrum of a sample containing TC-aptamer, Mn^{2+} and unlabeled TC (recorded with identical experimental parameters). As can be seen from Figure S8, the spectrum of the unlabeled sample features a significantly distorted baseline, that is also present in the spectrum of the sample containing ^{13}C-labeled TC.

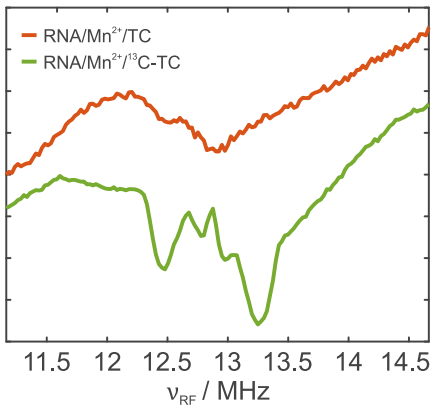

Figure S8: Raw ^{13}C-Mims ENDOR spectra of different Mn^{2+} complexes. Red: TC-aptamer with Mn^{2+} and TC, green: TC-aptamer with Mn^{2+} and ^{13}C-labeled TC.

A ^{13}C-Mims ENDOR spectrum with a higher τ value led to more distortions due to the Mims ENDOR suppression function $F_{ENDOR} \propto sin^2(\pi A\tau)$ (units of MHz and µs for A and τ). For $\tau = 500$ ns, blindspots appeared at 11.8 MHz and 14.8 MHz (asterisks in Figure S9). In return, signals close to the ^{13}C-Larmor frequency gained in intensity, however, no new information could be obtained.

Simulations using the Matlab toolbox EasySpin for two different τ values yielded two different possibilities for the larger ^{13}C-hyperfine coupling. These were $a_{iso} = 1.3$ MHz and $T = 0.6$ MHz (red, left column of Figure S9)

or $a_{iso} = -0.4\,\mathrm{MHz}$ and $T = -1.2\,\mathrm{MHz}$ (orange, right column of Figure S9),
105 although the second possibility gives a slightly better agreement. ^{13}C-Mn^{2+} distances extracted from the crystal structure do, however, favor the first possibility.

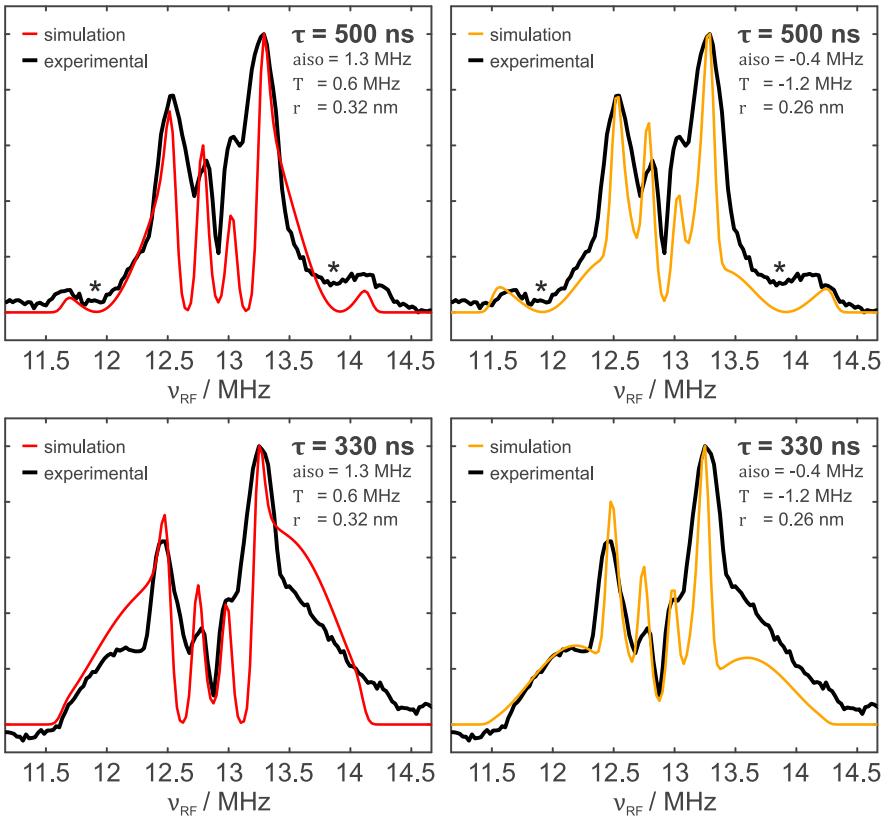

Figure S9: Q-band ^{13}C-Mims ENDOR spectra of a sample containing TC-aptamer, Mn^{2+} and ^{13}C-labeled TC (black) recorded at different τ values. First row: $\tau = 500\,\mathrm{ns}$, second row: $\tau = 330\,\mathrm{ns}$. Mims ENDOR blindspots are marked by asterisks. Simulations, convoluted with the Mims ENDOR suppression function, are shown in red or orange. Two different possibilities for the larger hyperfine coupling are presented. First column: $a_{iso} = 1.3\,\mathrm{MHz}$ and $T = 0.6\,\mathrm{MHz}$, second column: $a_{iso} = -0.4\,\mathrm{MHz}$ and $T = -1.2\,\mathrm{MHz}$.

Due to the featureless appearance of the smaller hyperfine coupling, we used values of $a_{iso} = 0.08\,\mathrm{MHz}$ and $T = 0.16\,\mathrm{MHz}$ for both cases. A Gaus-

sian linewidth of 0.9 MHz and a Lorentzian linewidth of 0.4 MHz were used for all simulations. Only the central electron transition was considered. Simulations were convoluted with the suppression function F_{ENDOR} to account for Mims ENDOR blindspots. This is an idealized assumption, as the experimental spectra do not exhibit zero intensity at the ^{13}C-Larmor frequency. F_{ENDOR} was therefore dampened to obtain a better agreement with experimental spectra. The non-ideal behavior of F_{ENDOR} most likely stems from the fact that the $\pi/2$ pulses are not infinitely short and perfect 90° pulses, which leads to a smeared out polarization grating. We did not attempt a multi-component fit of the larger ^{13}C-hyperfine coupling.

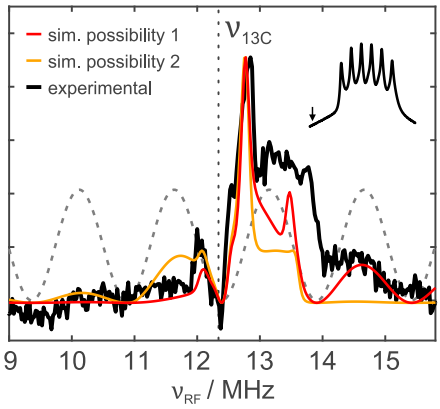

Figure S10: Q-band ^{13}C-Mims ENDOR spectrum ($\tau = 330$ ns) of a sample containing TC-aptamer, Mn^{2+} and ^{13}C-labeled TC (black) recorded on the low field edge of the echo-detected field-swept spectrum (1.16 T, marked by an arrow). The simulation of the first possibility ($a_{iso} = 1.3$ MHz and $T = 0.6$ MHz) is shown in red, the simulation of the second possibility is shown in orange ($a_{iso} = -0.4$ MHz and $T = -1.2$ MHz). Simulations were convoluted with the Mims ENDOR suppression function, which is shown in grey for $\tau = 330$ ns.

In order to reveal which possibility for the outer hyperfine coupling is more likely, we performed Mims ENDOR experiments at the low field edge of the echo-detected field-swept spectrum (1.16 T, 33.77 GHz). In such a case, the detection pulses should mainly excite the outer electron transitions $|m_S = -3/2\rangle \leftrightarrow |-1/2\rangle$ and $|m_S = -5/2\rangle \leftrightarrow |-3/2\rangle$. The nuclear resonances are then no longer centered symmetrically around the nuclear

Larmor frequency, but are shifted to either the right or left side of the spectrum, which depends on the sign of the hyperfine coupling and the sign of the nuclear g-value (which is known). Figure S10 shows that most of the intensity is confined to the right side of the Mims ENDOR spectrum. This supports the first possibility presented in Figure S9, as here nuclear transitions in electron spin manifolds of $|m_S = -3/2\rangle$ and $|m_S = -1/2\rangle$ should solely resonate at higher frequencies than the Larmor frequency (red simulation in Figure S10). For the second possibility (orange simulation in Figure S10), we would still expect an asymmetric spectrum with respect to the Larmor frequency, however, we would expect rather similar intensities on both sides of the Larmor frequency (if one ignores the sharp signal at 12.7 MHz). This is due to the fact that the powder pattern of one nuclear transition already resonates on both sides of the Larmor frequency (because $T > a_{iso}$).

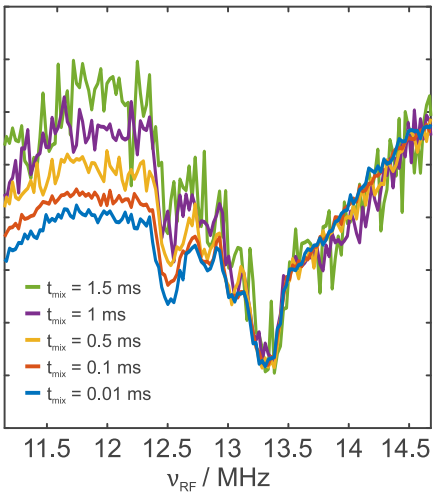

Figure S11: Q-band variable mixing time ^{13}C-Mims ENDOR spectra of a sample containing TC-aptamer, Mn^{2+} and ^{13}C-labeled TC. Different mixing times of $t_{mix} = 0.01$, 0.1, 0.5, 1 and 1.5 ms were used. For VMT Mims ENDOR spectra, no baseline correction was performed.

Another option to distinguish between the two possibilities presented in Figure S9 is to perform variable mixing time ENDOR (VMT ENDOR) ex-

periments [10]. In such an experiment, the time t_{mix} between the end of the RF pulse and the third detection pulse is varied. At higher mixing times and at sufficiently cold temperatures or high magnetic fields, the nuclear transitions in the $|m_S = \beta\rangle$ and $|m_S = \alpha\rangle$ manifold will exhibit different ENDOR efficiencies. More precisely, the ENDOR efficiency of the nuclear transition in the $|m_S = \alpha\rangle$ manifold will decrease, whereas the ENDOR efficiency of the nuclear transition in the $|m_S = \beta\rangle$ manifold will stay constant. Figure S11 shows that the intensity of the signal at 12.5 MHz decreases with longer mixing times t_{mix}, whereas the signal at 13.4 MHz stays constant. The signal at 12.5 MHz must therefore correspond to the nuclear transition in the $|m_S = \alpha\rangle$ manifold, which means that the hyperfine coupling must be positive. VMT ENDOR therefore supports the first possibility presented in Figure S9, which is in line with ENDOR studies performed on the low field edge (Figure S10).

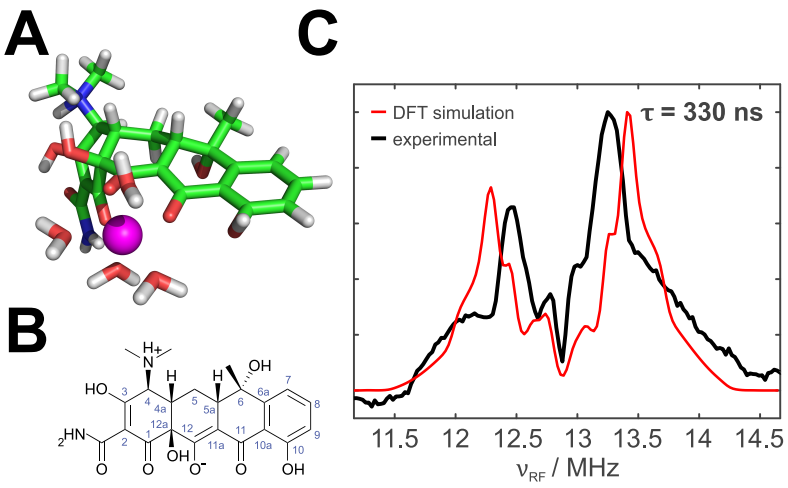

Figure S12: A) Stick presentation of TC and the divalent metal ion as found in the crystal structure. B) Secondary structure of TC with complete carbon numbering. DFT-calculations were performed on a zwitterionic TC form, which is expected to be the main conformation at pH = 7.5. C) Simulation (red, convoluted with suppression function F_{ENDOR}) of DFT-derived ^{13}C-hyperfine tensors of TC compared to the experimental ^{13}C-Mims ENDOR spectrum of a sample containing TC-aptamer, Mn^{2+} and ^{13}C-labeled TC (black).

We also performed DFT-calculations of a Mn-TC complex to further substantiate the findings of low field edge ENDOR (Figure S10) and VMT ENDOR (Figure S11). Figure S12A shows TC and the divalent metal ion as found in the crystal structure. Water molecules were added to complete a hexacoordinated Mn^{2+} ion. Figure S12B shows the secondary structure of TC with a complete numbering of the carbon atoms. DFT-calculations were carried out using ORCA 4.0 [11]. A *6-31+G(d,p)* basis set, the *PBE0* hybrid functional, the *Grid5* option and the *C-PCM* solvation model (water as solvent) were used. No further geometry optimization was performed. The $TightSCF$ option was used as convergence criteria.

	a_{iso} / MHz	T / MHz	ρ / MHz	r / nm
C11	1.7	0.72	0.065	0.30
C12	1.7	0.54	0.12	0.33
C11a	1.1	0.33	0.22	0.39
C10a	0.67	0.29	0.045	0.41
C12a	0.45	0.24	0.025	0.44
C10	0.083	0.19	0.035	0.47
C1	0.020	0.16	0.010	0.50
C5a	0.033	0.15	-	0.51
C6a	0.25	0.11	0.040	0.57
C4a	0.037	0.10	-	0.58

Table S2: DFT-derived ^{13}C-hyperfine tensors of Mn-TC that feature a significant isotropic hyperfine coupling constant a_{iso} and/or a dipolar coupling constant T.

Table S2 shows results of the DFT-calculation. For a better overview, only carbon atoms that feature a significant isotropic hyperfine coupling a_{iso} and/or a dipolar coupling T are shown. It is clear, that the hyperfine tensors of the closest carbon atoms (C11 and C12) agree more with the first possibility ($a_{iso} = 1.3\,\mathrm{MHz}$ and $T = 0.6\,\mathrm{MHz}$) than with the second possibility ($a_{iso} = -0.4\,\mathrm{MHz}$ and $T = -1.2\,\mathrm{MHz}$). This is in line with the low field ENDOR and VMT ENDOR results. Figure S12C shows a Mims ENDOR simulation (convoluted with F_{ENDOR}) based on all DFT-derived hyperfine tensors. The overall lineshape of the experimental spectrum is well reproduced. The splitting (mainly caused by a_{iso}) is slightly overestimated by the DFT-calculation.

6 Additional 2D EDNMR spectra

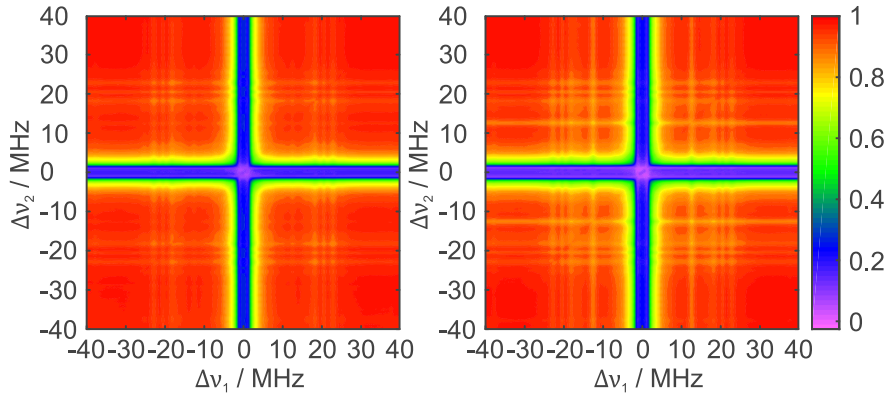

Figure S13: Primary Q-band 2D EDNMR spectra before background correction of samples containing TC-aptamer, Mn^{2+} and TC (left) and TC-aptamer, Mn^{2+} and ^{13}C-labeled TC (right).

Figure S14 and Figure S15 show all four quadrants of samples containing TC-aptamer, Mn^{2+} and unlabeled (Figure S14) or ^{13}C-labeled TC (Figure S15). As can be seen, the minus-minus and plus-minus quadrant (lower quadrants) are identical to the plus-plus and minus-plus quadrant, that were already presented in Figure 5 of the main manuscript. The "horizontal line" in the lower quadrants of Figure S14 is a consequence of a phase instability in a slice used for background correction, that thus propagated into the complete 2D EDNMR spectrum.

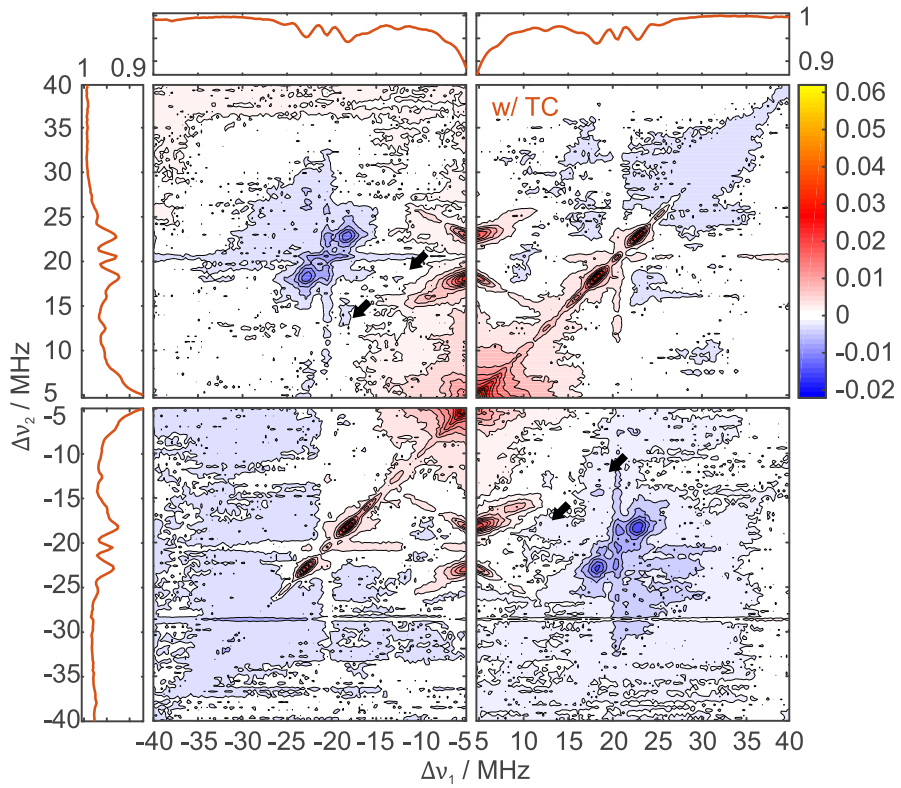

Figure S14: All four quadrants of a background-corrected Q-band 2D EDNMR spectrum of a sample containing TC-aptamer, Mn^{2+} and TC.

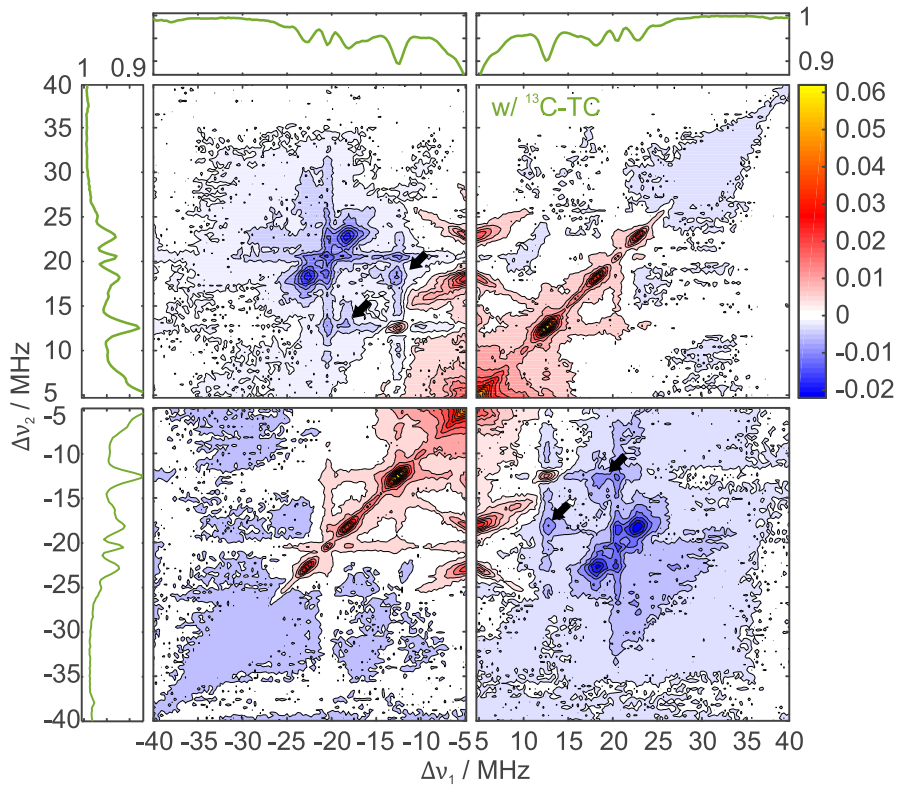

Figure S15: All four quadrants of a background-corrected Q-band 2D EDNMR spectrum of a sample containing TC-aptamer, Mn^{2+} and ^{13}C-labeled TC.

Figure S16, S17 and S18 show background-corrected Q-band EDNMR spectra of additional Mn^{2+} complexes. The 2D EDNMR spectrum of Mn^{2+} with inorganic phosphate (MnP_i) (Figure S16) shows clear correlation signals between ^{31}P and ^{23}Na, which is present in huge amounts, as sodium phosphate was used for formation of MnP_i. The "cross-like" signals, that were discussed in the main manuscript, are also present, although to a weaker extent (circles in Figure S16).

The 2D EDNMR spectrum of Mn-^{13}C-DOTA (Figure S17) is characterized by a series of congested correlation signals of ^{13}C and ^{14}N, which makes an in-depth analysis difficult. Surprisingly, a negative ^{14}N-^{14}N correlation of ^{14}N double quantum transitions at $(-10,10)$ and $(10,-10)$ MHz is absent, however, various ^{13}C-^{14}N correlation signals appear in all quadrants of the spectrum (positive and negative signals).

Not surprisingly, the 2D EDNMR spectrum of MnH_2O is finally free of any correlation signals (Figure S18). ^1H signals resonate at $\Delta\nu = \pm 50$ MHz, and are therefore not observed in Figure S18. We attribute the diagonal lines in the plus-plus and minus-minus quadrant to minor artifacts of the background correction.

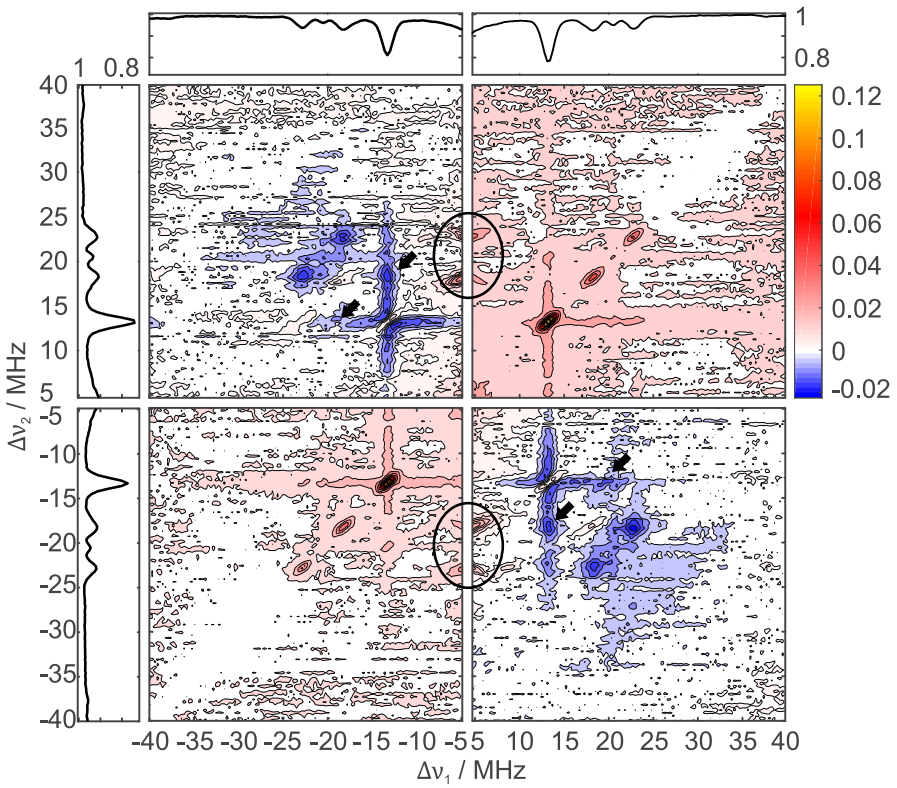

Figure S16: All four quadrants of a background-corrected Q-band 2D EDNMR spectrum of a sample containing Mn^{2+} (0.5 mM) and sodium phosphate (5 mM). Signals at ±13.5 MHz are due to Na^{+} ions, that interact via the negatively charged phosphate with Mn^{2+}. Black circles highlight "cross-like" signals, that were also observed in Figure 5 of the main manuscript.

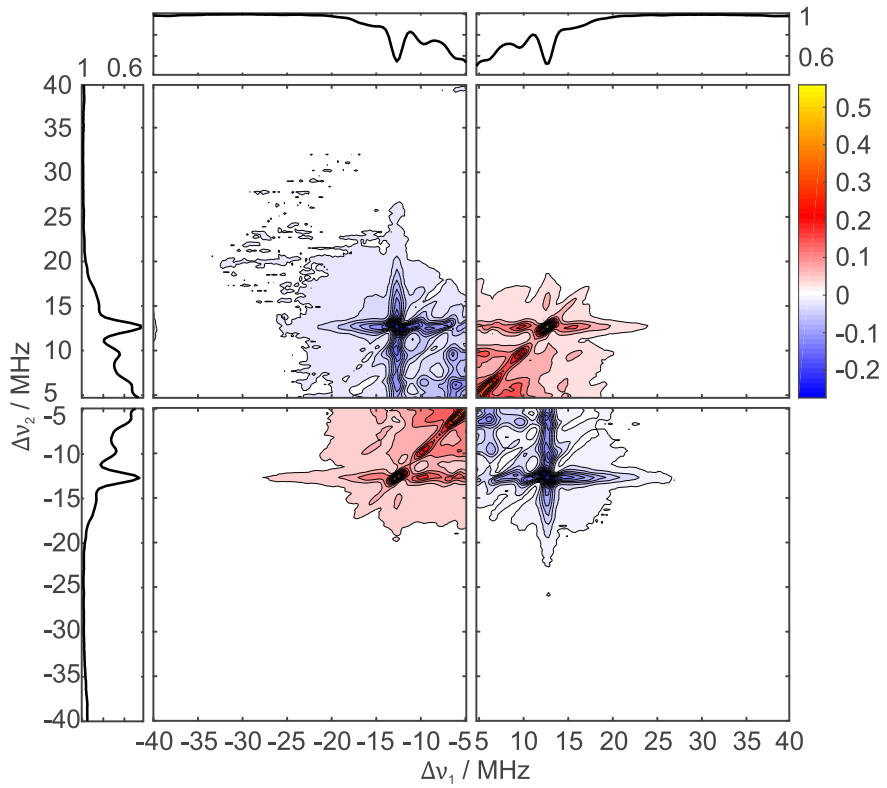

Figure S17: All four quadrants of a background-corrected Q-band 2D EDNMR spectrum of Mn-^{13}C-DOTA (2 mM).

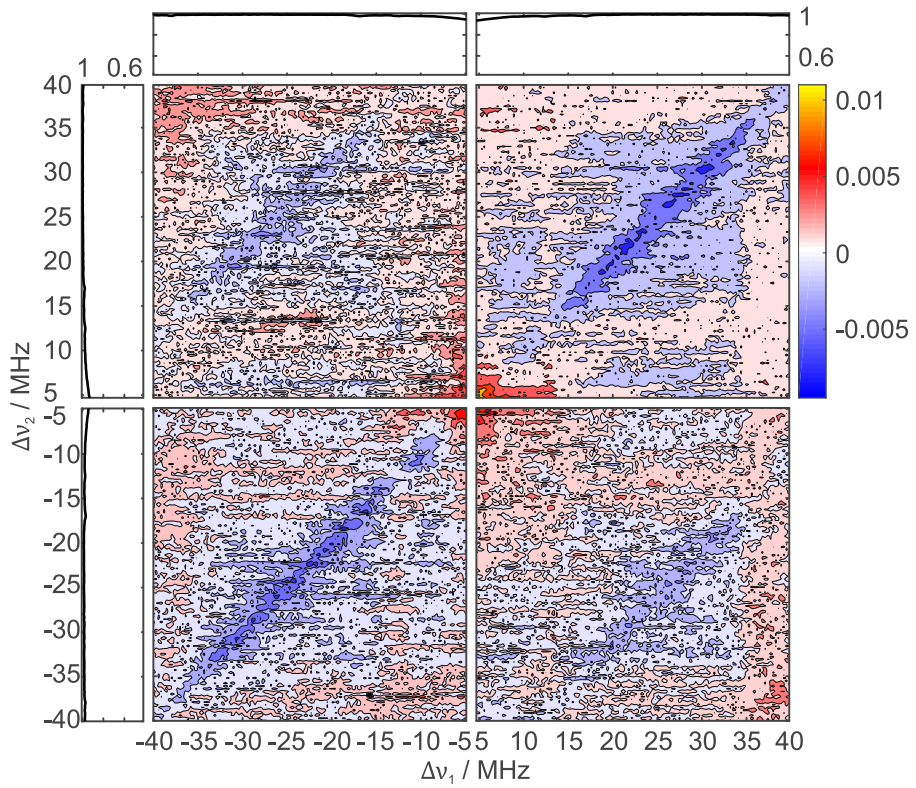

Figure S18: All four quadrants of a background-corrected Q-band 2D EDNMR spectrum of MnH_2O (1 mM). No discernible signals were observed in the region presented.

7 Additional THYCOS spectra

Figure S19 shows homonuclear ^{31}P-^{31}P THYCOS spectra of a sample containing TC-aptamer, Mn^{2+} and TC (THYCOS spectra of a sample with ^{13}C-labeled TC were identical to those presented in Figure S19). As also shown in the THYCOS model spectrum presented in Figure S2E, negative THYCOS signals are observed for those nuclear spin manifolds that were already affected by the ELDOR pulse. Positive THYCOS signals are observed for nuclear spin manifolds that originate from the other electron spin manifold. This homonuclear THYCOS pattern is clearly visible for the inner phosphorous hyperfine coupling (signals at 18.1 and 22.9 MHz).

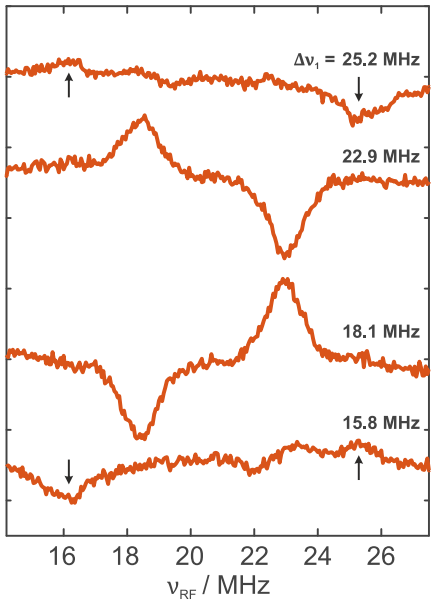

Figure S19: Q-band ^{31}P-^{31}P THYCOS spectra of a sample containing TC-aptamer, Mn^{2+} and TC. The frequency offsets of the ELDOR pulse $\Delta\nu_1$ were chosen to be on-resonance with the four ^{31}P signals that were also observed in the ^{31}P-Davies ENDOR spectrum (Figure 4A of the main manuscript). The arrows indicate self-correlation signals of the outer ^{31}P-hyperfine coupling.

For the outer hyperfine coupling, the analysis is a bit more difficult. Upon careful inspection, however, a positive signal at 25.2 MHz is visible if the nuclear spin manifold at $\Delta\nu_1 = 15.8$ MHz gets excited by the ELDOR pulse (and *vice versa*, see arrows in Figure S19). The positive signal at 25.2 MHz is absent if the inner phosphorous hyperfine coupling gets excited by the ELDOR pulse (18.1 or 22.9 MHz). We therefore conclude, that the two different phosphorous couplings do not interact with the same Mn^{2+} ion, which is in line with the aforementioned EDNMR freeze-thaw cycle experiments (Figure S5).

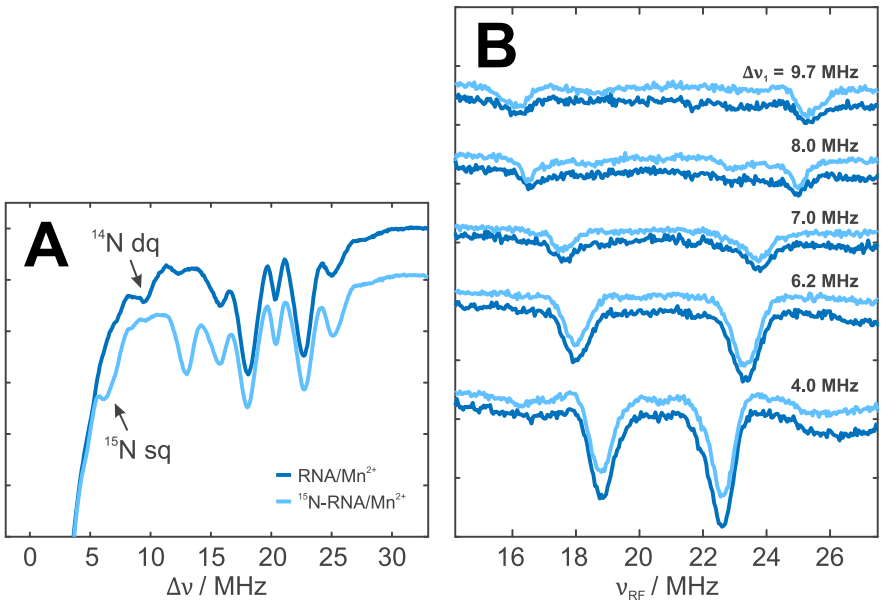

Figure S20: A) Q-band 1D EDNMR spectra of different Mn^{2+} complexes. Bold blue: TC-aptamer with Mn^{2+}, pale blue: ^{15}N-labeled TC-aptamer with Mn^{2+}. The ^{15}N-labeled TC-aptamer exhibits a strong ^{23}Na signal at 13.5 MHz from the RNA purification process, as no Na^+/K^+ buffer exchange was performed. B) Q-band THYCOS spectra of the aforementioned samples. The RF pulse was used to sample the ^{31}P region. The frequency offset of the ELDOR pulse, $\Delta\nu_1$, is indicated in the figure. Artifacts, due to off-resonance ELDOR pulse effects, gain in intensity with decreasing $\Delta\nu_1$ values.

Figure S20 shows a comparison of 1D EDNMR (Figure S20A) and THYCOS (Figure S20B) spectra for a sample containing TC-aptamer and Mn^{2+} (bold blue) and a sample containing ^{15}N-labeled TC-aptamer and Mn^{2+} (pale blue). Significant differences in the EDNMR spectra involve the strong ^{23}Na signal of the ^{15}N-labeled sample, as here no Na^+/K^+ buffer exchange was performed. More importantly, the ^{15}N-labeled sample features a ^{15}N single quantum (sq) signal at 6.2 MHz ($\nu_{15N} = 5.2$ MHz), which would correspond to $A_{15N} \approx 2.0$ MHz. The unlabeled sample obviously misses this signal, but is instead characterized by a ^{14}N double quantum signal (dq, $\Delta m_S = \pm 1$, $\Delta m_I = \pm 2$) at 9.7 MHz. More nitrogen signals at lower frequency offsets are obscured by the central blindspot. In spite of the differences of the EDNMR spectra, the THYCOS spectra of these two samples (Figure S20B) are essentially identical. Here, the RF pulse was used to sample the ^{31}P region, and the frequency offset $\Delta\nu_1$ of the ELDOR pulse matched the region of ^{15}N sq and ^{14}N dq signals. The similarity of the THYCOS spectra underlines that the observed negative THYCOS signals are not ^{14}N-^{31}P correlation signals, but rather a consequence of off-resonance effects caused by the ELDOR pulse as $\Delta\nu_1$ approaches zero. The signals observed in Figure S20B correspond to the "cross-like" signals, that were already observed in 2D EDNMR spectra (Figure S14, S15, S16 and Figure 5 in the main manuscript).

References

[1] A. J. Reuss, M. Vogel, J. E. Weigand, B. Suess, J. Wachtveitl, Tetracycline determines the conformation of its aptamer at physiological magnesium concentrations, Biophys. J. 107 (2014) 2962–2971. doi:10.1016/j.bpj.2014.11.001.

[2] T. Hetzke, M. Vogel, D. B. Gophane, J. E. Weigand, B. Suess, S. T. Sigurdsson, T. F. Prisner, Influence of Mg 2+ on the conformational flexibility of a tetracycline aptamer, RNA 25 (2019) 158–167. doi:10.1261/rna.068684.118.

[3] A. Potapov, B. Epel, D. Goldfarb, A triple resonance hyperfine sublevel correlation experiment for assignment of electron-nuclear double resonance lines, J. Chem. Phys. 128 (2008) 052320.1–052320.10. doi:10.1063/1.2833584.

[4] I. Kaminker, T. D. Wilson, M. G. Savelieff, Y. Hovav, H. Zimmermann, Y. Lu, D. Goldfarb, Correlating nuclear frequencies by two-dimensional ELDOR-detected NMR spectroscopy, J. Magn. Reson. 240 (2014) 77–89. doi:10.1016/j.jmr.2013.12.016.

[5] B. E. Sturgeon, J. A. Ball, D. W. Randall, R. D. Britt, 55Mn electron spin echo ENDOR of Mn2+ complexes, J. Phys. Chem. 98 (1994) 12871–12883. doi:10.1021/j100100a012.

[6] T. Hetzke, A. M. Bowen, T. F. Prisner, ELDOR-detected NMR at Q-band, Appl. Magn. Reson. 48 (2017) 1375–1397. doi:10.1007/s00723-017-0927-4.

[7] S. Stoll, A. Schweiger, EasySpin, a comprehensive software package for spectral simulation and analysis in EPR, J. Magn. Reson. 178 (2006) 42–55. doi:10.1016/j.jmr.2005.08.013.

[8] S. Un, E. M. Bruch, How bonding in manganous phosphates affects their Mn(II)-31P hyperfine interactions, Inorg. Chem. 54 (2015) 10422–10428. doi:10.1021/acs.inorgchem.5b01864.

[9] H. Xiao, T. E. Edwards, A. R. Ferré-D'Amaré, Structural basis for specific, high-affinity tetracycline binding by an in vitro evolved aptamer and artificial riboswitch, Chem. Biol. 15 (2008) 1125–1137. doi:10.1016/j.chembiol.2008.09.004.

[10] M. Bennebroek, J. Schmidt, Pulsed ENDOR spectroscopy at large thermal spin polarizations and the absolute sign of the hyperfine interaction, J. Magn. Reson. 128 (1997) 199–206. doi:10.1006/jmre.1997.1234.

[11] F. Neese, The ORCA program system, Wiley Interdiscip. Rev. Comput. Mol. Sci. 2 (2012) 73–78. doi:10.1002/wcms.81.

METHOD

Influence of Mg^{2+} on the conformational flexibility of a tetracycline aptamer

THILO HETZKE,[1] MARC VOGEL,[2] DNYANESHWAR B. GOPHANE,[3] JULIA E. WEIGAND,[2] BEATRIX SUESS,[2] SNORRI TH. SIGURDSSON,[3] and THOMAS F. PRISNER[1]

[1]Institute of Physical and Theoretical Chemistry and Center of Biomolecular Magnetic Resonance, Goethe University Frankfurt, 60438 Frankfurt am Main, Germany

[2]Department of Biology, Technical University of Darmstadt, 64287 Darmstadt, Germany

[3]Department of Chemistry, Science Institute, University of Iceland, 101 Reykjavik, Iceland

ABSTRACT

The tetracycline-binding RNA aptamer (TC-aptamer) is a synthetic riboswitch that binds the antibiotic tetracycline (TC) with exceptionally high affinity. Although a crystal structure exists of the TC-bound state, little is known about the conformational dynamics and changes upon ligand binding. In this study, pulsed electron paramagnetic resonance techniques for measuring distances (PELDOR) in combination with rigid nitroxide spin labels (Çm spin label) were used to investigate the conformational flexibility of the TC-aptamer in the presence and absence of TC at different Mg^{2+} concentrations. TC was found to be the essential factor for stabilizing the tertiary structure at intermediate Mg^{2+} concentrations. At higher Mg^{2+} concentrations, Mg^{2+} alone is sufficient to stabilize the tertiary structure. In addition, the orientation of the two spin-labeled RNA helices with respect to each other was analyzed with orientation-selective PELDOR and compared to the crystal structure. These results demonstrate for the first time the unique value of the Çm spin label in combination with PELDOR to provide information about conformational flexibilities and orientations of secondary structure elements of biologically relevant RNAs.

Keywords: tetracycline aptamer; conformational flexibility; divalent metal ions; PELDOR; DEER; synthetic riboswitches

INTRODUCTION

Over past years, the role of RNAs in life sciences has changed from a pure information carrier in protein biosynthesis to a more active component in gene regulation. One of the new roles for RNAs are riboswitches, which are typically found in the untranslated regions of bacterial mRNA and bind specific small molecules with high affinity. Binding of the ligand leads to a conformational change of the aptamer domain, which in turn alters gene regulation. Based on this concept, artificially engineered riboswitches have attracted attention, with the ultimate goal of using engineered riboswitches in gene therapy (Breaker 2012; Groher and Suess 2014; Hallberg et al. 2017).

A promising synthetic riboswitch is the approximately 60 nucleotide (nt) long tetracycline aptamer (TC-aptamer), discovered by SELEX in the Schroeder laboratory (Berens et al. 2001), that binds the antibiotic TC (Fig. 1A). Besides the nontoxicity and good cell permeability of TC (Chopra and Roberts 2001), several other aspects make the TC-aptamer widely used as a synthetic riboswitch. Firstly, the TC-aptamer exhibits a K_d value in the sub-nanomolar range (K_d = 800 pM), which is one of the highest affinities of an aptamer toward its ligand (Müller et al. 2006). Secondly, the TC-aptamer is one of the few aptamers that is known to function as a riboswitch in vivo, where it can control translation and splicing (Weigand and Suess 2007; Kötter et al. 2009; Vogel et al. 2018). Although several small molecule binding aptamers have been selected, only a few aptamers show riboswitch activity in vivo, namely the tetracycline, the theophylline, the neomycin and the biotin aptamer (Berens et al. 2015).

Therefore, a series of experimental studies have been performed in order to investigate which structural motifs are responsible for the unique properties of the TC-aptamer. Hanson and coworkers showed by using chemical probing experiments, in combination with fluorescence measurements, that loop 3 (*L3*, cyan in Fig. 1B,

Corresponding author: prisner@chemie.uni-frankfurt.de

Article is online at http://www.rnajournal.org/cgi/doi/10.1261/rna.068684.118.

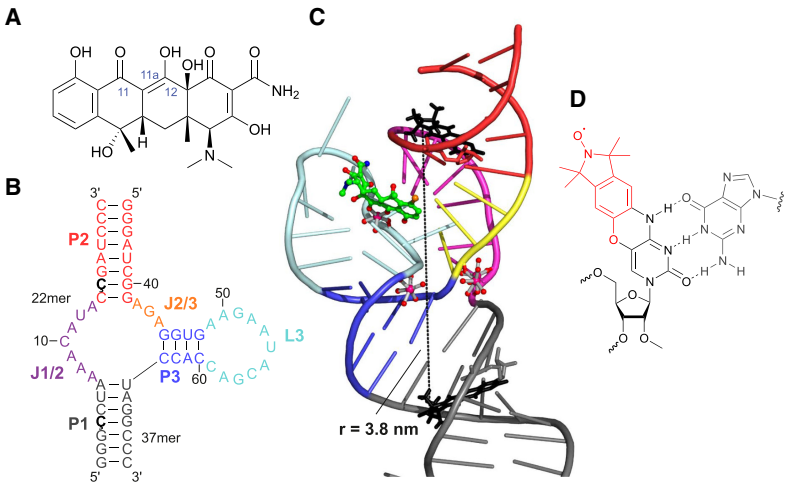

FIGURE 1. (*A*) Chemical structure of the antibiotic TC. Metal ligation typically occurs via O11 and O12. (*B*) Secondary structure of the TC-aptamer as used for Mg^{2+} titration experiments. Two Çm nucleosides are shown in black. (*C*) Cartoon representation of a TC-binding RNA aptamer based on the crystal structure by Xiao et al. (2008). Selected Mg^{2+}-ions are shown in magenta. TC is shown in green. Two rigid nitroxide spin labels (Çm) were attached to the crystal structure (shown in black). The expected distance between the two unpaired electron spins is 3.8 nm. (*D*) Chemical structure of Çm. Two covalent bonds between the nitroxide moiety (red) and cytidine significantly reduce the internal flexibility of Çm.

C) is crucial for binding of TC (Hanson et al. 2005), which was later confirmed by the crystal structure of the TC-aptamer bound to its cognate ligand (Xiao et al. 2008). The tertiary structure was found to be fairly complex, resembling an "h-shaped" structure that is reminiscent of larger, natural occurring riboswitches and rather unusual for other aptamers of comparable size (McCown et al. 2017). The crystal structure also revealed that TC binds as a Mg^{2+}-ion chelate to the aptamer (Fig. 1C). The TC chelate complex is further stabilized by a series of noncovalent interactions with different nucleotides in the binding pocket. In addition, more Mg^{2+} ions were found to bind near junctions *J1/2* and *J2/3* of the aptamer. Although a crystal structure yields a highly resolved three-dimensional picture, care has to be taken of interpreting structural motifs and their function solely based on crystal structure data (Nelson and Uhlenbeck 2006). It cannot be deduced from the crystal structure on how the tertiary structure looks in the absence of TC or how the Mg^{2+} concentration affects RNA folding and ligand binding. In addition, crystal-packing effects can distort the physiological conformation.

To answer these questions, Wunnicke and coworkers performed EPR (electron paramagnetic resonance) experiments on a nitroxide-labeled TC-aptamer in the absence and presence of TC (Wunnicke et al. 2011). They proposed a tertiary structure in the absence of TC in which mainly the junction *J1/2* between the stems *P1* and *P2* gets displaced. Förster and coworkers used time-resolved fluorescence measurements of the ligand TC to investigate the folding kinetics of the wild-type aptamer and three mutants (Förster et al. 2012). It was found that the ligand binds to the aptamer in a two-step process. In a first reversible process, the ligand is recognized by the RNA. In a second irreversible reaction, the aptamer forms its final tertiary structure. Out of the three mutants, mutant A9G had the strongest impact on the folding kinetics. Here, the kinetics were slowed down by several orders of magnitude. In a follow-up study, Reuss and coworkers examined the influence of Mg^{2+} concentration on the folding kinetics and thermodynamics of the aptamer by using isothermal titration calorimetry (ITC), circular dichroism (CD) spectroscopy, fluorescence spectroscopy, and melting studies. Among others, it was concluded that at high Mg^{2+} concentrations (>1.5 mM), the aptamer adopts its near-final tertiary structure, even in the absence of TC (Reuss et al. 2014).

In the present study, we used pulsed electron–electron double resonance spectroscopy (PELDOR, also called DEER) (Milov et al. 1981; Pannier et al. 2000) to measure intramolecular distances and thereby conformational flexibility of a frozen conformational ensemble of a doubly nitroxide-labeled TC-aptamer at different Mg^{2+} concentrations in the presence and absence of TC. In PELDOR, the integrated echo intensity of a refocused Hahn echo (RHE) is monitored as a function of the incremented time t before the pump pulse with the microwave frequency ν_B (Fig. 2A). As a result, the recorded PELDOR time traces oscillate with the dipolar coupling frequency ω_{dd}, which is inversely proportional to r^3. Tikhonov regularization of background-corrected PELDOR time traces (Fig. 2B, left) then yields a probability function $P(r)$ for the distance distribution (Fig. 2B, right). Another important parameter besides the distance distribution $P(r)$ is the modulation depth Δ. For a pure 2-spin system (as shown schematically in Fig. 2A) and experimental parameters of our Q-band experiments (see "Q-band PELDOR" section), Δ cannot exceed a value of 0.25 (or 25%).

As nitroxide spin probes we utilize the rigid and nonperturbing Çm spin label (Fig. 1D; Höbartner et al. 2012). In the study by Höbartner et al. (2012), thermodynamic melting experiments and CD spectroscopy on small RNA helices showed that insertion of the Çm spin label yields only small, negligible differences in comparison to an unmodified RNA. Rigid nitroxide spin labels, such as Çm, offer several advantages over flexible nitroxide spin labels. Due to the negligible internal freedom of motion of rigid spin

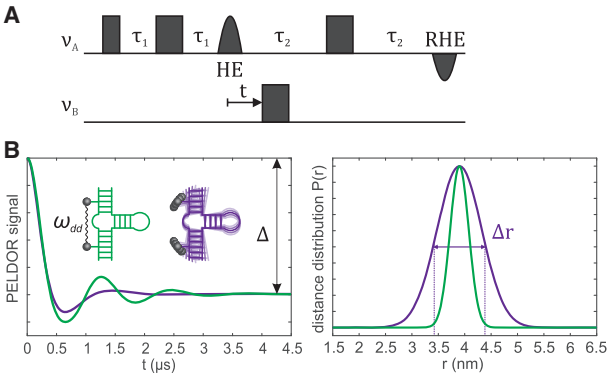

FIGURE 2. (*A*) Pulse sequence of a four-pulse PELDOR experiment (Pannier et al. 2000). The integrated echo intensity of the refocused Hahn echo (RHE) at $2\tau_1 + 2\tau_2$ is monitored as a function of the time *t* between the initial Hahn echo (HE) and the pump pulse with frequency ν_B. (*B*) Simulated PELDOR time traces (*left*) for a Gaussian distribution of distances centered at 3.9 nm (*right*). Two different distribution widths Δr (FWHM) of 0.4 nm (green) and 0.95 nm (purple) were simulated. Larger Δr values correspond to a higher conformational flexibility of the nitroxide-labeled helices, which causes a stronger dampening of the oscillations in the time domain. The PELDOR traces oscillate with the dipolar coupling frequency ω_{dd}, which is inversely proportional to r^3.

labels, the distance distributions *P*(*r*) tend to exhibit a small full width at half maximum (FWHM, Δr). Therefore, the distances and their distribution can be directly related to the structure and conformational flexibility of the nucleic acid itself. Thus, a system with high conformational flexibility would yield rather strongly dampened oscillations in the time domain and a broad probability distribution *P*(*r*) in the distance domain (purple data in Fig. 2B). Vice versa, a low degree of conformational flexibility would yield pronounced oscillations with a narrow probability distribution *P*(*r*) (green data in Fig. 2B).

More importantly, rigid spin labels can be used to study the relative orientation of two helices with respect to each other, a phenomenon that is typically referred to as orientation selection. Orientation selection of the rigid Çm spin label was first reported by Tkach and coworkers on an RNA model duplex (Tkach et al. 2013). Grytz and coworkers used the rigid Ç spin label, a derivative of Çm for DNA molecules, to determine helix orientations of a cocaine-binding DNA aptamer and a flexible DNA-motif (Grytz et al. 2016, 2017). Long-distance restraints of PELDOR measurements were combined with short-distance nuclear magnetic resonance (NMR) restraints to propose a global three-dimensional structure of a flexible DNA-motif (Grytz et al. 2017).

Thus, PELDOR in combination with rigid spin labels allows investigating the conformational flexibility of selected secondary structure elements in a parameter-free approach. The results of this study complement the aforementioned recent findings by Förster et al. (2012) and Reuss et al. (2014), where the conformational dynamics of a TC-aptamer were studied by performing melting, ITC, and CD studies of the whole aptamer itself and by looking at the fluorescence of the ligand. Whereas these latter two aforementioned studies examine kinetic and thermodynamic properties, such as free energies and rate constants, the present study quantitatively determines structural data such as distances and angular information and relates it to the conformational flexibility of the aptamer.

RESULTS AND DISCUSSION

In order to facilitate spin-labeling of the aptamer, the construct was separated into two components. As helices *P1* and *P2* are part of the scaffold and loop *L2* is not important for either binding of the ligand or folding of the aptamer, loop L2 was removed (Hanson et al. 2003; Suess et al. 2003), thus separating the TC-aptamer. The complete TC-aptamer (Fig. 1A) was then restored by hybridization of the two single strands. Entire hybridization and unaltered binding affinity toward TC was verified with native PAGE (Supplemental Fig. S2) and ITC measurements (Supplemental Fig. S3). The labeling positions were chosen as close to the binding pocket as possible, but without directly influencing it to ensure correct ligand binding. In silico simulations based on the crystal structure did not indicate any sterical clashes for the labeling position shown in Figure 1B.

The "Results" section is structured as follows: At first, PELDOR Mg^{2+}-titration studies at Q-band frequencies (≈34 GHz) in the absence and presence of TC are presented to investigate the conformational flexibility of the TC-aptamer. Q-band is the preferred microwave frequency for the titration studies, as here the influence of orientation selection is negligibly small, due to similar sizes of the g-tensor and hyperfine-tensor anisotropies. In this case, the distance distribution *P*(*r*) is free of any artificial peaks due to orientation selection. In a second step, orientation-selective PELDOR measurements at X-band frequencies (≈9.4 GHz) are presented to determine the relative orientation of the two Çm-labeled helices. At 9.4 GHz, the anisotropy of the hyperfine coupling of the ^{14}N-nucleus dominates the spectral shape, whereas the anisotropy of the electron Zeeman interaction is negligible (Supplemental Fig. S4). Therefore, different orientations can be excited by using different offsets $\Delta\nu$ ($\Delta\nu = \nu_A - \nu_B$). By combining PELDOR measurements at Q-band and X-band, distance information obtained at Q-band can be verified and directly related to the orientation of the crystal structure.

Structural changes of the TC-aptamer upon adding TC and/or Mg^{2+}

The conformational flexibility of the TC-aptamer was investigated with PELDOR spectroscopy as a function of different Mg^{2+} concentrations in the presence or absence of TC. Mg^{2+} concentrations of 0.22 mM, 0.45 mM, 1.2 mM, and 3.0 mM were chosen to mimic physiological Mg^{2+}

concentrations (Saris et al. 2000). For rigid spin labels, the probability function $P(r)$ of Q-band PELDOR data contains (i) information about the intramolecular distance of the two spin labels and (ii) information about the conformational flexibility of the macromolecule (width Δr of a distance peak).

Figure 3 shows PELDOR time traces and distance distributions of samples containing the TC-aptamer in the presence (Fig. 3A) or absence (Fig. 3B) of TC at different Mg^{2+} concentrations. For the "maximum" Mg^{2+} concentration of 3.0 mM (green) in the presence of TC, clear PELDOR oscillations, which correspond to a distance of 3.9 nm, are visible. This value is in very good agreement with the distance obtained from the crystal structure ($r_{X\text{-}ray} = 3.8$ nm). The main distance peak is characterized by a very narrow width of $\Delta r = 0.4$ nm. Thus, the tertiary structure of the TC-aptamer seems to have a low conformational flexibility at high Mg^{2+} concentrations in the presence of TC. For "intermediate" Mg^{2+} concentrations of 0.22 mM (violet), 0.45 mM (yellow), and 1.2 mM (cyan) the width of the main distance peak at 3.9 nm changes only slightly. Here, Δr increases from 0.4 nm for 1.2 mM Mg^{2+}, over 0.5 nm for 0.45 mM Mg^{2+} to 0.6 nm for 0.2 mM Mg^{2+} (Fig. 4).

In the absence of Mg^{2+} (red), the distance distribution is dominated by a very broad component at shorter distances. Due to the broad distribution width, it is impossible to give a quantitative interpretation. However, it is likely that the TC-aptamer adopts a variety of unfolded meta-stable structures in the absence of Mg^{2+}, hence yielding many distances and therefore a broad distance distribution. In general, shorter distances become more probable with decreasing Mg^{2+} concentrations (Fig. 3A, right). Therefore, it appears that an Mg^{2+}-dependent equilibrium exists between the well-defined folded tertiary structure and an ensemble of unfolded meta-stable conformations.

Figure 3B shows Q-band PELDOR time traces and distance distributions of samples containing the TC-aptamer at different Mg^{2+} concentrations in the absence of TC. PELDOR and distance data at 3 mM Mg^{2+} in the absence of TC (Fig. 3B, green) are essentially identical to the PELDOR trace and distance distribution shown in the presence of TC (Fig. 3A, green). Therefore, at 3 mM Mg^{2+}, TC is a negligible factor in formation and stabilization of the tertiary structure of the TC-aptamer.

This picture, however, changes when analyzing and comparing PELDOR data at "intermediate" Mg^{2+} concentrations (violet, yellow, and cyan data in Fig. 3B). Here, the widths of the main distance peaks are always broader than the equivalent distance peaks shown in Figure 3A (with TC). This becomes also apparent by looking at Figure 4, where the Δr values of the distance distributions of Figure 3 are plotted as a function of the Mg^{2+} concentration. For example, the yellow distance peak in Figure 3B (0.5 mM Mg^{2+}, without TC) is broader than the yellow distance peak in Figure 3A (0.5 mM Mg^{2+}, with TC). Both peaks, however, share an identical mean distance of 3.9 nm. In the absence of TC, Δr increases more drastically than in the presence of TC from 0.6 nm for 1.2 mM Mg^{2+}, over 0.8 nm for 0.45 mM Mg^{2+} to 1.5 nm for 0.2 mM Mg^{2+} (Fig. 4). This shows, that at "intermediate" Mg^{2+} concentrations, TC is essential for stabilizing the folded tertiary structure of the aptamer. In other words, in the presence of TC, intermediate concentrations of Mg^{2+} are already sufficient to significantly reduce the conformational flexibility of the folded tertiary structure of the aptamer. The PELDOR time trace and distance data without TC and any Mg^{2+} (red in Fig. 3B) are nearly identical to the time trace and distance data without any Mg^{2+} but in the presence of TC (red in Fig. 3A). This finding is not surprising, as it is

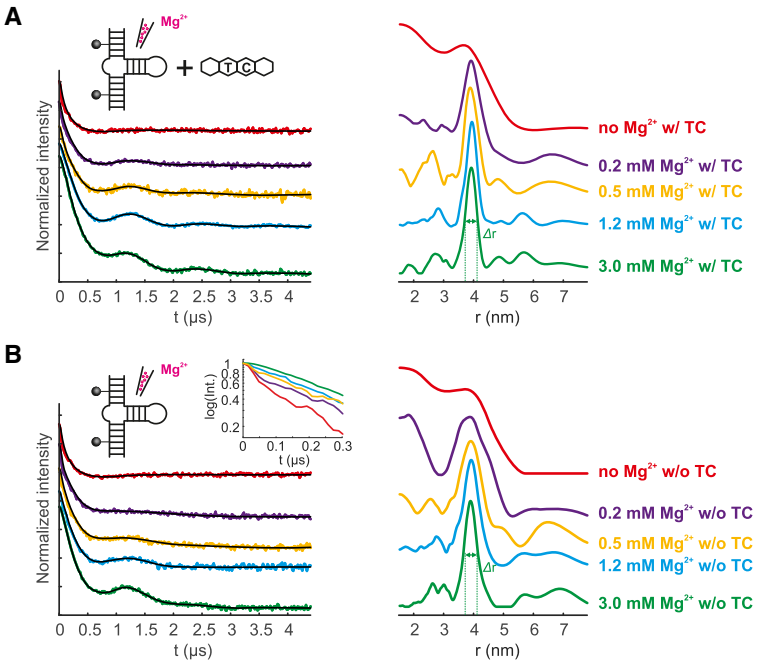

FIGURE 3. (*A*) Background-corrected Q-band PELDOR time traces and distance distributions $P(r)$ obtained by Tikhonov regularization of 150 µM TC-aptamer and 165 µM TC with varying Mg^{2+} concentrations. (*B*) Background-corrected Q-band PELDOR time traces and distance distributions $P(r)$ obtained by Tikhonov regularization of 150 µM TC-aptamer with varying Mg^{2+} concentrations. The *inset* on the *left* shows a half-logarithmic plot of the first 300 ns of background-corrected PELDOR time traces, which illustrates an increased probability for smaller distances with lower Mg^{2+} concentrations. The fits of the Tikhonov regularization are shown in black.

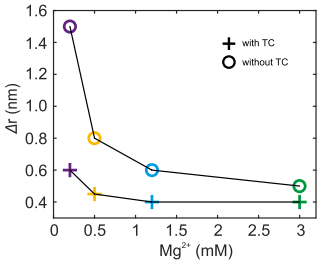

FIGURE 4. Width Δr (full width at half maximum) of the main distance peaks at 3.9 nm of the distance distributions shown in Figure 3 as a function of Mg^{2+} concentration. The color code is identical to Figure 3. Plus signs label samples in the presence of TC, whereas circles label samples in the absence of TC. The width Δr of samples without TC increases more strongly with decreasing Mg^{2+} concentration than for samples with TC. Samples containing no Mg^{2+} are not included in this plot, as here no reliable Δr values could be extracted.

generally known that Mg^{2+} is needed for folding of the TC-aptamer. For a direct comparison of data sets with the same Mg^{2+} concentration with and without TC, the reader is referred to Supplemental Figure S6.

The trend of increasing Δr values for decreasing Mg^{2+} concentrations is also consistent with an increased dampening of the PELDOR oscillations for decreasing Mg^{2+} concentrations. A stronger dampening of the oscillations in the time domain causes a broader distribution width in the distance domain (Fig. 2B). Consequently, a stronger dampening reflects an increased conformational flexibility of the RNA helices. For example, the yellow PELDOR time trace in Figure 3B (0.45 mM Mg^{2+}, without TC) exhibits a stronger dampening than the yellow PELDOR time trace in Figure 3A (0.45 mM Mg^{2+}, with TC). Therefore, the trend of Δr values is already clearly visible in the background-corrected PELDOR time traces.

Just as in Figure 3A, distance data in Figure 3B also show an increased probability for shorter distances with decreasing Mg^{2+} concentration. This behavior becomes more apparent when looking at the inset of Figure 3B, which shows a half-logarithmic plot of the first 300 ns of background-corrected and modulation-depth scaled PELDOR data. Here, a steeper slope corresponds to an increased probability of shorter distances in the distance domain. Due to the rather broad and unspecific profile of the distance distributions in the region from 1.8 to 3.0 nm, we did not attempt to compare these regions between Figure 3A (with TC) and Figure 3B (without TC) in a quantitative manner. It seems, however, that in the absence of TC, the aforementioned equilibrium is more shifted toward the side of metastable conformers.

In theory, intramolecular self-hybridization of the spin-labeled monomer (22-mer in Fig. 1B) could also yield small distances similar to those that were observed in Figure 3A,B. However, the helices were designed in such a way that the heterodimer is thermodynamically significantly more favorable than the monomer. The predicted free energy of the heterodimer was calculated to $\Delta G_{hetero} = -30.0$ kcal/mol, whereas the predicted free energy of the spin-labeled monomer was calculated to $\Delta G_{mono} = -1.2$ kcal/mol (Gruber et al. 2008). In addition, no band corresponding to a self-hybridized 22-mer was observed on a control gel (Supplemental Fig. S2). We therefore exclude the possibility of a self-hybridized monomer.

Helical stacking between TC-aptamers

The PELDOR time traces at 3 mM Mg^{2+} (Fig. 3A,B, green) seem to contain longer distances ($r > 5$ nm), as here the minimum of the first oscillation is not the overall minimum. In addition, the time traces with 3 mM Mg^{2+} exhibit a fairly large modulation depth Δ ($\Delta = 0.4$ for a sample with 3 mM Mg^{2+} and no TC). Multispin systems, where the number of intramolecular spins N is >2, are known to increase the modulation depth Δ (von Hagens et al. 2013).

Large distances and large modulation depths are indicative of RNA stacking, a phenomenon in which RNA helices stack on top of each other (Piton et al. 2007; Krstić et al. 2011). In our case (rather broad and undefined), distances at 3 nm and from 5 nm to 7 nm (asterisks in Supplemental Fig. S8D) could be explained by a very simplified model, in which two spin-labeled aptamers were stacked on top of each other (Supplemental Fig. S7). In addition, the modulation depth Δ exhibits a clear dependence on the Mg^{2+} concentration (Supplemental Fig. S8E). This correlation is reasonable, as negatively charged divalent metal ions are likely to act as bridging ions between two negatively charged RNA duplex ends. Thus, a higher Mg^{2+} concentration facilitates stacking, which manifests itself in an increased modulation depth Δ.

To test whether our results were due to helical RNA stacking, TC-aptamers with different single-nucleotide overhangs were prepared (Supplemental Fig. S8A). Q-band PELDOR revealed that construct II was essentially free of any stacking artifacts (no additional distances and no increased modulation depth), indicating that a pyrimidine-nucleotide overhang (cytidine, construct II) is more efficient in preventing end-to-end stacking than a purine-nucleotide overhang (guanine, construct III). This is reasonable, as a computational study recently showed that G-G-nucleobase-dimers are expected to be more prone to π–π-stacking than C-C-nucleobase-dimers (Mignon et al. 2005). Similar findings were recently reported by Weinrich and coworkers on a TAR-RNA system (Weinrich et al. 2018).

Orientation-selective PELDOR at X-band yields data in agreement with the X-ray crystal structure

Construct II (Supplemental Fig. S8A) was subsequently used to perform orientation-selective PELDOR

measurements at X-band frequencies with the goal of extracting the relative orientation of the two spin labeled RNA helices. Orientation-selective PELDOR with construct I and construct III would be much more challenging, as stacking artifacts can severely hamper data analysis of orientation-selective PELDOR experiments. The orientation-selective measurements were performed in the presence of 3 mM Mg^{2+} and TC.

The orientation of two nitroxide spin labels with respect to each other can be described by six parameters, namely the distance vector *r* (chosen to be parallel to the *z*-axis of the dipolar coordinate system), two Euler angles β_1 and γ_1 of nitroxide spin label 1 (because of symmetry the *x*-axis can be freely chosen, therefore the first Euler angle is set arbitrarily to $\alpha_1 = 0$) and the three Euler angles α_2, β_2, and γ_2 of nitroxide spin label 2. Euler angles describe the relative orientation of the principal axis system of a nitroxide spin label to the dipolar coordinate system, whose *z*-axis coincides with the distance vector *r*. Recent publications have focused on a detailed theoretical explanation and simulation of orientation-selective PELDOR data (Larsen and Singel 1993; Abé et al. 2012; Marko and Prisner 2013; Prisner et al. 2015). Therefore, only a brief summary about orientation-selective PELDOR at X-band frequencies is given here.

At X-band frequencies (9.4 GHz) the anisotropy of the ^{14}N-hyperfine interaction of nitroxide radicals dominates the spectral shape of the echo-detected field-swept spectrum. This becomes apparent by comparing the simulated field-swept spectra with its nitrogen hyperfine components at X-band and Q-band frequencies, respectively (Supplemental Fig. S4A,B). For X-band frequencies, different spin orientations can be excited by the detection pulses when using different pump/probe $\Delta\nu$ offsets, which typically range from 40 MHz to 90 MHz. The excitation of different orientations manifests itself in different oscillation patterns and modulation depths for different offsets $\Delta\nu$. By fitting orientation-selective X-band PELDOR data (Marko and Prisner 2013), mainly the orientation of the *z*-components z_1 and z_2 of the two hyperfine tensors with respect to the dipolar vector *r*, and therefore the bend angle ϕ between two RNA helices can be deduced (Fig. 5B). For more information, the reader is referred to Section S9 in the Supplemental Material.

Figure 5A shows background-corrected X-band PELDOR data with different pump/probe offsets. As expected, orientation selection manifests itself in different oscillation patterns for different offsets (the oscillation for $\Delta\nu = 90$ MHz is longer than the oscillation for $\Delta\nu = 40$ MHz). In addition, the modulation depth increases constantly from $\Delta_{40\ MHz} = 0.36$ to $\Delta_{90\ MHz} = 0.53$. Orientation selection manifests itself also in distortions of the Pake patterns obtained by Fourier transformation of the PELDOR time traces shown in Figure 5A (Supplemental Fig. S10).

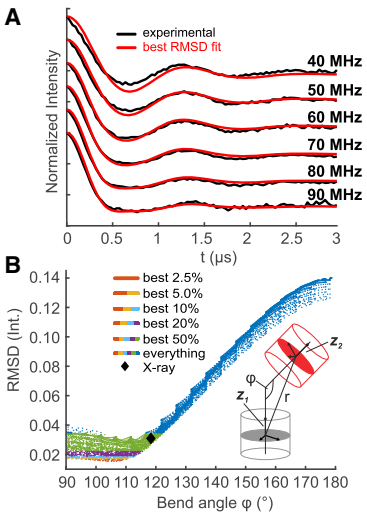

FIGURE 5. (*A*) Background-corrected X-band PELDOR time traces of 150 µM TC-aptamer (construct II, see Supplemental Fig. S8), 165 µM TC and 3 mM Mg^{2+} with different pump/probe offsets. Simulated PELDOR time traces with Euler angles that yielded the best RMSD are shown for comparison in red [$\alpha_1 = 0$ (0), $\beta_1 = 0.94$ (0.42), $\gamma_1 = -1.82$ (−1.82), $\alpha_2 = -0.88$ (−0.88), $\beta_2 = 2.63$ (2.36), $\gamma_2 = 2.06$ (2.06), given in radians, values in brackets correspond to the crystal structure]. (*B*) RMSD of PELDOR simulations with different sets of Euler angles as a function of the bend angle ϕ. β_1, α_2, and β_2 were varied around the Euler angles of the crystal structure in 5° increments (10 steps ± the start value = 21^3 simulations). The bend angle ϕ between the two RNA helices (red and gray helices in Fig. 1A,C) was calculated out of the angles β_1, α_2, and β_2. The bend angle of the crystal structure with its RMSD is shown as a black diamond.

In a next step, the Euler angles of spin labels that were attached to the X-ray crystal structure, were simulated, and compared to experimental data (Supplemental Fig. S11B). Although the oscillation pattern for smaller offsets could be reproduced by the simulation, a clear discrepancy is visible for larger offsets (80 MHz and 90 MHz). Therefore, the Euler angles β_1, α_2, and β_2 were varied in ±5° increment steps around the values obtained from the X-ray structure, 10 steps in each direction, thus yielding 21^3 different orientations that were simulated. The angles α_1, γ_1, γ_2 and the distance vector *r* were kept constant, because they are not sensitive to X-band PELDOR data (Abé et al. 2012; Marko and Prisner 2013). The quality of each simulation was evaluated by calculating the root mean square deviation (RMSD) over the whole length of the time traces. Simulations with Euler angles that yielded the best RMSD are shown in Figure 5A as red time traces. It should be mentioned that the ambiguities arising from the insensitivity of PELDOR to the sign of the z_1 and z_2 vectors do not apply in this approach (Abé et al. 2012). This is because for the present study prior knowledge about the molecular model is available by the crystal structure. Furthermore, the indistinguishability of the two spin labels is of no concern for data presented

within this study. This is based on the fact that the bend angle ϕ describes the relative orientation of the two spin labels and not the absolute position of each spin label (Abé et al. 2012).

For a better visualization, each orientation of the two spin labels, as defined by the three Euler angles β_1, α_2, and β_2, was transformed into the bend angle ϕ (for an explanation of the bend angle ϕ, see the inset of Fig. 5B or Section S9 of the Supplemental Material). The RMSD was then plotted as a function of the bend angle ϕ (Fig. 5B) and compared to the angle ϕ that was extracted from spin labels attached to the crystal structure (black diamond in Fig. 5B). The simulations exhibit a minimum bend angle at $\phi_{fit} = 106°$, which was in a reasonable agreement with the calculated angle of $\phi_{X\text{-}ray} = 118°$ for the crystal structure. Thus, the analysis of orientation-selective PELDOR data confirms that the structure obtained in frozen solution is in agreement with the structure obtained from X-ray data. The small deviation could indicate minor structural rearrangements due to crystal packing effects.

More simulated PELDOR time traces, including Euler angles that yielded the worst RMSD (within the given 5° variations) are presented in the supporting information (Supplemental Fig. S11). We also applied an iterative fitting algorithm, that was recently developed in our group (Marko and Prisner 2013), to the X-band PELDOR data. In this approach, the data were fitted over *n* iterative steps. In each step, the best-fitting simulated time trace for a conformer from a simulated library off all possible conformers was chosen. The collection of the best-fitting conformers of size *n* shows a very narrow distribution of its bend angles (Supplemental Fig. S12, middle row). In addition, the mean bend angle of this iterative fitting approach agrees perfectly with the best bend angle of Figure 5B, thus emphasizing the uniqueness of the simulation results presented in this study. The Δr values of the conformers shown in Figure 5A and Supplemental Figure S12 are also in very good agreement with experimental Δr values obtained from Q-band data (Supplemental Fig. S13).

We also recorded orientation-selective X-band PELDOR data at "intermediate" Mg^{2+} concentrations of 0.45 mM (Supplemental Figs. S14–S16). Simulations did not reveal significantly different best Euler and bend angles than for 3.0 mM Mg^{2+} and in the presence of TC. The results of Mg^{2+}-titration studies ("Structural changes of the TC-aptamer upon adding TC and/or Mg^{2+}" section) were, however, confirmed: Both orientation-selective PELDOR data for 0.45 mM Mg^{2+} in Supplemental Figure S15A,B exhibit a steeper slope at the beginning than orientation-selective PELDOR data with 3.0 mM Mg^{2+}. A steeper slope at the beginning corresponds to a higher probability for smaller distances. Just as with the Q-band Mg^{2+} titration studies, orientation-selective X-band PELDOR data with 0.45 mM Mg^{2+} in the absence of TC are characterized by stronger dampening of the oscillations than the orientation-selective PELDOR data with 0.45 mM Mg^{2+} in the presence of TC, which is consistent with a larger Δr value in the distance domain (Supplemental Fig. S16).

Conclusion

Besides yielding accurate intramolecular distances, the PELDOR time traces of the TC aptamer containing a pair of rigid spin labels provided more information about the dynamics and conformational flexibility of the aptamer.

Firstly, the width Δr of the main distance peak is a sensitive indicator for the intramolecular flexibility of the tertiary structure. More specifically, it was shown that the tertiary structure of the TC-aptamer needs TC at "intermediate" Mg^{2+} concentrations (0.22–1.2 mM) to form a stable tertiary structure. At a certain point (≥3 mM), Mg^{2+} alone is sufficient to stabilize the tertiary structure of TC. These results are in perfect agreement with recent findings by the Wachtveitl group on the TC-aptamer using fluorescence, ITC, CD, and melting studies (Reuss et al. 2014). Whereas the above-mentioned techniques look at the aptamer as a whole (melting point, ITC, or CD studies) or just at the ligand itself (fluorescence), PELDOR sheds light on selected secondary structure elements of RNA molecules. In the study by Reuss et al. (2014), a model was proposed in which the structure of the aptamer is in a preformed condition at intermediate Mg^{2+} concentrations and in the absence of TC. With the addition of TC, the final tertiary structure is formed out of the preformed conformation. The results of this study are in perfect agreement with the model by Reuss and coworkers – PELDOR is able to sample the preformed state by means of a broader distance distribution width at intermediate Mg^{2+} concentrations in the absence of TC (Fig. 3B).

Secondly, the relative orientation of the two helices *P1* and *P2* (Fig. 1A,B) could be investigated using orientation-selective PELDOR measurements. The relative orientation of the two helices agrees well with the X-ray crystal structure of the TC-aptamer in the TC-bound state. Given a good experimental signal-to-noise ratio, orientation-selective PELDOR in combination with rigid spin labels is therefore a sensitive method to study orientations of secondary structure elements of RNA molecules. This is of particular interest, as PELDOR (and pulsed dipolar EPR spectroscopy in general) is not restricted to size limitations as in NMR. In the present study, X-band PELDOR was used to determine an ≈10° difference of the bend angle ϕ between the two double-stranded helices *P1* and *P2* compared to the X-ray structure. PELDOR time traces simulated with the bend angle of the crystal structure ($\phi_{X\text{-}ray}$) revealed an experimentally significant different oscillation pattern than the experimental PELDOR time traces and exhibited a significant larger RMSD compared to simulations with the 10°-changed bend angle ϕ_{fit}. Two different fitting approaches (starting from the X-ray structure and ab initio iterative fitting of the PELDOR time traces) essentially

yielded identical results (bend angles), thus emphasizing the correctness of our simulations.

This study clearly illustrates the benefits of using rigid spin labels in combination with PELDOR measurements to study structural dynamics of nucleic acids. To our knowledge, this is the first time that the unique properties of the Çm spin label have been used to answer relevant questions about biologically active RNA systems. It should be noted that these results could not have been obtained with flexible spin labels, simply because the rotational freedom around the tether eliminates all orientation selection and gives rise to a broad signal in the distance distribution $P(r)$ that renders a detailed interpretation of the distance distribution width Δr impossible. The rotational freedom around the linker would also inhibit determination of additional angular restraints.

MATERIALS AND METHODS

RNA synthesis and purification

In order to facilitate synthesis of a spin-labeled construct, the aptamer was composed of two parts, a 5′ 22-mer and a 3′ 37-mer. After annealing, a complete TC-aptamer (Fig. 1B) can be restored.

The 22-mer of the construct shown in Figure 1B was synthesized via solid phase synthesis as described previously (Tkach et al. 2013) and analyzed by MALDI-TOF analysis (Supplemental Fig. S1). For more information on the synthesis of the 22-mer, the reader is referred to Section 1 of the Supplemental Material.

The 37-mer of the construct shown in Figure 1B was in vitro transcribed by enzymatic synthesis using a *Sma*I linearized plasmid as template. The plasmid codes for the T7 promoter followed by the aptamer sequence (the full plasmid sequence is available upon request). In vitro transcription was performed at 37°C overnight in a total volume of 10 mL containing 20 mM magnesium acetate, 0.2 M Tris-HCl pH 8.0, 20 mM DTT, 2 mM spermidine, 0.2 mg/mL linearized plasmid, 4 mM of each NTP, and 7.5 mg/mL of T7 polymerase (made in-house). After transcription, precipitated pyrophosphate was pelleted by centrifugation and 10% (v/v) EDTA (0.5 mM, pH 8.0) was added to the supernatant. Ethanol precipitation was performed and the RNA was purified by a denaturing polyacrylamide gel electrophoresis (10% PAA, 8 M urea). The RNA was detected via ultraviolet (UV) shadowing, cut out, and eluted from the gel in 0.3 M sodium acetate pH 6.5 at 4°C overnight. To remove the remaining gel slices, the supernatant was filtered using a 0.45 mm filter (Sarstedt) and again the RNA was precipitated using ethanol. Finally, the RNA was dissolved in double-distilled water and stored at −20°C.

The "right" RNA strands of constructs II and III (39-mer and mod 37-mer, see Supplemental Fig. S8A) were prepared as described in the previous paragraph. After purification, the "right" RNA strands of construct I, II, and III (Supplemental Fig. S8A) were hybridized with the "left" strand (22-mer) by mixing an equimolar amount of each RNA strand in water. The reaction mix was incubated at 95°C for 2 min and afterward temperature was reduced to 25°C by 1°C per minute. The hybridized RNA was stored at −20°C. Complete hybridization of the aptamer was checked by native PAGE (Supplemental Fig. S2).

ITC measurements

K_d measurements were determined by ITC experiments (Vogel and Suess 2016). ITC measurements of an unlabeled hybrid TC-aptamer were compared to ITC measurements of the Çm-labeled hybrid TC-aptamer. Both hybrids, the unlabeled construct (K_d = 6.5 nM) and the labeled construct (K_d = 7.0 nM), had identical binding constants as the full-length aptamer (Reuss et al. 2014), ensuring correct ligand binding. Thus, our hybrid aptamer faithfully recapitulates ligand binding and is a suitable model for structural analyses. For more details on ITC measurements, the reader is referred to Section 3 of the Supplemental Material and Supplemental Figure S3.

Sample preparation for EPR measurements

Aliquots of the frozen RNA solution were lyophilized and dissolved in a solution of D_2O containing 20 mM triethanolamine, 100 mM sodium chloride, and varying amounts of magnesium chloride (from 0 mM to 3 mM) at pH = 7.0. Twenty percent of the solution was deuterated ethylene glycol (v/v), used as a glassing agent. For X-band PELDOR samples, only the glassing agent was deuterated. The final RNA concentration was 150 µM. For PELDOR measurements in the presence of TC, the buffer solution also contained 165 µM of TC. All chemicals were certified RNase-free. RNA samples were transferred into 1.6 mm OD Suprasil tubes (10 µL) or 2.8 mm OD quartz tubes (20 µL) for Q-band and X-band PELDOR measurements, respectively. Samples were shock-frozen in liquid nitrogen *prior* to being inserted into the resonator.

X-band PELDOR

PELDOR measurements at X-band frequencies (≈9.4 GHz) were performed on a homebuilt X-band spectrometer equipped with a split-ring ER 4118X MS3 probehead. More details regarding the spectrometer design will be published elsewhere. A 1 kW traveling-wave tube by Applied Systems Engineering was used for microwave amplification. Temperature was kept at 50 K using a continuous-flow helium cryostat (CF935) and an ITC 502 temperature control unit, both from Oxford Instruments. The pump pulse was chosen to coincide with the maximum of the echo-detected field-swept spectrum. Detection was performed at frequency offsets between pump and probe pulses of $\Delta\nu$ = 40, 50, 60, 70, 80, and 90 MHz (Supplemental Fig. S4A contains a simulated echo-detected field-swept spectrum with visualized pump/probe positions and pulse excitation profiles). Detection pulses had a length of 32 ns, pump pulses were optimized for a length of 12 ns. Tau values of τ_1 = 430 ns and τ_2 = 3500 ns were used. The shot repetition time was set to 4 µs. A tau averaging cycle of 8 × 56 ns was used in order to suppress deuterium modulations. A total of 118 data points were collected along the time dimension with an increment of 32 ns. Depending on the sample quality, 30–150 scans were accumulated.

Q-band PELDOR

PELDOR measurements at Q-band frequencies (≈34 GHz) were performed on a Bruker E580 spectrometer equipped with a

dielectric EN 5170 D2 ENDOR probehead. A Bruker AmpQ 10 W solid-state amplifier was used for microwave amplification. Temperature settings were identical to X-band PELDOR measurements. The pump pulse was chosen to coincide with the maximum of the echo-detected field-swept spectrum. Detection was performed at a frequency offset of $\Delta\nu = \nu_A - \nu_B = -50$ MHz (Supplemental Fig. S4B contains a simulated echo-detected field-swept spectrum with visualized pump/probe positions and pulse excitation profiles). Detection pulses had a length of 32 ns, pump pulses were optimized for a length of 21 ns. Tau values of $\tau_1 = 130$ ns and $\tau_2 = 5000$ ns were used. The shot repetition time was set to 7 µs. A tau averaging cycle of 8 × 16 ns was used in order to suppress deuterium modulations. A total of 310 data points were collected along the time dimension with an increment of 16 ns. Depending on the sample quality, 10–50 scans were accumulated. For both, X-band and Q-band measurements, primary PELDOR data were background-corrected by fitting an exponential decay function assuming a homogeneous spatial distribution of the nucleic acid molecules. Tikhonov regularization was performed on background-corrected PELDOR data to obtain the distance probability function $P(r)$. Data processing was done using the Matlab toolbox *DeerAnalysis* (Jeschke et al. 2006).

SUPPLEMENTAL MATERIAL

Supplemental material is available for this article.

ACKNOWLEDGMENTS

We thank Dr. Alice Bowen and Dr. Philipp Spindler for help in setting up initial Q-band and X-band PELDOR measurements. We also thank Dr. Claudia Grytz, Nicole Erlenbach, and Dr. Andriy Marko for help with PELDOR X-band simulations. S.Th.S. acknowledges financial support from the Icelandic Research Fund (141062-051). T.F.P., B.S., and J.E.W. acknowledge financial support from the Collaborative Research Center 902 – Molecular Principles of RNA-based regulation of the German Research Foundation (3214020004).

Received September 6, 2018; accepted October 16, 2018.

REFERENCES

Abé C, Klose D, Dietrich F, Ziegler WH, Polyhach Y, Jeschke G, Steinhoff HJ. 2012. Orientation selective DEER measurements on vinculin tail at X-band frequencies reveal spin label orientations. *J Magn Reson* **216:** 53–61. doi:10.1016/j.jmr.2011.12.024

Berens C, Thain A, Schroeder R. 2001. A tetracycline-binding RNA aptamer. *Bioorg Med Chem* **9:** 2549–2556. doi:10.1016/S0968-0896(01)00063-3

Berens C, Groher F, Suess B. 2015. RNA aptamers as genetic control devices: the potential of riboswitches as synthetic elements for regulating gene expression. *Biotechnol J* **10:** 246–257. doi:10.1002/biot.201300498

Breaker RR. 2012. Riboswitches and the RNA world. *Cold Spring Harb Perspect Biol* **4:** a003566. doi:10.1101/cshperspect.a003566

Chopra I, Roberts M. 2001. Tetracycline antibiotics: mode of action, applications, molecular biology, and epidemiology of bacterial resistance. *Microbiol Mol Biol Rev* **65:** 232–260. doi:10.1128/MMBR.65.2.232-260.2001

Förster U, Weigand JE, Trojanowski P, Suess B, Wachtveitl J. 2012. Conformational dynamics of the tetracycline-binding aptamer. *Nucleic Acids Res* **40:** 1807–1817. doi:10.1093/nar/gkr835

Groher F, Suess B. 2014. Synthetic riboswitches—a tool comes of age. *Biochim Biophys Acta* **1839:** 964–973. doi:10.1016/j.bbagrm.2014.05.005

Gruber AR, Lorenz R, Bernhart SH, Neuböck R, Hofacker IL. 2008. The Vienna RNA websuite. *Nucleic Acids Res* **36:** W70–W74. doi:10.1093/nar/gkn188

Grytz CM, Marko A, Cekan P, Sigurdsson ST, Prisner TF. 2016. Flexibility and conformation of the cocaine aptamer studied by PELDOR. *Phys Chem Chem Phys* **18:** 2993–3002. doi:10.1039/C5CP06158J

Grytz CM, Kazemi S, Marko A, Cekan P, Güntert P, Sigurdsson ST, Prisner TF. 2017. Determination of helix orientations in a flexible DNA by multi-frequency EPR spectroscopy. *Phys Chem Chem Phys* **19:** 29801–29811. doi:10.1039/C7CP04997H

Hallberg ZF, Su Y, Kitto RZ, Hammond MC. 2017. Engineering and in vivo applications of riboswitches. *Annu Rev Biochem* **86:** 515–539. doi:10.1146/annurev-biochem-060815-014628

Hanson S, Berthelot K, Fink B, McCarthy JEG, Suess B. 2003. Tetracycline-aptamer-mediated translational regulation in yeast. *Mol Microbiol* **49:** 1627–1637. doi:10.1046/j.1365-2958.2003.03656.x

Hanson S, Bauer G, Fink B, Suess B. 2005. Molecular analysis of a synthetic tetracycline-binding riboswitch. *RNA* **11:** 503–511. doi:10.1261/rna.7251305

Höbartner C, Sicoli G, Wachowius F, Gophane DB, Sigurdsson ST. 2012. Synthesis and characterization of RNA containing a rigid and nonperturbing cytidine-derived spin label. *J Org Chem* **77:** 7749–7754. doi:10.1021/jo301227w

Jeschke G, Chechik V, Ionita P, Godt A, Zimmermann H, Banham J, Timmel CR, Hilger D, Jung H. 2006. DeerAnalysis2006—a comprehensive software package for analyzing pulsed ELDOR data. *Appl Magn Reson* **30:** 473–498. doi:10.1007/BF03166213

Kötter P, Weigand JE, Meyer B, Entian KD, Suess B. 2009. A fast and efficient translational control system for conditional expression of yeast genes. *Nucleic Acids Res* **37:** e120. doi:10.1093/nar/gkp578

Krstić I, Hänsel R, Romainczyk O, Engels JW, Dötsch V, Prisner TF. 2011. Long-range distance measurements on nucleic acids in cells by pulsed EPR spectroscopy. *Angew Chem Int Ed Engl* **50:** 5070–5074. doi:10.1002/anie.201100886

Larsen RG, Singel DJ. 1993. Double electron–electron resonance spin–echo modulation: spectroscopic measurement of electron spin pair separations in orientationally disordered solids. *J Chem Phys* **98:** 5134–5146. doi:10.1063/1.464916

Marko A, Prisner TF. 2013. An algorithm to analyze PELDOR data of rigid spin label pairs. *Phys Chem Chem Phys* **15:** 619–627. doi:10.1039/C2CP42942J

McCown PJ, Corbino KA, Stav S, Sherlock ME, Breaker RR. 2017. Riboswitch diversity and distribution. *RNA* **23:** 995–1011. doi:10.1261/rna.061234.117

Mignon P, Loverix S, Steyaert J, Geerlings P. 2005. Influence of the π–π interaction on the hydrogen bonding capacity of stacked DNA/RNA bases. *Nucleic Acids Res* **33:** 1779–1789. doi:10.1093/nar/gki317

Milov AD, Salikhov KM, Shchirov MD. 1981. Use of the double resonance in electron spin echo method for the study of paramagnetic center spatial distribution in solids. *Fiz Tverd Tela* **23:** 975–982.

Müller M, Weigand JE, Weichenrieder O, Suess B. 2006. Thermodynamic characterization of an engineered tetracycline-binding riboswitch. *Nucleic Acids Res* **34:** 2607–2617. doi:10.1093/nar/gkl347

Nelson JA, Uhlenbeck OC. 2006. When to believe what you see. *Mol Cell* **23:** 447–450. doi:10.1016/j.molcel.2006.08.001

Pannier M, Veit S, Godt A, Jeschke G, Spiess H. 2000. Dead-time free measurement of dipole–dipole interactions between electron spins. *J Magn Reson* **142:** 331–340. doi:10.1006/jmre.1999.1944

Piton N, Mu Y, Stock G, Prisner TF, Schiemann O, Engels JW. 2007. Base-specific spin-labeling of RNA for structure determination. *Nucleic Acids Res* **35:** 3128–3143. doi:10.1093/nar/gkm169

Prisner TF, Marko A, Sigurdsson ST. 2015. Conformational dynamics of nucleic acid molecules studied by PELDOR spectroscopy with rigid spin labels. *J Magn Reson* **252:** 187–198. doi:10.1016/j.jmr.2014.12.008

Reuss AJ, Vogel M, Weigand JE, Suess B, Wachtveitl J. 2014. Tetracycline determines the conformation of its aptamer at physiological magnesium concentrations. *Biophys J* **107:** 2962–2971. doi:10.1016/j.bpj.2014.11.001

Saris NE, Mervaala E, Karppanen H, Khawaja JA, Lewenstam A. 2000. Magnesium—an update on physiological, clinical and analytical aspects. *Clin Chim Acta* **294:** 1–26. doi:10.1016/S0009-8981(99)00258-2

Suess B, Hanson S, Berens C, Fink B, Schroeder R, Hillen W. 2003. Conditional gene expression by controlling translation with tetracycline-binding aptamers. *Nucleic Acids Res* **31:** 1853–1858. doi:10.1093/nar/gkg285

Tkach I, Pornsuwan S, Höbartner C, Wachowius F, Sigurdsson ST, Baranova TY, Diederichsen U, Sicoli G, Bennati M. 2013. Orientation selection in distance measurements between nitroxide spin labels at 94 GHz EPR with variable dual frequency irradiation. *Phys Chem Chem Phys* **15:** 3433. doi:10.1039/c3cp44415e

Vogel M, Suess B. 2016. Label-free determination of the dissociation constant of small molecule-aptamer interaction by isothermal titration calorimetry. *Methods Mol Biol* **1380:** 113–125. doi:10.1007/978-1-4939-3197-2_9

Vogel M, Weigand JE, Kluge B, Grez M, Suess B. 2018. A small, portable RNA device for the control of exon skipping in mammalian cells. *Nucleic Acids Res* **46:** e48. doi:10.1093/nar/gky062

von Hagens T, Polyhach Y, Sajid M, Godt A, Jeschke G. 2013. Suppression of ghost distances in multiple-spin double electron–electron resonance. *Phys Chem Chem Phys* **15:** 5854–5866. doi:10.1039/c3cp44462g

Weigand JE, Suess B. 2007. Tetracycline aptamer-controlled regulation of pre-mRNA splicing in yeast. *Nucleic Acids Res* **35:** 4179–4185. doi:10.1093/nar/gkm425

Weinrich T, Jaumann EA, Scheffer U, Prisner TF, Göbel MW. 2018. A cytidine phosphoramidite with protected nitroxide spin label: synthesis of a full-length TAR RNA and investigation by in-line probing and EPR spectroscopy. *Chemistry* **24:** 6202–6207. doi:10.1002/chem.201800167

Wunnicke D, Strohbach D, Weigand JE, Appel B, Feresin E, Suess B, Müller S, Steinhoff HJ. 2011. Ligand-induced conformational capture of a synthetic tetracycline riboswitch revealed by pulse EPR. *RNA* **17:** 182–188. doi:10.1261/rna.2222811

Xiao H, Edwards TE, Ferré-D'Amaré AR. 2008. Structural basis for specific, high-affinity tetracycline binding by an in vitro evolved aptamer and artificial riboswitch. *Chem Biol* **15:** 1125–1137. doi:10.1016/j.chembiol.2008.09.004

Influence of Mg^{2+} on the conformational flexibility of a tetracycline aptamer

Thilo Hetzke, Marc Vogel, Dnyaneshwar B. Gophane, et al.

RNA 2019 25: 158-167 originally published online October 18, 2018
Access the most recent version at doi:10.1261/rna.068684.118

Influence of Mg^{2+} on the conformational flexibility of a tetracycline aptamer

Thilo Hetzke[1], Marc Vogel[2], Dnyaneshwar B. Gophane[3], Julia E. Weigand[2], Beatrix Suess[2], Snorri Th. Sigurdsson[3] and Thomas F. Prisner[1]

[1]Institute of Physical and Theoretical Chemistry and Center of Biomolecular Magnetic Resonance, Goethe University Frankfurt, Frankfurt am Main, Germany, [2]Department of Biology, Technical University of Darmstadt, Darmstadt, Germany, [3]Department of Chemistry, Science Institute, University of Iceland, Reykjavik, Iceland

Table of Content

1. RNA synthesis, purification and analysis of Çm-labeled 22mer

The 22 mer **Çm**-labeled 5'- GGG**Çm**CUAAAACAUAC**Çm**GAUCCC RNA oligonucleotide was synthesized on an automated Expedite Nucleic Acid Synthesis System by using a trityl-off protocol and phosphoramidites with standard protecting groups on 1.0 mmol scale, using 1000 Å CPG columns. All commercial phosphoramidites, CPG columns, and solutions were purchased from Glen Research Corporation or LinkTechnologies Ltd. **Çm** was incorporated into RNA oligoribonucleotides by solid phase synthesis using the previously reported protocol (Höbartner et al. 2012).

Since the **Çm** phosphoramidite had limited solubility in acetonitrile, which is commonly used as a solvent for coupling during chemical synthesis of RNA, it was dissolved at a concentration in 1,2-dichloroethane (100 mM). The coupling time was 5 min, using 250 mM benzylthiotetrazole as a coupling agent. Oxidation was performed with tert-butylhydroperoxide in toluene (1 M). Capping and detritylation were performed using standard conditions for RNA synthesis. Upon completion of the synthesis, the oligoribonucleotide was cleaved from the solid support and the nucleobases and the phosphodiesters deprotected in a 1:1 mixture of conc. aqueous NH_3 and $MeNH_2$ in EtOH (8 M, 2 mL) at 65 °C for 40 min. The supernatant was collected, the beads washed three times with a mixture of EtOH:H_2O (1:1, 300µL), and the combined washes were dried. The 2′-O-TBDMS groups were removed by treatment with a mixture of Et_3N•3HF:DMF (3:1,800 µL) at 55 °C for 1.5 h, followed by addition of H_2O (200 µL). This mixture was transferred to a 50 mL Falcon tube, *n*-butanol (40 mL) was added, the mixture stored at -20 °C for 12 h, centrifuged and the solvent decanted from the RNA pellet. The crude RNA was subsequently purified by 20% denaturing polyacrylamide gel electrophoresis.

The RNA oligonucleotide bands were visualized under UV light, excised from the gel, crushed, and eluted from the gel with a Tris buffer (2x10 mL; Tris (10 mM, pH 7.5), NaCl (250 mM), Na_2EDTA (1 mM)). The RNA elution solutions were filtered through a 0.45 mm cellulose acetate membrane (Whatman) and desalted using a Sep-Pak cartridge (Waters Corporation). The dried oligoribonucleotide was dissolved in sterile H_2O (400 mL) and its final concentrations was calculated according to Beer's law based on UV absorbance of oligoribonucleotides at 260 nm. Extinction coefficients

were determined by using the UV WinLab oligoribonucleotide calculator (V2.85.04; Perkin Elmer). Molecular weights of the oligoribonucleotide was determined by MALDI-TOF analysis (Bruker, Autoflex III) after calibration with an external standard. The calculated monoisotopic mass (M+H) is 7413.209, whereas observed monoisotopic mass (M+H) is 7413.856 (Figure S1).

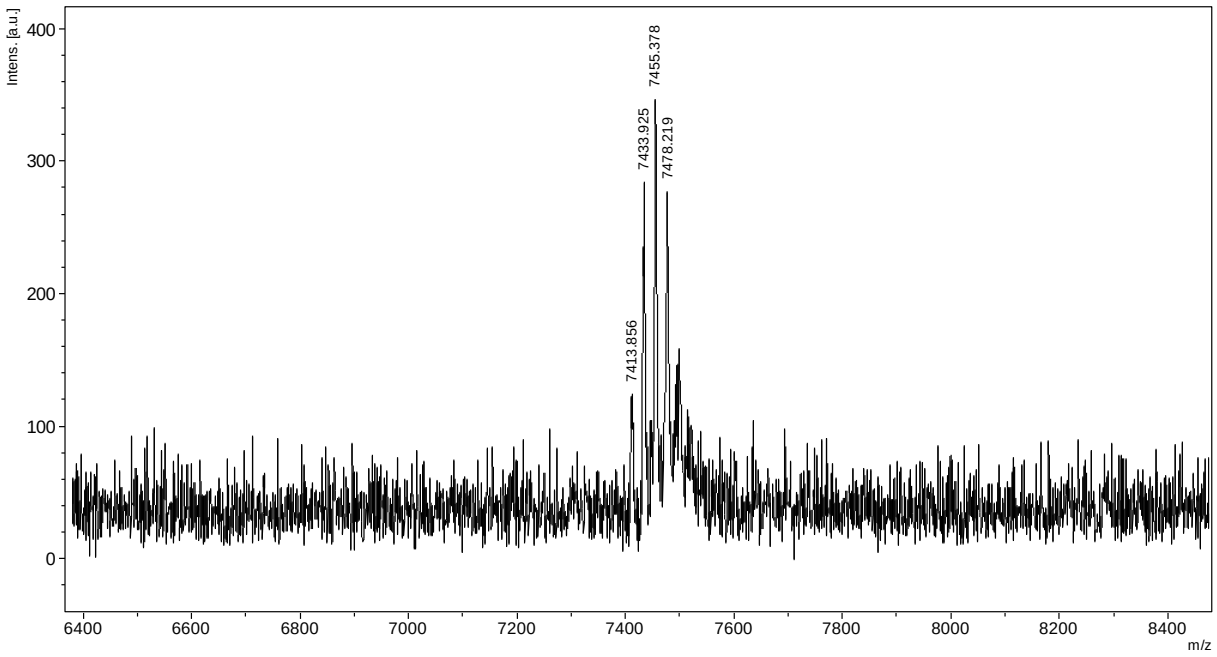

*Figure S1 Maldi-TOF spectrum of **Çm**-labeled 22mer.*

2. Native PAGE

Hybridization of the **Çm** labeled aptamer was verified on a 12% native polyacrylamide gel. As references, the two monomers (22mer and 37mer) as well as the full-length aptamer (TC-ESR) were analyzed on the same gel.

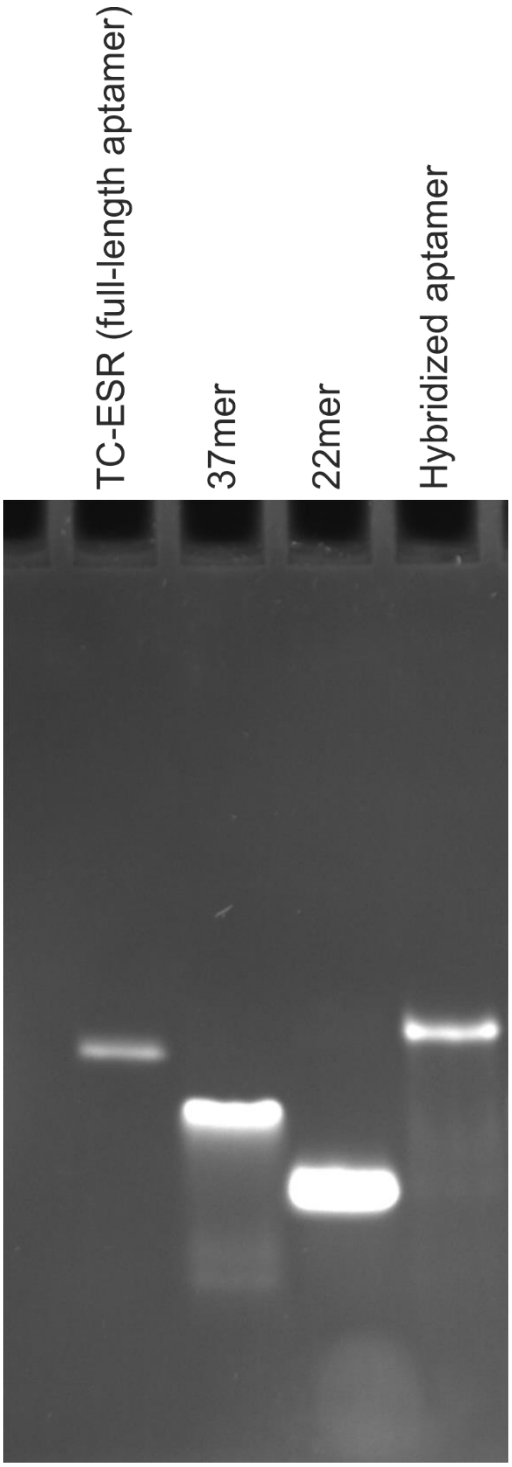

Figure S2 Native polyacrylamide gel of the full-length aptamer (wildtype), the 37mer, the 22mer and the hybrid aptamer. The gel shows complete hybridization of the hybrid construct.

3. ITC-measurements of the hybridized TC-aptamer

ITC measurements were performed in an iTC200 microcalorimeter (MicroCal, GE Healthcare, Chalfont St. Giles, UK) at 25°C. The sample cell (0.2 ml) contained the RNA and the syringe contained 100 µM of the ligand TC. For all measurements, a 20 mM potassium phosphate buffer at pH = 7.5 with 100 mM sodium chloride and 10 mM magnesium chloride was used. The ITC cell contained 5 µM of the unlabeled or labeled aptamer. After preequilibration and an initial delay of 180 s, a first injection of 0.2 ml was performed, followed by 15 serial injections (2.5 ml each) with spacing of 180 s. Stirring speed was 1000 rpm and the reference power was 6 mcal/s. Data were recorded as power (mcal/s) over time (min). Afterwards, the heat associated with each titration step was integrated and plotted against the molar ratio between the titrant and the RNA. Each binding isotherm was background corrected for dilution effects.

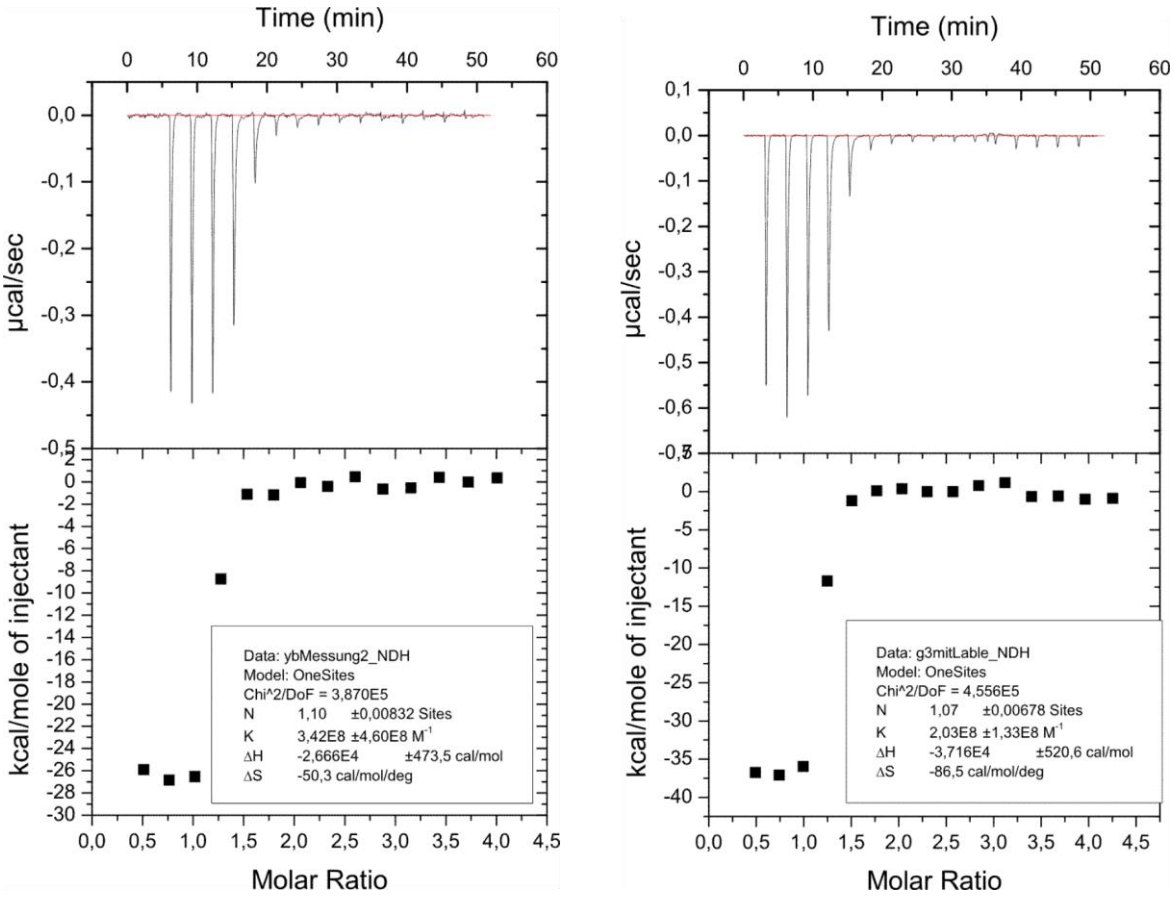

*Figure S3 ITC-measurements of the unlabeled hybrid construct (left) and the **Çm**-labeled hybrid construct (right). Experiments were performed twice. Averaged K_d-values of 6.5 nM (unlabeled) and 7.0 nM (labeled) were obtained.*

4. Pump/probe positions for X-band and Q-band PELDOR

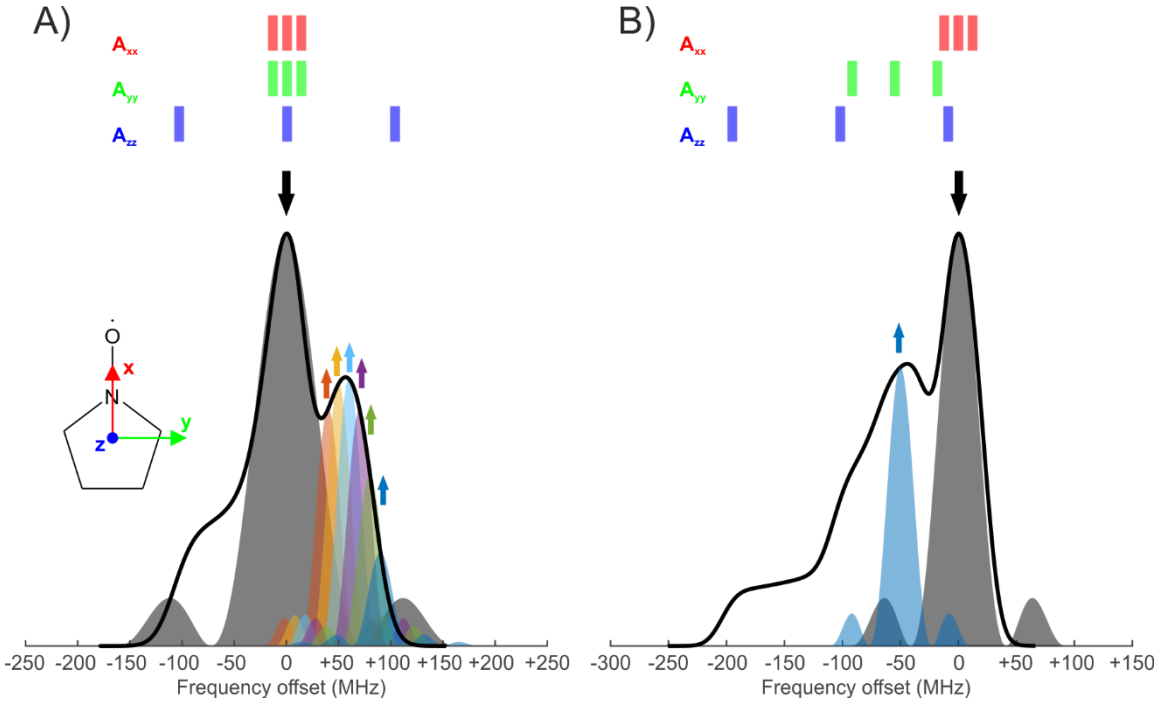

Figure S4 Simulated echo-detected field-swept spectrum using a home written Matlab script (Prisner et al. 2015) *at X-band frequencies (9.4 GHz, black line, A) or Q-band frequencies (34 GHz, black line, B). The frequency position as well as the pulse profile of the pump pulse (12 ns for X-band, 21 ns for Q-band, arrow down, black) and the detection pulses at different frequencies (32 ns for X-band and Q-band, arrow up) are also shown. Offsets of 40, 50, 60, 70, 80 and 90 MHz or -50 MHz were used for X-band and Q-band, respectively. The schematic splitting of the different components of the hyperfine tensor is also shown (red, green and blue). At X-band frequencies, the A_{zz}-component of the hyperfine tensor is spectrally better resolved, thus enabling for orientation selective measurements at X-band.*

5. Primary PELDOR time traces of Mg^{2+} titration experiments

A three-dimensional exponential background correction, assuming a homogenous spatial distribution of the nanoobjects, was used for all PELDOR time traces presented in Figure S5. The area of the exponential fitting was identical for all time traces, that is from 3000 to 4400 ns.

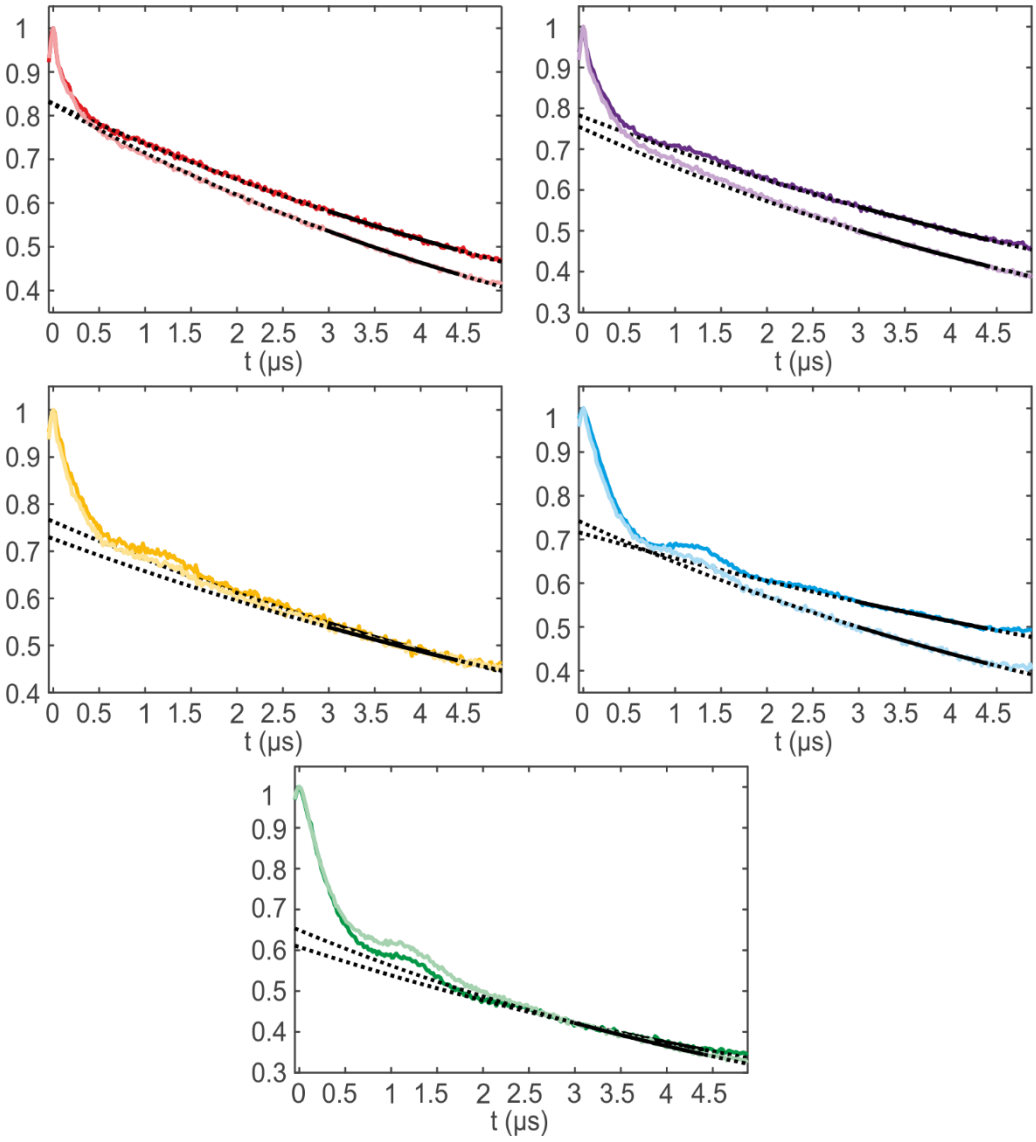

Figure S5 Primary PELDOR traces of Mg^{2+} titration experiments in the presence (bold colors) or absence of TC (pale colors). Mg^{2+} concentrations ranged from 0 mM (red), over 0.22 mM (violet), 0.45 mM (yellow), 1.2 mM (cyan) to 3.0 mM (green). The concentration of RNA was 150 µM. The concentration of TC was 165 µM. Fitted background functions are shown in black.

6. Direct comparison of equivalent PELDOR and distance data w/ and w/o TC

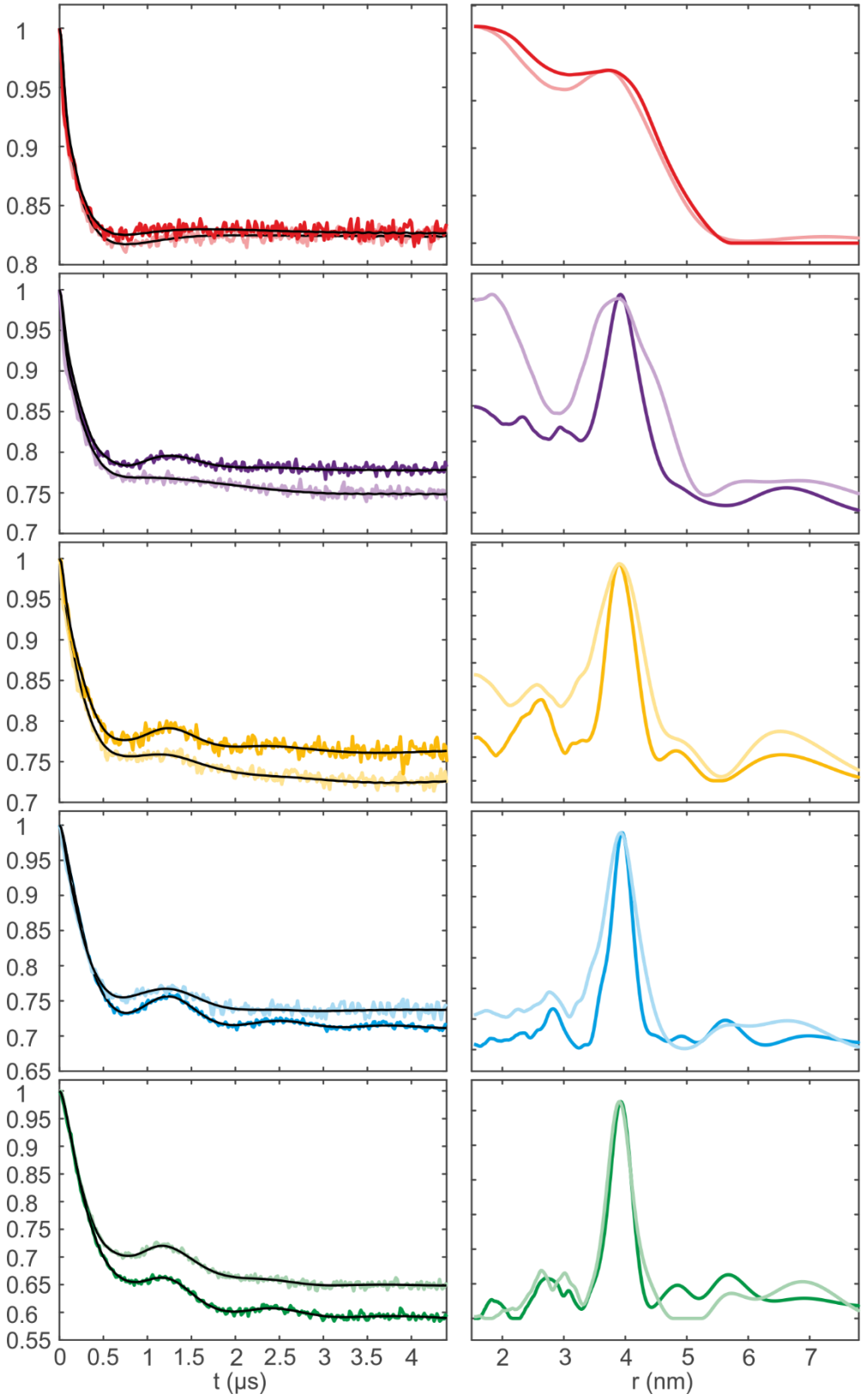

Figure S6 Direct comparison of Mg^{2+} titration experiments in the presence (bold) or absence of TC (pale). Mg^{2+} concentrations ranged from 0 mM (red), over 0.22 mM (violet), 0.45 mM (yellow), 1.2 mM (cyan) to 3.0 mM (green). The concentration of RNA was 150 µM. The concentration of TC was 165 µM. Tikhonov fits are shown in black.

7. Stacked crystal structures of the TC-aptamer

End-to-end stacking of two crystal structures of the TC-aptamer yielded additional distances between the nitroxide spin labels of 2.0 nm, 5.0 nm, 5.5 nm and 8.5 nm (red connection vectors in Figure S7). Due to the rather unspecific nature of helical RNA stacking, rather broad distances due to stacking are expected. It should be noted, that the picture below is a very simplified model. The unmodified TC-aptamer used in this study possesses two blunt ends, whereas the TC-aptamer of the crystal structure still contained the *L1* closing loop of stem *P1* (the loop is cut in Figure S7). Therefore, another 'stacking conformation' with additional stacking distances is possible. However, these distances are expected to be similar to those given in this section.

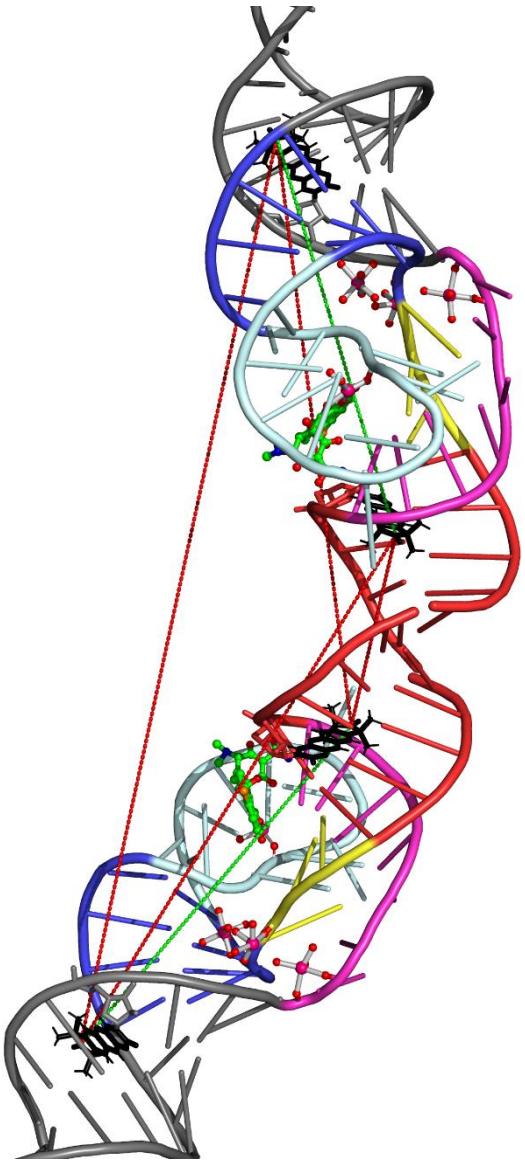

Figure S7 Two crystal structures of the tetracycline-binding aptamer (Xiao et al. 2008) *with two* ***Çm*** *nucleobases each (shown in black) stacked on top of each other to illustrate helical RNA stacking observed with PELDOR. Red connection vectors correspond to distances observed due to stacking. Green connection vectors correspond to the actual intramolecular distance of 3.8 nm.*

8. End-to-end stacking investigated using PELDOR

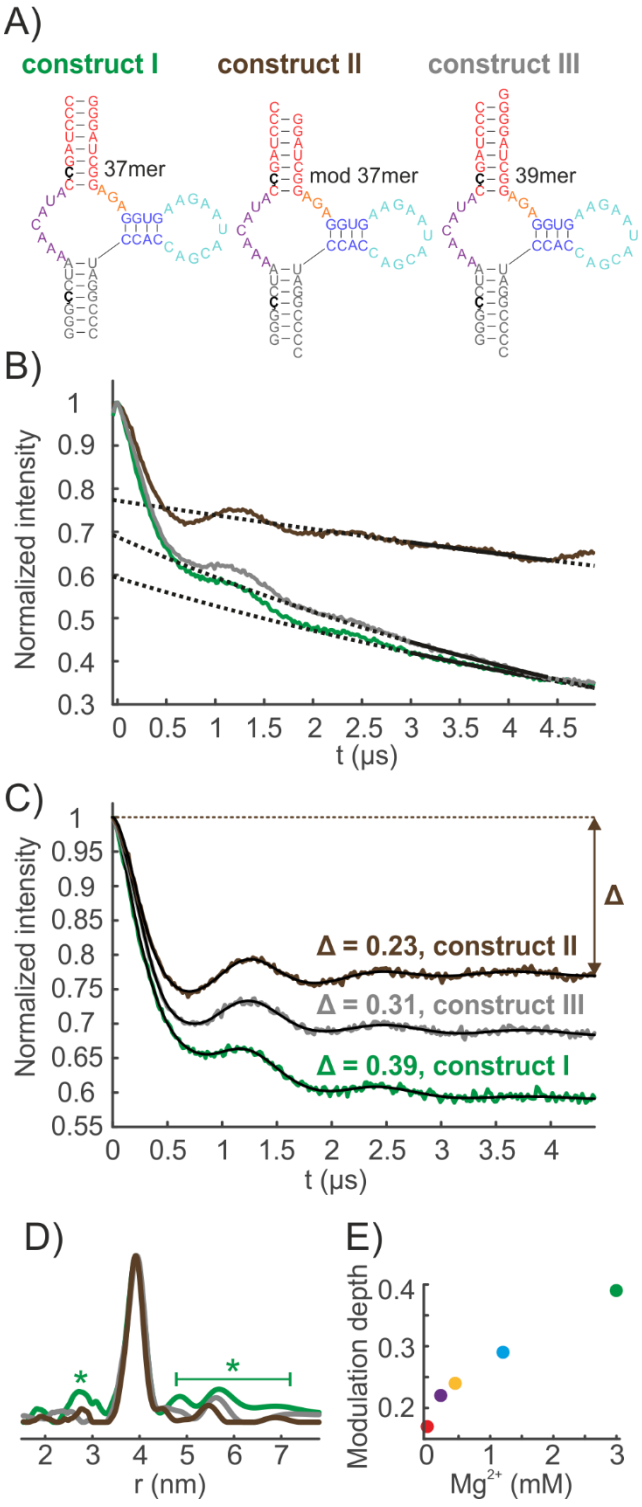

Figure S8 A) Secondary structure of modified TC-aptamers with overhanging ends to prevent stacking (construct II and construct III). The unmodified aptamer of the Mg^{2+} titration studies is also shown (construct III). B) Primary Q-band PELDOR time traces of construct I, II and III. Fitted background functions are shown in black. C) Background corrected Q-band PELDOR time traces of construct I, II and III. Tikhonov fits are shown in black. The time trace of construct II is completely free of stacking artefacts. D) Distance distributions obtained by Tikhonov regularization. All samples contained 150 μM RNA, 165 μM TC and 3 mM Mg^{2+} to ensure folding of the RNA. Distance peaks marked by an asterisk are most likely due to stacking. E) Modulation depth Δ of the PELDOR time traces of Figure 3A as a function of Mg^{2+} concentration.

Figure S8 shows PELDOR data of modified TC-aptamers to investigate helical end-to-end stacking. Two aptamers with different single-nucleotide overhangs were prepared (construct II and III, Figure S8A). Data of modified aptamers are compared to PELDOR data of an unmodified aptamer (construct I, green in Figure S8B-D). Large modulations depths of $\Delta > 0.25$ and additional distances (Figure S8D and Figure S7) are indicative of helical end-to-end stacking. For a pure 2-spin system, where no stacking is possible, and our given experimental parameters the modulation depth cannot exceed a value of $\Delta = 0.25$. If stacking is present, multi-spin interactions of 3,4…-spin systems will lead to an increased modulation depth. Figure S8C and D show that construct III is more prone to stacking than construct II. This is reasonable, as a purine-nucleotide forms the single-overhang of construct III, which is more prone to π-π-stacking than a smaller pyrimidine based single-overhang as used for construct II.

9. Calculation of z_1, z_2 and bend angle φ out of Euler angles

By definition of the two nitroxide principal axis systems ($\boldsymbol{x_i}$, $\boldsymbol{y_i}$, $\boldsymbol{z_i}$) and the dipolar coordinate system ($\boldsymbol{x}$, $\boldsymbol{y}$, $\boldsymbol{z}$), the angle α_1 is always zero. In addition, the angles γ_1 and γ_2 cannot be deduced from X-band PELDOR data, as here the x- and y-components of the hyperfine tensor (A_{xx} and A_{yy}, Figure S3) have similar magnitudes and are spectrally not resolved. However, at higher frequencies (94 GHz, 180 GHz and 260 GHz) the x- and y- components of the spin Hamiltonian are spectrally resolved, so that the angles γ_1 and γ_2 can be assigned unambiguously (Marko et al. 2011; Tkach et al. 2014; Grytz et al. 2017). As the distance vector *r* is known from Q-band measurements, only three parameters remain (β_1, α_2 and β_2) unknown. These angles can be obtained by simulating and fitting orientation selective PELDOR data. If β_1, α_2 and β_2 are known, they can be used to calculate the vectors $\boldsymbol{z_1}$ and $\boldsymbol{z_2}$. Under the assumption that the vectors $\boldsymbol{z_1}$ and $\boldsymbol{z_2}$ are parallel to the z-axis (rotation axis) of the principal axis systems of helices 1 and 2 (grey and red in Figure 1B and Figure 5B), the bend angle φ between the two RNA helices can be calculated.

The bend angle φ can be calculated using the following relation:

$$\varphi\,[deg] = \cos^{-1}(z_1 \cdot z_2) * \frac{180^\circ}{\pi}, \qquad (1)$$

where $\boldsymbol{z_1}$ and $\boldsymbol{z_2}$ correspond to the z-component of the hyperfine tensor of each nitroxide spin. By definition, the $\boldsymbol{z}$ vector is perpendicular to the plane of the five-membered ring. In principle, the dot product of $\boldsymbol{z_1}$ and $\boldsymbol{z_2}$ can be either negative (from -1 to 0) or positive (0 to 1). A positive dot product yields a bend angle φ smaller than 90°, whereas a negative dot product yields a bend angle φ larger than 90°. By looking at the crystal structure, it becomes clear that a bend angle of φ > 90° is far more likely. Therefore, only combinations of $\boldsymbol{z_1}$ and $\boldsymbol{z_2}$ that yielded a negative dot product were considered.

The $\boldsymbol{z_1}$ and $\boldsymbol{z_2}$ vectors of the crystal structure were extracted out of the xyz-matrix of the spin labels by first computing the $\boldsymbol{x_i}$ vector. The $\boldsymbol{x_i}$ vector can be calculated once the xyz-coordiantes of the N- and O-atom of the nitroxide moiety are known. An additional vector *L* can be calculated out of the xyz-coordinates of the N-atom and a neighboring C-atom. Then, the cross product of *L* and $\boldsymbol{x_i}$ can be used to calculate $\boldsymbol{z_i}$.

The $\boldsymbol{z_1}$ and $\boldsymbol{z_2}$ vectors of the simulations were calculated out of the Euler angles β_1, α_2 and β_2. $\boldsymbol{z_1}$ was calculated using the following relation:

$$z_1 = \begin{pmatrix} 1 & 0 & 0 \\ 0 & \cos\beta_1 & -\sin\beta_1 \\ 0 & \sin\beta_1 & \cos\beta_1 \end{pmatrix} \begin{pmatrix} 0 \\ 0 \\ 1 \end{pmatrix}. \quad (2)$$

z_2 was calculated using the following relation:

$$z_2 = \begin{pmatrix} \cos\alpha_2 & -\sin\alpha_2 & 0 \\ \sin\alpha_2 & \cos\alpha_2 & 0 \\ 0 & 0 & 1 \end{pmatrix} \begin{pmatrix} 1 & 0 & 0 \\ 0 & \cos\beta_2 & -\sin\beta_2 \\ 0 & \sin\beta_2 & \cos\beta_2 \end{pmatrix} \begin{pmatrix} 0 \\ 0 \\ 1 \end{pmatrix}. \quad (3)$$

10. Primary PELDOR data of orientation selective X-band PELDOR (3mM Mg^{2+} w/ TC)

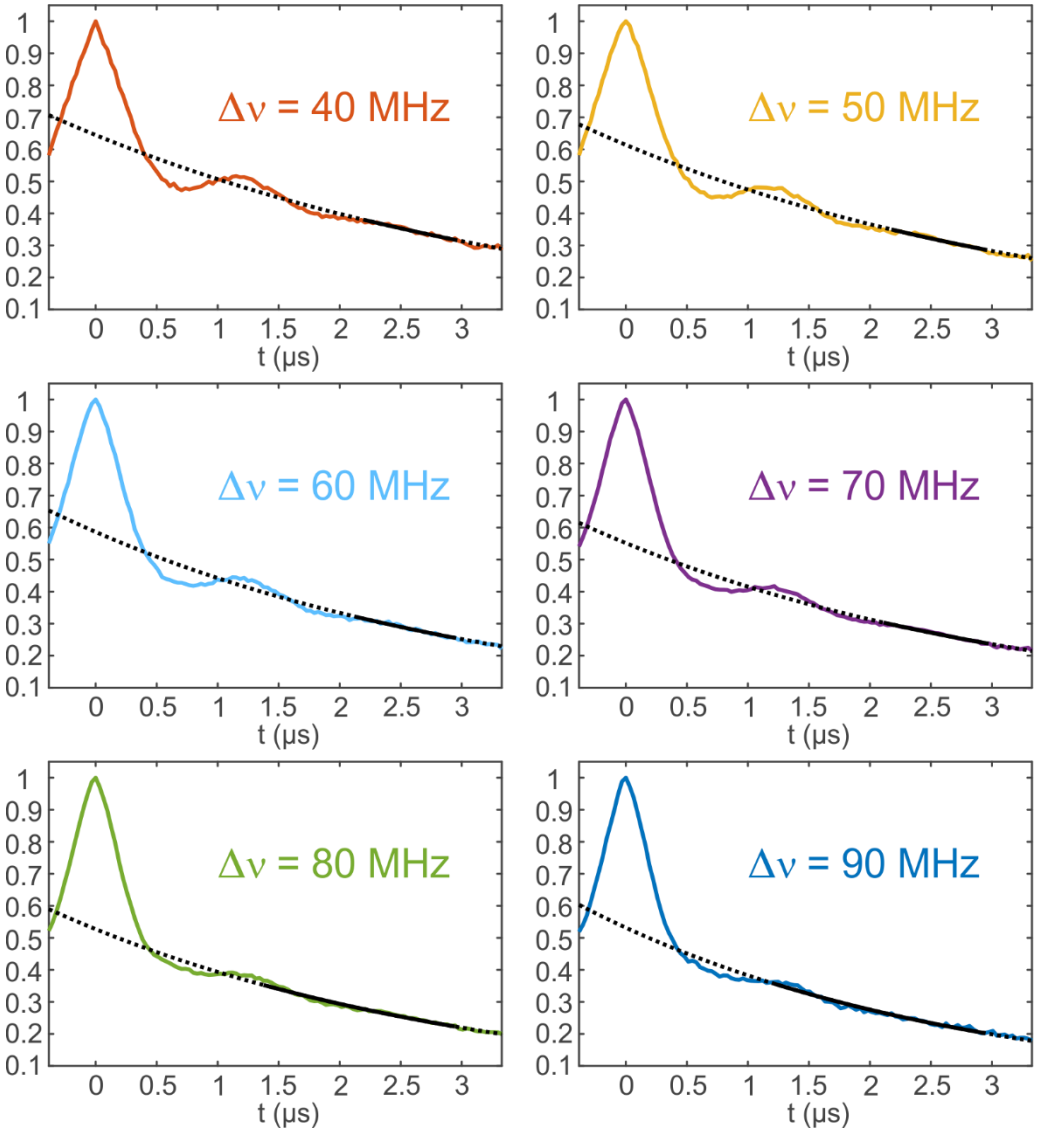

Figure S9 Primary orientation selective PELDOR time traces at X-band frequencies of a sample containing 150 µM RNA, 165 µM TC and 3 mM Mg^{2+}. The color code is identical to the one used in Figure S4. Fitted background functions are shown in black.

11. Distance and frequency domain data of orientation selective X-band (3mM Mg^{2+} w/ TC)

Figure S10A and B show primary and background-corrected PELDOR data of the sum over all offsets presented in Figure S9. Figure S10C and D show Pake patterns and the distance distribution of the different offsets obtained by Fourier transformation and Tikhonov regularization, respectively. With larger offsets, the Pake patterns in Figure S10C gain intensity at $2\omega_{dd}$ (≈ ±1.5 MHz), which is a clear indication for orientation selection. The distance distributions of larger offsets in Figure S10D are also characterized by an artificial distance peak at ≈ 3.1 nm (corresponds to $2\omega_{dd}$). This is because *DeerAnalysis* is not able to process orientation selective PELDOR data. The artificial signal in the distance domain is, however, largely eliminated if the sum over all offsets is processed (bold green distance distribution in Figure S10D).

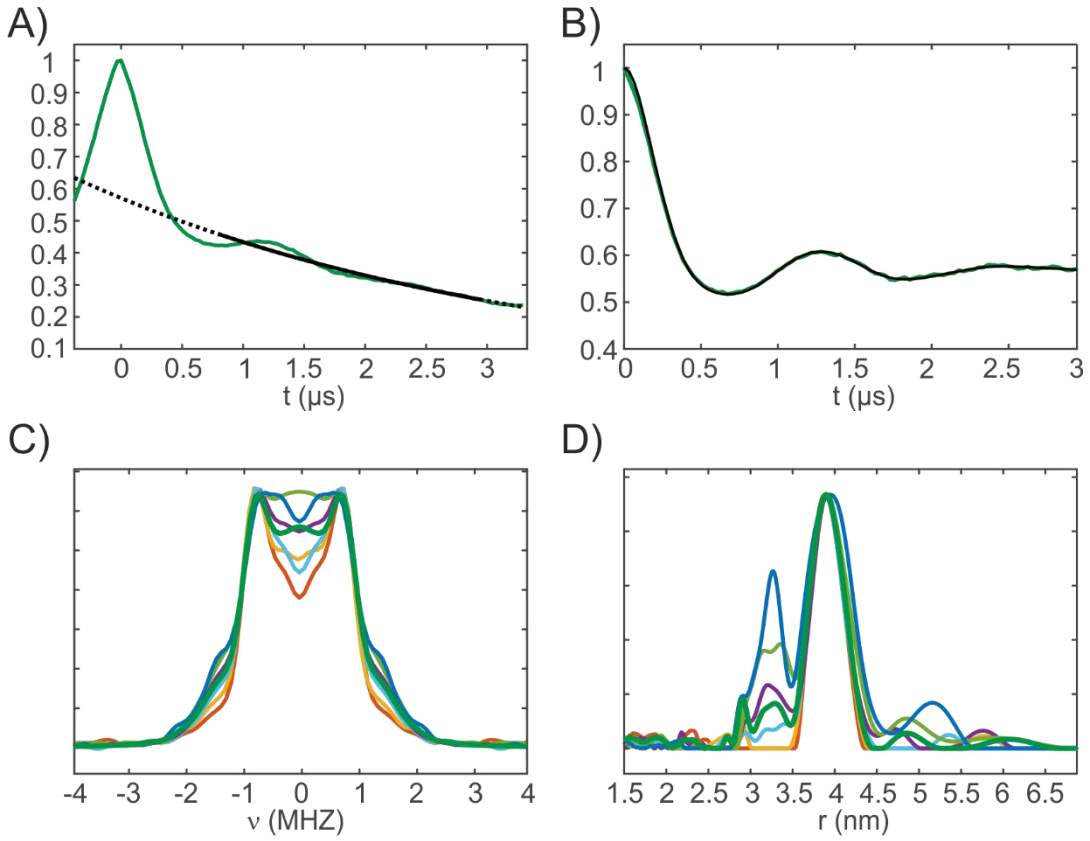

Figure S10 Upper panel: Primary (A) and background-corrected PELDOR time traces (B) of the sum of all PELDOR time traces/offsets presented in Figure S9. The fitted background function and the Tikhonov fit are shown in black. Lower panel: Pake patterns obtained by Fourier transformation (C) and distance distribution obtained by Tikhonov regularization of background-corrected PELDOR time traces presented in Figure S9. The color code is identical to Figure S9. The pake pattern as well as the distance distribution of the sum is also shown for comparison (green).

12. Additional simulated PELDOR time traces

Figure S11 shows additional simulations of PELDOR time traces. Figure S11A shows simulated PELDOR time traces with Euler angles extracted from the crystal structure. Although the experimental oscillation pattern is reasonable well reproduced for offsets of 40 MHz up to 70 MHz, a clear discrepancy is visible for offsets of 80 and 90 MHz respectively. In addition, the experimental time traces are characterized by a stronger dampening of the oscillations.

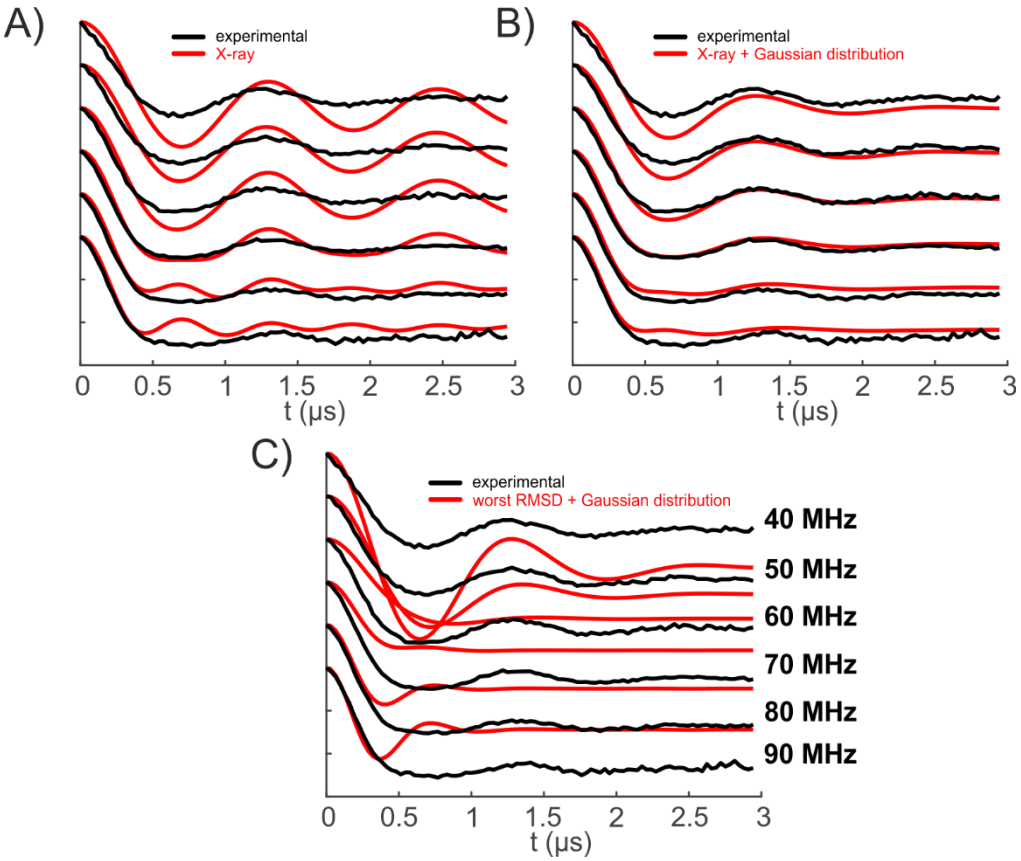

Figure S11 Additional simulations of PELDOR time traces. A): Simulation of Euler angles extracted from the crystal structure. B): Euler angles are identical to A). However, Euler angles β_1, α_2, β_2 and the distance r were convoluted with a Gaussian distribution centered at the respective Euler angle and distance r to account for flexibility of the RNA helices. C) Simulation with set of Euler angles that yielded the worst RMSE. Just as in B), Euler angles β_1, α_2 and β_2 were convoluted with a Gaussian distribution centered at the respective Euler angle and distance r. All simulations used an intraspin distance of r = 3.9 nm. Simulations are compared to experimental data of a sample containing 150 µM RNA, 165 µM TC and 3 mM Mg^{2+}.

To account for the stronger dampening, each Euler angle (β_1, α_2 and β_2) and the distance *r* was convoluted with a Gaussian distribution centered at the respective Euler angle or distance *r*. The Gaussian distributions had standard variations of σ = 0.0625 rad (angles) and σ = 0.225 nm (distance). The Gaussian distribution effectively considers the intrinsic flexibility of the RNA helices. Although the Gaussian distribution leads to a better fit for the offsets of 40 MHz up to 70 MHz (Figure S11B), the

experimental offsets of 80 and 90 MHz are still insufficiently described (the simulations exhibit a clear $2\omega_{dd}$ oscillation, which is not present in experimental data).

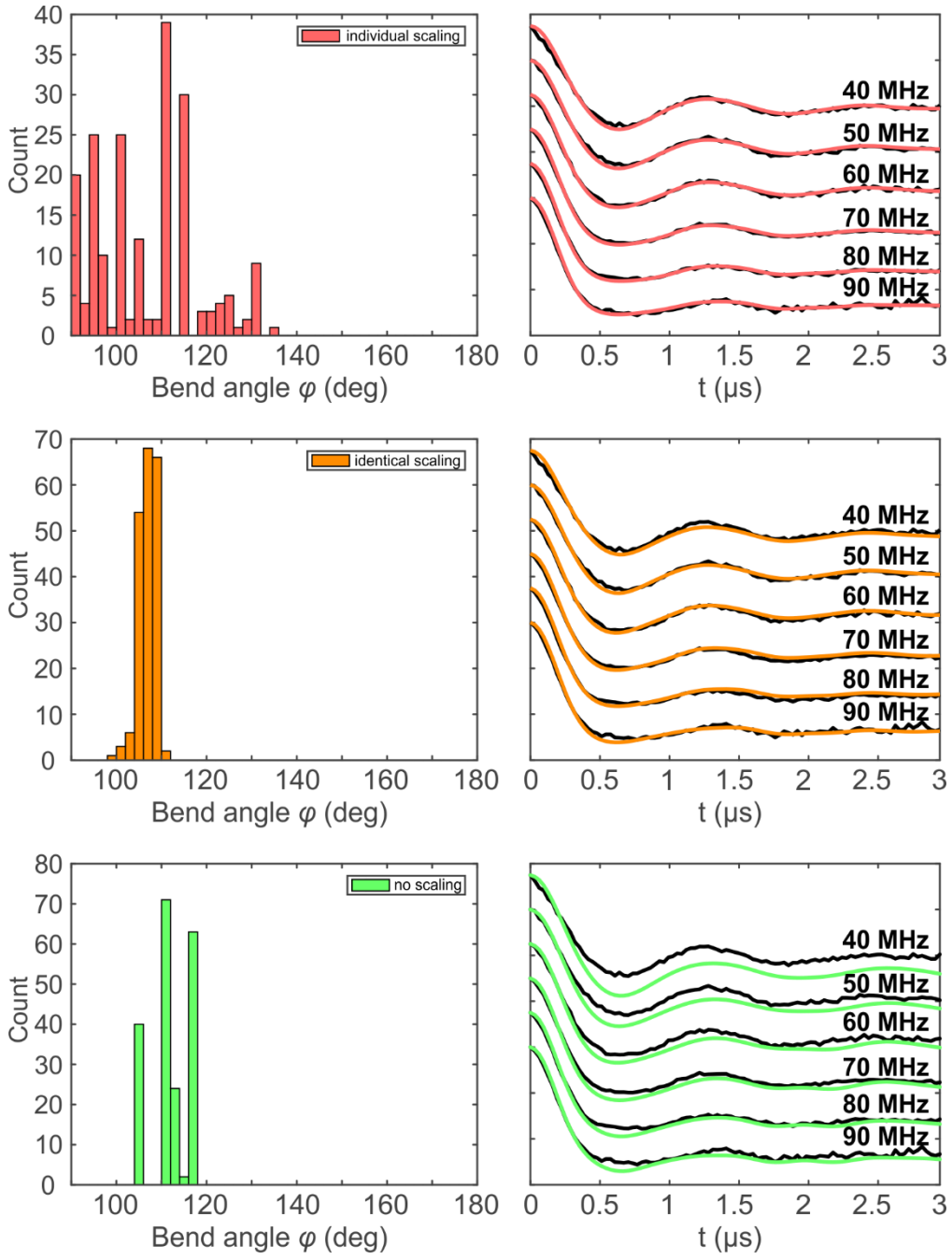

Figure S12 Results of an iterative fitting procedure (Marko and Prisner 2013)*. The first row (pink) presents simulated and fitted data in which the modulation depth of each offset was individually scaled. In the second row (orange), one identical modulation depth scaling factor was applied for all offsets. In the third row (green), no scaling at all was applied. The first column shows a histogram containing the bend angles of 200 iterative fitting steps. The bin size was 2°. The right columns shows the simulated PELDOR time traces out of the 200 iteration steps. The simulated data are compared to experimental data of a sample containing 150 µM RNA, 165 µM TC and 3 mM Mg^{2+}.*

Figure S11C presents simulations of PELDOR time traces that yielded the worst RMSE. Clearly, the oscillation pattern as well as the modulation depth are not well reproduced. The fitting algorithm presented in Figure S11 and Figure 5 include an

identical modulation depth scaling for all six offsets to account for example for incomplete spin labeling. In our cases, the scaling factor was around 0.9 for best simulations.

We also attempted to fit the experimental data using an iterative fitting procedure. A detailed description has been published elsewhere (Marko and Prisner 2013). In a first step, a PELDOR database is created, which contains PELDOR time traces with all possible orientation for Euler angles β_1, α_2 and β_2 and distances. In a second step, an iterative fitting procedure with *n* iterative steps was performed to find the best sum of certain conformers. The above said can be summarized in the following equation:

$$\left\| n^{-1}\left(S_{r,1} + \cdots + S_{r,n-1} + S_{r,n}\right) - S_{exp} \right\|^2 \rightarrow min. \quad (4)$$

Here, *n* represents the number of iterative fitting steps. $S_{r,n}$ represents the simulated PELDOR data of the conformer of the n^{th} iterative fitting step that yielded the best RMSD. S_{exp} represents the experimental PELDOR data. In this study, 200 iterative fitting steps were performed. In contrast to simulations presented in Figure S11, the Euler angles were not convoluted with a Gaussian distribution. The iterative fitting was performed with no scaling of the modulation depth, identical modulation depth scaling for all offsets and individual modulation depth scaling for individual offsets. The bend angles of the 200 iteration steps with identical modulation depth scaling agree perfectly with results presented in Figure 5.

13. *Δr* values of simulated X-band PELDOR data

In order to verify our simulated X-band PELDOR data, we simulated Q-band time traces of the conformers that yielded the best RMSD in Figure 5B and of the conformer pools of the iterative fitting approach (Figure S12). Q-band time traces were then fitted with a two-Gaussian model system or subjected to a Tikhonov regularization in order to obtain distance distributions. The linewidths of all distance distributions agreed very well with the experimental width *Δr*. Data were simulated at Q-band frequencies, because no orientation selection is expected at those frequencies.

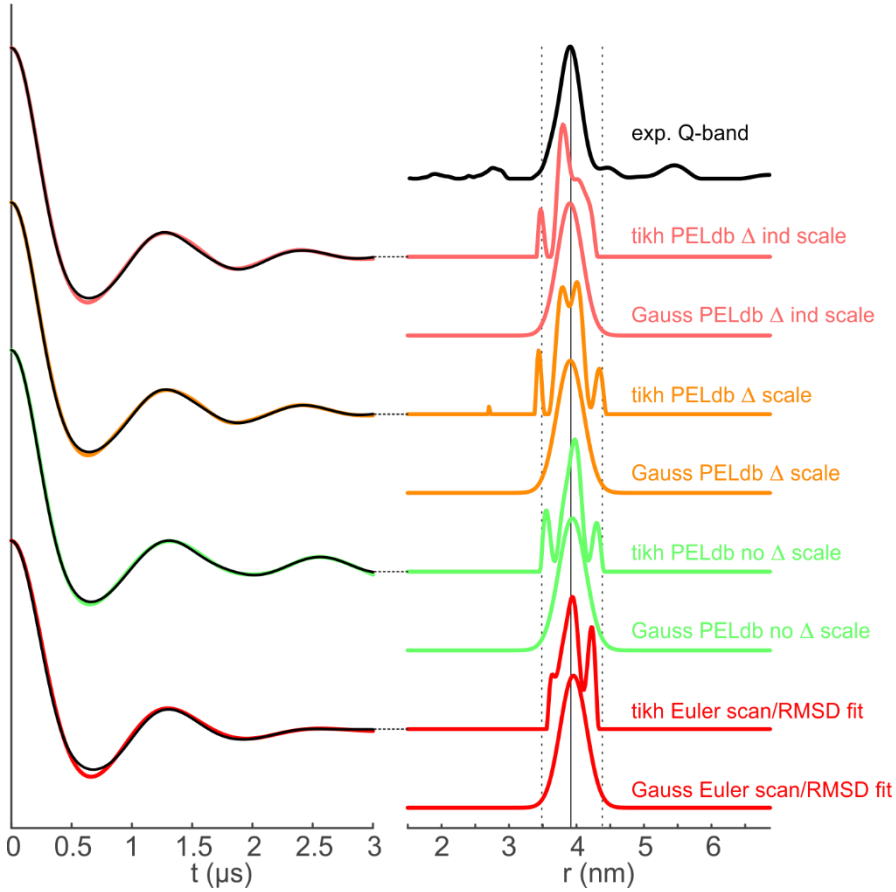

Figure S13 Simulated Q-band PELDOR time traces of conformers that yielded the best RMSD in Figure 5B (red data) and of the conformer pools that were obtained by using an iterative fitting approach (Figure S12). For the iterative fitting approach, the modulation depth was i) not scaled at all (green data), ii) scaled by an identical factor for all offsets (orange data) or iii) scaled individually for different offsets (pink). Distance distributions were obtained by either performing a Tikhonov regularization or by applying a 2-Gaussian model fit. The experimental distance distribution of Q-band PELDOR data of construct II is shown for comparison in black. Simulated PELDOR time traces are shown on the left in their respective color code. The Tikhonov fits are shown in black.

14. Orientation selective X-band PELDOR data at intermediate Mg^{2+} concentrations (0.45 mM Mg^{2+} w/ and w/o TC)

This section presents orientation selective PELDOR data of samples containing 150 µM RNA and 0.45 mM Mg^{2+}, either in the presence (bold colors) or absence (pale colors) of 165 µM TC. Figure S14 shows primary PELDOR data with offsets ranging from 40 MHz to 90 MHz.

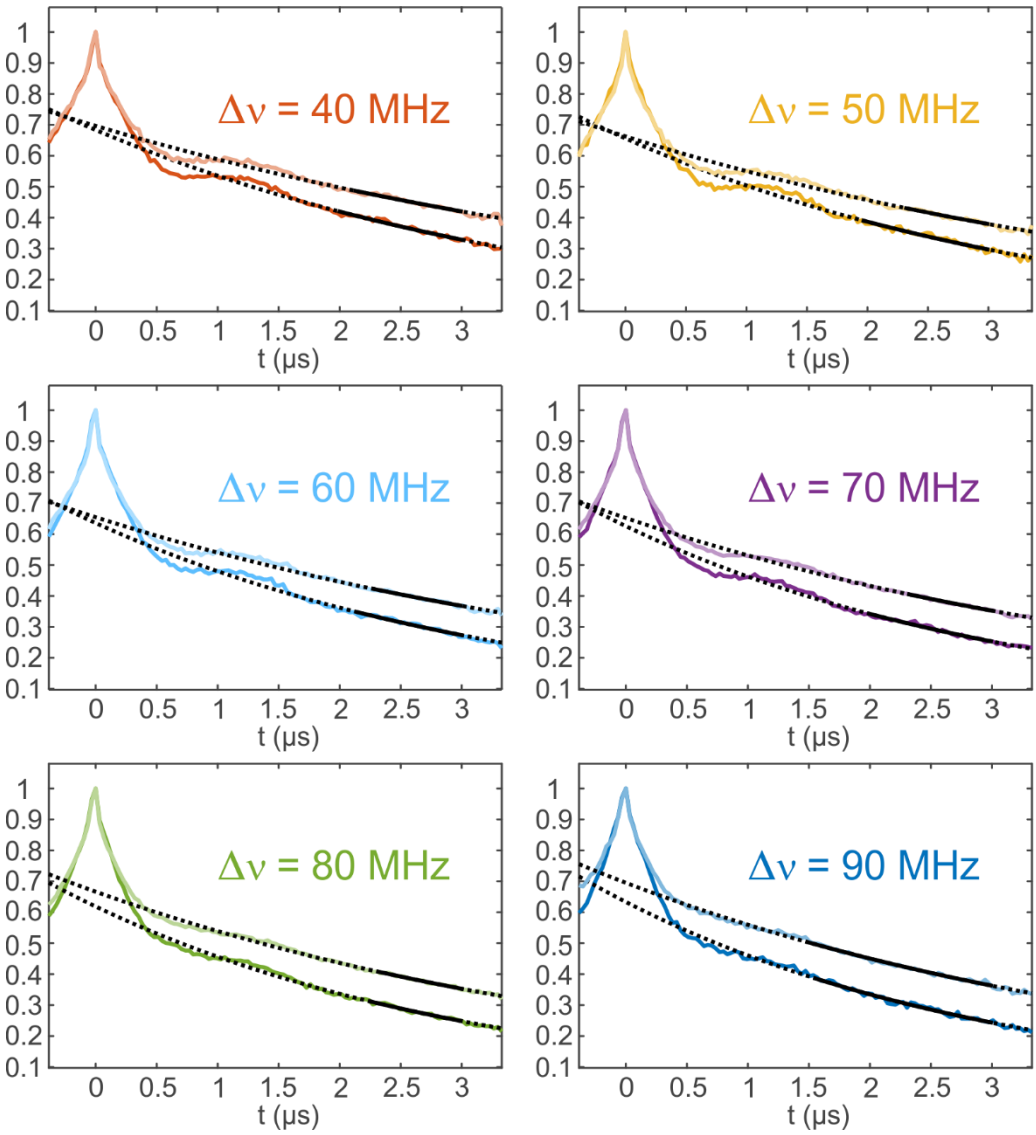

Figure S14 Primary orientation selective X-band PELDOR data of a sample containing 150 µM RNA, 165 µM TC and 0.45 mM Mg^{2+} (bold colors) and of a sample containing 150 µM RNA and 0.45 mM Mg^{2+} (pale colors). The color code for the offsets is identical to the one used in Figure S4. Fitted background functions are shown in black.

Figure S15 shows processed PELDOR data of samples containing 150 µM RNA and 0.45 mM Mg^{2+}, either in the presence (left column, bold colors) or absence (right column, pale colors) of 165 µM TC. The first row shows background-corrected

PELDOR data A) and B), the seconds row shows Pake pattern obtained by Fourier transformation C) and D) and the third row shows the distance distribution obtained by Tikhonov regularization E) and F). The color code of the offsets is identical to Figure S14.

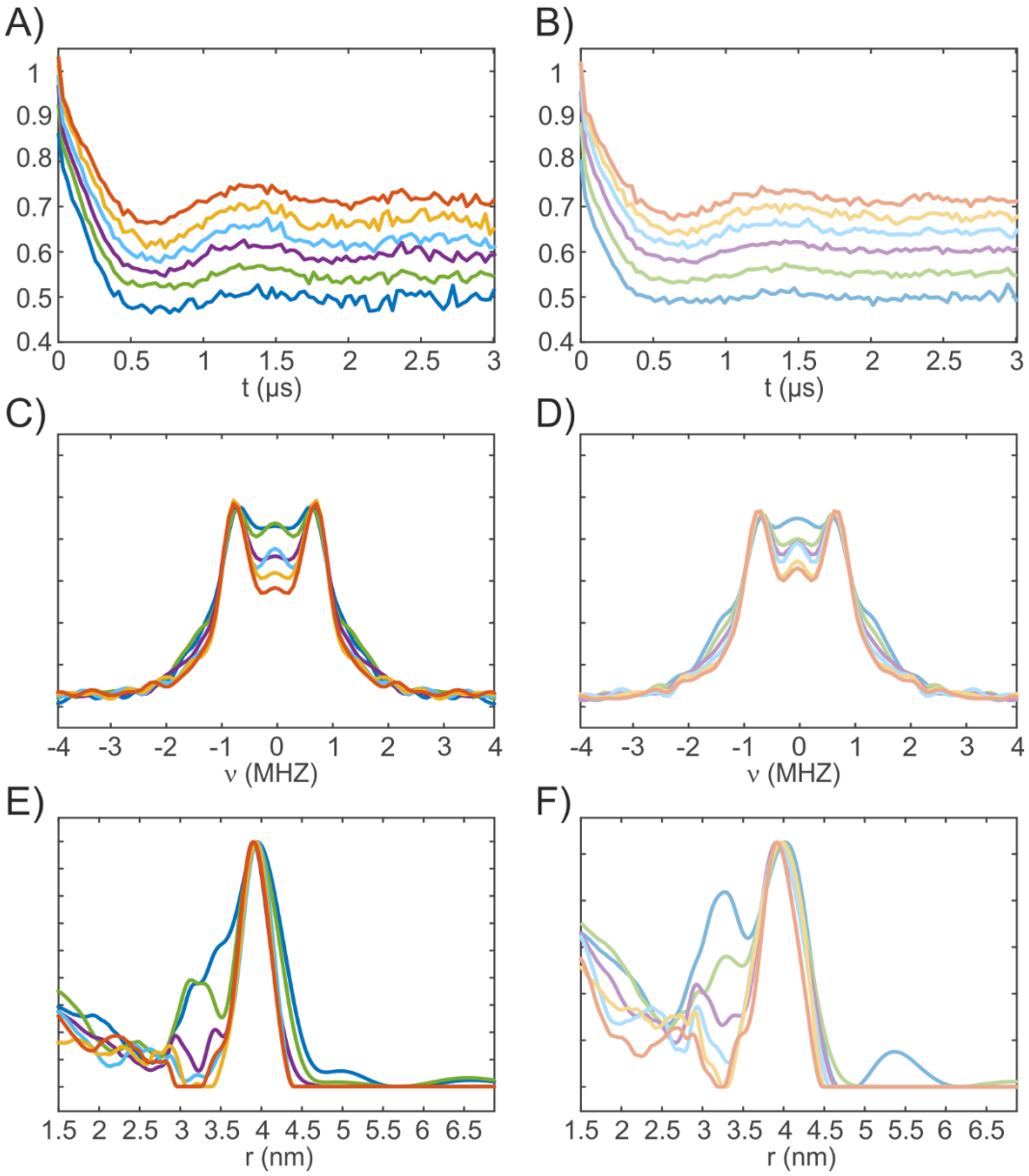

Figure S15 Processed PELDOR data of samples containing 150 μM RNA and 0.45 mM Mg^{2+} either in the presence (left column, A), C) and E)) or absence of TC (right column, B), D) and F)). The first row shows background-corrected PELDOR data previously shown in Figure S14. The second column shows Pake patterns for different offsets obtained after Fourier transformation. The third column shows distance distributions for different offsets obtained after Tikhonov regularization. The color code for the offsets is identical to the previous Figure S14.

For both samples, clear orientation selection is visible. Surprisingly, orientation selection seems stronger for a sample without any TC (right column, Figure S15B, D and F). However, one should remember that at intermediate Mg^{2+} concentrations, samples without TC show a higher probability for shorter distances. These shorter

distances stack upon the artificial $2\omega_{dd}$-distance peak due to orientation selection, which leads to an apparent higher degree of orientation selection for a sample without TC. Simulation of the traces presented in Figure S15A and B did not yield significant different orientations (bend angles) than those presented in Figure S12.

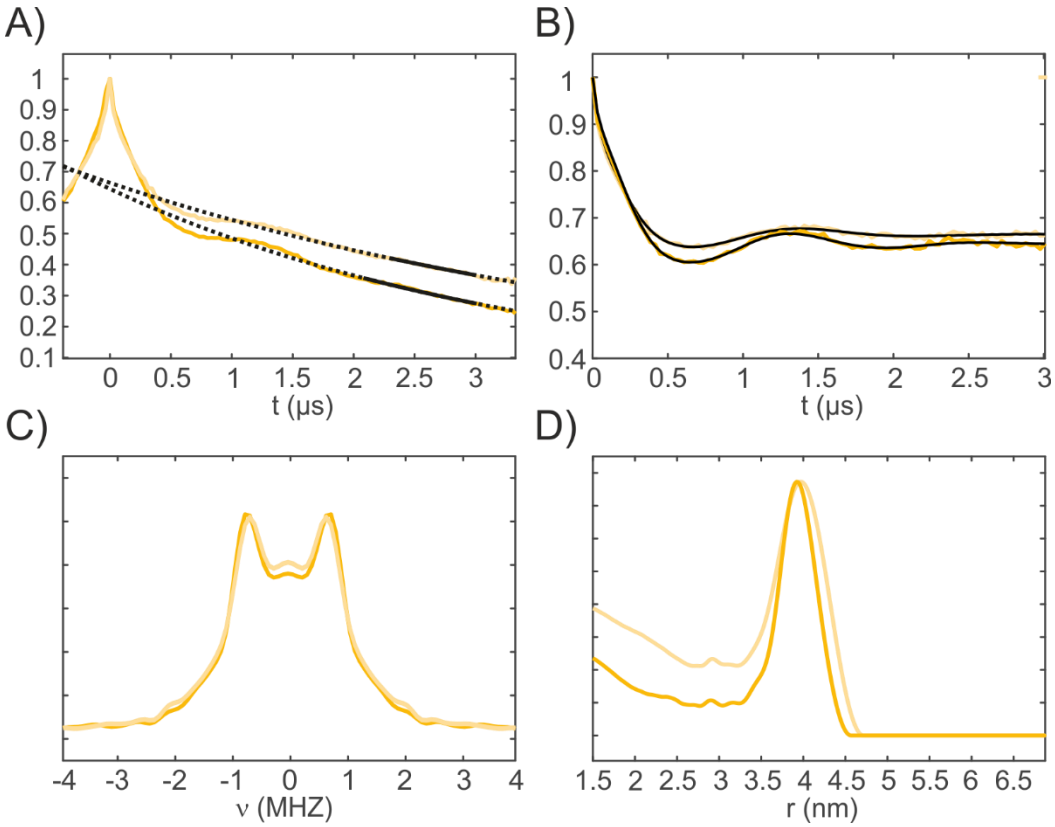

Figure S16 Primary and processed PELDOR data of the sum over all offsets of data presented in Figure S14 and Figure S15. Yellow lines correspond to a sample 150 µM RNA, 165 µM TC and 0.45 mM Mg^{2+}. Pale yellow lines correspond to a sample containing 150 µM RNA and 0.45 mM Mg^{2+}. A) Primary PELDOR data with the fitted background function shown in black. B): Background-corrected PELDOR data with the Tikhonov fits shown in black. C): Pake patterns obtained after Fourier transformation. D): Distance distributions obtained after Tikhonov regularization.

Summation over all offsets of primary PELDOR data presented in Figure S14 yielded data that are in agreement with Q-band Mg^{2+} titration studies, which were presented in Section 3.1 of the main text. Summed X-band PELDOR time traces of a sample containing 150 µM RNA and 0.45 mM Mg^{2+} exhibit stronger dampening and a broader linewidth Δr in the distance domain (pale yellow lines in Figure S16B and D), than summed X-band PELDOR time traces of a sample containing 150 µM RNA, 165 µM TC and 0.45 mM Mg^{2+} (bold yellow lines in Figure S16B and D). The sample without TC has also a higher probability for smaller distances (Figure S16D).

15. References

Grytz CM, Kazemi S, Marko A, Cekan P, Güntert P, Sigurdsson ST, Prisner TF. 2017. Determination of helix orientations in a flexible DNA by multi-frequency EPR spectroscopy. *Phys Chem Chem Phys* **19**: 29801–29811.

Höbartner C, Sicoli G, Wachowius F, Gophane DB, Sigurdsson ST. 2012. Synthesis and characterization of RNA containing a rigid and nonperturbing cytidine-derived spin label. *J Org Chem* **77**: 7749–7754.

Marko A, Denysenkov V, Margraf D, Cekan P, Schiemann O, Sigurdsson ST, Prisner TF. 2011. Conformational flexibility of DNA. *J Am Chem Soc* **133**: 13375–13379.

Marko A, Prisner TF. 2013. An algorithm to analyze PELDOR data of rigid spin label pairs. *Phys Chem Chem Phys* **15**: 619–627.

Prisner TF, Marko A, Sigurdsson ST. 2015. Conformational dynamics of nucleic acid molecules studied by PELDOR spectroscopy with rigid spin labels. *J Magn Reson* **252**: 187–198.

Tkach I, Halbmair K, Höbartner C, Bennati M. 2014. High-frequency 263 GHz PELDOR. *Appl Magn Reson* **45**: 969–979.

Xiao H, Edwards TE, Ferré-D'Amaré AR. 2008. Structural Basis for Specific, High-Affinity Tetracycline Binding by an In Vitro Evolved Aptamer and Artificial Riboswitch. *Chem Biol* **15**: 1125–1137.